UNIVERSITY OF THESSALY
SCHOOL OF ENGINEERING
DEPARTMENT OF MECHANICAL ENGINEERING

Doctoral Thesis

NUMERICAL & THEORETICAL STUDY OF THE STATIC RESPONSE OF COATED MICROBUBBLES SUBJECT TO UNIFORM AND DISTRIBUTED LOAD-APLLICATION ON THE ESTIMATION OF THE SHELL ELASTIC PROPERTIES

by
ALKMINI D. LYTRA
Diploma in Mechanical Engineering, University of Thessaly, 2011
M.Sc. in Mechanical Engineering, University of Thessaly, 2013

Thesis
Submitted in partial fulfillment of the requirements
for the degree of Doctor of Philosophy in Mechanical Engineering
Volos, February 2017

Approved by the members of the Examination Committee:

1st Member (Supervisor)	Dr. Nikos Pelekasis, Professor Dept. of Mechanical Engineering University of Thessaly
2nd Member	Dr. Antonios Giannakopoulos, Professor Dept. of Civil Engineering University of Thessaly
3rd Member	Dr. Vasilis Bontozoglou, Professor Dept. of Mechanical Engineering University of Thessaly
4th Member	Dr. Nikolaos Andritsos, Professor Dept. of Mechanical Engineering University of Thessaly
5th Member	Dr. Spyridon Karamanos, Professor Dept. of Mechanical Engineering University of Thessaly
6th Member	Dr. Athanasios Papathanasiou, Assistant Professor School of Chemical Engineering National Technical University of Athens
7th Member	Dr. Vassilis Sboros, Reader Institute of Biological Chemistry, Biophysics & Bioengineering Heriot-Watt University, Edinburgh, UK

Acknowledgments

First and foremost, I wish to express my sincere gratitude to my advisor Professor Nikos Pelekasis, for giving me the opportunity to work in his research team and for everything I learned these past six years under his supervision. His guidance helped me in all these years of research and in writing this thesis as well. He stands as a mentor to me and has influenced my understanding of science.

In addition, I would like to thank all the members of the examination committee for their useful remarks and suggestions. I am also grateful to Professor A. Giannakopoulos for his valuable suggestions and discussions on contact mechanics. In addition, I would like to acknowledge the contribution of Professor V. Sboros and Professor V. Koutsos, who provided to me the experimental AFM data. The comparison of numerical results with the experiments gave a more complete picture and supported the present work. Moreover, I would like to thanks Professor S. Karamanos as his post-graduate course «Finite elements and stability of structures» gave me the initial insights in the field.

Most part of the present thesis was financially supported by the research project «CONTAGEUSNUMSTADY» in the context of the program Aristeia I. I would also like to acknowledge the financial support that the Department of Mechanical Engineering gave me through a scholarship during my master studies and a funding for the participation in two conferences as PhD student.

Furthermore, I wish to thank my colleagues Dr. M. Vlachomitrou, Dr. K. Efthymiou and PhD student E. Benos for the excellent collaboration and the pleasant working environment. Especially, I would like to thank Dr. M. Vlachomitrou, who among other aspects introduced me in the Linux environment reducing significantly the computational time. A special thanks goes also to Dr. K. Tsiglifis and Dr. D. Dimopoulos who were always interested in the progress of my thesis and for their contribution in this research, which is always a reference for me.

I cannot forget my friends, who always support and encourage my efforts. Thus, I want to thank them for being always there for me.

Finally, I would also like to express my gratitude to my family who always support me, especially when I chose to continue my studies these last years. The present thesis is dedicated with love and respect to my family.

Alkmini D. Lytra
Volos, February 2017.

Ευχαριστίες

Αρχικά, θα ήθελα να εκφράσω ένα ειλικρινές ευχαριστώ στον επιβλέποντά μου, Καθηγητή Νίκο Πελεκάση, που με δέχθηκε στην ερευνητική του ομάδα και όλα όσα έμαθα υπό την επίβλεψη του. Όλα αυτά τα χρόνια παρακολουθεί την διατριβή από πολύ κοντά και με καθοδήγησε με επιστημονικό τρόπο από την πρώτη μέρα στο να μελετήσω τον θαυμαστό κόσμο της μηχανικής των μικροφυσαλίδων. Ο τρόπος σκέψης και η διορατικότητα του κατά την επίλυση προβλημάτων στέκονται για μένα ως παράδειγμα ζωής.

Ιδιαίτερα ευγνώμων είμαι σε όλους τους καθηγητές της 7μελούς εξεταστικής επιτροπής για την ανάγνωση της διατριβής, τα σχόλια και τις παρατηρήσεις τους που θα αναδείξουν διάφορες πτυχές της ή και σημεία που απαιτούν περαιτέρω μελέτη. Ταυτόχρονα, θα ήθελα να ευχαριστήσω ιδιαιτέρως τον Καθηγητή Α. Γιαννακόπουλο, για τις πολύ σημαντικές του παρατηρήσεις πάνω σε θέματα μηχανικής και ιδιαιτέρως προβλημάτων επαφής. Τους Καθηγητές Β. Σμπόρο και Β. Κουτσό, για την ευγενική παραχώρηση πειραματικών αποτελεσμάτων από AFM, καθώς και την μεταφορά της πολύτιμης εμπειρίας τους πάνω σε αυτό. Επιπλέον, θα ήθελα να ευχαριστήσω τον Καθηγητή Σ. Καραμάνο για την διδασκαλία των μαθημάτων πεπερασμένων στοιχείων και ευστάθειας των κατασκευών στο μεταπτυχιακό πρόγραμμα σπουδών, θέτοντας έτσι τις βάσεις σε αυτά τα πεδία.

Το μεγαλύτερο μέρος αυτής της διατριβής έχει χρηματοδοτηθεί μέσω του ερευνητικού προγράμματος «CONTAGEUSNUMSTADY», στο πλαίσιο του Αριστεία Ι. Ιδιαιτέρως θα ήθελα να ευχαριστήσω το Τμήμα Μηχανολόγων Μηχανικών του Π.Θ. για την χορήγηση υποτροφίας κατά την διάρκεια των μεταπτυχιακών μου σπουδών και την χρηματοδότηση για συμμετοχή σε δύο συνέδρια ως διδακτορική φοιτήτρια.

Ταυτόχρονα, θέλω πω ένα μεγάλο ευχαριστώ στα υπόλοιπα μέλη της ερευνητικής ομάδας, την Δρ. Μ. Βλαχομήτρου, τον Δρ. Κ. Ευθυμίου και τον υπ. Δρ. Ε. Μπένο για την άριστη συνεργασία και το ιδιαίτερα ευχάριστο περιβάλλον καθ' όλη τη διάρκεια της διατριβής. Ιδιαιτέρως να ευχαριστήσω την κα Βλαχομήτρου, καθώς ανάμεσα σε πολλά άλλα, με εισήγαγε στο περιβάλλον linux και αρκετές από τις προσομοιώσεις διεξήχθησαν εκεί, μειώνοντας σημαντικά τον υπολογιστικό χρόνο. Ένα ιδιαίτερο ευχαριστώ στους Δρ. Κ. Τσιγκλιφή και Δρ. Δ. Δημόπουλο για το ενδιαφέρον που δείχνουν πάντα για την πορεία της διατριβής, αλλά και για τη σημαντική συμβολή τους σε ερευνητικά θέματα, που αποτελεί πλέον αναφορά.

Οι φίλοι είναι συνήθως εκείνοι οι άνθρωποι, που ίσως να μην γνωρίζουν με λεπτομέρειες με τι ασχολείσαι, αλλά ξέρουν να σε στηρίζουν σε κάθε πτυχή της καθημερινότητας. Έτσι, θέλω ευχαριστήσω τους Δημήτρη, Έφη, Σπύρο, Βασίλη, Γιάννη, Μαρία, Κώστα, Κώστα, Δάφνη, Κώστα, Δήμητρα, Μάκη, Ξανθούλα, Φαίδρα και Θένια που το ενδιαφέρον και η στήριξη τους είναι ιδιαιτέρως ειλικρινή και έμπρακτα.

Τέλος, θα ήθελα να ευχαριστήσω την οικογένειά μου, που με στηρίζει σε κάθε επιλογή μου και ιδιαίτερα στην παρούσα χρονική συγκυρία που επέλεξα να συνεχίσω τις σπουδές μου. Εύχομαι κι εγώ με την σειρά μου να στάθηκα επάξια σε αυτό που μου ανατέθηκε. Η διατριβή αφιερώνεται με αγάπη και σεβασμό στην οικογένειά μου.

Αλκμήνη Δ. Λύτρα,
Βόλος, Φεβρουάριος 2017.

This work was performed in the framework of the operational program: «Education and lifelong learning» - «**Aristeia I**» and was cofounded by the European Union (European Social Fund) and national resources.

Η παρούσα έρευνα υλοποιήθηκε στο πλαίσιο της πράξης «Αριστεία Ι » του επιχειρησιακού προγράμματος «Εκπαίδευση και Δια Βίου Μάθηση» και συγχρηματοδοτήθηκε από την Ευρωπαϊκή Ένωση (Ευρωπαϊκό Κοινωνικό Ταμείο-ΕΚΤ) και από εθνικούς πόρους.

NUMERICAL & THEORETICAL STUDY OF THE STATIC RESPONSE OF COATED MICROBUBBLES SUBJECT TO UNIFORM AND DISTRIBUTED LOAD-APLLICATION ON THE ESTIMATION OF THE SHELL ELASTIC PROPERTIES.

Alkmini D. Lytra
University of Thessaly, Dept. of Mechanical Engineering, 2017

Supervisor: Dr. Nikos Pelekasis, Professor of Computational Fluid Dynamics

Abstract

The static response of contrast agent microbubbles is investigated by means of theoretical and numerical formulation. The shell coating is biocompatible and provides mechanical strength, thus renders the microbubbles as excellent enhancers in medical imaging and drug delivery vectors (in vivo). Characterization of shell parameters, namely stretching and bending moduli, is of great importance for the above applications. Two major families of coated microbubbles are normally employed, namely those coated by polymeric and phospholipid shells. The former type of shells is characterized by larger elasticity modulus in comparison with phospholipid shells. Lately, the atomic force microscope (AFM) has emerged as a powerful tool for estimation of the above properties through force-deformation curves. In this context, one of the major targets of the present doctoral dissertation is the modelling of the static response of coated microbubbles as they are compressed by the AFM cantilever. In addition, a methodology is proposed for the estimation of the elastic properties for both types of shells.

Two theoretical and numerical models have been developed in order to describe the contact between the cantilever and the shell. The cantilever is considered as a flat and rigid surface, while the shell as an elastic membrane and the encapsulated gas is treated as compressible. In the first model is a simple representation of the loading, which is assumed as a point at the end of the contact line, while in the second the shell is loaded by the disjoining pressure as a result of the thinning of the liquid phase between the shell and the cantilever. The degree of thinning describes the resulting force between the two surfaces, attraction or repulsion, depending on their relevant position. In any case, the normal and tangential force balances along with the isothermal compression are solved via finite elements. The elastic tensions are described by appropriate constitutive laws, the disjoining pressure by the derivative of an adhesive potential and the deformations are considered as axisymmetric. Benchmark calculations against analytical results verify the validity of modeling. The results of each model are presented in force-deformation curves, where the possibility of buckling near the contact is investigated. In the first model, the response is initially linear (Reissner regime) and when buckling takes place (Pogorelov regime) the response in non-linear curved downwards. The linear solution is still an option after the buckling point, but has higher energy than the buckling solution. A third non-linear curved upwards regime is detected in relative high values of deformation in the post-buckling solution, as a result of significant increase of the internal pressure in comparison with shell rigidity. The above regimes are recovered also in the intermolecular forces model. In both models, the dimensionless bending

stiffness, $\hat{k}_b$, which defines the relative importance of bending rigidity in comparison with stretching, specify the position of the bifurcation point. Microbubbles coated with polymer have usually a relative small dimensionless bending resistance $\hat{k}_b \sim 10^{-5}$, which explains the buckling behavior of experimental AFM force-deformation curves, while in shell covered with lipid the dimensionless bending resistance is higher $\hat{k}_b \sim 10^{-3}$, thus buckling is not the energetically favorable solution, because the resistance to bending is high. In addition, when adhesion is strong, the local buckling is translated to higher values of force and deformation or in extreme cases postponed, because the shell is in significant attraction with the cantilever, thus tensile tensions are developed which prevent buckling. The internal pressure tends to increase when surface tension is accounted for, while the opposite happens when the shell has residual compressive tensions, which also tend to low the buckling point. The above aspects are studied via parametric analysis.

In addition, upon appropriate modification of the equilibrium equations, a similar study is also conducted for free microbubbles, which are not covered with elastic material and they response is governed by the surface tension and the internal pressure. In this case, buckling was not detected, as it was expected, and their response in force-deformation curve is almost quadratic. This study is usufull for nano-bubbles, which usually are not covered.

Employing the analytical equations for the linear and non-linear regimes, Reissner and Pogorelov, respectively, on the experimental force-deformation curves of microbubbles coated with polymer the Young modulus and the shell thickness are calculated simultaneously. The results are in very good agreement with the experimental estimates. In addition, the force – deformation curves of microbubbles covered with lipid monolayer are almost linear and in high values of deformation a regime dominated by the gas pressure is detected. Combination of Reissner equation with a Lulevich et al and Shanahan analytical results can provide the area dilatation and the bending moduli. Perfoming simulations with both models the experimental response is recovered.

The second problem that the present thesis studies is the buckling of the above microbubbles subject to a uniform and normal static load in order to construct the bifurcation diagrams for both types of materials. The same equations are solved, but the loading is known and it is applied across the generative curve. Benchmark calculations against similar numerical calculations and recovering the theoretical buckling load verify the validity of modeling.

In this problem, as the pressure increases, the shell is compressed, but remains spherical, which is considered as the basic solution. When the load reaches the buckling threshold, the jacobian matrix has one more unstable eigenvalue, where disturbing the spherical shape with the corresponding eigenvector, the buckling curve emerges, with shapes that are asymmetric or symmetric with respect to the equator.

In polymers, when the first instability is dominated by an asymmetric eigenmode, the solution evolves only subcritically. The second instability on the spherical solution is dominated by a symmetric mode and evolves transcritically. The shapes corresponding to supercritical symmetric branch are prolate, while the shapes of the subcritical symmetric branch are oblate. On the contrary, when the first instability is dominated by symmetric mode is still a transcritical bifurcation, but the second instability on the sphere, characterized by an asymmetric mode; it was not possible to evolve. However, the subcritical symmetric branch

very soon exhibits a new unstable eigenvalue, which lead to an asymmetric branch. In any case, the subrcritical branches as evolve exhibit a limit point, which turns the solution to loads, which are higher than the buckling threshold. In the regime after the limit point, each branch has one less unstable eigenvalue in comparison with the bifurcation point and additionally their total energy is less than the sphere. The volume is reduced significantly and the poles tend to form a contact zone. In the microbubbles covered with phospholipid, the above trend is similar, but when the first instability is dominated by symmetric shapes, the asymmetric solution is not evolving from the sphere, but either from the symmetric branch.

In the context of the present thesis, parametric analysis was contacted in order to understand how the dimensionless bending modulus, $\hat{k}_b$, defines the shape of the first instability. The first instability for a microbubble with a relative small $\hat{k}_b$ is symmetric with prolate and oblate shapes, but as the dimensionless bending stiffness decreases the first instability is asymmetric, thus forming one dimple of indentation in order to relax the compressive tensions. Decreasing further the $\hat{k}_b$ one dimple is not enough for the relaxation of the tensions, thus a second dimple is formed. It should pointed out, that when both post buckling solutions coexist in the regime of relative small volumes and before the contact zone, the asymmetric is always the solution with the lower energy. In addition, in shell covered with lipid, where the gas compression is important in comparison with the elasticity, the limit point of the subcritical branch leads to sharp change of the required loading, without significant reduction of the volume, while in polymers after the limit point the volume must be reduced significantly in order to form a contact line.

ΑΡΙΘΜΗΤΙΚΗ & ΘΕΩΡΗΤΙΚΗ ΜΕΛΕΤΗ ΤΗΣ ΣΤΑΤΙΚΗΣ ΑΠΟΚΡΙΣΗΣ ΜΙΚΡΟΦΥΣΑΛΙΔΩΝ ΜΕ ΕΛΑΣΤΙΚΟ ΚΕΛΥΦΟΣ ΣΕ ΟΜΟΙΟΜΟΡΦΑ ΚΑΙ ΚΑΤΑΝΕΜΗΜΕΝΑ ΦΟΡΤΙΑ-ΕΦΑΡΜΟΓΗ ΣΤΗΝ ΕΚΤΙΜΗΣΗ ΠΑΡΑΜΕΤΡΩΝ ΤΟΥ ΚΕΛΥΦΟΥΣ

Αλκμήνη Δ. Λύτρα
Πανεπιστήμιο Θεσσαλίας, Τμήμα Μηχανολόγων Μηχανικών, 2017

Επιβλέπων: Δρ. Νίκος Πελεκάσης, Καθηγητής Υπολογιστικής Ρευστοδυναμικής

Περίληψη

Στην παρούσα διδακτορική διατριβή μελετάται θεωρητικά και υπολογιστικά η στατική απόκριση φυσαλίδων τύπου contrast agent (σκιαγραφικό μέσο). Το ελαστικό περίβλημα που τις καλύπτει είναι βιο-συμβατό και παρέχει μηχανική αντοχή καθιστώντας τες κατάλληλες για εφαρμογές όπως η στοχευμένη διανομή φαρμάκου και απεικόνιση παθολογικών ιστών (in-vivo). Ο χαρακτηρισμός των ιδιοτήτων του κελύφους, του μέτρου ελαστικότητας και του μέτρου κάμψης, είναι κεντρικής σημασίας για τη βέλτιστη λειτουργία τους. Δύο βασικοί τύποι κελυφών συναντώνται σε αυτές τις εφαρμογές: Μικροφυσαλίδες επικαλυμμένες με πολυμερές και μικροφυσαλίδες με μονές στιβάδες λιπιδίου. Οι πρώτες χαρακτηρίζονται από υψηλότερο μέτρο ελαστικότητας σε σχέση με τις δεύτερες. Τα τελευταία χρόνια το μικροσκόπιο ατομικής δύναμης (AFM) έχει αναδειχθεί σημαντικό εργαλείο για την εκτίμηση των παραπάνω ιδιοτήτων μέσω των καμπυλών δύναμης-παραμόρφωσης. Σε αυτή την κατεύθυνση, αρχικός σκοπός αυτής της διατριβής είναι η μοντελοποίηση της στατικής απόκρισης φυσαλίδων επικαλυμμένων με ελαστικό περίβλημα κάτω από τον πρόβολο του AFM και η ανάπτυξη μιας μεθοδολογίας για την εκτίμηση των ελαστικών ιδιοτήτων και για τους δύο τύπους κελυφών.

Στο πλαίσιο της διατριβής έχουν αναπτυχθεί δύο θεωρητικά και αριθμητικά μοντέλα για την περιγραφή του προβλήματος της επαφής μεταξύ προβόλου και φυσαλίδας. Ο πρόβολος θεωρείται ως μια επίπεδη και απαραμόρφωτη επιφάνεια, ενώ η φυσαλίδα περιγράφεται ως μια ελαστική μεμβράνη και το αέριο στο εσωτερικό της ως συμπιεστό. Το πρώτο μοντέλο είναι μια απλή θεώρηση στην οποία όλο το φορτίο είναι συγκεντρωμένο στο τέλος της γραμμής επαφής, ενώ στο δεύτερο ο μηχανισμός φόρτισης του κελύφους περιγράφεται μέσω της πίεσης αποσύνδεσης (disjoining pressure) ως αποτέλεσμα της τοπικής λέπτυνσης της υγρής φάσης μεταξύ προβόλου και μικροφυσαλίδας. Ο βαθμός λέπτυνσης του υγρού φιλμ περιγράφει την δύναμη μεταξύ των δύο επιφανειών, απωστική ή ελκτική, ανάλογα την σχετική τους θέσης. Σε κάθε περίπτωση επιλύονται μέσω πεπερασμένων στοιχείων το ισοζύγιο ορθών και εφαπτομενικών δυνάμεων, καθώς και η εξίσωση της ισοθερμοκρασιακής συμπίεσης του αερίου. Οι ελαστικές τάσεις περιγράφονται με τη βοήθεια καταστατικών νόμων, η πίεση αποσύνδεσης μέσω ενός δυναμικού πρόσφυσης και γίνεται παραδοχή αξονικής συμμετρίας. Η αξιοπιστία της αριθμητικής μεθοδολογίας έχει ελεγχθεί συγκρίνοντας με ανάλογα αναλυτικά αποτελέσματα. Τα αποτελέσματα κάθε μοντέλου περιγράφονται κυρίως με τη μορφή καμπυλών δύναμης- παραμόρφωσης, στις οποίες διερευνάται ο λυγισμός του κελύφους στην περιοχή της επαφής. Στο πρώτο μοντέλο επαφής η απόκριση είναι αρχικά γραμμική (περιοχή Reissner), ενώ όταν συμβαίνει λυγισμός (περιοχή Pogorelov) η καμπύλη

γίνεται μη γραμμική με τα κοίλα προς τα κάτω. Η γραμμική λύση συνεχίζει να υπάρχει και μετά το σημείο λυγισμού, αλλά χαρακτηρίζεται από περισσότερη ενέργεια σε σχέση με την λύση λυγισμού. Μια τρίτη, μη γραμμική με τα κοίλα προς τα πάνω, περιοχή παρατηρείται σε σχετικά μεγάλες παραμορφώσεις της μεταλυγισμικής και συνδέεται με την σημαντική αύξηση της εσωτερικής πίεσης σε σχέση με την ελαστικότητα του κελύφους, ως αποτέλεσμα της σημαντικής μείωσης του όγκου. Οι παραπάνω περιοχές ανακτώνται και στην περίπτωση του μοντέλου της πίεσης αποσύνδεσης. Σε κάθε περίπτωση το αδιάστατο μέτρο κάμψης, $\hat{k}_b$, δηλαδή ο λόγος της αντίστασης σε κάμψη σε σχέση με την αντίσταση σε εφελκυσμό, καθορίζει τη θέση του σημείου λυγισμού. Τα πολυμερικά κελύφη έχουν σχετικά μικρό $\hat{k}_b\left(\sim 10^{-5}\right)$ και για αυτό στις αντίστοιχες πειραματικές καμπύλες AFM παρατηρείται λυγισμός, ενώ σε κελύφη καλυμμένα με λιπίδιο το αδιάστατο μέτρο κάμψης είναι σχετικά μεγαλύτερο , $\sim 10^{-3}$, και έτσι ο λυγισμός δεν είναι προτιμητέα λύση, καθώς η αντίσταση σε κάμψη είναι σχετικά μεγάλη. Επιπλέον, όταν η πρόσφυση είναι ισχυρή, ο τοπικός λυγισμός μεταφέρεται σε μεγαλύτερες τιμές δύναμης-παραμόρφωσης ή σε ακραίες περιπτώσεις δεν παρατηρείται, διότι το κέλυφος βρίσκεται σε σημαντική έλξη με τον πρόβολο, αυξάνοντας έτσι τις εφελκυστικές τάσεις που προστατεύουν τον λυγισμό. Η επιφανειακή τάση τείνει να αυξήσει την εσωτερική πίεση, ενώ παραμένουσες θλιπτικές τάσεις τείνουν να την μειώσουν και να μεταφέρουν το σημείο λυγισμού σε χαμηλότερες τιμές. Τα παραπάνω μελετώνται εκτενώς μέσω παραμετρικής μελέτης.

Επιπλέον, με κατάλληλη τροποποίηση των εξισώσεων ισορροπίας, γίνεται ανάλογη μελέτη για φυσαλίδες που δεν είναι καλυμμένες με ελαστικό περίβλημα, οι οποίες χαρακτηρίζονται ως ελεύθερες, και η συμπεριφορά τους διέπεται από την επιφανειακή τάση και το εσωτερικό αέριο. Σε αυτή την περίπτωση, λυγισμός δεν συμβαίνει ποτέ, όπως αναμένονταν, ενώ η απόκριση στις αντίστοιχες καμπύλες δύναμης-παραμόρφωσης είναι σχεδόν τετραγωνική. Μια τέτοια προσέγγιση είναι χρήσιμη για την περίπτωση νανο-φυσαλίδων, στις οποίες δεν υπάρχει ελαστικό περίβλημα.

Αξιοποιώντας αναλυτικές σχέσεις της βιβλιογραφίας για τη γραμμική και μη γραμμική περιοχή (Reissner-Pogorelov) των πειραματικών καμπυλών για φυσαλίδες επικαλυμμένες με πολυμερές, υπολογίζονται ταυτόχρονα το μέτρο ελαστικότητας και το πάχος του κελύφους με πολύ ικανοποιητική συμφωνία με τις πειραματικές τιμές. Επιπλέον, οι αντίστοιχες καμπύλες δύναμης-παραμόρφωσης για φυσαλίδες επικαλυμμένες με λιπίδιο δεν εμφανίζουν μετάπτωση από τη γραμμική στη μη γραμμική περιοχή, αλλά είναι γραμμικές. Σε αρκετά μεγάλη παραμόρφωση τείνουν να στρέψουν τα κοίλα προς πάνω. Σε αυτή την περίπτωση η εκτίμηση των ελαστικών παραμέτρων γίνεται συνδυάζοντας τη σχέση του Reissner με τη σχέση των Lulevich et al. και Shanahan. Πραγματοποιώντας προσομοιώσεις και με τα δύο αριθμητικά μοντέλα, θεωρώντας τις παραμέτρους που υπολογίστηκαν με τις προηγούμενες μεθόδους, η πειραματική απόκριση και των δύο τύπων φυσαλίδων ανακτάται ιδιαίτερα ικανοποιητικά, αναδεικνύοντας την ορθότητα των υπολογισμών.

Το δεύτερο πρόβλημα που μελετάει η παρούσα διατριβή είναι ο λυγισμός των προηγούμενων κελυφών όταν συμπιέζονται υπό την επίδραση ενός ομοιόμορφου πεδίου πίεσης, κάθετο ως προς την επιφάνεια του κελύφους με σκοπό την κατασκευή των διαγραμμάτων διακλάδωσης για τους δύο τύπους κελυφών. Επιλύονται οι ίδιες εξισώσεις, όπως παραπάνω, αλλά η φόρτιση είναι γνωστή και επιβάλλεται σε όλη την γενέτειρα

καμπύλη. Η αξιοπιστία των αποτελεσμάτων για αυτό το πρόβλημα έχει ελεγχθεί συγκρίνοντάς τα με αντίστοιχα αριθμητικά αποτελέσματα και ανακτώντας τη θεωρητική τιμή του κρίσιμου φορτίου λυγισμού.

Σε αυτό το πρόβλημα, καθώς η πίεση αυξάνεται το κέλυφος συμπιέζεται, αλλά το σχήμα του παραμένει σφαιρικό, το οποίο θεωρείται ως η βασική λύση. Όταν το φορτίο γίνει ίσο με το κρίσιμο φορτίο λυγισμού, ο πίνακας της ιακωβιανής έχει μία παραπάνω ασταθή ιδιοτιμή, όπου διαταράσσοντας τη σφαιρική λύση με το αντίστοιχο ιδιοδιάνυσμα, προκύπτει ο μεταλυγισμικός κλάδος ο οποίος χαρακτηρίζεται από ασύμμετρα ή συμμετρικά ως προς τον ισημερινό σχήματα.

Όταν η πρώτη αστάθεια πάνω στον σφαιρικό κλάδο των πολυμερών κυριαρχείται από ασύμμετρη ιδιομορφή, ο κλάδος λυγισμού αναπτύσσεται υποκρίσιμα μόνο (subcritical bifurcation). Η δεύτερη αστάθεια στον σφαιρικό κλάδο κυριαρχείται από συμμετρική λύση και αναπτύσσεται τόσο προς τα πάνω, όσο και προς τα κάτω του φορτίου λυγισμού (transcritical bifurcation). Τα σχήματα του υπερκρίσιμου (supercritical) συμμετρικού κλάδου είναι τεντωμένα στους πόλους και συμπιεσμένα στον ισημερινό (prolate), ενώ τα σχήματα του υποκρίσιμου (subcritical) συμμετρικού κλάδου είναι πεπλατυσμένα (oblate). Αντίθετα, όταν η πρώτη αστάθεια κυριαρχείται από συμμετρική ιδιομορφή, αυτή αναπτύσσεται ξανά και στις δύο κατευθύνσεις, αλλά η δεύτερη αστάθεια της σφαίρας που χαρακτηρίζεται από ασύμμετρη ιδιομορφή δεν είναι δυνατό να εξελιχθεί. Ωστόσο, ο υποκρίσιμος συμμετρικός κλάδος γρήγορα παρουσιάζει μία ακόμα ασταθή ιδιοτιμή, που οδηγεί σε ασύμμετρο υποκρίσιμο λυγισμό. Σε κάθε περίπτωση, καθώς εξελίσσονται οι υποκρίσιμοι κλάδοι, εμφανίζουν κρίσιμο σημείο (limit point), που τους οδηγεί στο να εξελιχθούν σε υψηλότερες πιέσεις από το φορτίο λυγισμού. Σε αυτή την περιοχή ο αριθμός των ασταθών ιδιοτιμών είναι κατά ένα λιγότερος σε σχέση με το σημείο διακλάδωσης και έχουν χαμηλότερη ενέργεια από τη σφαίρα. Στην περιοχή αυτή επιπλέον ο όγκος έχει μειωθεί σημαντικά και οι δύο πόλοι του κελύφους τείνουν να προχωρήσουν στη δημιουργία ζώνης επαφής. Στα κελύφη λιπιδίου η εικόνα είναι παρόμοια, με τη διαφορά πως, όταν η πρώτη αστάθεια είναι συμμετρική, δεν προκύπτει ο ασύμμετρος κλάδος ούτε από την σφαίρα, αλλά ούτε από την συμμετρική λύση.

Στο πλαίσιο της διατριβής διεξήχθη παραμετρική μελέτη για να γίνει κατανοητό πως το αδιάστατο μέτρο κάμψης, $\hat{k}_b$, καθορίζει το σχήμα της πρώτης αστάθειας. Για μια φυσαλίδα με σχετικά μικρό $\hat{k}_b$, η πρώτη αστάθεια είναι συμμετρική, καθώς όμως μειώνεται το $\hat{k}_b$, ή ισοδύναμα το πάχος του κελύφους, η πρώτη ιδιομορφή είναι ασύμμετρη, ώστε σχηματίζοντας μία μόνο περιοχή με έντονη παραμόρφωση να μειωθούν οι τάσεις στο κέλυφος, καθώς η μείωση του $\hat{k}_b$ ισοδυναμεί με αύξηση του επιφανειακού μέτρου ελαστικότητας. Μειώνοντας περαιτέρω το μέτρο πάχος του κελύφους, δεν είναι αρκετή μία περιοχή λυγισμό για να μειώσει τις τάσεις και έτσι μια δεύτερη περιοχή με λυγισμό σχηματίζεται, οδηγώντας σε συμμετρικά σχήματα. Θα πρέπει όμως να σημειωθεί ότι όταν συνυπάρχουν οι δύο ιδιομορφές σε σχετικά μικρούς όγκους λίγο πριν από τη δημιουργία ζώνης επαφής, ο ασύμμετρος κλάδος είναι αυτός με τη χαμηλότερη ενέργεια. Επιπλέον στα κελύφη από λιπίδιο, όπου η αντίσταση της συμπίεσης του αερίου είναι σημαντική σε σχέση με την ελαστικότητα, το κρίσιμο σημείο (limit point) των υποκρίσιμων κλάδων οδηγεί σε γρήγορη αύξηση της απαιτούμενης πίεσης, χωρίς να είναι απαραίτητο να μειωθεί σημαντικά ο όγκος. Στα πολυμερή αντιθέτως, μετά το κρίσιμο σημείο ο όγκος μειώνεται σημαντικά μέχρι να επιτευχθεί ζώνη επαφής.

Τα κυριότερα συμπεράσματα της παρούσας διατριβής συνοψίζονται στα παρακάτω σημεία:

Πρόβλημα επαφής:

- Το μοντέλο των διαμοριακών δυνάμεων είναι ένα καινοτόμο εργαλείο, που μπορεί να περιγράψει τις πειραματικές καμπύλες δύναμης-παραμόρφωσης και για τους δύο τύπους κελυφών (πολυμερή και μονές στιβάδες λιπιδίου).
- Οι ελαστικές ιδιότητες μικροφυσαλίδων επικαλυμμένων με πολυμερές μπορούν να εκτιμηθούν από τις πειραματικές καμπύλες δύναμης-παραμόρφωσης μέσω της μετάπτωσης από την γραμμική περιοχή Reissner (προ-λυγισμική) στη μη γραμμική Pogorelov (μετά-λυγισμική).
- Διεξάγοντας προσομοιώσεις για τις μικροφυσαλίδες επικαλυμμένες με λιπίδιο δεν παρατηρήθηκε λυγισμός. Η στατική τους απόκριση αρχικά ακολουθεί την λύση Reissner, όπου το βασικό ισοζύγιο είναι μεταξύ των αντιστάσεων λόγω συμπίεσης και κάμψης. Στη συνέχεια, η συμπεριφορά γίνεται μη γραμμική (Δ^3), όπου κυριαρχεί η αντίσταση της συμπίεσης του αερίου μαζί με την διόγκωση του κελύφους στην περιοχή του ισημερινού.
- Οι ελαστικές ιδιότητες, δηλαδή το επιφανειακό μέτρο ελαστικότητας και το μέτρο κάμψης, για τις μικροφυσαλίδες επικαλυμμένες με λιπίδιο μπορούν να εκτιμηθούν από την μετάβαση από την περιοχή Reissner στην περιοχή που κυριαρχεί η συμπίεση του αερίου.
- Η παραμετρική μελέτη δείχνει ότι το αδιάστατο μέτρο κάμψης καθορίζει την θέση του σημείου λυγισμού. Ωστόσο, όταν η πρόσφυση του κελύφους στον πρόβολο είναι σημαντική, απαιτείται μεγαλύτερη δύναμη για να λυγίσει το κέλυφος ή σε περιπτώσεις πολύ υψηλής πρόσφυσης, το κέλυφος δεν λυγίζει και παραμένει προσκολλημένο στον πρόβολο.
- Οι προσομοιώσεις δείχνουν πως η γραμμική συμπεριφορά, που παρατηρείται έντονα και στις πειραματικές καμπύλες, είναι συνδεδεμένη με την ελαστικότητα. Αντιθέτως, στις ελεύθερες φυσαλίδες δεν παρατηρείται γραμμική απόκριση. Επομένως, οι μικροφυσαλίδες που είναι επικαλυμμένες με μονή στιβάδα λιπιδίου (Definity) μπορούν να χαρακτηριστούν ως ιξωδοελαστικές στερεές μεμβράνες.

Διαγράμματα διακλάδωσης:

- Στα διαγράμματα διακλάδωσης η πρώτη αστάθεια καθορίζεται από την σχετική σημασία του μέτρου κάμψης ως προς το επιφανειακό μέτρο ελαστικότητας, δηλαδή του αδιάστατου μέτρου κάμψης $\hat{k}_b$.
- Πιο συγκεκριμένα, σε σχετικά μεγάλες τιμές του $\hat{k}_b$ η πρώτη αστάθεια χαρακτηρίζεται από συμμετρικά σχήματα, ενώ καθώς το $\hat{k}_b$ μειώνεται τα σχήματα γίνονται ασύμμετρα και σε εξαιρετικά χαμηλές του $\hat{k}_b$, η πρώτη αστάθεια έχει πάλι συμμετρικά σχήματα.
- Η εναλλαγή από συμμετρικά σε ασύμμετρα και πάλι σε συμμετρικά είναι αποτέλεσμα της διαφοροποίησης της αντίστασης σε κάμψη σε σχέση με την αντίσταση σε εφελκυσμό/συμπίεση και σε συνδυασμό με τον σχηματισμό δύο ή ενός λοβών στους πόλους οδηγεί σε ελαχιστοποίηση της συνολικής ενέργειας.
- Οι ασύμμετροι κλάδοι αναπτύσσονται μόνο υποκρίσιμα, ενώ οι συμμετρικοί τόσο υποκρίσιμα όσο και υπερκρίσιμα.
- Στις μικροφυσαλίδες επικαλυμμένες με πολυμερές, όταν η πρώτη αστάθεια είναι συμμετρική, η ασύμμετρη προκύπτει από τον συμμετρικό κλάδο ως λύση και όχι από την σφαίρα.
- Στις μικροφυσαλίδες επικαλυμμένες με πολυμερές, όταν η πρώτη αστάθεια είναι συμμετρική, η ασύμμετρη λύση υπάρχει πάνω στην σφαίρα ως δεύτερη αστάθεια, αλλά δεν αναπτύσσεται. Επιπλέον, στην συμμετρική λύση δεν παρατηρείται νέα αστάθεια που μπορεί να οδηγήσει σε ασύμμετρη, όπως συμβαίνει στα πολυμερή.
- Καθώς οι υποκρίσιμοι κλάδοι αναπτύσσονται προς τιμές χαμηλότερες του φορτίου λυγισμού, εμφανίζουν κρίσιμο σημείο και είναι γραμμικά ευσταθείς. Μετά το κρίσιμο σημείο αναπτύσσονται αυξάνοντας την απαιτούμενη εξωτερική πίεση και πολύ σύντομα η συνολική τους ενέργεια γίνεται χαμηλότερη από την σφαίρα. Η λύση παρακολουθείται μέχρι σχηματισμό ζώνης επαφής, δηλαδή μέχρι οι δύο πόλοι να έρθουν πολύ κοντά. Για τον εντοπισμό λύσεων με πλήρη επαφή απαιτείται νέος μαθηματικός φορμαλισμός.
- Τέλος, στα πολυμερή η ζώνη επαφής εντοπίζεται σε πολύ χαμηλούς όγκους και αντίστοιχα υψηλή υπερπιέση. Αντίθετα, στα λιπίδια μετά το κρίσιμο σημείο η υπερπίεση αυξάνεται σχετικά απότομα, αποτρέποντας τη λύση να πάει σε χαμηλούς όγκους. Αυτή είναι μία σημαντική διαφορά στους δύο τύπους κελυφών και είναι αποτέλεσμα της σημαντικής αντίστασης σε συμπίεση που έχουν τα λιπίδια σε σχέση με τα πολυμερή. Έτσι, στα πρώτα αποτρέπεται η σημαντική μείωση του όγκου, ώστε να μην αυξηθεί και γίνει ακόμα πιο σημαντική η εσωτερική πίεση, που δεν θα οδηγούσε σε ισορροπία.

Table of contents

List of figures

List of Tables

List of Symbols and Abbreviations

Symbol (English)	Name	Dimensions
b	Parameter of Mooney-Rivlin constitutive law	-
B_i	i-Basis function	-
C	Parameter of Skalak constitutive law	-
E	Young modulus	Pa
e_s, e_φ	Deformation ratio in s and φ	-
F	Force	N
G_s	Shear modulus	N/m
h	Shell Thickness	M
k_b	Bending modulus	N·m
k_c	Cantilever stiffness	N/m
k_s ,k_φ	Principle curvature in s and φ	m^{-1}
K_s, K_φ	Bending strains	m^{-1}
ℓ	Element length	-
m_s, m_φ	Bending moment in s and φ	N·m
N	Number of nodes	-
P_{cr}	Critical buckling load	Pa
P_G, P_A	Gas and Ambient Pressure	Pa
q	Shear tension	N/m
r	Spherical coordinate (radial distance)	M
R_i	i-Residual	-
R_o	Bubble radius	m
s	Arc-Length	m
u	Amount of pre-stress	m
V	Volume	m^3
$w^{HK,SK,MR}$	Energy Function $^{Constitutive\ law}$	N/m
$W(y)$	Potential Energy Function	N/m
W_o	Wetting parameter-Adhesive energy per unit area	N/m
y	Distance from the substrate	m

Symbol (Greek)	Name	Dimensions
γ	Polytropic index of the ideal gas law	-
γ_{BW}	Surface Tension between bubble and water	N/m
δ_A	Characteristic potential length	m
θ	Spherical coordinate (polar angle)	-
λ_s, λ_φ	Stretching ratio in s and φ	-

ν	Poisson ratio	-
ξ	Lagrangian parameter	-
τ_s, τ_φ	In plane tension in s and φ	N/m
φ	Spherical coordinate (azimuth angle)	-
χ	Area dilatation modulus	N/m

Matrices-Vectors	Name
$\vec{\nabla}_s$	Surface divergence operator
$\vec{n}, \vec{t}_s, \vec{t}_\varphi$	Normal and tangential vectors
$\vec{x}$	Unknown vector
$[J]$	Jacobian matrix

Abbreviation	Full Form	
AFM	Atomic Force Microscopy	
f-d	Force-deformation	-
FE(M)	Finite Element (Method)	

Chapter 1. Introduction

In the first chapter introductory ideas are discussed about the motivation, the existing literature on the topic and the rest of the dissertation is briefly outlined. The major area of application of microbubbles is the medical imaging and drug/gene delivery systems. The appropriate modeling of their elastic properties is a key in order to optimize their static and dynamic response. Force-deformation curves of their static response have been mainly investigated experimentally with the atomic force microscopy. Current asymptotic models estimate the Young modulus from Reissner theory, while the shell thickness is assumed as known. Available numerical studies on the simulation of a microbubble are very limited and more applicable in polymeric shells. Bifurcations diagrams are well known in the literature, but the inert gas compressibility, and the effect of surface tension and constitutive law are not accounted for. The present dissertation aims at contributing in the research on microbubbles by investigating the above aspects.

1.1 Motivation

The last decades coated microbubbles have received significant attention in the field of medical imaging and drug/gene delivery. Gramiak and Shah [1] were the first to use microbubbles in order to enhance ultrasound images. Since then, scientists and manufactures make a great effort in developing and optimizing their structure and properties. Initially, air microbubbles without coating were introduced and therefore they had small life time in vivo [2]. Nowadays, coated microbubbles, also known as contrast agents, have emerged as powerful contrast enhancers in medical imaging via ultrasound [3, 4] and as drug/gene delivery vectors [2, 5] with highly localized impact on selected tissue. Their viscoelastic coating plays a central role in stabilizing them against dissolution while adding targeting ligands along with an extra oil layer dissolving the therapeutic agent allows for efficient targeting and drug release [2, 6] near specific tissue where therapeutic treatment is required. Sonication provides the means to control the dynamic response of the microbubbles. Figure 1-1 illustrates schematically three possible ways of drug release into a blood capillary and in Figure 1-2 clinical imaging with microbubbles of vital organs is compared against convectional imaging. Moreover, in both applications with contrast-agent microbubbles paramagnetic materials, such as contrast liquid media for MRI, or short wave length radiation for X-ray, even the chemotherapeutic agents, are not required and therefore the side effects for patients are less, since the dosage does not affect the entire body, is more frequent and has better resolution [7], but at the moment the cost is relatively high, thus treatment with microbubbles is not yet introduced in clinic. Furthermore, it is not only their small size that makes microbubbles suitable for the visualization of very small blood capillaries, but also their ability to oscillate nonlinearly in response to ultrasound waves near the walls of small capillaries that mostly behave as linear scatterers. Thus, they have been successfully used for treatment in the liver [8], kidney [9] and heart [10] among others.

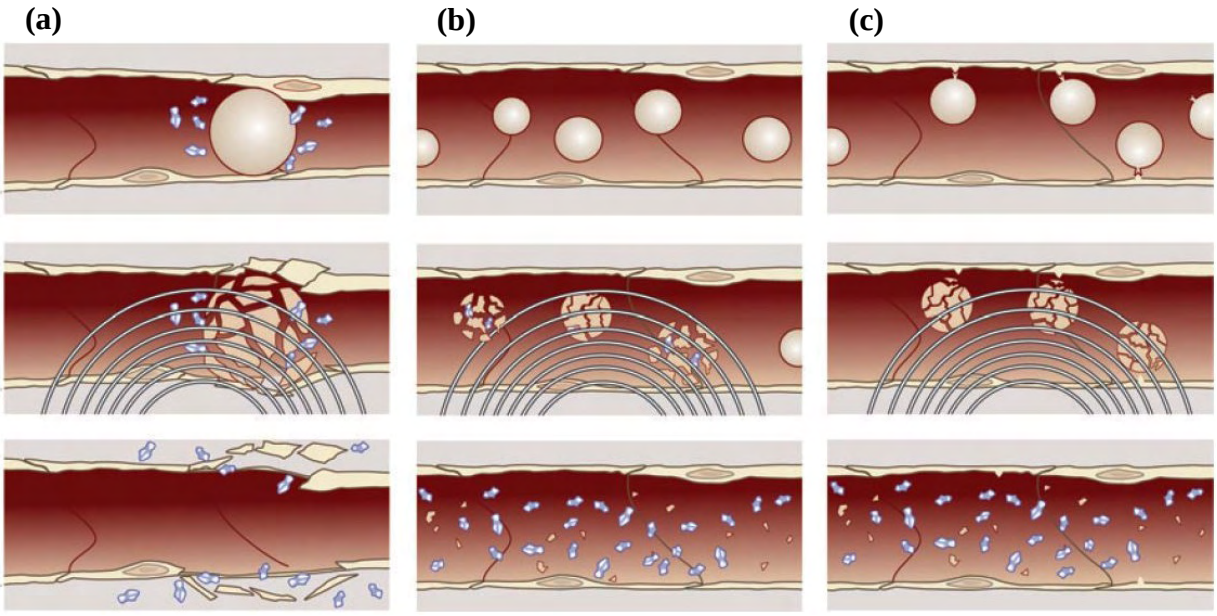

Figure 1-1: (a) Ultrasound contrast agents are freely circulating in small vessels along with drug particles (blue). Once a sufficiently strong ultrasound pulse is applied to the area, the contrast agent expands rupturing the endothelial lining. Drug is then able to extravasate. **(b)** Drug-laden ultrasound contrast agents are freely circulating throughout the vasculature. A pulse of ultrasound is applied and ruptures the contrast agent, thereby liberating the drug payload. Because ultrasound is only applied in the region of interest, drug is preferentially delivered locally. **(c)** Drug-laden ultrasound contrast agents baring surface ligands targeted to specific endothelial receptors are freely circulating. The ligand preferentially binds the ultrasound contrast agent in the target region, increasing local agent accumulation. An ultrasound pulse is then applied liberating the drug payload. *Figure and legend adopted from ref.* [2].

Coated microbubbles have an initial diameter from 2 to 5 μm and the shell coating is an elastic biomaterial with thickness 5-50 nm, Figure 1-3. The core contains a gas phase , usually nitrogen, CO_2 or perfluorochemicals [11], see also Table 1-1, which produces the local density gradient that is vital for the ultrasound. To this end two major families of coated microbubbles are normally employed, namely those coated by polymeric and phospholipid shells. The former type shells are characterized by larger elasticity modulus hence they are identified as «hard», whereas the latter are characterized by, relatively, smaller elasticity modulus and a thinner shell hence they are identified as «soft» and more deformable shells. Phospholipid shells are also more amenable to chemical treatment so that they can be attached to neighboring tissue and consequently are better suited for drug delivery applications. Moreover, phospholipid monolayers are self-assembly structures and their hydrophobic tail is oriented to gas phase. Both numerical and experimental studies [12, 13] suggest that the backscatter signal during an ultrasound measurement is strongly depended on the shell properties (elasticity, thickness, material non linearity, viscosity, etc.).

Accurate estimation of their elastic properties is a key to design and predict their response in biological capillaries or tissues. Thus, in this context the present thesis aims at developing a numerical/theoretical model in order to calculate and characterize the elasticity properties of the coating by employing the theory of shells in conjunction with the appropriate numerical techniques.

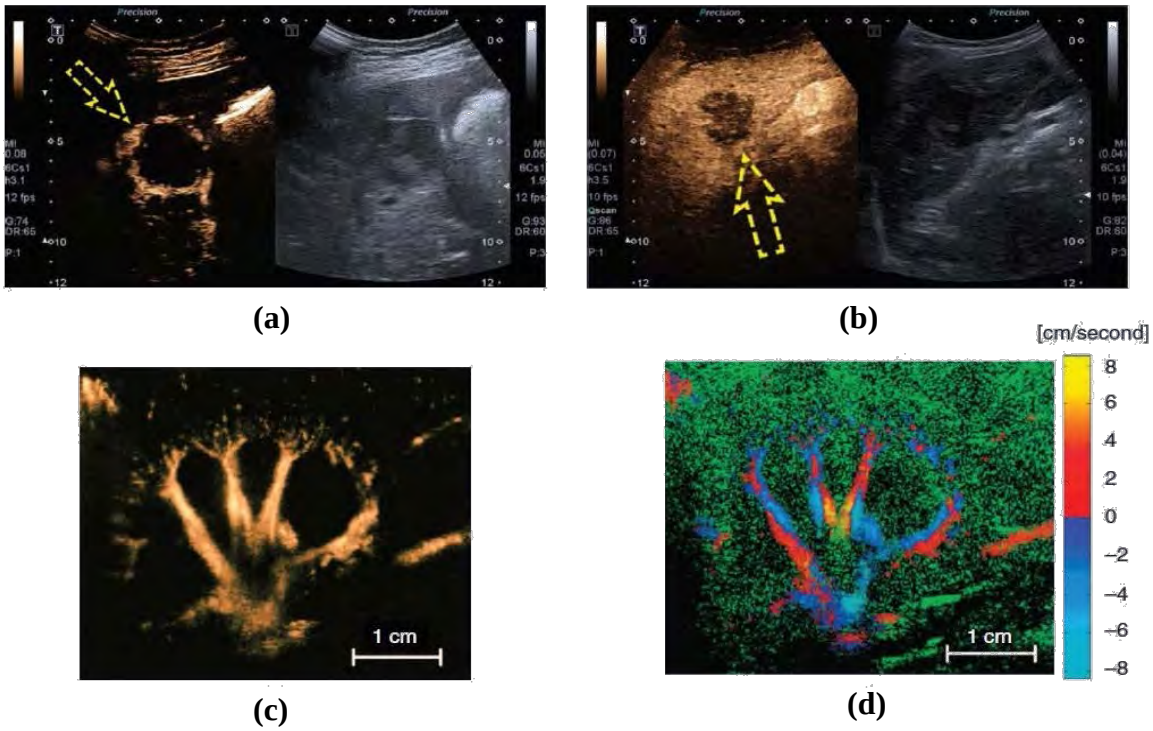

Figure 1-2: The comparison of side by side contrast enhanced ultrasound (CEUS) specific image (color) versus standard ultra sound (US) B-mode image (grayscale) for **(a)** a liver arterial hemangioma and **(b)** a liver metastasis. Both lesions are clearly visible in the contrast specific images but not the standard B-mode images. In the contrast specific images, the haemangioma is shown to be surrounded by a ring of contrast enhancement [arrow in (a)], while the metastasis is shown as a dark area [arrow in (b)]. **(c)** CEUS image and **(d)** nonlinear Doppler CEUS image of a rabbit kidney vasculature. Nonlinear Doppler shows additional information including the direction of flow (blue and red) as well as microcirculation information (green). *Figure and legend adopted from ref.* [4].

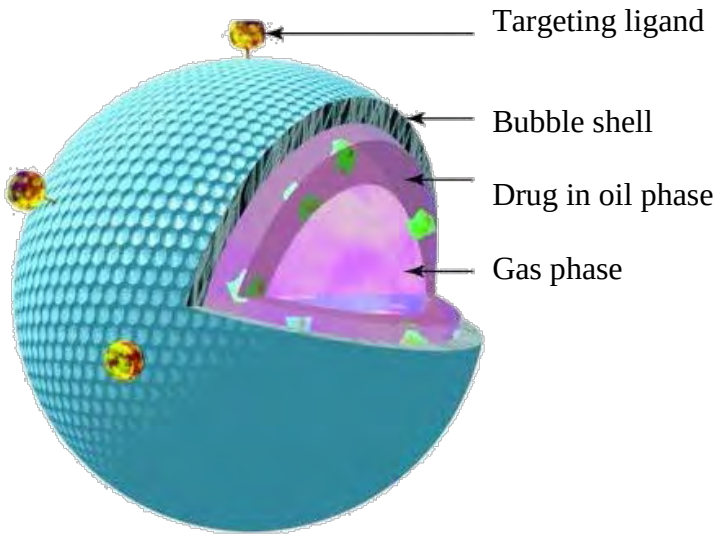

Figure 1-3: Schematic representation of a microbubble constructed for drug delivery. *Figure adopted from ref* .[14].

Name	Shell (stiffness)		Gas (solubility)		Size (μm)
Albunex	Albumin	H	Air	H	4.3
Quantison™	Albumin	H	Air	H	NA
Optison™	Albumin	H	Octafluorpropane	L	4.5
MP1950	Lipid	L	Decafluorobutane	L	2.0
PESDA	Albumin	NA	Decafluorobutane	L	4.7
Definity	Lipid/surfactant	L	Octafluorpropane	L	1.1-3.3
Imagent	Lipid/ surfactant	L	Nitrogen/perfluoroh exane	L	6.0
Sonovue	Lipid	L	Sulfur hexafluoride	L	2.0
BR14	Lipid	L	Perfluorobutane	L	2.6
Levovist	Lipid/Galactose	L	Air	H	2.0-4.0
biSphere™	Polylactide/albumin	H	Nitrogen	H	3.0
Acusphere	Polylactide	NA	Perfluoropropane	L	NA
Sonazoid	Lipid/surfactant	NA	Perfluorobutane	L	2.2
ST68-PFC	Lipid/surfactant	L	Decafluorobutane	L	1.8
Sonavist	Cyanoacrylate	H	Air	H	NA

Table 1-1: Microbubble contrast agents Shell stiffness is noted as high (H) and low (L) and gas solubility is noted as high (H), low (L) or not available (NA). *Table adopted from ref.* [11].

1.2 Atomic force microscopy experiments

Although the ultrasound environment is the area of application of contrast agent microbubbles, an acoustical experiment cannot easily provide the elastic properties of the shell, because a lot of parameters must be taken into account. In case of an acoustic experiment/simulation the shell is treated dynamically [15-19] and apart from the elasticity, the viscous stresses from the shell and/or the surrounding liquid must be also considered providing an accurate but more complex picture in the attempt to characterize the material coating where dynamic effects may also play a role. However, during of a static experiment the number of the involved parameters is smaller and more easily controlled. Toward this direction, the atomic force microscopy (AFM) has been successfully used for the visualization of three dimensional shapes (topography and roughness) and it is also possible to perform force measurements. The AFM was developed by researchers who tried to extend the scanning tunneling microscope (STM). In 1986 Binnig and Quate demonstrated [20] for the first time that AFM is a capable tool that could measure forces less than nN and until nowadays the AFM has been developed performing accurate measurements of thin films [21], living cells [22, 23] and artificial vessels [24-27], such as contrast agent microbubbles. More details on the operation principles and the physics of a modern AFM can be found in [28].

In the present dissertation, the experimental force-deformation (to be referred to as f-d henceforth for brevity) curves obtained with an AFM for microbubbles with polymer by Glynos et al. [29] and lipid by Bucher Santos et al. [30] coating are employed, in order to estimate their elastic

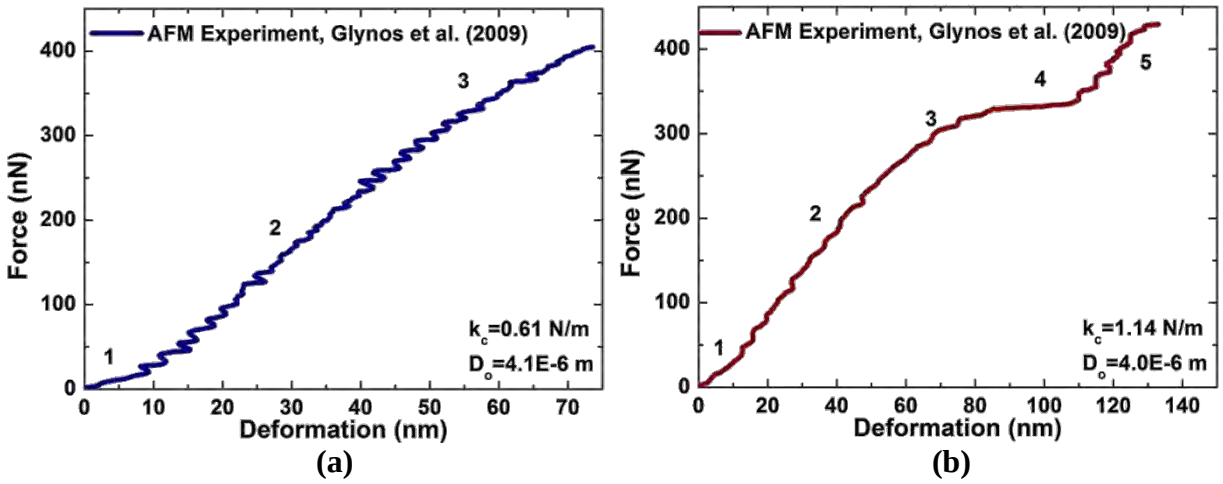

Figure 1-4: Force-deformation curves for microbubbles covered with polymeric biomaterial obtained by the AFM [29] **(a)** k_c=0.67 N/m and **(b)** k_c=1.14 N/m.

properties, namely Young and bending modulus. The choice of these two material coatings is based on the fact that they are quite different from each other in terms of their elasticity modulus and the results could collectively characterize the properties of a whole group of microbubbles that are typically used in ultrasound medicine.

During the AFM experiments the microbubble is attached to a petri-disc, which is located under and parallel to the cantilever. When the measurement starts the cantilever compresses the microbubble and through the detector, a software records force and deformation. It must be noted that the actual procedure is much more complicated and beyond the scope of the present thesis, however, the reader could find more details about the experiment operation and the sample preparation in the available literature. Moreover, the measurements are performed by keeping the velocity of the cantilever at 6-7 μm/s; therefore it could be assumed that the shell is in quasi-static equilibrium. Also, a similar experimental study [25] suggests that the f-d profiles are not affected by the cantilever velocity. In any case, the shell radius is directly measured by the microscope.

As it is already mentioned the polymeric coatings result in stiff shells with elasticity modulus on the order of GPa. This becomes mostly evident by the f-d curves of Glynos et al. [29], which show that the required force is up to 400 nN in order to obtain a deformation of almost 150 nm. Their work contains an extensive number of f-d curves using tipless cantilevers with different stiffness (k_c). Moreover, the shell thickness is estimated by a linear relation provided by the manufacturer [31].

The f-d curves obtained by a cantilever with stiffness k_c=0.61 N/m have three different regimes; see Figure 1-4(a). An initial nonlinear regime, denoted with 1 occurs for very small values of the applied force, on the order of 10 nN and less, where the Albumin outer layer (thickness: ~10 nm) and intermolecular/surface adhesion forces between the shell and the cantilever are conjectured to participate in the dominant force balance with elastic forces. As the external load increases a linear regime appears, denoted with 2, followed by a nonlinear regime, denoted by 3, that is curved downwards. The linear regime is the Reissner [32, 33] regime where stretching and bending forces coming from the stiff polylactide shell balance each other over a flattened contact area that characterizes the microbubble shape. This is the

part of the f-d curve that is typically used in the literature in order to infer the shell elasticity modulus once the shell thickness (h) and radius (R_o) are known [24, 29]. The third regime occurs as the external load further increases and it is known in the literature as Pogorelov [34] regime. It appears as the compressive load on the flattened part of the shell exceeds a certain value, in which case the shell bents forming a crater at the pole region while a dimple forms at some distance from the pole where most of the bending energy is stored. The f-d curves obtained by a cantilever with stiffness k_c=1.14 N/m they have initially the same three regimes as it is already described, but they have two additional regimes after the third, see also Figure 1-4(b). So, the fourth regime is an almost linear curve with zero slope, that is associated with the post buckling stage and the final regime is described by a linear curve with positive slope.

On the other hand, the lipid coatings [30] are softer and for deformation up to 500 nm the required force is only 12 nN, since their Young modulus is in the order of MPa. In this set of measurements the employed cantilevers have lower stiffness k_c=0.25 and 0.07 N/m and the shell thickness is assumed to be 5 nm for all the interrogated microbubbles.

In contrast with the f-d curves obtained from polymeric shells, f-d curves from lipid shells is quite different, Figure 1-5. In particular, the above regimes are not identified and most part of the curve responds linearly, indicating that Pogorelov regime is bypassed by an extended regime that is characterized by an almost flat contact region, e.g. buckling is not taking place. It is also important to notice that the required force for the shell deformation is not only quite small, but it is also on the order of intermolecular forces resulting by the interaction of two bodies approaching each other. Moreover, between the cantilever and the shell a thin film of water is formed, due to the hydrophilic nature of the lipid head, which is compressed as the cantilever approaches the shell. The compression of the water film causes a local pressure change in comparison with the bulk aqueous phase, known as disjoining pressure [35, 36]. Thus, apart from stretching and bending tensions, the disjoining pressure also contributes to the force equilibrium and stabilizes the shell, which remains attached to the water-cantilever interface thus delaying or even bypassing buckling. This argument is verified by calculations of the present thesis that conform with the absence of shell buckling. However, the current experimental set-up for both type of materials does not allow for side view photos in order to investigate experimentally the shell buckling. Moreover, Bucher Santos et al. [30] confirm that Reissner linear equation does not provide a reliable estimate of the shell elastic properties. They also consider the model proposed by Lulevich et al. [25] where bending dominates very small deformations whereas stretching dominates at larger deformations. They consider the latter model as more reliable that Reissner's theory without, however, arriving at any conclusive procedure for estimating shell elastic properties.

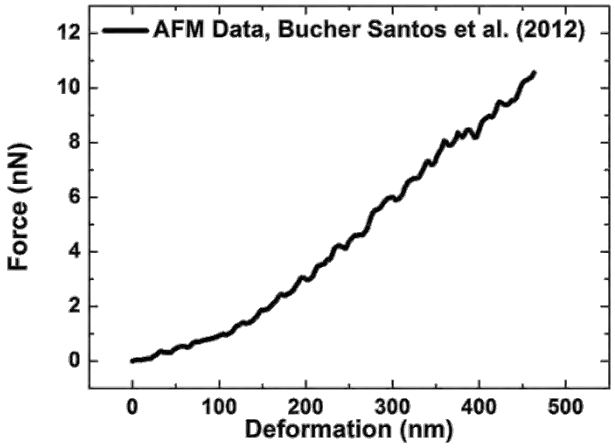

Figure 1-5: Force-deformation curves for microbubbles covered with lipid biomaterial obtained by the AFM [30].

In addition, the thin water film exists not only in lipid experiments, but also in the above experiments for polymers. The only reason for not taking into account its effect is that the resulting disjoining pressure is negligible compared with the elasticity modulus of polymers. Finally, there is one more significant difference between polymers and lipids, which is considered in the present thesis: the shell thickness. The former type of coating is a stiff material and is therefore described by classic shell mechanics [37], i.e. the bending modulus is a function of the area dilatation modulus $\left(k_b \sim \chi h^2\right)$. On the other hand, the bending stiffness and area dilatation modulus are treated as independent parameters for lipid monolayer and bilayer shells, [38, 39].

1.3 Literature review

Doubly/singly curved with positive or negative curvature, the shells have always been in the center of interest for engineers and scientists, because they usually are light constructions, which guarantee stability and architectural design. Most of them are inspired by the nature, like water drops, egg shells and bones. In the history of mechanics, the theory and the governing equations have been initially developed mainly for artificial shells, like tanks, domes and pipes, where Timoshenko [37], Landau [40] and Reissner [32, 33] had been working and developing the field since the early ‘30s. Meanwhile, the advances in medicine since the early 1970’s as they are described in session 1.1, demand appropriate design and optimization, which is a highly interdisciplinary area, including chemistry, engineering, material science, medicine etc. The present thesis investigates the elastic properties and the static response in the context of classic shell mechanics.

In the literature the elastic properties of contrast agent microbubbles, namely Young and bending modulus, have been mainly studied experimentally by the AFM and the resulting force-deformation curves are fitted with available asymptotic equations. In the following, relevant studies from the literature will be reviewed in order to describe the available models and their applications/limitations. The experiments from Glynos et al. [27, 29] and Bucher Santos et al. [30] will not be further discussed in the present session. Lulevich et al. [25]

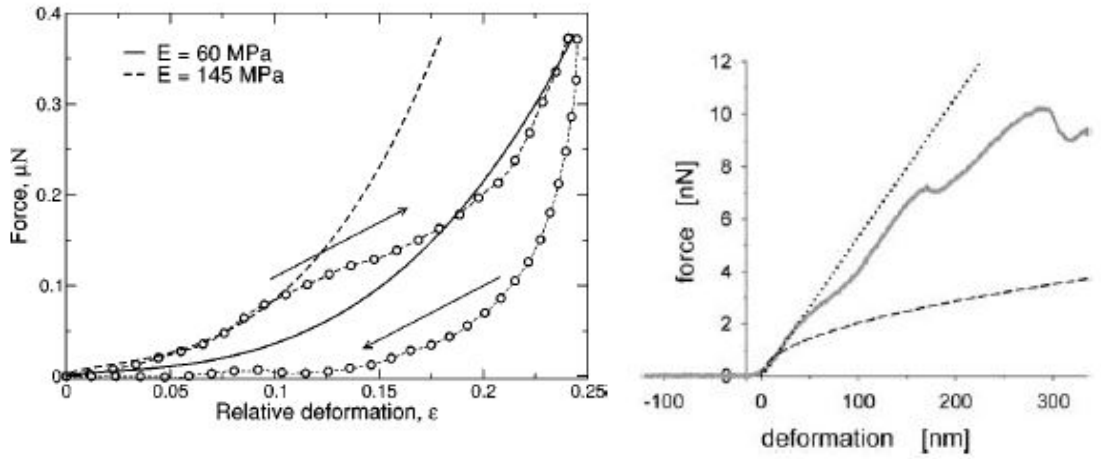

(a) **(b)**

Figure 1-6: Force-deformation curves obtained by **(a)** Lulevich et al. [25] and **(b)** Elsner et al. [41] with the AFM.

perform AFM measurements for polymeric microbubbles (poly-DL-lactic acid (PLA) and monodisperse melamine formaldehyde (MF) particles) using a cantilever with a spherical tip, and the f-d profiles they obtained are similar with the ones presented by Glynos et al. [29], Figure 1-6(a). In the same paper, they have developed an asymptotic relation, based on classic elasticity theory, where it is assumed that the bending term could be omitted in relatively high values of deformation. The resulting Young modulus is about 1-100 MPa and by comparison with an experiment on osmotically induced deformation of the same microbubbles, it was found to be an order of magnitude lower [42]. Moreover, Elsner et al. [41] study the deformation of polyelectrolyte multilayer capsules (polyallylamine and polystyrene-sulfonate, PAH/PSS) and estimate the Young modulus based on Reissner theory, Figure 1-6(b). It is of interest that in their work they examine the validity of Reissner theory for such experiments via FE simulations (Abaqus), since the Reissner analytical solution is more suitable for point loading whereas, on the other hand, the AFM cantilever is an extended plate. They prove that Reissner theory is an accurate analytical solution for AFM experiments with tipless cantilever as far as small deformations are considered and for microbubbles covered with materials that have relatively high Young modulus, thus, they behave as the conventional shells. Moreover, the effect of temperature in shell stiffness is investigated for phospholipid microbubbles [43] and for air or liquid filled capsules [44] by employing the AFM and Reissner theory. They found that increasing the temperature from 10 to 37 °C the shell stiffness decreases significantly.

On the other hand, studies that simulate the compression of a microbubble under the AFM are very limited and most of the available numerical results refer mainly on the general problem of the compression of an elastic shell by a rigid and flat surface. Such calculations are more suitable for microbubbles covered with a polymeric biomaterial, as their behavior is closer to convectional shells. Hertz [45] was the first to formulate the contact between two elastic spheres. In his work, Hertz estimates the contact pressure to be a quadratic function of contact length, assuming frictionless contact. Updike and Kallins in a series of papers [46-48] solve the problem of the compression of an elastic shell under a rigid and flat surface. Initially

they perform stability analysis and they prove that for small deformations the shell and the plate stay in contact, but with further increase of the external load buckling takes place. The first buckling is axisymmetric and occurs when the contact angle is about to 8°, however in higher values of deformation they observe non-symmetric buckling. Moreover, they estimate the contact pressure to be an almost zero function along the contact area, except the end of contact, where the pressure takes in infinite value. Therefore, they suggest that the pressure load could be simulated by a point load at the end of contact. Furthermore, Johnson, Kendall and Roberts (JKR) [49] extend Hertz theory accounting also for surface energy. They estimate analytically the force required for separation of two elastic spheres, which was found to be proportional to sphere radius and surface energy. They also conclude that the surface energy for high elasticity modulus materials is negligible and vice versa for softer materials. Lately, Shanahan [50] modify and extend the JKR theory in order to calculate the pull-off force between an elastic shell and a rigid plate, assuming a linear material and isothermal compression for the inert gas. Shanahan's solution predicts a pull-off force 33% smaller compared with JKR solution.

In addition, a significant amount of research has been carried out on the 3D deformation of spherical elastic shells subject to a concentrated point load [51], or under a flat surface [52] at static conditions or subject to an external Stokes flow [53]. Most of them report that initially buckling is axisymmetric while for higher values of deformation 3d buckling wrinkles are observed. Regarding this, the present thesis treats the shell as axisymmetric, since in the experimental data the deformation is relatively small.

Moreover, another major group of publications that is in the center of interest of the present thesis is the one of buckling of elastic shell subject to a uniform pressure. Timoshenko [54] has calculated the critical buckling load for small deformations and linear material in which the shell from a compressed sphere buckles into an axisymmetric or symmetric shapes. Koga and Hoff [55] solve numerically the problem of a spherical shell under uniform pressure with an initial geometric imperfection. The first buckling is characterized by an asymmetric mode, while the second by a symmetric. The post buckling behavior of elastic tubes with opposite sides in contact is investigated by Flaherty et al. [56], where they calculate the value of the required pressure for contact, as function of the number of pods. More recently, Gao et al. [42] investigate experimentally the osmotic buckling of polyelectrolyte capsules and they observe buckling instability with asymmetric shape. The buckling behavior of elastic capsules in shear flow has been studied by Walter et al. [57] for prolate or oblate shapes and by Ramanujan and Pozrikidis [58] for spherical and non-spherical initial shapes. The dynamic buckling and stability of contrast agent microbubbles are investigated numerically by Tsiglifis and Pelekasis [13, 38] subject to acoustic disturbances. They prove that the elasticity parameters and the constitutive law control the buckling by performing an extensive numerical and parametric analysis. Vlachomitrou and Pelekasis [19] have developed a numerical method for the dynamic behavior of a contrast agent microbubble when the viscous forces are accounted for. Thus, the dynamic evolution is captured until static equilibrium. The static shapes are obtained also in the post-buckling regime characterized by asymmetric or symmetric modes. Efthymiou and Pelekasis [15] investigate the dynamic response of encapsulated microbubbles near a rigid wall, assuming inviscid and incompressible flow. They observe dynamic buckling and a variety of post-buckling symmetric or asymmetric shapes.

Moreover, jet formation was not detected, since the shell elasticity and viscosity balance external disturbances. Knoche and Kierfeld [59] have studied numerically the static buckling of spherical soft shells under negative pressure or reduced capsule volume. They employ the equations of equilibrium and by minimization of total energy they demonstrate a rich bifurcation behavior. They examine two major categories of capsules regarding the ratio of bending modulus with respect to the area dilatation modulus. In both types of capsules the first bifurcation is dominated by an asymmetric mode, followed by a symmetric bifurcation. Their calculations allow also for the contact of two opposite sides, thus in extremely small shell volumes, asymmetric or symmetric shapes with an extensive contact area are evaluated.

The surface energy between two bodies in contact has been an area of research for a long time, when Young [60] described the balance of energies between three phases: Solid, liquid and gas, as function of the apparent contact angle, and later Young and Laplace [35, 36] quantify the capillary pressure difference across two static liquids as function of the surface tension. However, when the problem comes up to the scale of molecular dimensions, forces rising by the electrostatic interaction of molecules must be also considered. In this case, the Young-Laplace equation has an additional term referred to as disjoining pressure. The disjoining pressure is expressed as the derivative of the potential energy, which describes the interaction of two bodies that approach each other. The idea of disjoining pressure is widely used when soft matter, like lipid shells, are considered: Kalliadasis and Chang [61] employ the disjoining pressure in their formulation in order to estimate the contact angle of a gas-liquid meniscus by the balance of capillary, viscous and intermolecular forces and they use a long range attractive potential. They investigate the asymptotic behavior of the contact angle as function of the capillary number and intermolecular forces. Moreover, Chamakos et al. [62] perform simulations of a drop resting on a patterned surface by employing a short range repulsive-long range attractive energy potential. Various wetting equilibrium states were found and their stability was investigated. Accordingly, Blount et al. [63] investigate a vesicle, that has only bending resistance, adhered to a substrate. In this fashion, they calculate static shapes by employing the balance between disjoining pressure, bending resistance, surface tension and pressure difference between the vesicle interior and the ambient phase. They also provide an extensive asymptotic analysis in order to determine the main force balances across the vesicle surface. They show that around the transition region, defined between the adhered area and the outer shell, the bending resistance balances the disjoining pressure and in the outer region bending resistance is equally important as the pressure difference. Lipid bilayers adhered to a flat surface are also simulated by Cantat et al. [64] with a long range attractive-short range repulsive potential. And finally, Leite et al. [65] in their review suggest when that the AFM measurements can be modeled with a potential energy function.

1.4 Novelty and scientific contribution of the dissertation

As it can be gleaned from the above review, in all of the available studies for the estimation of the elasticity properties, the shell thickness is treated as known, while the Young modulus is estimated most of the times based on Reissner theory for both lipids and polymers, even though the main concertation of literature is on polymers. Thus, the present dissertation aims at presenting a novel method to estimate simultaneously both Young and bending modulus from the force-deformation curve. So, the proposed relations are an additional tool especially for experimentalists that perform AFM measurements and wish to estimate the above properties, without prior knowledge of the shell thickness, which is usually provided by the manufacturer or is based on empirical observations.

Secondly, two numerical models that, not only recover the AFM experiments, but also explain the mechanisms of deformation of microbubbles have been developed in the context of present thesis. In particular, the former model based on classic shell mechanics verifies that the behavior of polymeric shells is closer to convectional shells. The latter has been developed for shells covered with lipid, where the effect of intermolecular forces is accounted for. A modification of the second FE model verifies that lipid shells behave like elastic shells and not like surfactants. Moreover, the inert gas is treated as ideal and its compression is investigated. The effect of pre-stress is also accounted in both models justifying that some of the microbubbles have experienced some gas leakage.

In addition, the microbubbles are investigated subject to a uniform pressure and bifurcations diagrams of their static buckling and stability are demonstrated, when the gas compressibility and surface tension are accounted for. Through a parametric analysis is showed that for shells with relative high elasticity modulus the first buckling is dominated by an asymmetric eigenmode, which followed by a second symmetric buckling. However, in softer shells the first buckling is characterized by a symmetric shape. In both cases a limit point was detected in the secondary branches, associated with a change in the number of negative eigenvalues. Moreover, the gas compressibility and surface tension tend to increase the effective stiffness of the shell and the value of critical buckling load, in comparison with classic buckling, where stretching and bending are the only terms that balance the external load.

The above models contribute in the relevant scientific research on the static deformation of microbubbles.

1.5 Thesis outline

The rest of the thesis is divided into six chapters from chapter 2 up to 7, where the governing equations, along with results and conclusions are discussed. More specifically:

In chapter 2 all the governing equations that describe each problem are presented. The first part of the chapter 2 contains some preliminary relations form differential geometry. In the second part the elastic tensions, moments and the constitutive laws are reviewed. The formulation of the microbubble under the AFM is in third part of the chapter 2 and it is investigated separately for the different types of microbubbles. Therefore, a subparagraph contains the equations for a polymeric microbubble and a following subparagraph contains the formulation for a microbubble covered with lipid biomaterial. In the fourth part of the chapter 2, the microbubble is investigated subject to a uniform pressure field. Finally, the concept of a pre-stressed elastic shell is studied and the residual stresses are calculated.

In chapter 3 the finite element methodology and the discretized equations are defined. Initially, the basis functions are presented and they are followed by the weak formulation. In the same part of the chapter 3 the Newton-Raphson method is reviewed, along with continuation techniques. At the end of the chapter 3, a paragraph consecrates on benchmark calculations and comparison with available results from the literature.

In chapter 4 numerical results employing the formulation developed for the contact problem are presented. In particular, the chapter is divided into three paragraphs with numerical results pertaining to the classic contact model, the intermolecular forces model and the case of a free microbubble, respectively. In any case, an initial microbubble is investigated, which serves as a reference and then parametric study is performed in order to investigate the effect of different parameters on the shell equilibrium. The main results are demonstrated in force-deformation curves and energy-deformation curves, along with the shape of the microbubble in deformed configuration.

Chapter 5 contains the bifurcation diagrams (pressure-volume) for both microbubbles covered with polymer or lipid. The total energy and eigenvalues of the post-buckling solutions are investigated in order to characterize the stability of each branch. An extensive parametric analysis is also carried out in order to highlight how the different parameters change these diagrams.

In chapter 6 the analytical solutions developed by Reissner and Pogorelov for the linear and non-linear regimes of the force-deformation curves, respectively, are demonstrated in order to estimate the slopes of the relative regimes in experimental force-deformation curves and estimate simultaneously the Young modulus and the shell thickness. In addition asymptotic analysis is performed in order to understand better the numerical results especially for the intermolecular forces model. Furthermore, a novel methodology for estimating the area dilatation modulus and bending stiffness is proposed, by coupling the slope of the experimental curve in the bending stiffness dominated Reissner regime with the cubic dependence on deformation in the gas compressibility dominated regime for microbubbles covered with phospholipid.

Finally, in chapter 7 the main findings and conclusions are discussed, while at the end of the chapter some ideas are presented for future work.

Chapter 2. Problem Formulation

The second chapter contains the governing equations defining the geometry of the problem, the constitutive laws and equilibrium equations, in order to formulate the response of a coated microbubble subject to a static load. The shell surface is regarded as axisymmetric and it is parameterized by a lagrangian variable. The elastic coating develops internal elastic tensions and moments in order to balance the external forcing. Three constitutive laws are examined, namely Hook, Mooney-Rivlin and Skalak, in order to investigate different material response (linear, strain-softening and strain hardening). The formulation of polymers and lipids under the AFM is investigated separately. A classic contact model is adopted for the former case, a model with intermolecular forces for the latter and simulations were performed in order to conduct an extensive parametric study for both cases. Moreover, the microbubble is also investigated subject to a uniform pressure field. Finally, the effect of pre-stress is discussed in terms of residual strains and stresses.

2.1 Lagrangian Description

In the present thesis a microbubble is investigated subject to different types of static loads and materials. Nevertheless, in any case the interface of the microbubble is considered as a group of lagrangian particles, where every particle described by a relevant variable ξ, which takes values in the interval [0, 1] corresponding to the first and final node of the physical domain, respectively. Upon introducing the independent variable ξ, is it possible to describe complex shapes of the interface by following these particles. Therefore, the spherical coordinates for an axisymmetric surface can be written as function of ξ:

$$r = r(\xi) \quad \text{and} \quad \theta = \theta(\xi) \quad \text{for} \quad 0 \le \xi \le 1 \tag{2-1}$$

Moreover, the normal and tangential vectors of any node are written as:

$$\vec{n} = r\theta_s \vec{e}_r - r_s \vec{e}_\theta, \quad \vec{t}_s = r_s \vec{e}_r + r\theta_s \vec{e}_\theta \quad \text{and} \quad \vec{t}_\varphi = r\sin\theta \vec{e}_\varphi \tag{2-2}$$

where, $\vec{e}_r, \vec{e}_\theta, \vec{e}_\varphi$ are the unit vectors in spherical coordinates and *s* denotes the arc-length along the generator curve (meridional plane for φ=0) and when it is used as subscript denotes differentiation [66], see also Appendix A. It is also possible and more convenient to write the unit vectors in terms of ξ. After introducing the relation of arc-length *s* with ξ, eq. (2-2) reads as:

$$\vec{n} = \frac{r\theta_\xi \vec{e}_r - r_\xi \vec{e}_\theta}{s_\xi}, \quad \vec{t}_s = \frac{r_\xi \vec{e}_r + r\theta_\xi \vec{e}_\theta}{s_\xi} \quad \text{and} \quad \vec{t}_\varphi = r\sin\theta \vec{e}_\varphi \tag{2-3}$$

where $s_\xi = \frac{ds}{d\xi} = \left(r_\xi^2 + r^2\theta_\xi^2\right)^{1/2}$, see also Figure 2-1. In the same way, when ξ is used as subscript denotes differentiation. Moreover, in Figure 2-1, *z* and σ, denote the axes of a

relevant cylindrical coordinate system for φ=0, with the same origin as the spherical one. It must be noted that when the microbubble is investigated under the AFM, it is taken to be symmetric with respect to the equator, i.e. $\theta \in \left[0, \frac{\pi}{2}\right]$, Figure 2-1(a). However, in the case where the microbubble is investigated under a uniform pressure, this symmetry is not considered, i.e. $\theta \in [0, \pi]$, because asymmetric configurations with respect to the equator are also possible, Figure 2-1(b). After introducing the unit vectors of the surface, the curvature tensor can be defined as:

$$\underline{\underline{B}} = \vec{\nabla}_s \vec{n} \tag{2-4}$$

with its components in the covariant $(\vec{a}_1, \vec{a}_2, \vec{n}) = (\vec{t}_s, \vec{t}_\varphi, \vec{n})$ basis to be $b_{ij} = a_i \cdot \underline{\underline{B}} \cdot a_j$, $i, j = 1,2$. $\vec{\nabla}_s$ is the surface gradient operator with: $\vec{\nabla}_s = \sum_{i=1}^{2} \vec{a}^i \frac{\partial}{\partial u_i}$, $u_1 = s$ and $u_2 = \varphi$, and $\vec{a}^i$ are the contravariant vectors: $\vec{a}^i = \frac{(-1)^j \vec{a}_j \times \vec{n}}{\left|\vec{a}_1 \cdot \vec{a}_2 \times \vec{n}\right|}$, $i, j = 1,2$ and $i \neq j$. The principal curvatures and directions are computed via diagonalization of $\underline{\underline{B}}$ matrix:

$$\begin{aligned} k_1 = k_s &= \frac{r_\xi^2 \theta_\xi + r\left(r_\xi \theta_{\xi\xi} - r_{\xi\xi} \theta_\xi\right)}{s_\xi^3} + \frac{\theta_\xi}{s_\xi} = \frac{\sigma_\xi z_{\xi\xi} - \sigma_{\xi\xi} z_\xi}{s_\xi^3} = \frac{1}{r_s} \\ k_2 = k_\varphi &= \frac{\theta_\xi}{s_\xi} - \frac{r_\xi \cot\theta}{r s_\xi} = \frac{z_\xi}{\sigma s_\xi} = \frac{1}{r_\varphi} \end{aligned} \tag{2-5}$$

The corresponding eigenvectors are the $\vec{t}_s$ and $\vec{e}_\varphi$, therefore the principal directions are the *s* and *φ*. In addition, r_s and r_φ denote the local radii of curvature along *s* and *φ*. Then, the mean curvature is $k_m = \left(k_s + k_\varphi\right)/2$.

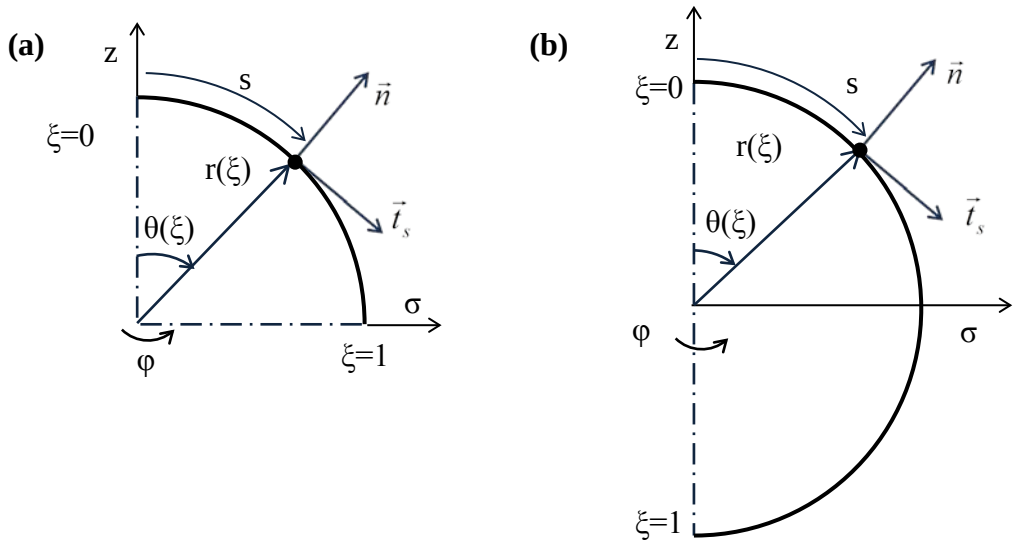

Figure 2-1: Lagrangian description of the interface for the **(a)** AFM case and **(b)** uniform pressure.

2.2 Elastic Tensions, Moments and Constitutive Laws

The microbubble is covered by a biocompatible material, usually phospholipid or polymer, in order to decelerate gas diffusion in water or blood. The encapsulation provides also mechanical strength, thus the microbubble is possible to balance external forces by developing elastic tensions and moments. In the present dissertation, the elastic tensions and moments are described in the context of theory of thin elastic shells and continuum mechanics [37]. In the elastic shell, in-plane and shear tensions along with bending moments are developed as a result of deformation of the shell subject to an external load. In Figure 2-2 the tensions and moments are illustrated if the curve assumed to undergo axisymmetric deformations. As it can be gleaned, both tensions and moments are written in the curvilinear [*s*, *φ*, *n*] basis for simplicity, because the [*s*, *φ*, *n*] coincides with principal directions [38, 67]. Therefore, the meridional (τ_{ss}) and azimuthal ($\tau_{\varphi\varphi}$) tensions are introduced, which correspond to the in-plane stress resultant. The transverse shear stress *q* lies perpendicular on an *s*-*φ* plane along with the meridional (m_{ss}) and azimuthal ($m_{\varphi\varphi}$) bending moments. The total tension tensor is:

$$\underline{\underline{T}} = \underline{\underline{\tau}} + \vec{q}\vec{n} = \left(\tau_{ss}\vec{t}_s\vec{t}_s + \tau_{\varphi\varphi}\vec{t}_\varphi\vec{t}_\varphi\right) + q\vec{t}_s\vec{n} \tag{2-6}$$

and contains both in plane and shear tensions. In the same manner, the bending moment tensor is defined as:

$$\underline{\underline{m}} = m_{ss}\vec{t}_s\vec{t}_s + m_{\varphi\varphi}\vec{t}_\varphi\vec{t}_\varphi \tag{2-7}$$

Most of the elastic materials respond linearly in the presence of an external load for small values of deformations [38, 68]. However, with further increase of the load the force-deformation relation might be non-linear, even if buckling or other phenomena do not occur.

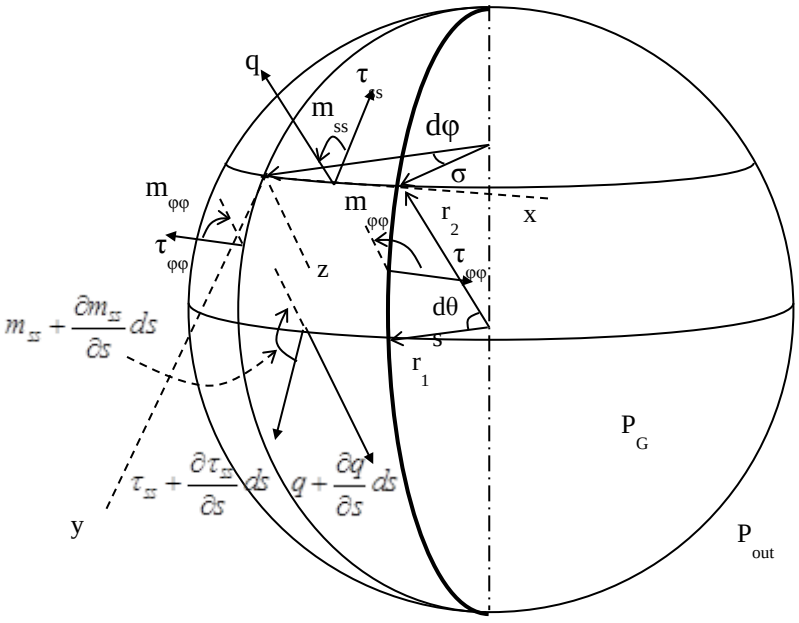

Figure 2-2: Stresses and moments around an infinitesimal patch with dimensions (σdφ)×ds

In this case, their behavior is characterized as strain softening or strain hardening, depending on the values of the effective elasticity modulus. The strain softening materials exhibit a smaller elasticity modulus as the deformation increases, while the opposite happens in strain hardening materials. These observations can be described mathematically using the appropriate constitutive law. For the first group of materials the Hook's law is more relevant, while for the strain softening and strain hardening materials Mooney-Rivlin and Skalak constitutive laws are used, respectively. The strain softening behavior was proposed by Mooney [69] for rubber like materials for the description of the hyperelastic stress-strain relation and later Rivlin [70] expressed the energy function in terms of the strain tensor invariants. Moreover, the energy function for the strain hardening behavior was introduced by Skalak et al. [71] in order to calculate the elasticity modulus of red blood cells.

In the following, the surface gradient displacement $\underline{\underline{A}}$ is introduced, written in cartesian coordinates [72], so that the mathematical form of the above constitutive laws will be described:

$$\underline{\underline{A}} = \left(\underline{\underline{I}} - \vec{n}\vec{n}\right) \cdot \frac{\partial \vec{x}}{\partial \vec{X}} \cdot \left(\underline{\underline{I}} - \vec{N}\vec{N}\right) \tag{2-8}$$

where $\vec{X}$, $\vec{x}$ denote the position vector of a surface particle and $\vec{N}, \vec{n}$ are the normal to the surface vectors, in the referential and deformed configurations, respectively. And then, the left Cauchy-Green deformation tensor $\underline{\underline{C}}$ is defined as:

$$\underline{\underline{C}} = \underline{\underline{A}} \cdot \underline{\underline{A}}^T = \lambda_i^2 t_i t_i \tag{2-9}$$

which has two non-zero eigenvalues, λ_s^2 and λ_φ^2, associated with two orthogonal eigenvectors corresponding to local principal axes of deformation in the tangential membrane plane. The stretching ratios are given by the next relation:

$$\lambda_s = \frac{ds}{ds^{SF}} = \frac{s_\xi}{s_\xi^{SF}} \quad ; \quad \lambda_\varphi = \frac{\sigma d\varphi}{\left(\sigma d\varphi\right)^{SF}} = \frac{\sigma}{\sigma^{SF}} \tag{2-10}$$

where the superscript *SF* stands for the stress free state and $\sigma = r\sin\theta$. Then the Green-Lagrange deformation tensor $\underline{\underline{e}}$ is defined as:

$$\underline{\underline{e}} = \frac{1}{2}\left[\underline{\underline{C}} - \left(\underline{\underline{I}} - \vec{N}\vec{N}\right)\right] \tag{2-11}$$

And the tension tensor $\underline{\underline{\tau}}$:

$$\underline{\underline{\tau}} = \frac{2}{J_s}\left[\frac{\partial w}{\partial I_1}\underline{\underline{A}} \cdot \underline{\underline{A}}^T + \frac{\partial w}{\partial I_2} J_s^2 \left(\underline{\underline{I}} - \vec{n}\vec{n}\right)\right] \tag{2-12}$$

In the above equations, I_1 and I_2 are the invariants of $\underline{\underline{e}}$ strain tensor, measuring the local change in length and area, and J_s is the ratio between the current and reference local area:

$$I_1 = 2\mathrm{tr}\left(\underline{\underline{e}}\right) = \lambda_s^2 + \lambda_\varphi^2 - 2 \quad ; \quad I_2 = J_s^2 - 1 = \lambda_s^2\lambda_\varphi^2 - 1$$
$$J_s = \lambda_s\lambda_\varphi = \left(\underline{\underline{A}} \cdot \underline{\underline{A}}^T + \vec{N}\vec{N}\right)^{1/2} \tag{2-13}$$

and w is the strain energy function due to in plane tensions. The exact form of the strain energy function depends on the elastic behavior of the material. When linear materials are examined, the energy function w^{HK} of the Hook's law reads as follows [73]:

$$w^{HK} = \frac{G_s}{4(1-\nu)}\left[\left(\lambda_s^2 - 1\right)^2 + 2\nu\left(\lambda_s^2 - 1\right)\left(\lambda_\varphi^2 - 1\right) + \left(\lambda_\varphi^2 - 1\right)^2\right] \tag{2-14}$$

And then by substitution in eq. (2-12), the in plane tension τ_{ss} is:

$$\tau_{ss}^{HK} = \frac{G_s}{\lambda_\varphi(1-\nu)}\left[\lambda_s^2 - 1 + \nu\left(\lambda_\varphi^2 - 1\right)\right] \tag{2-15}$$

where, $G_s = \dfrac{\chi}{2(1+\nu)}$ and corresponds to surface shear modulus [N/m] and χ is the surface dilatation modulus, $\chi = Eh = 3Gh = 3G_s$, with E, G denoting the 3D Young's modulus and shear modulus, respectively, and h the shell thickness.

For Mooney-Rivlin materials (strain softening) [69, 70]:

$$w^{MR} = w\left(I_1, I_2\right) = \frac{G_{MR}}{2}\left[(1-b)\left(I_1 + 2 + \frac{1}{I_2 + 1}\right) + b\left(\frac{I_1 + 2}{I_2 + 1} + I_2 + 1\right)\right] \tag{2-16}$$

$$\tau_{ss}^{MR} = \frac{G_{MR}}{\lambda_s\lambda_\varphi}\left[\lambda_s^2 - \frac{1}{\left(\lambda_s\lambda_\varphi\right)^2}\right]\left[1 + b\left(\lambda_\varphi^2 - 1\right)\right] \tag{2-17}$$

with $G_{MR} = \dfrac{\chi}{3}$ and b is dimensionless parameter, $b \in [0,1]$, defining the nonlinearity of the Mooney-Rivlin law. The case b=0 corresponds to a neo-Hookean membrane and as b tends to zero the membrane becomes softer. Moreover, the description of the strain softening behavior with Mooney-Rivlin law allows for unlimited dilatation of the membrane, which is satisfied by a progressive membrane thinning.

For Skalak materials (strain hardening) [71]:

$$w^{SK} = w\left(I_1, I_2\right) = \frac{G_{SK}}{4}\left[I_1^2 + 2I_1 - 2I_2 + CI_2^2\right] \tag{2-18}$$

$$\tau_{ss}^{SK} = \frac{G_{SK}}{\lambda_s \lambda_\varphi}\left\{\lambda_s^2\left(\lambda_s^2 - 1\right) + C\left(\lambda_s\lambda_\varphi\right)^2\left[\left(\lambda_s\lambda_\varphi\right)^2 - 1\right]\right\} \tag{2-19}$$

with $G_{SK} = \frac{\chi\left(1+C\right)}{2\left(1+2C\right)}$ and parameter C a positive number that controls the area dilatation. Despite the fact that the above law was originally developed for red blood cells, which are lipid bilayer structures with an almost incompressible response in which case C>>1, the Skalak law is very general and therefore it is suitable for a strain hardening membrane whether it is area compressible or not.

In addition, note that the $\tau_{\varphi\varphi}$ tension is obtained by interchange of subscripts in eq. (2-15), (2-17) and (2-19).

Moreover, shear tensions are also acting on the shell along the thickness. The shear tension is related with the bending moments by writing a moment balance on an infinitesimal patch [67]:

$$\vec{q} = \vec{\nabla}_s \cdot \underline{\underline{m}} \cdot \left(\underline{\underline{I}} - \vec{n}\vec{n}\right) \tag{2-20}$$

Zarda et al. [39] suggested a linear constitutive law, similar to the membrane constitutive equations, for the bending moments:

$$m_{ss} = \frac{k_b}{\lambda_\varphi}\left(K_s + \nu K_\varphi\right) \quad ; \quad m_{\varphi\varphi} = \frac{k_b}{\lambda_s}\left(K_\varphi + \nu K_s\right) \tag{2-21}$$

where $K_s = \lambda_s k_s - k_s^{SF}$, $K_\varphi = \lambda_\varphi k_\varphi - k_\varphi^{SF}$ are the bending strains along the principal directions s,φ, respectively. Moreover, for a spherical stress-free shell: $k_s^{SF} = k_\varphi^{SF} = 1$. k_b denotes the bending modulus and according to classic shell theory for a three dimensional elastic shell with Young modulus E and thickness h [37]:

$$k_b = \frac{Eh^3}{12\left(1-\nu^2\right)} \tag{2-22}$$

Therefore assuming a linear constitutive law for the bending moments, the total bending energy is a quadratic function of bending strains:

$$w_b = \frac{k_b}{2}\left(K_s^2 + 2\nu K_s K_\varphi + K_\varphi^2\right) \tag{2-23}$$

In the final part of this subparagraph the equations of the elastic equilibrium will be discussed for the general case of static elastic membrane that separates two fluids. Thus, following Tsiglifis & Pelekasis [38] the force balance on the interface reads as:

$$\left(P_{in}-P_{out}\right)\underline{\underline{I}}\cdot\vec{n}=2k_m\gamma_{BW}\vec{n}+\Delta\vec{F} \tag{2-24}$$

where, P_{in} and P_{out} is the internal and the external pressure, $\underline{\underline{I}}$ is the 2×2 identity matrix, γ is the surface tension, $\vec{n}$ is the normal vector that points towards the surrounding fluid and $\Delta\vec{F}$ is the vector of stresses that arise due to elasticity which reads as [67]:

$$\Delta\vec{F}=\Delta F_n\vec{n}+\Delta F_s\vec{t}_s=-\vec{\nabla}_s\cdot\underline{\underline{T}} \tag{2-25}$$

Then, substituting the previous analysis in (2-25):

$$\begin{aligned}\Delta F_n&=k_s\tau_{ss}+k_\varphi\tau_{\varphi\varphi}-\frac{1}{\sigma}\frac{\partial\left(\sigma q\right)}{\partial s}\\ \Delta F_s&=-\left[\frac{\partial\tau_{ss}}{\partial s}+\frac{1}{\sigma}\frac{\partial\sigma}{\partial s}\left(\tau_{ss}-\tau_{\varphi\varphi}\right)+k_s q\right]\end{aligned} \tag{2-26}$$

and similarly for (2-20):

$$q=\frac{1}{\sigma}\frac{\partial\sigma}{\partial s}\left[\frac{\partial\left(\sigma m_{ss}\right)}{\partial\sigma}-m_{\varphi\varphi}\right] \tag{2-27}$$

Finally, it should be noted that the above analysis refers to the mid-surface of the shell.

2.3 Formulation for a microbubble under the AFM

A microbubble under the compression of a rigid and tipless cantilever is investigated. The microbubble is assumed to follow axisymmetric deformations and therefore only a generator curve is studied. Different formulation is followed for microbubbles covered with a polymeric shell and a lipid monolayer. The main reason of this choice is that the latter group of microbubbles is softer, it is deformed by forces in the range of nN's, and therefore the intermolecular forces should be accounted for. On the contrary, microbubbles covered with a polymeric shell are stiffer they are deformed in the range of 0-400 nN and consequently the intermolecular forces are negligible. Therefore, a classic contact model is presented for the case of polymeric microbubbles and a contact model including the intermolecular forces is employed for microbubbles covered with a lipid monolayer.

2.3.1 The polymeric shell-classic contact model

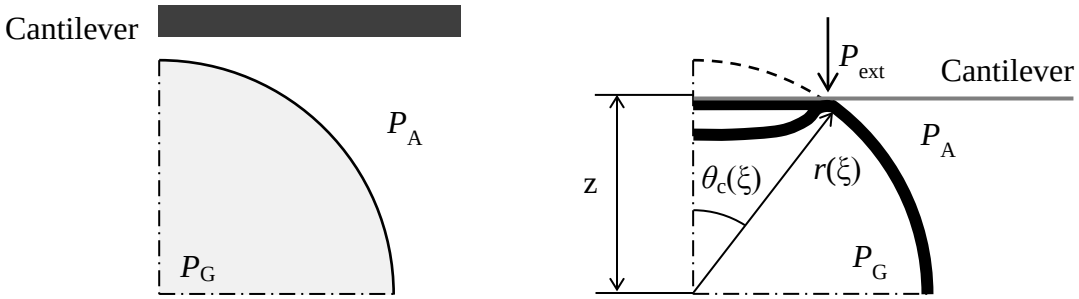

(a) Reference State **(b)** Deformed State

Figure 2-3: Schematic representation of a microbubble covered with polymer compressed by a cantilever. **(a)** Reference state, **(b)** Deformed state with flat and buckling configuration.

A microbubble covered with a polymeric elastic shell is investigated under the compression of the cantilever of the AFM, Figure 2-3, and symmetry is assumed with respect to the axis that is perpendicular to the cantilever and with respect to the equatorial plane. While the shell is compressed, elastic tensions are developed in order to balance the external load (P_{ext}), and at the same time the shell volume is reduced assuming isothermal compression while the gas pressure (P_G) increases. Moreover, the shape of the shell remains flattened for small values of deformation, but with further increase of the external load the shell buckles, forming a dimple around the pole, as a result of high compressive tensions. For flattened shapes, the cantilever is in contact with the microbubble with the corresponding contact length to be $R\sin(\theta_c)$. However, after buckling, only a small region at the end of the dimple is in contact with the cantilever.

In order to simulate the above problem, the force balance between elastic and external forces is employed, coupled with an isothermal gas compression equation. The force balance is written as follows:

$$\left(P_G - P_A\right)\underline{\underline{I}} \cdot \vec{n} = \Delta\vec{F} + \gamma_{BW}\left(\vec{\nabla}_s \cdot \vec{n}\right)\vec{n} \tag{2-28}$$

or in terms of components in normal ($\vec{n}$) and tangential direction ($\vec{t}_s$):

$$\begin{cases} \vec{n}: \left(P_G - P_A\right) = k_s\tau_{ss} + k_\varphi\tau_{\varphi\varphi} - \dfrac{1}{\sigma}\dfrac{\partial(\sigma q)}{\partial s} + \gamma_{BW}\left(\vec{\nabla}_s \cdot \vec{n}\right) \\ \vec{t}_s: -\left[\dfrac{\partial\tau_{ss}}{\partial s} + \dfrac{1}{\sigma}\dfrac{\partial\sigma}{\partial s}\left(\tau_{ss} - \tau_{\varphi\varphi}\right) + k_s q\right] = 0 \end{cases} \tag{2-29}$$

The surface tension between the bubble and the water is denoted with the γ_{BW}. The isothermal gas compression reads as:

$$P_G V_f^{\gamma} = P_A V_i^{\gamma} \tag{2-30}$$

where P_G and V_f are the gas pressure and the volume at the deformed configuration, respectively. P_A and V_i denote the same quantities but in the reference state, where it is assumed that the initial internal pressure is equal to the ambient pressure. Superscript γ denotes the polytropic index, here γ=1, for isothermal compression.

Moreover, an equation is required in order to capture the finite contact length. As a first attempt the following kinematic condition is considered:

$$\frac{dz}{d\xi} = \frac{d\left(r\cos\theta\right)}{d\xi} = 0 \quad \text{for all of the contact elements} \tag{2-31}$$

After applying the eq. (2-31), a pressure distribution of the external load (P_{ext}) is calculated. However, this kinematic condition is quite strict and fails to capture the buckling configuration. Moreover, the calculated load distribution has an almost zero value in the intermediate elements and a non-zero value at the end of contact. Due to this abrupt change in the applied load along the contact region, numerical solution with an increasing number of elements is difficult introducing wiggles around the edge of the contact region. Therefore, it is possible to apply the eq. (2-31) only at the last node of the contact area, eq. (2-32), and consequently to reduce the pressure distribution into an unknown point pressure at the end of contact. A similar formulation is followed by Updike & Kallins [46-48].

$$\frac{d\left(r\cos\theta\right)}{d\xi} = 0, \quad \theta{=}\theta_c \tag{2-32}$$

for the last node of the contact region. In this case the Lagrangian node on which the point load, P_{Ext}, is applied is treated as known leaving the load itself as one of the unknowns, Moreover, the normal force balance that corresponds to the last contact node is modified by adding the point pressure P_{ext} on the LHS.

$$P_{ext} + P_G - P_A = k_s \tau_{ss} + k_\varphi \tau_{\varphi\varphi} - \frac{1}{\sigma}\frac{\partial(\sigma q)}{\partial s} + \gamma_{BW}\left(\vec{\nabla}_s \cdot \vec{n}\right) \tag{2-33}$$

In this fashion both flat and buckled shapes can be captured and their relative stability can be investigated in the context of AFM measurements.

The problem formulation is rendered dimensionless by introducing the characteristic length scale, R_o. Then the solution depends mainly on three dimensionless parameters, namely $\hat{k}_b$, $\hat{P}_A$ and $\hat{\gamma}_{BW}$:

$$\hat{r} = \frac{r}{R_o};\ \hat{k}_b = \frac{k_b}{\chi R_o^2};\ \hat{P}_A = \frac{P_A R_o}{\chi};\ \hat{\gamma}_{BW} = \frac{\gamma}{\chi};\ \hat{\chi} = 1 \tag{2-34}$$

χ signifies the area dilatation modulus of the shell, which is introduced in order to eliminate the shell thickness from the formulation. For polymeric shells that normally have thicker coatings, bending resistance is related to the elastic modulus and the shell thickness, eq. (2-22).

Hence,

$$\hat{k}_b = \frac{k_b}{\chi R_o^2} = \frac{\frac{Eh^3}{12\left(1-\nu^2\right)}}{EhR_o^2} = \frac{1}{12\left(1-\nu^2\right)}\left(\frac{h}{R_o}\right)^2 \tag{2-35}$$

and the ratio between the shell thickness and the microbubble radius emerges as an independent dimensionless number. It should be stressed that the above three parameters, $\hat{k}_b$, $\hat{P}_A$ and $\hat{\gamma}_{BW}$, denote the relative importance among the four resistances to shell deformation, namely the stretching, bending stiffness of the shell as well as gas compressibility and surface tension. Typical values of these parameters for the polymeric microbubbles investigated in the present dissertation are: $\hat{k}_b \approx 10^{-5}$, $\hat{P}_A \approx 10^{-4}$ and $\hat{\gamma}_{BW} \approx 10^{-5} - 10^{-4}$. In the following the dimensionless $\hat{r}$ and its derivatives will be r for simplicity. Finally, an additional dimensionless parameter can be defined, $\hat{P}_{ext} = \frac{P_{ext} R_o}{\chi}$, as a measure of the intensity of the external disturbance.

In addition, the polymers are, as already mentioned, stiff materials, characterized by high Young's modulus (~GPa). Although it is not clear from the literature what the most appropriate constitutive equation is, some polymers are treated as strain hardening and therefore the Skalak law must be used. On the other hand the range of deformation in the AFM experiments is quite small, in which case the effect of a non-linear constitutive law is negligible. In the present formulation, Hook's law is considered as the constitutive law, although the choice of the constitutive equation is left to be subject of parametric study. Moreover, the effect of pre-stress is also taken into account in order to capture gas leakage in

the aqueous phase, see also paragraph 2.5. Boundary conditions of axisymmetry are applied at the edges of the domain:

$$r_{\xi} = \frac{dr}{d\xi} = 0 \quad \text{at} \quad \xi = 0 \quad \text{and} \quad \xi = 1 \tag{2-36}$$

$$\theta_{\xi\xi} = \frac{d^2\theta}{d\xi^2} = 0 \quad \text{at} \quad \xi = 0 \quad \text{and} \quad \xi = 1 \tag{2-37}$$

$$\begin{aligned} &\theta = 0 \quad \text{at} \quad \xi = 0 \\ &\theta = \frac{\pi}{2} \quad \text{at} \quad \xi = 1 \end{aligned} \tag{2-38}$$

The unknowns of the above formulation are the position of the lagrangian particles (r,θ), the gas pressure (P_G) and the external applied point load (P_{ext}). Finally, it is important to define deformation in order to compare the numerical results with the experimental. During the AFM measurements the deformation of the shell is not directly measured, but it is associated with the position of the cantilever. Therefore, in the present investigation the deformation is defined as the difference of the z-component of the position of the last contact node from its origin position in the undeformed configuration, Figure 2-3, in which case the situation with a buckled shell can also be accounted for. Multiplicity of solutions can be captured in this manner. More specifically, setting the angle θ_c in the undeformed shape on which the point load is applied two different solution families can be captured pertaining to the flat and buckled shape, the latter characterized by a lower value of the point load. The load for which such a multiplicity arises is the buckling point from which a new solution family emerges characterized by crater formation at the north pole of the shell. More details on this process is provided in Section 3 dedicated to the numerical solution and in Section 4 where the results of the simulations are discussed.

2.3.2 Phospholipid shell-Intermolecular forces

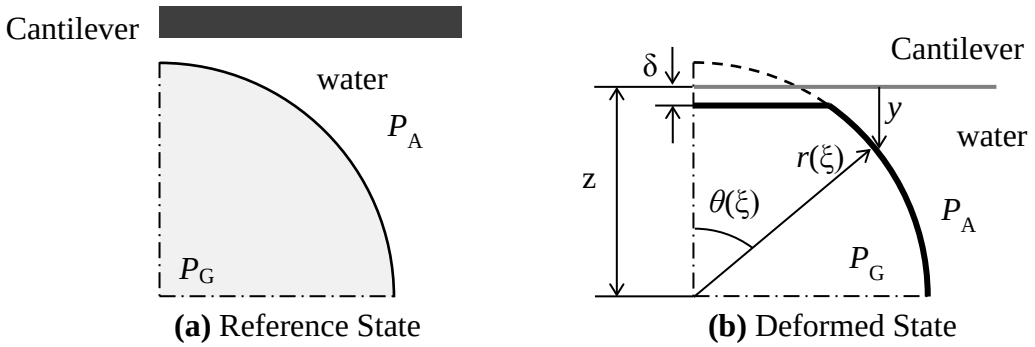

Figure 2-4: Schematic representation of a microbubble covered with lipid compressed by a cantilever. (a) Referential state, (b) Deformed state.

In the present paragraph, a microbubble covered with a lipid monolayer is investigated under the AFM, Figure 2-4, with the same symmetry conditions as with polymeric shells. The shell material is hydrophilic and soft in terms of elasticity (~MPa). As a result of its soft nature, the range of applied forces from the AFM is in [0-10] nN, which is in the order of the intermolecular forces. Moreover, due to the hydrophilic nature of the shell and cantilever, an ultrathin water layer occupies the space between them that resists thinning as the external pressure increases. This constitutes an additional resistance to the cantilever's advancement which is modelled as an additional pressure of the water near the contact area in comparison with the bulk aqueous phase. This pressure difference is the sum of intermolecular forces that act between the water film (with thickness δ) and the shell and it is known as disjoining pressure [35, 36]. This concept is adopted here for the description of the interaction between the cantilever and the shell in the present formulation by introducing a long range attractive-short range repulsive potential function. A typical form of the potential is:

$$W\left(y\right)=W_o\left[\left(\frac{\delta_A}{y}\right)^4-2\left(\frac{\delta_A}{y}\right)^2\right] \tag{2-39}$$

where δ_A denotes the distance where the potential takes the minimum negative value W_o, see also Figure 2-5. The energy due to intermolecular forces (*IF*) is:

$$\hat{w}_{IF}=\int_A W\left(y\right)dA \tag{2-40}$$

where dA is the infinitesimal deformed area of the shell with $dA=\left(\sigma d\varphi\right)ds=s_\xi r\sin\theta\,\mathrm{d}\varphi d\xi$.

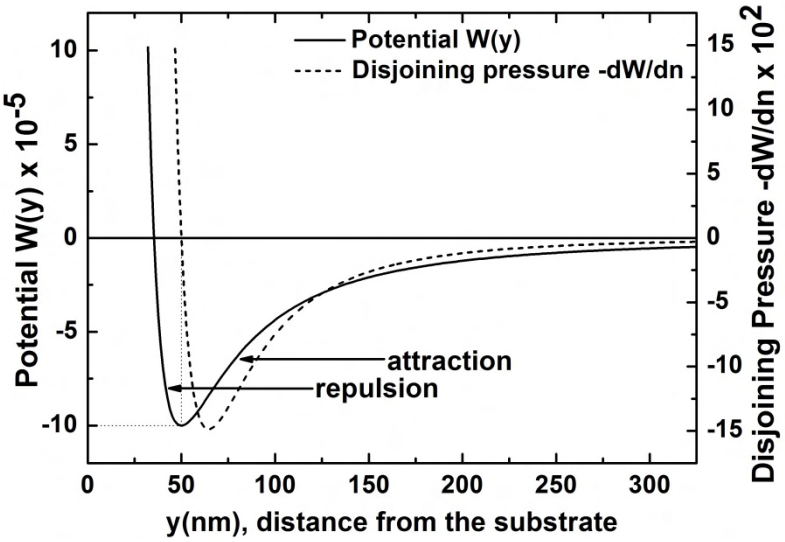

Figure 2-5: Potential (continuous line & left vertical axis) and disjoining pressure (dashed line & right vertical axis) as a function of the distance *y* from the substrate, with δ_A=50 nm and W_o=10^{-4} N/m.

As the two bodies are quite far from each other ($y>>\delta_A$) the potential is essentially zero and no interaction between the bodies is detected. While the cantilever approaches the shell, in other words *y* decreases, the potential has a decreasing negative value ($y\sim\delta_A$). This is the regime where the two bodies are in attraction, the disjoining pressure and the resulting force are also negative. At $y=\delta_A$ the potential has a minimum value, this the point where the disjoining pressure and the force are zero and with further decrease of their distance ($y<\delta_A$), the two bodies are in repulsion, thus the disjoining pressure and the force change sign. The total force is calculated by the integral of the disjoining pressure on the shell surface, with n pointing towards the surrounding liquid:

$$F = -\int_A \frac{\partial W}{\partial n} dA \tag{2-41}$$

By minimizing the total energy the disjoining pressure and the potential are introduced in the components of the force balance [63] that assume the form:

$$\begin{cases} \vec{n}: \left(P_G - P_A\right) = k_s \tau_{ss} + k_\varphi \tau_{\varphi\varphi} + \left(\gamma_{BW} + W\right)\left(\vec{\nabla}_s \cdot \vec{n}\right) - \dfrac{1}{\sigma}\dfrac{\partial(\sigma q)}{\partial s} + \dfrac{\partial W}{\partial n} \\ \vec{t}_s: -\left[\dfrac{\partial \tau_{ss}}{\partial s} + \dfrac{1}{\sigma}\dfrac{\partial \sigma}{\partial s}\left(\tau_{ss} - \tau_{\varphi\varphi}\right) + k_s q\right] = 0 \end{cases} \tag{2-42}$$

The dimensionless parameters in this problem are:

$$\hat{r} = \frac{r}{R_o};\ \hat{k}_b = \frac{k_b}{W_o R_o^2};\ \hat{P}_A = \frac{P_A R_o}{W_o};\ \hat{\gamma}_{BW} = \frac{\gamma_{BW}}{W_o};\ \hat{\chi} = \frac{\chi}{W_o};\ \hat{W}_o = 1 \tag{2-43}$$

Measuring the relative stiffens of bending, stretching, gas compressibility and surface tension with respect to interfacial energy W_o of the two bodies interaction. Moreover, for the

lipid monolayers the bending stiffness and the area dilatations modulus are assumed to be independent parameters, since the shell thickness is a relative small parameter and cannot be easily defined [39]. Typical values of the above dimensionless parameters for the experiments examined here are: $\hat{k}_b \approx 1$, $\hat{P}_A = 1.5 \cdot 10^3$, $\hat{\gamma}_{BW} \approx 10^2$ and $\hat{\chi} \approx 5 \cdot 10^2$. In the rest of the problem formulation the dimensionless $\hat{r}$ will be designated as r for simplicity. In addition, the Mooney-Rivlin has been chosen as the constitutive law to relate the elastic tensions with strains. Alternatively, the above equations of equilibrium can be derived in terms of energy:

$$F \Delta z = U_T^f - U_T^{in} \tag{2-44}$$

where F is the total force that moves the cantilever by Δz and U_T is the total energy in the final and initial stage. Five energies constitute the total energy:

$$U_T = \hat{w}_{str} + \hat{w}_b + \hat{w}_c + \hat{w}_s + \hat{w}_{IF} \tag{2-45}$$

namely, energy due to stretching $\hat{w}_{str}$, bending $\hat{w}_b$, gas compression $\hat{w}_c$, surface tension $\hat{w}_s$ and the energy due to intermolecular forces, where,

$$\hat{w}_{str} = \int_A w_{str} dA, \quad \text{with } w_{str} = \begin{cases} w_{str}^{HK}, & \text{Hook law} \\ w_{str}^{MR}, & \text{Mooney-Rivlin law} \\ w_{str}^{SK}, & \text{Skalak law} \end{cases} \tag{2-46}$$

$$\hat{w}_b = \int_A w_b dA = \int_A \frac{k_b}{2} \left(K_s^2 + 2\nu K_s K_\varphi + K_\varphi^2 \right) dA \tag{2-47}$$

The above two energies refer to the energy due to elasticity and they are also described in details in section 2.2.

$$\hat{w}_c = V \left(P_A + \Delta P + \frac{P_G}{\gamma - 1} \right) - V_o \left(P_A + \frac{P_A + 2\gamma_{BW}}{\gamma - 1} \right) \tag{2-48}$$

where, P_A is the ambient pressure and V_o and V denote the initial and the current volume, respectively.

$$\hat{w}_s = \int_A \gamma_{BW} dA \tag{2-49}$$

It is important to note that the energy due to intermolecular forces can be interpreted as a deficit or excess energy in comparison with the case in the absence of the solid substrate. Consequently, when adhesive or very mild repulsive forces prevail the energy due to intermolecular forces is negative thus tending to stabilize the overall static configuration. This aspect of the interaction between hydrophilic phospholipid shells and the cantilever is crucial in the observed static arrangement when such shells are interrogated via AFM.

Next, the minimization of the energy due to intermolecular forces is demonstrated in order to recover the terms of disjoining pressure and potential in the normal force balance:

The energy due to intermolecular forces is: $\hat{w}_{IF} = \iint_A W_{IF} dA$, therefore, its variation for a 2d shell in cylindrical coordinates is:

$$\delta \hat{w}_{IF} = \iint_A \frac{\delta W_{IF}}{\delta \vec{r}} \cdot \delta \vec{r}\, dA + \iint_A W_{IF} \frac{\delta (dA)}{\delta \vec{r}} \cdot \delta \vec{r} \tag{2-50}$$

and then, the first term of the above equation is calculated:

$$\frac{\delta W_{IF}}{\delta \vec{r}} = \vec{\nabla} W_{IF} = \underbrace{\frac{\partial W_{IF}}{\partial \sigma}}_{=0} \vec{e}_\sigma + \frac{\partial W_{IF}}{\partial z} \vec{e}_z = \frac{\partial W_{IF}}{\partial z} \vec{e}_z \tag{2-51}$$

In addition, $\vec{n} = \sigma_s \vec{e}_z - z_s \vec{e}_\sigma$, $\vec{t}_s = \sigma_s \vec{e}_\sigma + z_s \vec{e}_z$, in which case $\vec{e}_z \cdot \vec{n} = \sigma_s$ and $\vec{e}_z \cdot \vec{t}_s = z_s$. Thus $\vec{e}_z = z_s \vec{t}_s + \sigma_s \vec{n}$, and therefore:

$$\frac{\delta W_{IF}}{\delta \vec{r}} = \frac{\partial W_{IF}}{\partial z} \vec{e}_z = \frac{\partial W_{IF}}{\partial z} \left(z_s \vec{t}_s + \sigma_s \vec{n} \right) = \frac{\partial W_{IF}}{\partial s} \vec{t} + \frac{\partial W_{IF}}{\partial n} \vec{n}\,. \tag{2-52}$$

Returning to the variation of the total energy due to intermolecular forces we have that:

$$\iint_A W_{IF} dA = \ell \oint_s W_{IF} ds = \ell \oint_s W_{IF} g^{1/2} da \tag{2-53}$$

where g : metric, $\mathrm{g} = \left(\frac{ds}{da} \right)^{1/2} = \frac{\partial \vec{r}}{\partial a} \cdot \frac{\partial \vec{r}}{\partial a}$, $\frac{\partial \vec{r}}{\partial a} = \vec{r}'$, $\quad g = \sqrt{\vec{r}' \cdot \vec{r}'}$, $\quad \vec{t}_s = \frac{\vec{r}'}{\left(\vec{r}' \cdot \vec{r}' \right)^{1/2}}$

Consequently,

$$\iint_A W_{IF} \frac{\delta (dA)}{\delta \vec{r}} = \ell \oint_s W_{IF} \left(\frac{\delta g^{1/2}}{\delta \vec{r}'} \delta \vec{r}' + \frac{\delta g^{1/2}}{\delta \vec{r}} \delta \vec{r} \right) da = \ell \oint_s W_{IF} \left[\frac{1}{2} \frac{2 \frac{\partial \vec{r}}{\partial a} \delta \vec{r}'}{\left(\frac{\partial \vec{r}}{\partial a} \cdot \frac{\partial \vec{r}}{\partial a} \right)^{1/2}} \right] da =$$

$$= -\ell \oint_s \frac{d}{da} \left[W_{IF} \frac{\vec{r}'}{\left(\vec{r}' \cdot \vec{r}' \right)^{1/2}} \right] \delta \vec{r}\, da + \underbrace{\left. \frac{\ell W_{IF} \vec{r}' \delta \vec{r}}{\left(\vec{r}' \cdot \vec{r}' \right)^{1/2}} \right|_0^s}_{=0 \text{ for a closed body}} =$$

$$= -\ell \oint_s \frac{dW_{IF}}{da} \frac{\vec{r}' \cdot \delta \vec{r}}{\left(\vec{r}' \cdot \vec{r}' \right)^{1/2}} da - \ell \oint_s W_{IF} \underbrace{\frac{\vec{r}'' \left(\vec{r}' \cdot \vec{r}' \right)^{1/2} - \vec{r}' \frac{1}{2} \frac{2 \vec{r}' \cdot \vec{r}''}{\left(\vec{r}' \cdot \vec{r}' \right)^{1/2}}}{\vec{r}' \cdot \vec{r}'}}_{= \frac{\partial \vec{t}_s}{\partial a}} \cdot \delta \vec{r}\, da =$$

$$= -\ell \oint_s \frac{dW_{IF}}{da} \frac{\vec{r}' \cdot \delta \vec{r}}{\left(\vec{r}' \cdot \vec{r}' \right)^{1/2}} da - \ell \oint_s W_{IF} \frac{\partial \vec{t}_s}{\partial a} \cdot \delta \vec{r}\, da =$$

$$= -\ell \oint_s \frac{dW_{IF}}{da} \vec{t}_s \cdot \delta \vec{r}\, da - \ell \oint_s W_{IF} \frac{\partial \vec{t}_s}{\partial a} \cdot \delta \vec{r}\, da = -\iint_A \frac{dW_{IF}}{ds} \vec{t}_s \cdot \delta \vec{r}\, dA - \iint_A W_{IF} \frac{\partial \vec{t}_s}{\partial s} \cdot \delta \vec{r}\, dA =$$

$$= -\oiint_A \frac{dW_{IF}}{ds}\vec{t}_s \cdot \delta\vec{r}dA + \oiint_A W_{IF} c\vec{n} \cdot \delta\vec{r}dA \tag{2-54}$$

where c denotes the mean curvature of a 2d surface. Therefore, (2-50) after introducing (2-51) and (2-54) becomes:

$$\begin{aligned} \delta\hat{w}_{IF} &= \oiint_A \left(\frac{\partial W_{IF}}{\partial s}\vec{t}_s + \frac{\partial W_{IF}}{\partial n}\vec{n} \right) \cdot \delta\vec{r}dA + \oiint_A \left(-\frac{\partial W_{IF}}{\partial s}\vec{t}_s + cW_{IF}\vec{n} \right) \cdot \delta\vec{r}dA \Rightarrow \\ \delta\hat{w}_{IF} &= \oiint_A \left(\frac{\partial W_{IF}}{\partial n} + cW_{IF} \right) \vec{n} \cdot \delta\vec{r}\ dA \end{aligned} \tag{2-55}$$

The case of an axisymmetric body is presented in Appendix B.

Furthermore, as in the case with a polymeric shell, the shell volume decreases as the external force increases and consequently the internal pressure increases. In order to capture the effect of pressure changes, an isothermal gas compression equation is written:

$$P_G V_f^{\gamma} = P_A V_i^{\gamma} \tag{2-56}$$

Boundary conditions of axisymmetry are applied at the edges of the domain:

$$r_{\xi} = \frac{dr}{d\xi} = 0 \quad \text{at} \quad \xi = 0 \quad \text{and} \quad \xi = 1 \tag{2-57}$$

$$\theta_{\xi\xi} = \frac{d^2\theta}{d\xi^2} = 0 \quad \text{at} \quad \xi = 0 \quad \text{and} \quad \xi = 1 \tag{2-58}$$

$$\begin{aligned} &\theta = 0 \quad \text{at} \quad \xi = 0 \\ &\theta = \frac{\pi}{2} \quad \text{at} \quad \xi = 1 \end{aligned} \tag{2-59}$$

In addition, the effect of pre-stress could also be considered, see paragraph 2.5. Solving the system of the above equations it is possible to calculate the shape of the deformed shell, the internal pressure and the required external force for various values of the elasticity (bending - stretching) and the potential parameters. The comparison of the theoretical results with available experimental data can be used to characterize the shell in terms of Young's and bending modulus. However, some researchers characterize the lipid monolayers as shells without elasticity assuming that their behavior is dominated by surface tension only. In order to examine this argument, the elasticity terms of normal and tangential force balance are omitted. Then, the normal force balance reads as follows:

$$\vec{n} : \left(P_G - P_A \right) = \left(\gamma_{BW} + W \right) \left(\vec{\nabla}_s \cdot \vec{n} \right) + \frac{\partial W}{\partial n} \tag{2-60}$$

Eq.(2-60) is known as the augmented Young-Laplace equation [62]. However, the tangential force balance becomes a trivial equation, as the derivative of the potential with respect to arc-length *s* is a negligible term. Therefore, in order to balance the number of

unknowns and equation, instead of the tangential force balance the arc-length equation is written:

$$\left(rd\theta\right)^2+\left(dr\right)^2=\left(ds\right)^2 \tag{2-61}$$

where, $d\theta$, dr and ds denote the infinitesimal lengths of θ, r and s, respectively. Thus, the nodes of the shell surface are equally distributed along the generator curve or alternatively the thickness of the elements is constant. In addition, if the lagrangian variable ξ is introduced, the arc-length is written in the following form:

$$r^2\left(\frac{d\theta}{d\xi}\right)^2+\left(\frac{dr}{d\xi}\right)^2=\left(\frac{ds}{d\xi}\right)^2 \Rightarrow r^2\theta_\xi^2+r_\xi^2=s_\xi^2 \tag{2-62}$$

However, for equally distributed elements: $s=\xi s_{\max} \Rightarrow \frac{ds}{s\xi}=s_\xi=s_{\max}$, where s_{max} is the value of the arc-length at the end of the domain, where it takes its maximum value and it is not priori known, which consequently increases the number of the unknown variables. In order to handle the new unknown variable s_{max}, the boundary condition (2-59) does not replace an arc-length equation, but it is considered as an extra equation:

$$\theta=\frac{\pi}{2} \quad \text{at} \quad \xi=1 \tag{2-63}$$

The equation of isothermal gas compression remains the same, as well as the rest of the boundary conditions. Solving again the equations of the modified formulation it is possible to treat the microbubble as a shell free of elasticity.

2.4 Formulation for a microbubble subject to a uniform pressure

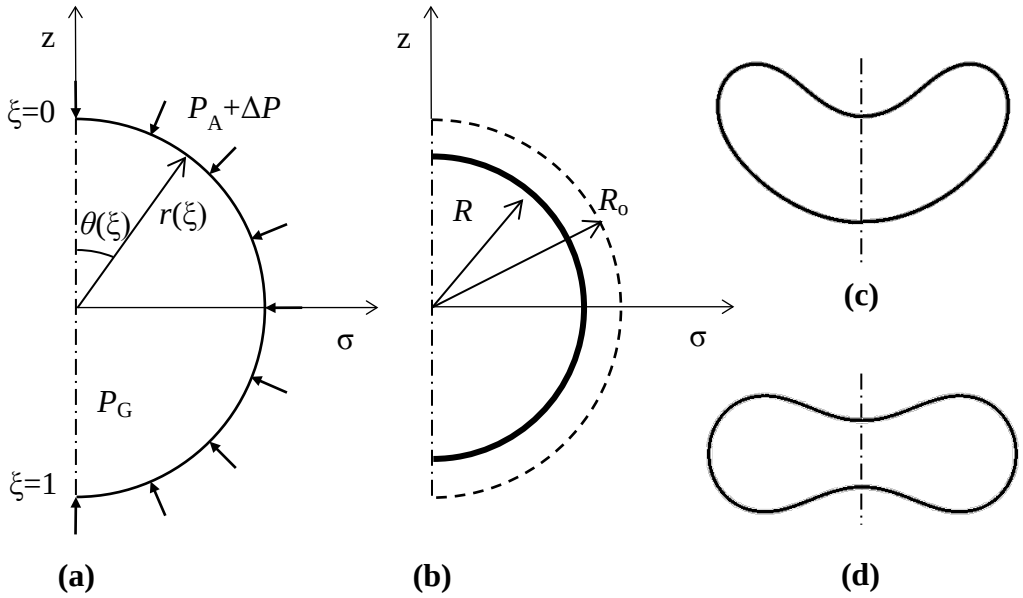

Figure 2-6: Schematic representation of a microbubble subject to a uniform load **(a)** Reference state (dashed line), **(b)** Deformed state-sphere (solid line), **(c)** Deformed state-asymmetric mode, **(d)** Deformed state-symmetric mode.

The second problem that the present thesis investigates is the deformation of a microbubble subject to a uniform overpressure field ΔP, see Figure 2-6 (a). Initially, the microbubble's shape is spherical characterized by a rest radius R_o. Up to a critical value of the external load ΔP_{cr} the shell is compressed into a spherical shape with smaller radius R, Figure 2-6 (b). However, with further increase of the external load and beyond its critical value the spherosymmetric configuration remains a possible static arrangement, but a second solution arises as a bifurcation, which is known as a buckling solution that corresponds to axisymmetric shells that are asymmetric or symmetric with respect to the equator, Figure 2-6 (c), (d). The emerging solution family evolves subcritically towards larger volumes indicating an unstable branch. However, in the presence of a small but large enough geometric imperfection [54, 55], they become accessible in the presence of an external load of the same magnitude with the one leading to the compressed sphere. It must be noted that in Figure 2-6 (c) and (d) the shell is plotted in [0, 2π] for visual reasons only. In order to capture the above series of solutions, the normal and tangential force balance are employed, assuming axisymmetry with respect to z axis:

$$\begin{cases} \vec{n}: \left(P_G - P_A - \Delta P\right) = k_s \tau_{ss} + k_\varphi \tau_{\varphi\varphi} - \dfrac{1}{\sigma}\dfrac{\partial(\sigma q)}{\partial s} + \gamma_{BW}\left(\vec{\nabla}_s \cdot \vec{n}\right) \\ \vec{t}_s: -\left[\dfrac{\partial \tau_{ss}}{\partial s} + \dfrac{1}{\sigma}\dfrac{\partial \sigma}{\partial s}\left(\tau_{ss} - \tau_{\varphi\varphi}\right) + k_s q\right] = 0 \end{cases} \tag{2-64}$$

The constitutive law could be Mooney-Rivlin, Skalak or Hook. The encapsulated gas is assumed to be ideal and undergoes isothermal compression:

$$P_G V_f^{\gamma} = P_A V_i^{\gamma} \tag{2-65}$$

Moreover, in order to avoid a net translation of the shell as a rigid body, the *z* component of the mass center is imposed to be zero.

$$z_{CG} = \frac{\int_V \vec{r} \cdot \vec{e}_z dV}{V} = 0 \Rightarrow \int_V \vec{r} \cdot \vec{e}_z dV = 0 \Rightarrow \int_0^1 r^3 \cos^2\theta \sin\theta \left(r\theta_\xi \cos\theta + r_\xi \sin\theta \right) d\xi = 0 \tag{2-66}$$

The σ component of the mass center is identically zero due to axisymmetry. Analogous dimensionless parameters can be defined as in the previous problems: $\hat{k}_b = \frac{k_b}{\chi R_o^2}$, $\hat{P}_A = \frac{P_A R_o}{\chi}$, $\hat{\gamma}_{BW} = \frac{\gamma}{\chi}$ and $\hat{\chi} = 1$ for both type of materials, assuming that for lipid shells the bending stiffness and the area dilatation are independent parameters. Finally, boundary conditions of axisymmetry are applied at the domain edges:

$$r_\xi = \frac{dr}{d\xi} = 0 \quad \text{at} \quad \xi = 0 \quad \text{and} \quad \xi = 1 \tag{2-67}$$

$$\theta_{\xi\xi} = \frac{d^2\theta}{d\xi^2} = 0 \quad \text{at} \quad \xi = 0 \quad \text{and} \quad \xi = 1 \tag{2-68}$$

$$\begin{aligned} &\theta = 0 \quad \text{at} \quad \xi = 0 \\ &\theta = \pi \quad \text{at} \quad \xi = 1 \end{aligned} \tag{2-69}$$

Solving the above system of equations the *r* and θ coordinates of all lagrangian markers are calculated, along with the internal pressure P_G, for different values of the parameter ΔP.

As it is already mentioned, when the external load reaches a critical value it is possible to find different solutions for the same ΔP, which correspond to buckling of the shell into symmetric or asymmetric shapes. The new branch is characterized with one more negative eigenvalue in comparison with the main solution (sphere) for the same value of the ΔP and exists for smaller values of the critical load; therefore, this solution corresponds to a subcritical bifurcation. The theoretical value of the critical buckling load, obtained from continuous shell theory and performing linear stability analysis on the spherical configuration, in the limit of small overpressure to external pressure ratio ΔP_{cr}, is provided in [54]:

$$\Delta P_{cr} = \frac{2E}{\sqrt{3\left(1-\nu^2\right)}} \left(\frac{h}{R_o} \right)^2 \tag{2-70}$$

Furthermore, calculating the total energy of the post-buckling solution it is possible to characterize the stability of the emerging branch in comparison with the main solution. Finally, following Tsiglifis & Pelekasis [38] the shape of the solution is decomposed in Legendre polynomials in order to calculate the dominant mode of the solution.

2.5 The effect of pre-stress

As it was mentioned in the introduction, a gas phase is encapsulated in the shell core. The microbubble is a self-assembling structure and the initial radius corresponds to a stress-free state, where no residual strains are acting. However, after some time and before the measurements with the AFM, some gas might escape through the protective coating and eventually cause a reduction in the shell volume and consequently induce initial compressive tensions. Therefore, in order to account for the effect of pre-stress in the present thesis, the dimensionless quantity u is introduced in order to quantify the amount of pre-stress:

$$R^{SF} = R^0 - u \tag{2-71}$$

where R^{SF} is the stress free shell radius and R^0 is the radius at the beginning of the AFM experiment, Figure 2-7. In the above equation when $u<0$, the stress-free radius is bigger than the R^0 radius, which means that some gas has been released in the aqueous phase and the shell is compressed and vice versa. Thus, at the beginning of the simulation the shell has residual strains $\lambda_s = \lambda_\varphi = \frac{R^0}{R^0 - u}$, resulting residual stresses τ_{ss}, $\tau_{\varphi\varphi}$, which are calculated by the eqs. (2-15), (2-17) and (2-18).

Moreover, it is assumed that the gas pressure in the stress-free state is equal to the ambient pressure, but if the surface tension and some pre-stress are also taken into account, then the initial gas pressure, P_G, from normal force balance, (2-24) - (2-26), and for initial radius R^0 is [38, 74]:

$$P_G = P_A + 2\gamma_{BW} + \tau_{ss} + \tau_{\varphi\varphi} \tag{2-72}$$

In addition, it must be noted that even when the shell is not no pre-stressed the initial gas pressure will be different from the external pressure by a term $2\gamma_{BW}$, as it is described by the Young-Laplace equation, due to surface tension. Another important point that arises from eq. (2-72) is that the increase in gas pressure caused by surface tension may be cancelled by the drop caused by compressive tensions ($\tau_{ss}+\tau_{\varphi\varphi}<0$) the amount of which strongly depends on the shell area dilatation modulus.

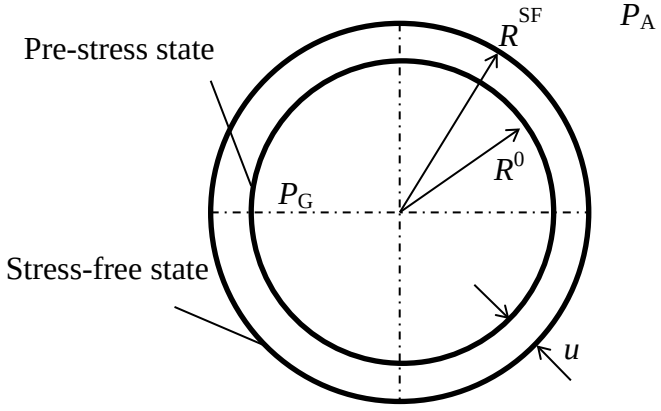

Figure 2-7: Schematic illustration of a pre-stress microbubble.

Chapter 3. Numerical Analysis - Validation

The third chapter describes the numerical methodology that is employed in order to solve the above problems. More specifically, the equations that describe the problems of the present dissertation constitute a set of nonlinear ordinary differential equations (ode's), which are solved numerically via the finite element method (fem), with b-cubic splines as basis functions. The Newton-Rapson method is employed for the solution of the nonlinear algebraic problem that arises performing simple or arc-length continuation. Furthermore, benchmark calculations are conducted in order to investigate the validity of the above formulation and numerical implementation.

3.1 Spline representation

The modelling of the elasticity terms for thin shells with finite thickness requires the mathematical description of the first derivative of shear tension; therefore the derived equations contain high order derivatives. As a result, the basis function for the finite elements must be polynomials of high order and therefore the b-cubic splines are used, which are piecewise cubic curves and have the following form [75, 76]:

$$B_i(\xi)=\frac{1}{\ell^3}\begin{cases}\left(\xi-\xi_{i-2}\right)^3, & \text{if } \xi\in\left[\xi_{i-2},\xi_{i-1}\right]\\ \ell^3+3\ell^2\left(\xi-\xi_{i-1}\right)+3\ell\left(\xi-\xi_{i-1}\right)^2-3\left(\xi-\xi_{i-1}\right)^3, & \text{if } \xi\in\left[\xi_{i-1},\xi_i\right]\\ \ell^3+3\ell^2\left(\xi_{i+1}-\xi\right)+3\ell\left(\xi_{i+1}-\xi\right)^2-3\left(\xi_{i+1}-\xi\right)^3, & \text{if } \xi\in\left[\xi_i,\xi_{i+1}\right]\\ \left(\xi_{i+2}-\xi\right)^3, & \text{if } \xi\in\left[\xi_{i+1},\xi_{i+2}\right]\\ 0, & \text{otherwise}\end{cases} \tag{3-1}$$

where ℓ denotes the element thickness $\left(\ell=\xi_{i+1}-\xi_i\right)$, which is the same for all elements, since in the present dissertation the mesh is uniform across the domain. As shown in Figure 3-1(a) a spline polynomial is a non-zero function on the inside of four continuous elements and therefore the Kronecker delta identity is not satisfied, in particular it is:

$$B_i\left(\xi_j\right)=\begin{cases}1, & \text{if } j=i\\ 1/4, & \text{if } j=i-1 \text{ or } j=i+1\\ 0, & \text{if } j=i-2 \text{ or } j=i+2\end{cases} \tag{3-2}$$

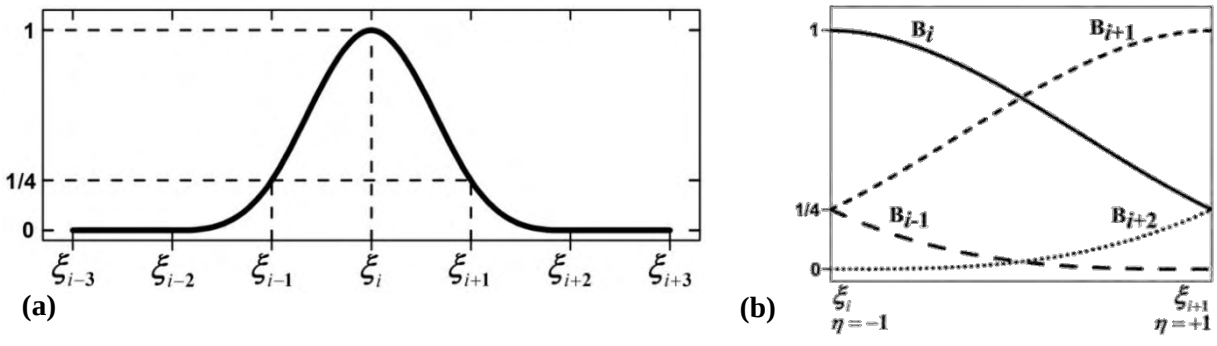

Figure 3-1: (a) Schematic representation of B_i spline, **(b)** Spline representation into one element.

Hence, the unknowns r and θ at the nodes are different from the spline coefficients and they are described as follows:

$$r(\xi)=\sum_{j=0}^{N+1} a_j B_j(\xi) \tag{3-3}$$

$$\theta(\xi)=\sum_{j=0}^{N+1} b_j B_j(\xi) \tag{3-4}$$

where a_j and b_j are the unknown coefficients of the spline representation and N is the number of nodes. The two coefficients that correspond to fictitious nodes outside the domain, i.e. a_o, a_{N+1}, b_o and b_{N+1}, are calculated by the boundary conditions of each problem.

Also, b cubic splines maintain smoothness and continuity of higher order derivatives; in particular they ensure continuity of the function as well as of the first and second derivative. Therefore, upon integrating the terms of elasticity by parts twice the order of ode is reduced. Further discussion on the last topic can be found in the next paragraph (3.2).

3.2 Weak form and Newton-Raphson method

The governing equations of the above problems are two non-linear ordinary differential equations corresponding to the normal and tangential force balance. For their solution the Galerkin finite element method is employed in order to transform the ode into a set of non-linear algebraic equations [77, 78] that are solved for the r, θ coordinates of shell location. Initially the unknowns r, θ and their derivatives in the above equations are substituted by eqs (3-3) and (3-4) and then the differential equations is multiplied with the trial function and integrated over the shell surface. The new integral equation corresponds to the weak form of the differential equation. Subsequently, integration by parts is performed twice in the normal force balance, operating on the term that contains the shear tension derivative, in order to reduce the fourth order derivative. In the same manner, the derivative of τ_{ss} tension in the tangential force balance is eliminated. All the resulting integrals are calculated by performing Gauss integration with four points over each element in the domain [-1,1], see also Figure 3-1(b). In this fashion numerical error is dominated by the interpolation of the unknown functions instead of the gaussian integration [79]. In the following, the final equations in their weak form are written for each problem:

The normal force balance:

$$\begin{aligned} R_1=\int_0^1 \left[\left(k_s\tau_{ss}+k_\varphi\tau_{\varphi\varphi}+2k_m(\gamma_{BW}+W)+P(\xi)+P_A-P_G+\frac{\partial W}{\partial n}\right)B_i\sigma s_\xi\right]d\xi \\ -\int_0^1\left[\frac{\sigma\left(B_{i,\xi\xi}s_\xi-B_{i,\xi}s_{\xi\xi}\right)}{s_\xi^2}+\frac{m_\varphi B_{i,\xi}\sigma_\xi}{s_\xi}\right]d\xi+\left[\frac{\sigma m_s B_{i,\xi}}{s_\xi}-\sigma q B_i\right]_{\xi=0}^{\xi=1}=0 \end{aligned} \tag{3-5}$$

The tangential force balance:

$$R_2 = \int_0^1 \left[\tau_{ss} B_{i,\xi} \sigma + B_i \sigma_\xi \tau_{\varphi\varphi} + \sigma m_s \left(k_{s,\xi} B_i + k_s B_{i,\xi} \right) + k_s m_\varphi B_i \sigma_\xi \right] d\xi - \left[\left(k_s m_s + \tau_{ss} \right) \sigma B_i \right]_{\xi=0}^{\xi=1} = 0 \tag{3-6}$$

The isothermal gas compression:

$$R_3 = P_G V^\gamma - P_A V_0^\gamma = 0 \tag{3-7}$$

The kinematic condition:

$$R_4 = z_\xi = r_\xi \cos\theta - r\theta_\xi \sin\theta = 0 \quad \text{at} \quad \xi = \xi_c \tag{3-8}$$

The arc-length:

$$R_5 = \frac{dS}{d\xi} = S_{max} = \left(r_\xi^2 + r^2 \theta_\xi^2 \right)^{0.5} \Rightarrow \int_0^1 \left[S_{max} - \left(r_\xi^2 + r^2 \theta_\xi^2 \right)^{0.5} \right] B_i \sigma s_\xi d\xi = 0 \tag{3-9}$$

The position of the center of mass:

$$R_6 = \int_0^1 r^3 \cos^2\theta \sin\theta \left(r\theta_\xi \cos\theta + r_\xi \sin\theta \right) d\xi = 0 \tag{3-10}$$

where $\sigma = r\sin\theta$; $\sigma_\xi = r_\xi \sin\theta + r\theta_\xi \cos\theta$ and the square brackets contain the boundary terms resulting by the integration by parts.

According to chapter 2, when the classic contact problem is investigated, the R_1, R_2, R_3 and R_4 residuals are solved, with W_o=0 and $P(\xi) = \begin{cases} P_{ext}, & \xi = \xi_c \\ 0, & \text{otherwise} \end{cases}$. The contact model that accounts for the intermolecular forces, surface tension and elasticity is solved by the R_1, R_2 and R_3 residuals with $P(\xi)$=0. However, in the same contact model, if the elasticity terms are omitted, then the R_1, R_5 and R_3 residuals are solved, setting χ=0 and k_b=0. The equation that produces residual R_5 is a statement regarding the distribution of Lagrangian markers on the shell. In particular it enforces the Lagrangian markers to be placed so that they form elements of the same length. Finally, for the bifurcation diagrams residuals R_1, R_2, R_3 and R_6 are solved with W_o=0 and $P(\xi) = \Delta P, \quad \forall \xi \in [0,1]$. It must be noted that the boundary terms vanish in both edges of the domain (ξ=0 and 1) for the problem with a homogeneous external load whereas they only vanish at ξ=0 in contact problems while remaining non-zero at the equatorial plane, i.e. at ξ=1, where symmetry conditions are imposed. In the latter case it is assumed that an equal force is applied on the shell from both poles and this reflects in the symmetry conditions at the equatorial plane. Consequently, the boundary terms are calculated for the three final residuals of the normal and tangential force balance.

Furthermore, the classic contact model contains a concentrated point force at the end of contact length which will introduce a discontinuity in the distribution of shear tension, *q*. The jump in shear tension is also supported by the b-cubic splines, because their third derivative is not a continuous function at the domain nodes. As it is already mentioned the b-cubic splines guarantee continuity up to the second derivative, therefore the in plane tensions and bending moments are continuous functions, a behavior which conforms well with the physical problem, where external moments or in-plane stresses are not acting on the shell. On the contrary, in the problem where the interaction between the cantilever and the shell is simulated in the presence of intermolecular forces, the external loading is a smooth function rather than a point force and therefore the distribution of the shear tension will follow the distribution of disjoining pressure.

In the rest of the present session the Newton-Raphson method along with continuation techniques are discussed for the above systems of equations, which have the following form:

$$\vec{R}\left(\vec{x}\right)=0 \tag{3-11}$$

where $\vec{x}$ denotes the unknown vector. Seeking for solutions of the eq. (3-11), the Newton-Raphson [80] method is employed and then eq. (3-11) is written in the following form:

$$\left[J\right]\cdot\delta\vec{x}=-\vec{R} \tag{3-12}$$

[*J*] denotes the jacobian matrix and contains the derivatives of all equations with respect to each unknown $\left(J_{ij}=\partial R_i/\partial x_j\right)$, $\delta\vec{x}$ is the correction of the unknown vector $\vec{x}$, that move each function R_i closer to zero. The new potential solution is updated by the:

$$\vec{x}^{NEW}=\vec{x}^{OLD}+\delta\vec{x} \tag{3-13}$$

and the whole process is iterated until convergence. Moreover, the jacobian matrix is calculated analytically and consequently the rate of convergence is quadratic [80]. Next, the jacobian for each problem is given in matrix form:

$$
[J]=\begin{bmatrix}
\mathrm{BC} & & & & & & & \\
\vdots & \ddots & \ddots & \cdots & \cdots & \cdots & \cdots & \vdots \\
0 & \ddots & R^{1,i}_{a_j} & R^{1,i}_{b_j} & \cdots & 0 & R^{1,i}_{P_G} & R^{1,i}_{P_{EXT}} \\
0 & \cdots & R^{2,i}_{a_j} & R^{2,i}_{b_j} & \ddots & 0 & 0 & 0 \\
\vdots & \cdots & \cdots & \ddots & \ddots & \cdots & \vdots & \vdots \\
 & & & & \mathrm{BC} & & & \\
\cdots & \cdots & R^{3}_{a_j} & R^{3}_{b_j} & \cdots & \cdots & R^{3}_{P_G} & 0 \\
\cdots & \cdots & R^{4}_{a_j} & R^{4}_{b_j} & \cdots & \cdots & 0 & 0
\end{bmatrix}
\begin{matrix}
\mathrm{i}=1,2\ \&\ 4 \\
\vdots \\
2\mathrm{i}+1 \\
2\mathrm{i}+2 \\
\vdots \\
\mathrm{i}=2\mathrm{N}+2,2\mathrm{N}+4 \\
\mathrm{i}=2\mathrm{N}+5 \\
\mathrm{i}=2\mathrm{N}+6
\end{matrix}
$$

Figure 3-2: Jacobian matrix of the classic contact problem.

The jacobian matrix for the classic contact problem is captured in Figure 3-2 and its dimension is $(2N+6)\times(2N+6)$, where N is the number of nodes. Moreover, in the first $(2N+4)\times(2N+4)$ part of the above matrix the jacobian entries of normal (R_1) and tangential (R_2) force balance are written with respect to radius (a_j) & theta (b_j) coefficients, $R^{1,i}_{a_j}=\dfrac{\partial R_{1,i}}{\partial a_j}$ and so on. It is important to notice that this part of the matrix has non-zero entries in a zone with bandwidth 15. Moreover, the last two rows contain the jacobian entries of the isothermal equation (R_3) and the kinematic condition (R_4), with respect to radius and theta coefficients. The last two columns contain the entries to the jacobian pertaining to the variation of the normal force balance with respect to the internal (P_G) and external (P_{ext}) overpressure. Therefore, the full matrix is of an arrow form and can be separated into four smaller matrices in order to avoid the storage of zeros out of the bandwidth. The four matrices are the banded part $(2N+4)\times(2N+4)$, the bottom $2\times(2N+4)$, the head (2×2) and the right part $(2N+4)\times 2$. A typical form of an arrow matrix is depicted in Figure 3-3.

[*J*]=

Banded (2N+4)×(2N+4)	**Right** (2N+4)×2
Bottom 2×(2N+4)	**Head** 2×2

Figure 3-3: Schematic illustration of an arrow matrix

Finally, the boundary conditions (BC) of the problem are applied in the first three and the final three rows of the banded matrix. After storing the equations in the above form the jacobian is reversed by a standard routine, written for arrow matrices. Then the unknown vector is calculated via the Newton-Rapson as it is described above. Finally, for the classic contact problem the unknown vector is: $\vec{x}=\left(a_o,b_o,.....,a_j,b_j,.....,a_{N+1},b_{N+1},P_G,P_{ext}\right)^T$ with dimension 2*N*+6.

The jacobian matrix that is produced from the problem that includes the adhesive potentialis of similar form. The main difference is that the kinematic condition is not applied and therefore the dimension of the jacobian is now $\left(2N+5\right)\times\left(2N+5\right)$ or alternatively the last row and column of the previous matrix are eliminated. In this case the unknown vector is: $\vec{x}=\left(a_o,b_o,.....,a_j,b_j,.....,a_{N+1},b_{N+1},P_G\right)^T$ with dimension 2*N*+5.

However, in the case of the bifurcation diagrams the equation that fixes the center of mass (R_6) replaces the tangential force balance in the *N*+2'th row. The jacobian entries of the mass center $\left(\frac{\partial R_6}{\partial a_j}\text{ and }\frac{\partial R_6}{\partial b_j}\right)$ form a row-vector with non-zero entries in every column, Figure 3-4. Therefore the jacobian is a full matrix and for its inversion the dgesv Lapack routine is used. The unknown vector is: $\vec{x}=\left(a_o,b_o,.....,a_j,b_j,.....,a_{N+1},b_{N+1},P_G\right)^T$ with dimension 2*N*+5.

The stability of a certain branch is determined by the number of negative eigenvalues corresponding to the converged solutions obtained for varying external overpressure. The eigenvectors corresponding to the unstable eigenvalues are calculated so that an initial guess is generated, which, for a suitable disturbance ε on the basic spherical configuration, will provide a large enough geometric imperfection that will direct Newton's iterations towards the emerging subcritical branch [38].

$$[J]=\begin{bmatrix}
\mathrm{BC} & & & & & & & & & & & \\
\vdots & \dots & \ddots & \ddots & \ddots & \dots & \dots & \dots & \dots & \dots & \dots & \vdots \\
0 & \dots & \ddots & R^{1,i}_{a_j} & R^{1,i}_{b_j} & \ddots & \dots & 0 & 0 & 0 & 0 & R^{1,i}_{P_G} \\
0 & 0 & \ddots & R^{2,i}_{a_j} & R^{2,i}_{b_j} & \ddots & \dots & \dots & 0 & 0 & 0 & 0 \\
\vdots & \dots & \dots & \ddots & \ddots & \ddots & \dots & \dots & \dots & \dots & \dots & \vdots \\
R^{6}_{a_o} & R^{6}_{b_o} & \dots & R^{6}_{a_j} & R^{6}_{b_j} & \dots & R^{6}_{a_m} & R^{6}_{b_m} & \dots & R^{6}_{a_{N+1}} & R^{6}_{b_{N+1}} & 0 \\
\vdots & \dots & \dots & \dots & \dots & \ddots & \ddots & \ddots & \dots & \dots & \vdots & \vdots \\
0 & 0 & 0 & \dots & \dots & \ddots & R^{1,k}_{a_m} & R^{1,k}_{b_m} & \ddots & 0 & 0 & R^{1,k}_{P_G} \\
0 & 0 & 0 & 0 & \dots & \ddots & R^{2,k}_{a_m} & R^{2,k}_{b_m} & \ddots & \dots & 0 & 0 \\
\vdots & \dots & \dots & \dots & \dots & \dots & \ddots & \ddots & \ddots & \dots & \dots & \vdots \\
 & & & & & & & & & & \mathrm{BC} & \\
R^{3}_{a_o} & R^{3}_{b_o} & \dots & R^{3}_{a_j} & R^{3}_{b_j} & \dots & R^{3}_{a_m} & R^{3}_{b_m} & \dots & R^{3}_{a_{N+1}} & R^{3}_{b_{N+1}} & R^{3}_{P_G}
\end{bmatrix} \quad i=N+2$$

Figure 3-4: Jacobian matrix of the uniform pressure problem

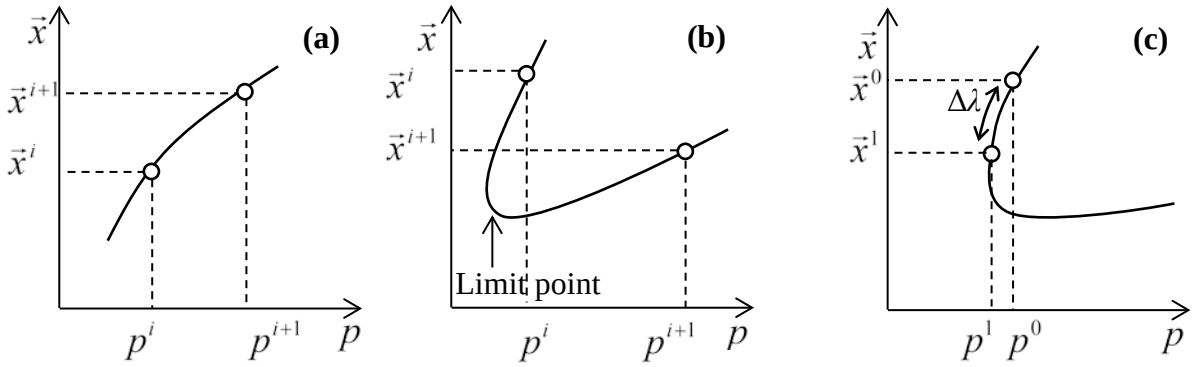

Figure 3-5: (a) Simple continuation and **(b)** Arc-length continuation around limit points

In every problem, solutions are sought for different values of the control parameter. Therefore, a previously converged solution can be used as initial guess for a new solution corresponding to a new value of the parameter. This idea can be easily illustrated in the Figure 3-5(a). Simple continuation is performed when the solution is smooth and without limit points. In this case the control parameter (p) changes independently by a step Δp:

$$p^{i+1} = p^i + \Delta p, \quad \text{where} \quad \Delta p > 0 \text{ or } < 0 \tag{3-14}$$

Then, the corresponding solution is the $\vec{x}^{i+1}$ and an initial guess for the Newton-Raphson procedure is provided by the $\vec{x}^{i+1,k=0} = \vec{x}^i$ solution vector.

However, if the solution has a limit point, Figure 3-5(b), a solution in the direction that Δp predicts does not exist especially near the limit point and at the limit point the jacobian matrix becomes singular and then the simulation breaks, therefore the simple continuation is not the most appropriate technique to proceed the solution. In order to overcome this problem arc-length continuation is considered as an alternative, which is a standard technique for detection of instabilities in shells and drops [81, 82]. In this instance, one more equation is added in the formulation and the control parameter is now part of the solution. The extra equation is the arc-length written in the *M*-space of the solution:

$$\Phi = \sum_{j=1}^{M} \left(x_j^{i+1} - x_j^i \right)^2 + \left(p^{i+1} - p^i \right)^2 - \Delta\lambda^2 \tag{3-15}$$

where $\Delta\lambda$ is a constant parameter to represent the arc-length of the solution branch in the *M*+1 dimension space formed by the unknown vector and the parameter *p*. In the same way with the simple continuation, x_j^i denotes the last converged solution for the parameter p^i. In order to estimate the value of the arc-length $\Delta\lambda$, as a first step simple continuation is performed before the limit point for a relative small value of Δp starting from the solution vector $\vec{x}^0$ and moving to $\vec{x}^1$, see Figure 3-5(c), thus it is possible to calculate the arc-length from the eq. (3-15). Consequently, adding eq. (3-15) in the formulation the jacobian of each problem has one more row and one more column. The augmented problem is now:

$$\begin{bmatrix} J & R_p^j \\ \Phi_{x_j} & \Phi_p \end{bmatrix} \begin{bmatrix} \delta x_j \\ \delta p \end{bmatrix} = - \begin{bmatrix} R_j \\ \Phi \end{bmatrix} \tag{3-16}$$

where [*J*] is the jacobian matrix as it is defined in the above problems; R_p^i is a column vector of dimension *M* and denotes the derivative of each residual with respect to the parameter *p*; Φ_{x_i} a *M* row vector, is the derivative of equation Φ with respect to all unknowns x_i; Φ_p is the derivative of Φ with respect to *p*, and δp is the update of *p*. It should be noted that even if the [*J*] becomes singular, the augmented matrix remains non-singular and therefore the simulation continues around limit points.

After solving the system described by eq. (3-16) with the Newton-Rapson method, the initial guess for the next solution is made by solving the following set of equations:

$$\begin{bmatrix} J & R_p^j \\ \Phi_{x_j} & \Phi_p \end{bmatrix} \begin{bmatrix} \partial x_j / \partial\lambda \\ \partial p / \partial\lambda \end{bmatrix} = - \begin{bmatrix} \partial R_j / \partial\lambda \\ \partial\Phi / \partial\lambda \end{bmatrix} \tag{3-17}$$

note that $\partial R_j / \partial\lambda = 0$ and $\partial\Phi / \partial\lambda = -2\Delta\lambda$. Then the initial guess for the next solution is:

$$x_j^{i+1} = x_j^i + \left.\frac{\partial x_j}{\partial \lambda}\right|^i \delta\lambda \tag{3-18}$$

and the corresponding parameter is also:

$$p^{i+1} = p^i + \left.\frac{\partial p}{\partial \lambda}\right|^i \delta\lambda \tag{3-19}$$

where for the first continuation with the arc-length (i=2), the initial guess of the derivatives $\left.\frac{\partial x_j}{\partial \lambda}\right|^1$ and $\left.\frac{\partial p}{\partial \lambda}\right|^1$ is the following:

$$\left.\frac{\partial x_j}{\partial \lambda}\right|^2 = \frac{x_j^{\,1} - x_j^{\,0}}{\Delta\lambda}, \forall j \in [1, M] \quad \text{and} \quad \left.\frac{\partial p}{\partial \lambda}\right|^2 = \frac{p^1 - p^0}{\Delta\lambda} \tag{3-20}$$

Finally, in the closure of the present paragraph, the steps in terms of an algorithm for each of the above problems are outlined.

Classic contact problem:

a) Initially, for a specific constitutive material law and geometry, the microbubble is assumed to have a spherical shape and the initial internal pressure is calculated by eq. (2-72).

b) Then, an unknown external point pressure (P_{ext}) is applied at the end of the first element, i.e. the angle θ_c pertaining to the Lagragian marker placed at the edge of the contact region in the undeformed configuration, is fixed to $\theta_c = \pi/(\text{Number of Elements})/2$.

c) Solving the system of eqs.(3-5) - (3-8) with Newton-Raphson method the unknown position (r,θ) of the lagrangian particles is calculated, along with the external (P_{ext}) and internal pressure (P_G).

d) After convergence is obtained, the new external point pressure is applied to the end of the next element, i.e. the angle θ_c is doubled, and the above calculation is repeated until a new solution is obtained.

e) For every converged solution the required post processing is performed, in order to calculate the corresponding eigenvalues, force, energy and deformed shape of the solution.

Similarly, for the *adhesive potential* model:

a) At first, a spherical shape is assumed, with or without pre-stress for a specific constitutive material law, geometry and again the initial internal pressure is estimated by eq. (2-72).

b) Then, the cantilever is positioned three or five bubble radius away from the shell.

c) The system of eqs. (3-5), (3-6) or (3-9) and (3-7) is solved by Newton-Raphson method and the unknown shell position (r,θ) and the internal pressure (P_G) are calculated.

d) Then, the process is repeated by decreasing the distance between the shell and the cantilever by conducting simple or arc-length continuation.

e) Finally, post processing is performed, in order to capture the corresponding force, energy and deformed shape of the solution.

Finally, for the *uniform pressure* model:

a) For a spherical shape, with or without pre-stress, specific constitutive material law, geometry, the initial internal pressure is estimated by eq. (2-72).

b) Then, a uniform static pressure is applied along the entire generator curve of the shell.

c) The unknown position (r,θ) and the internal pressure (P_G) are calculated by solving the system of eqs. (3-5) - (3-7) and (3-10). Then a new solution is requested by increasing the external overpressure with simple or arc-length continuation.

d) In every solution, the eigenvalues of the corresponding jacobian matrix are calculated in order to seek buckling solutions around bifurcation points.

e) At the end, post processing is performed, in order to calculate the corresponding bifurcation diagram, energy, the deformed shape and Legendre mode decomposition of the solution.

In the Figure 3-6 a typical flow chart of the above steps is illustrated, when simple continuation is considered. For the arc-length continuation, the loop of p-steps is replaced by a do while loop: $p \le p_f$, where p_f is the value of the parameter p, where the solution is satisfactory evolved and the simulation can be terminated.

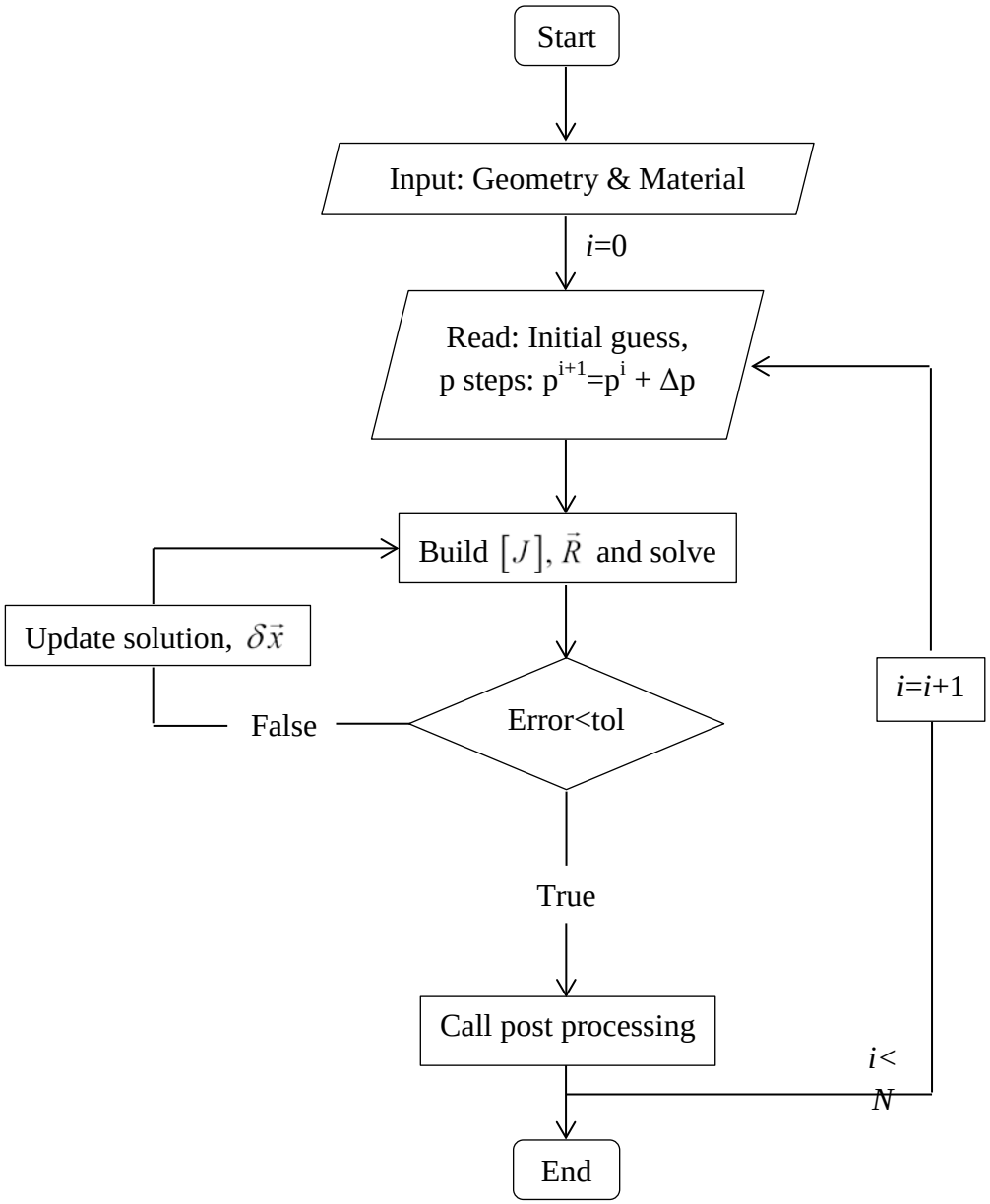

Figure 3-6: Flow chart of the numerical procedure.

3.3 Benchmark of formulation

3.3.1 Benchmark of the classic contact problem

In order to investigate the validity of the formulation developed in paragraph 2.3.1 simulations are performed with parameters that Updike & Kallins [47] used in their work, i.e. $E=10^9$ Pa, $R_o/h=100$, $k_b=8\cdot10^{-20}$ N·m, $\nu=0.3$, $\gamma_{BW}=0$ N/m, $\gamma=0$, Hook's law, no pre-stress and 400 elements, where they solved the same problem for the contact region and assuming a spherical unloaded shell in the reference state. In this direction, the classic contact problem is solved with contact angle to be known and employing the kinematic condition described by the eq. (2-31), a pressure distribution is calculated along the contact length, see Figure 3-7, which is a zero function along the contact line and takes a non zero value at the end of contact All of the solutions correspond to flat shapes in the contact line, as the kinematic condition requires, and as it was previously discussed such a kinematic condition is not capable of predicting the buckling solution. However, the resulting pressure profile indicates that the unknown function can be replaced by an unknown point force at the end of the contact regime and thus the kinematic condition can be eliminated only at the last node of contact, eq. (2-32). Hence, performing again simulations with the above parameters a force-deformation curve is calculated and it is compared with the one from [47], see Figure 3-8 (a). During simulation the angle (θ_c) is the control parameter, i.e. a series of solutions is obtained by increasing the contact angle by a step $\Delta\theta_c$.Figure 3-8(a) illustrates the dimensionless force required to obtain the deformation of the shell d/h, where d denotes the z-component of deformation of the last lagrange particle at the end of contact line and h the shell thickness. Updike and Kallins [47] describe the solution of the contact problem as the intersection of two solution branches. The first is the main branch, where the force-deformation is linear and the shell in contact region is flat, and the secondary branch with non-linear response and buckling of the shell. This response is recovered in the present thesis by employing the formulation developed in previous session. More specifically, the linear and the non-linear response are depicted in Figure 3-8(a) with white squares and triangles, respectively, while the solution of Updike and Kallins follows the continuous black line. The results of the present analysis are in good agreement with [47] for both branches, justifying that the present formulation is an appropriate

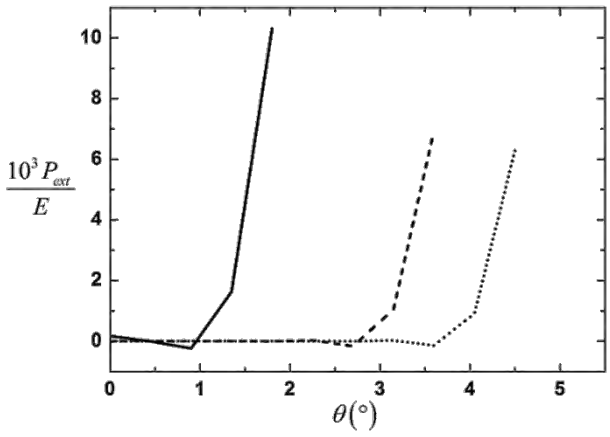

Figure 3-7: Pressure distribution when θ_c=1.5°(solid line), θ_c=3.5° (dash line) and θ_c=4.5° (dot line)

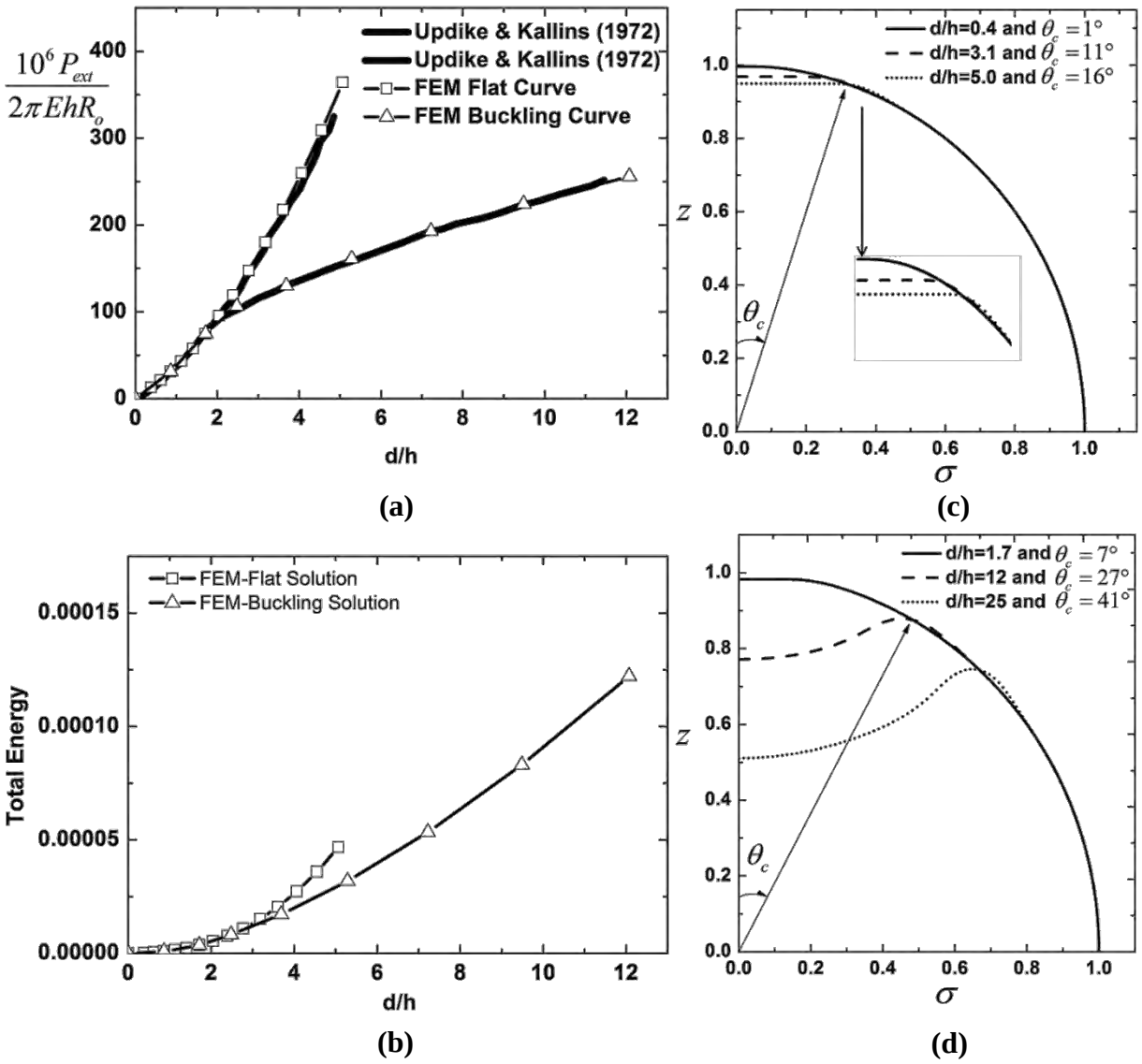

Figure 3-8: (a) Force-deformation curve, comparison between the present analysis (white squares and triangles) and Updike & Kallins (continuous black), (**b**) Total energy of deformed shell for flat and buckling solutions, **(c)** & **(d)** Microbubble in deformed configuration, flat and buckling solutions, for different values of the cantilever position. The axes are dimensionlized as it is described in paragraph 2.3.1

model to describe the contact between a spherical and elastic shell against a flat and rigid surface. Typical mesh refinement calculations verify the above response. The corresponding shapes of the shell in different deformed states are illustrated in Figure 3-8(c) and (d). The shell in the flat solution is characterized by a zero curvature area around the contact region, while the buckling solution shapes have a progressively larger dimple in the north pole region with negative curvature and at the end of contact a small region is formed with high curvature, where most of bending energy is concentrated.

The stability of the solution is investigated by performing further analysis and calculating the eigenvalues of the jacobian matrix. The linear part of the force-deformation curve has one negative eigenvalue, but after the buckling point the same curve has one more negative eigenvalue. However, the buckling curve has the same number of negative

eigenvalues with the pre-buckling curve, which means that the buckling point is also a bifurcation point and corresponds to a supercritical bifurcation. Moreover, the linear curve after buckling is an unstable solution, due to higher total energy (i.e. the sum of energies from stretching, bending and gas compression) in comparison with the non-linear solution for the same value of deformation, see also Figure 3-8(b).

Thus, during simulation the microbubble spontaneously follows the stable buckling solution, while in order to obtain the flat solution after the buckling point special manipulation of the contact elements is required. More specifically, for the buckling solution to be followed a step $\Delta\theta_c \approx 6.75°$ is employed while the flat solution is obtained by selecting a smaller value for $\Delta\theta_c \approx 2.25°$. Moreover, the change in the number of negative eigenvalues can also provide the buckling point in terms of the corresponding values for the critical deformation and force. In this fashion the calculated buckling point via FEM is $\left(\frac{d}{h}, \frac{10^6 P_{ext}}{2\pi E h R_o}\right) = (2.4, 120)$, while in [47] it is $(2.5, 130)$, and the corresponding contact angle from FEM is θ_c=9^o and from [47] θ_c=8^o.

3.3.2 Benchmark of the uniform pressure problem

The formulation of a microbubble subject to a uniform overpressure field (paragraph 2.4) is investigated for its validity by performing simulations with the same parameters that Knoche & Kierfeld [59] use. In [59] a spherical axisymmetric vessel is subject to a negative internal pressure assuming given volume or pressure. The former case corresponds to a shell filled with incompressible fluid, while the latter is a shell that contains a gaseous phase, even though the compressibility is neglected. Therefore, the most suitable case is the second and more specifically a case which corresponds to relatively stiff shell with $k_b/\chi R_o^2 = 10^{-3}$, where the internal pressure is not a dominant resistance, which means that the effect of compressibility could be omitted or if it is incorporated in the modelling it will not significantly affect the results. Following the above scenario, simulations are performed with: E=2.64·10^8 Pa, R_o=2·10^{-6}m, h=1.9·10^{-7} m, k_b=2·10^{-13} N·m, ν=0.5, γ_{BW}=0 N/m, γ=1.07, Hook's law and no pre-stress. Figure 3-9(a) illustrates the evolution of different solution branches in the plane defined by the dimensionless external overpressure, $\Delta P/P_{cr}$, and the relative volume change between the deformed and the initial state of the shell, V/V_o; a uniform mesh of 200 and 400 elements was used for the discretization of the shell surface and agreement was verified between the numerical solution (FEM) of the present study and the [59].

Initially, as the shell is compressed by a uniform overpressure ΔP, the relation between loading and volume is a linear curve (black line), the shape of the shell is spherical with a decreasing radius and the jacobian matrix has one negative eigenvalue. However, with further increase of the absolute value of the external pressure the number of negative eigenvalues rises to two. The corresponding eigenvector is used with a small imperfection in order to calculate the initial guess for the secondary branch solution. The numerically obtained diagram confirms that the asymmetric branch (red line) emerges first as the dominant instability for $\Delta P = 3.2\cdot10^6$ Pa, that is, roughly, 0.92 of the theoretical value (ΔP_{cr}), eq. (2-70). This is in direct agreement with the critical value taken from a similar diagram in [59]. Furthermore, the secondary bifurcation leading to a symmetric solution family (dark green line) was also recovered. Therefore, agreement between the two approaches is justified, despite the different treatment of the internal pressure variation adopted herein, due to the negligible resistance to compression of the microbubble indicated by the very small value of the dimensionless pressure, $P_A R_o/\chi = 4\cdot10^{-3}$.

Furthermore, the asymmetric branch is linearly unstable with two negative eigenvalues whereas the symmetric branch that follows is characterized by three negative eigenvalues. Both branches evolve subcritically and have more total energy than the spherical branch, Figure 3-9(b). Therefore, they require imposition of a geometric disturbance of a certain amplitude, in the form of the eigenvector provided by stability analysis as was explained above, on the base spherical shape in order to perform parametric continuation along them. The evolution of both branches was followed for a wide range of external overpressures, also in agreement with the above study, and the minimum external overpressure for nonlinear transition to an asymmetric shape to be possible, starting from the spherical configuration, was recovered. In particular, the spherical branch for $\Delta P/P_{cr} = 0.92$ and $V/V_o = 0.91$ has one more

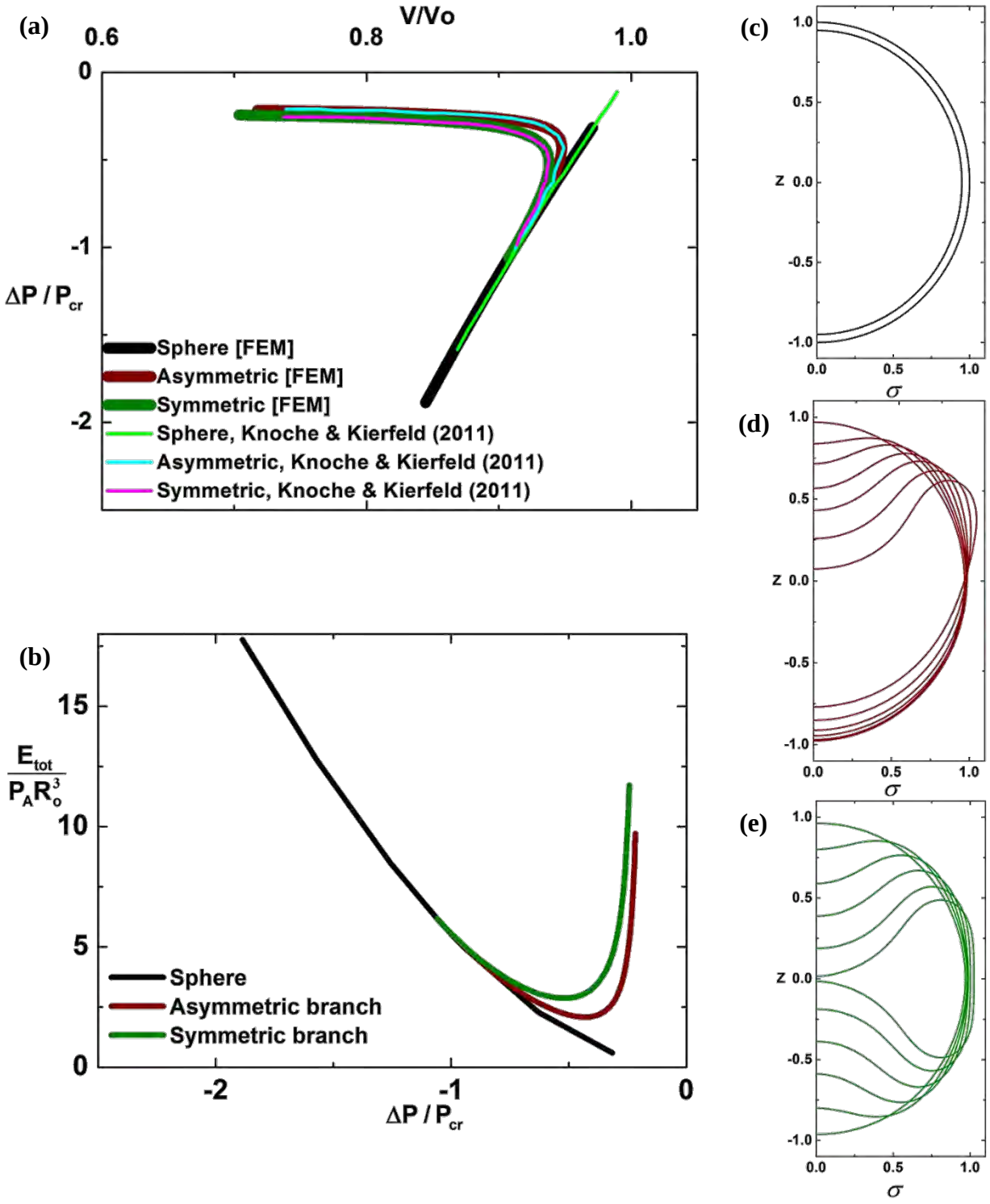

Figure 3-9: (a) Bifurcation diagram-Comparison between the present analysis and literature, **(b)** Bifurcation diagram in terms of total energy, **(c)** Evolution of spherical solution shapes, **(d)** Evolution of asymmetric solution shapes and **(e)** Evolution of symmetric solution shapes. The almost spherical shapes in (d) and (e) correspond in the bifurcation point and then a sequel of solutions is presented dominated by the asymmetric and symmetric eigenmode, respectively, for reduced shell volume.

negative eigenvalue and the corresponding eigenvector is dominated by P_3 Legendre eigenmode, which with a small disturbance ($\varepsilon \sim 10^{-2}$) is imposed on the last spherical shape and

through simple continuation the new solution branch is evolved. When the solution is on the asymmetric branch further disturbance on the eigenvector is not required. On a same way the symmetric branch is evolved from the spherical branch, but starting from $\Delta P/P_{cr} = 1.05$ and $V/V_o = 0.9$, when the spherical solution has on more negative eigenvalue and disturbing the corresponding eigenvector dominated by the P2 Legendre eignemode. The deformed shapes associated with the above solutions are presented in Figure 3-9(c), (d) and (e) for reduced shell volume. The spherical shell is dominated by the P_0 Legendre eigenmode, associated with volume changes, while the asymmetric and symmetric shapes are dominated by the P_3 and P_2 modes, respectively.

Chapter 4. Numerical results: Simulation of a microbubble under the AFM

In the fourth chapter of the present thesis the numerical models developed previously are employed in numerical simulations that investigate the static response of coated microbubble under the AFM. Subsection 4.1 contains numerical results for the classic contact problem, while the results for the model that accounts for the intermolecular forces are presented in session 4.2. In both problems, a reference case is initially studied and then an extensive parametric analysis is carried out in order to investigate the role of the different parameters on the equilibrium. In the case of the classic contact problem for microbubbles covered with polymeric material the two solution families corresponding to flat and buckled shapes are recovered, confirming that the buckling stage is energetically favorable. When microbubbles covered with phospholipid monolayers are investigated with the intermolecular forces model, buckling is not seen to take place and the shell around the contact area remains flattened, when the dimensionless bending modulus is relatively high, $k_b / (\chi R_0^2) > 1$. *The parametric study for both problems shows that the elasticity moduli, namely stretching and bending, tend to increase the slope in f-d curve. Similar behavior is observed when the surface tension of shell-water interface is accounted on the equilibrium. A pre-stressed shell with compressive residual stresses has lower slope than a shell with zero residual stresses and vice versa when the residual stresses are tensile. Furthermore, the gas compressibility acts as an extra stiffness on the shell, when the relative importance of the gas pressure to area dilatation modulus is higher than one;* $P_{St} R_0 / \chi \sim 1$. *This fits well with the lipid monolayers, while for the polymeric shells the effect of gas compressibility is negligible in the regime of small deformations. Especially for the intermolecular forces problem the adhesive energy per unit area can also affect the f-d curve. Through the parametric analysis it is shown, that when the interaction potential* W_o *increases not only the slope of the f-d curve increases, but also the amplitude of the maximum adhesive force;* $W_0 / \chi \sim 1$ *.Thus two cases are investigated pertaining to weak and strong adhesion. In addition, the characteristic length* δ_A *does not affect the slope of the f-d curve, but as* δ_A *decreases the response around the maximum adhesive force becomes sharper. In the same context, three regions along the shell are defined; the contact, the transition and outer regimes depending on the disjoining pressure profile. The lengths of the above regimes are also part of the parametric analysis, where it is shown that the length of transition regime is decreased as the length* δ_A *decrease and the energy* W_o *increase. Surface tension tends to decrease the contact length, while the transition remains unaffected. Finally, on the intermolecular forces problem, an additional case is investigated, where the microbubble is assumed to be free of elasticity, and then it is the surface tension and the gas compression that balance the disjoining pressure.*

4.1 The classic contact model

4.1.1 Study of single microbubble

Chapter 2 contains two formulations for the static response of a coated microbubble under the AFM and, as it was explained there, the shells covered with polymeric material behave like conventional shells. Thus for their description a classic contact formulation is adopted, while a model with intermolecular forces is developed for shell covered with lipid monolayers; see below for results. In addition, in paragraph 3.3.2 it was shown that the distribution of the applied contact force may be treated as a line load that vanishes everywhere on the shell except for the circular arc that joins the contact with the free area. Hence, due to axisymmetry, it is possible to replace the load distribution with an unknown point load at the end of the contact region. Thus, in the first subparagraph of the present chapter the methodology developed for the classic contact problem, paragraph 2.3.1, is employed and simulations with simple continuation are performed for the investigation of the static response of a microbubble in terms of the f-d curve, post-buckling behavior, the energy distribution of each solution branch and the tensions - moments along the shell. In order to facilitate comparison between different types of shells we use the area dilatation, χ, and bending resistance, k_b, throughout this study, with the understanding that for polymeric shells the elasticity modulus, E, and shell thickness h are the more relevant physical shell parameters. For the purposes of the present study, the parameters of Table 4-1 are considered, which are similar with the ones that Glynos et al. [29] employ for the estimation of shell properties for biSphere microbubbles via AFM. The relevant dimensionless numbers are:

$$\hat{k}_b = \frac{k_b}{\chi R_o^2} = \frac{1}{12\left(1-\nu^2\right)}\left(\frac{h}{R_0}\right)^2 = 3\times 10^{-5};\ \hat{P}_A = \frac{P_A R_o}{\chi} = 3\times 10^{-3};\ \hat{\gamma}_{BW} = \frac{\gamma_{BW}}{\chi} = 0;\ \chi = Eh,$$

Initially, the cantilever is imposed on top of the shell and for a known contact angle; $\theta_c = 1.8°$, a solution is seeking and by performing simple continuation with $\Delta\theta_c = 1.8°$ a series of solution is obtained, where the resultant force can be calculated for some deformation of the shell. As it is already described the deformation in f-d curves is defined as the displacement of the current cantilever position from its original. Thus, a f-d curve is obtained for the parameters assumed here, Figure 4-1(a), and the two branches of solution are recovered. The linear branch is characterized, as in benchmark calculations, by one negative eigenvalue and at $d = 105$ nm, $F = 435$ nN and $\theta_c = 11°$ a bifurcation point appears that leads to the second solution branch, which also has one negative eigenvalue, that is initially curved downwards,

Shell thickness:	$h = 47$ nm	Young's modulus:	$E = 1.7$ GPa	
Initial radius:	$R_o = 2.75$ μm	Poisson ratio:	$\nu = 0.42$	
Constitutive law:	Hook	Pre-stress:	$u = 0$ μm	
Surface tension:	$\gamma_{BW} = 0$ N/m	Polytropic index:	$\gamma = 1.07$	400 elements

Table 4-1: Simulation parameters for the force-deformation curve of a microbubble covered with polymer.

while at relatively high deformation tends to curve upwards. The linear branch continues further from the bifurcation point, but now has two negative eigenvalues, indicating that this part of the solution is unstable. This is also in agreement with the total energy of the two solutions, Figure 4-1(b), where it can be seen that the total energy content of the secondary

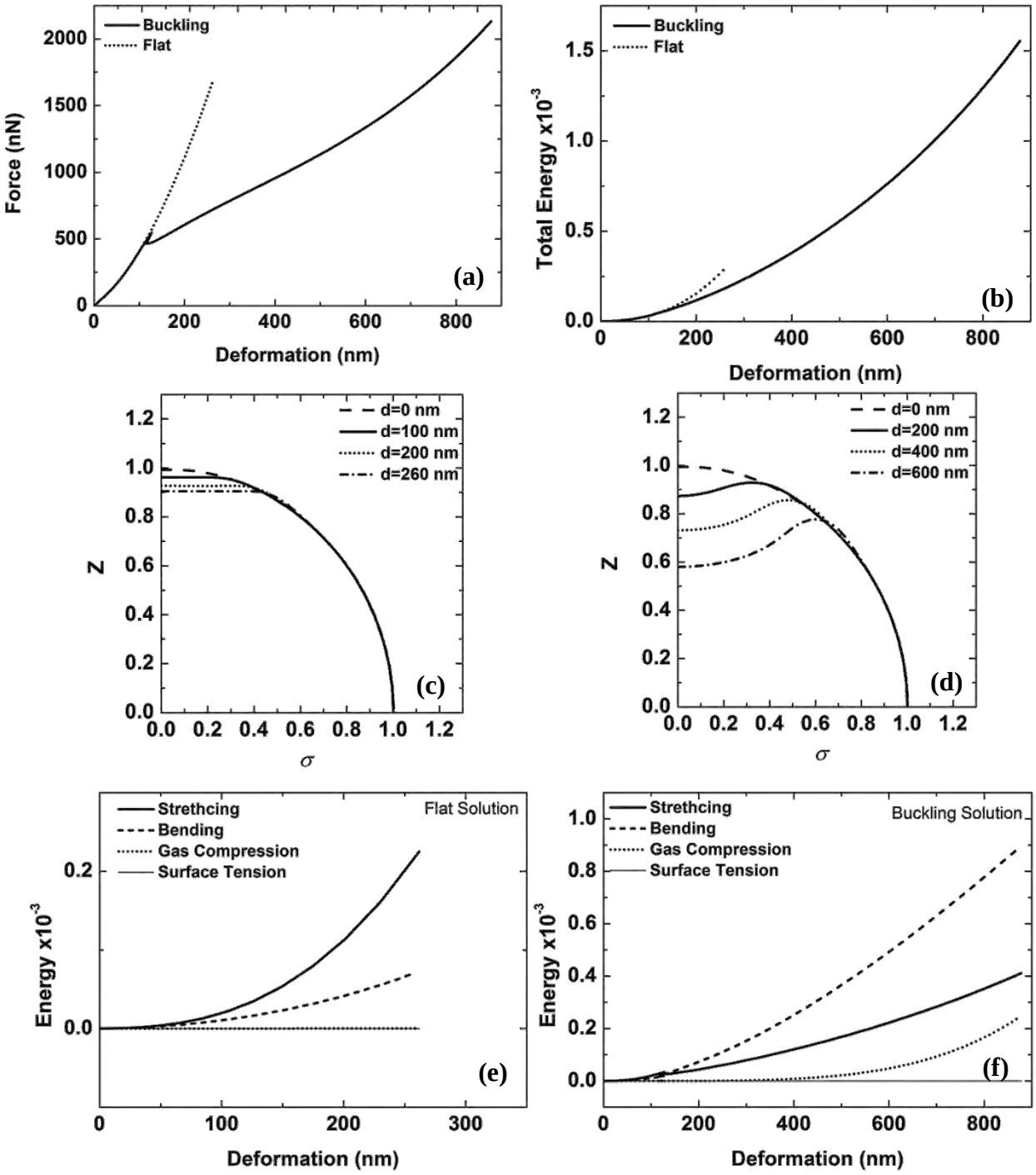

Figure 4-1: (a) Force-deformation curves, **(b)** Total energy-deformation curves of flat and buckling solutions, **(c)** and **(d)** Shape of deformed microbubble for selected values of deformation corresponding to flat and buckling solutions (The cylindrical coordinated system (σ, z) is dimensionalized with the initial radius R_o.) and **(e)** and **(f)** Components of total energy for the pre- and post-buckling stages. The axes and elasticity moduli are dimensionalized as it is described in paragraph 2.3.1.

solution is smaller in comparison with that of the linear branch as this evolves beyond the bifurcation point, hence the former is energetically favorable. The corresponding shape of the microbubbles in the linear part of the f-d curve is flat whereas buckling has taken place in the non-linear part, Figure 4-1(c) and (d). In addition, the total energy components are demonstrated in Figure 4-1(e) and (f) for the flat and buckling solutions, where the energy due to bending becomes higher than stretching after the buckling point, which is reasonable because after the bifurcation point the area around contact is an almost mirror image of the initial unstretched spherical cap. As a result the energy due to stretching increases with a lower slope. In addition, the energy due to gas compression is initially negligible, however beyond a certain level of deformation, d≥500 nm, it starts to increase as it acts as an additional stiffens on the equilibrium thus explaining the upwards curved f-d curve. Moreover, with further post processing calculations the distribution of total energy components is plotted against the distance from the axis of symmetry, σ, for two configurations that correspond to pre- and post-buckling stages, Figure 4-2(a) and (b), respectively. In the pre-buckling solution most of the elastic energy is concentrated near the contact area for $\sigma \leq 0.2$, with the energy due to bending being slightly higher than stretching. The distribution of bending energy is significantly higher than stretching in the buckling solution and has a pick at the end of contact, where a dimple is formed with small curvature. The shell outside the contact area remains almost spherical, thus both elastic energies vanish.

Another interesting result that characterizes the solution and gives a more complete picture of the shell deformation is the distribution of in plane and shear tensions along with bending moments. In Figure 4-3(a) and (b) the tensions are depicted as function of the distance from the axis of symmetry, σ, for the pre- and post-buckling solutions. In both cases, the in plane tensions τ_{ss} and $\tau_{\varphi\varphi}$ have negative values, which means that the shell is under compression especially in the contact area, where most of the deformation is located. Moreover, the shear tension q is almost zero along the shell, except at the points $\sigma = 0.2$ and $\sigma = 0.5$, where the external point force is applied. This is in direct agreement with the classic theory. In addition, the bending moments m_{ss} and $m_{\varphi\varphi}$ are equal and almost constant along the contact area in the pre buckling stage, Figure 4-3(c). In both pre- and post-buckling the discontinuity of the shear tension at the end of contact is reflected as gradient discontinuity in the bending moments, as it is expected by the theory, see eq. (2-20). Finally, around the end of the contact area, positive moments are concentrated, because a dimple is formed with high curvature.

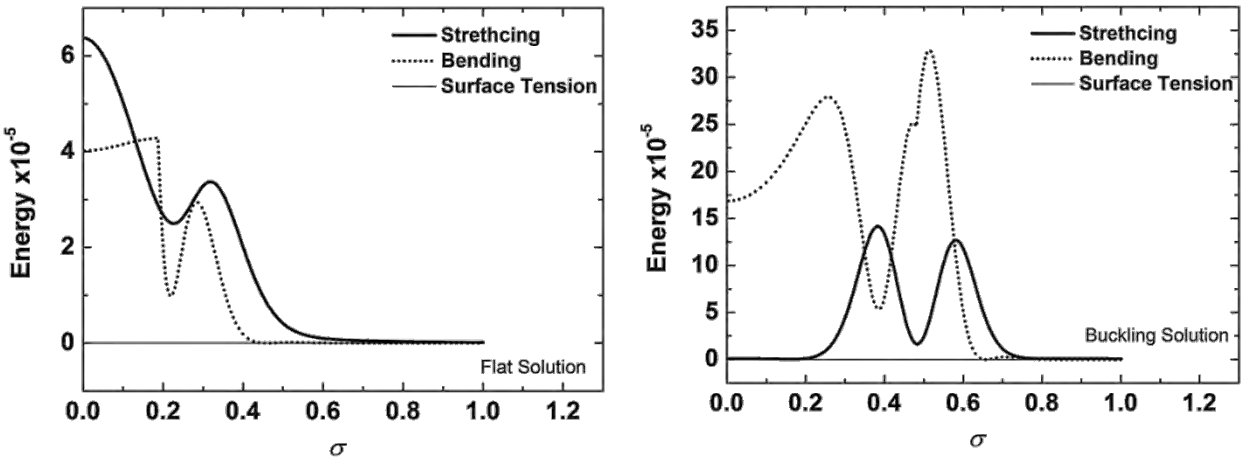

Figure 4-2: Distribution of energies due to stretching and bending along the distance from the axis of symmetry, σ. **(a)** Pre-buckling stage with deformation d=100 nm and **(b)** Post-buckling stage with deformation d=400 nm. The elasticity moduli and the surface tension are dimensionalized as it is described in paragraph 2.3.1 and the horizontal axis with the initial radius R_o

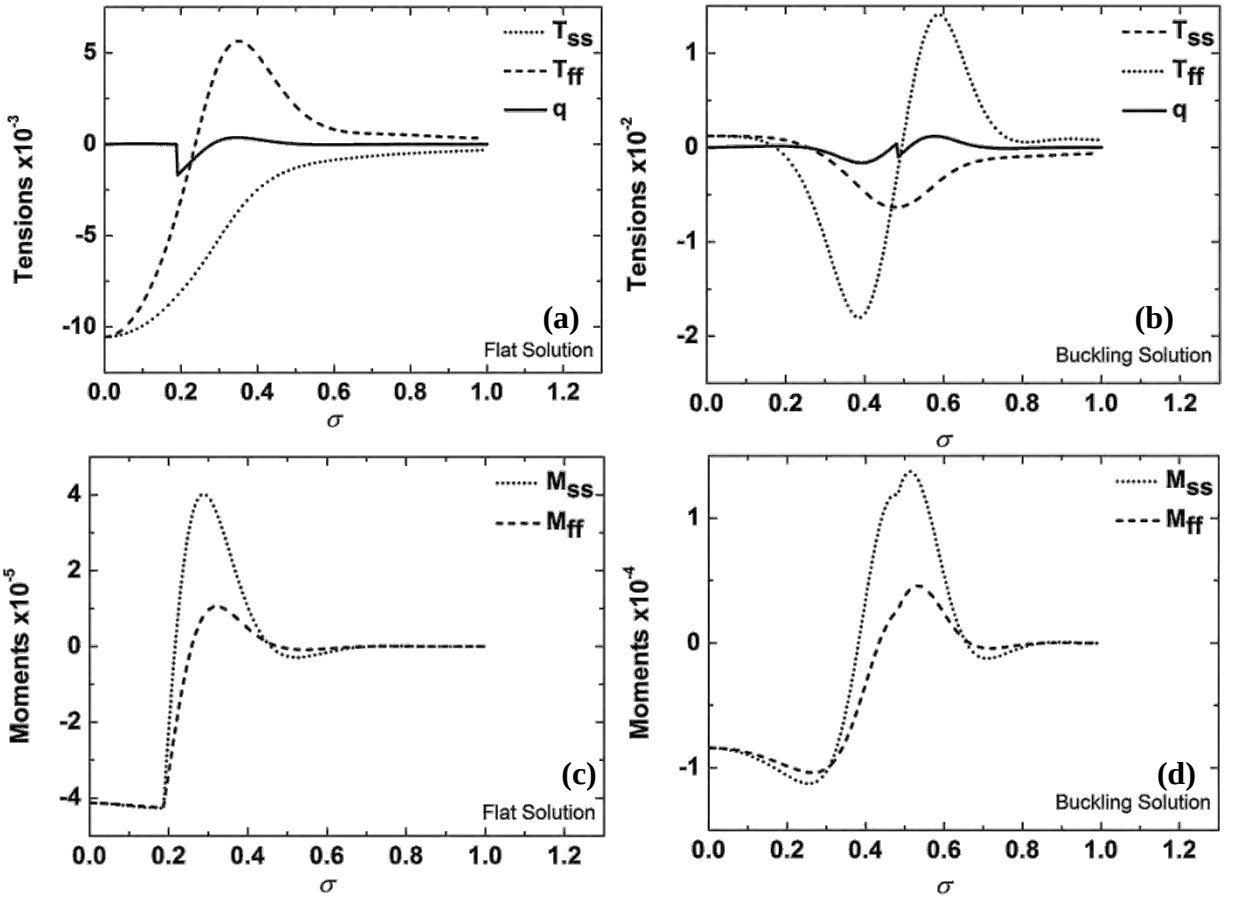

Figure 4-3: (a) and **(b)** Distribution of in plane and shear tensions in flat (d=100 nm) and buckling solution (d=400 nm), respectively. **(c)** and **(d)** Distribution of bending moments in flat (d=100 nm) and buckling solution (d=400 nm), respectively. The elasticity moduli are dimensionalized as it is described in paragraph 2.3.1 and the horizontal axis with the initial radius R_o.

4.1.2 Parametric Study

In the following session a parametric study is carried out in order to investigate the effect of different parameters that are involved in the shell equilibrium, namely stretching and bending rigidity, constitutive law, pre-stress, surface tension and gas compressibility. The rigidities that are associated with elasticity are the most extensively investigated parameters through the years for such a classic problem, however, for the sake of completeness in the first part of the present paragraph the effect of elasticity moduli is studied. In addition, the case investigated in subsection 4.1.1 will be used as the reference case.

Effect of elasticity moduli (stretching-χ & bending k_b)

Initially, a microbubble is investigated, which in comparison with the case studied in subsection 4.1.1, see Table 4-1, has twice the stretching and bending modulus, E=3.4 GPa or χ=159.8 N/m and $k_b = 3.6\times10^{-14}\,\text{Nm}$. Thus the dimensionless bending modulus remains the same: $\hat{k}_b = \dfrac{k_b}{\chi R_o^2} = 3\times10^{-5}$ and the dimensionless ambient pressure $\hat{P}_A = \dfrac{P_A R_o}{\chi} = 1.5\times10^{-3}$ decreases, i.e. the gas compressibility is less important than rigidity. In Figure 4-4(a) the f-d curve of the above case is compared against the one from subsection 4.1.1 , to be referred to as reference case henceforth for brevity. The f-d curve of the new microbubble has higher slope, as it was expected since it is a shell with higher rigidity. This will be verified in Section 6 where the asymptotic analysis by Reissner, pertaining to the linear regime of the f-d curve, will be presented for spherical shells compressed by a rigid plate. There it will be seen that the slope of the linear part of the f-d curve is proportional to the elasticity modulus E. Furthermore, the bifurcation point of the case shown in Figure 4-4(a) occurs at the same deformation and contact angle, i.e. $d = 105\,\text{nm}$ and $\theta_c = 11°$, but the required force is higher. However, the two elastic shells have the same dimensionless bending modulus, $\hat{k}_b$, or alternatively the same ratio thickness to radius, thus in dimensionless form the two curves coincide, Figure 4-4(b), for the most part. On the other hand, the two buckling curves respond differently in higher deformations because the third rigidity of the equilibrium, i.e. the gas compressibility, starts to become important. In the reference case the dimensionless pressure is $\hat{P}_A = 3\times10^{-3}$. Consequently, the compression of the encapsulated gas is relatively more significant, in comparison with the stretching rigidity, for the reference case than in the case examined here with $\hat{P}_A = 1.5\times10^{-3}$.

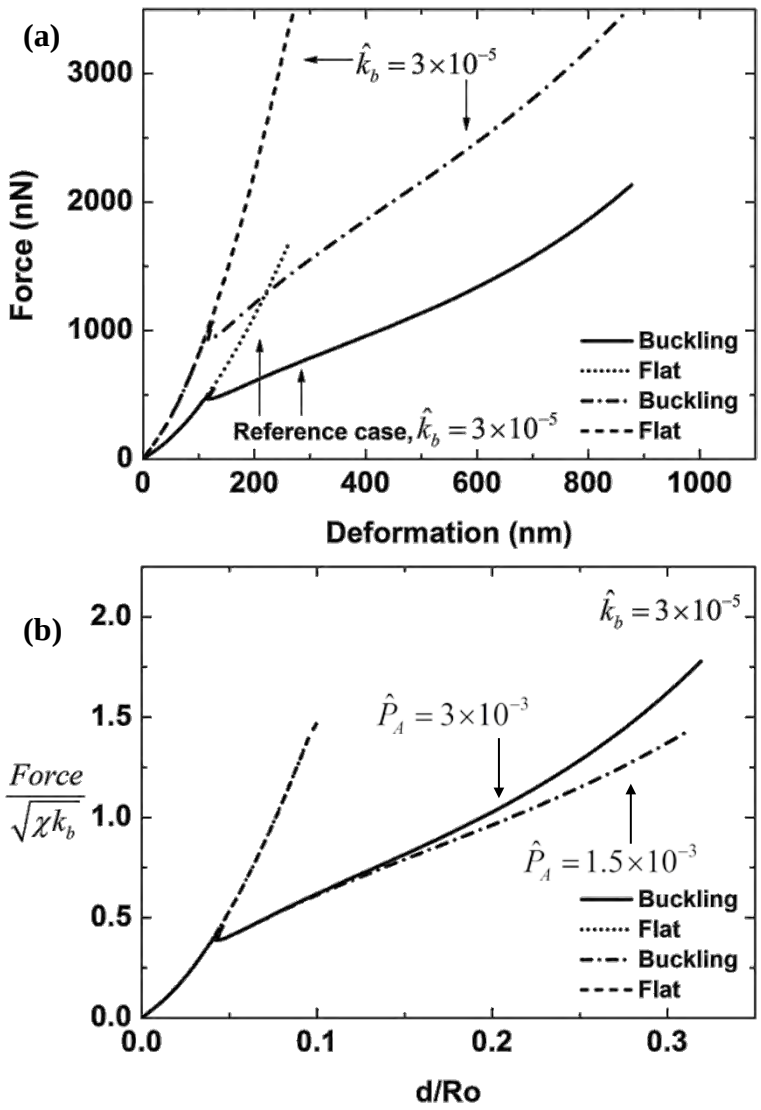

Figure 4-4: Comparison of f-d curves with different elasticity moduli and the same dimensionless bending modulus, $\hat{k}_b = 3\times10^{-5}$ **(a)** Axes with dimensions and **(b)** Dimensionless axes.

In the next of a microbubble with higher dimensionless bending is investigated with the same simulation parameters as in Table 4-1, but with *h*=94 nm. Consequently, the dimensionless numbers are: $\hat{k}_b = 10^{-4}$ and $\hat{P}_A = 1.5\times10^{-3}$. As can be gleaned from Figure 4-5(a) depicting the f-d curve, for both flat and buckling solutions the required force is higher than the reference case. In addition, the buckling branch of the

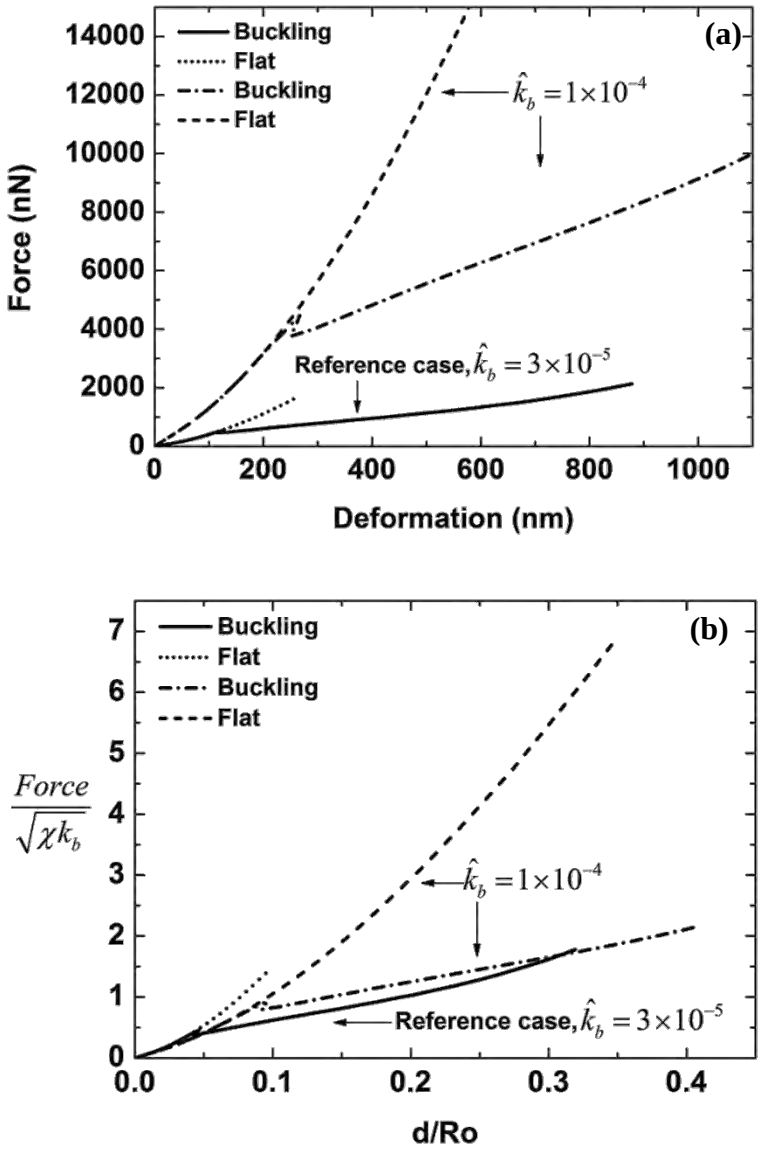

Figure 4-5: Comparison of f-d curves with different elasticity moduli and dimensionless bending modulus, $\hat{k}_b$ **(a)** Axes with dimensions and **(b)** Dimensionless axes.

$\hat{k}_b = 10^{-4}$ case emerges from the flat solution at around $d = 220$ nm and $\theta_c = 16°$. Thus, the dimensionless bending modulus controls the position of the bifurcation point and the onset of buckling. In the present numerical study the bifurcation point is a clear and sharp change in f-d curve and the detection of the bifurcation point in experimental-AFM data could be of great importance in order to estimate the elastic properties (χ, k_b) of the elastic coating, based on the deformation and force exerted at the onset of bifurcation.

Effect of gas compressibility

In the next part of the present parametric analysis the effect of the gas compression is specifically studied. In the reference case the gas is assumed to undergo isothermal variations of its pressure, i.e. as the volume is reduced the gas pressure increases. This is a constraint added to problem formulation in order to account for the compressible nature of the gas. For conventional shells that are either very rigid or operate in the regime of small deformations, such a constraint is not necessary. Thus the formulation follows in general what Updike & Kalnins [46-48] suggest for the present analysis without the isothermal equations. To this end, gas compressibility may be omitted by setting the polytropic index, γ=0, which leaves the internal pressure constant and the shell volume independent from pressure. Figure 4-6(a) compares the resultant f-d curve for the buckling solution when γ=0 with the compressible gas case. As it is seen, after a level of deformation on the order of d=300 nm the required force is higher, because the internal pressure starts to increase significantly and its impact on the composite bubble rigidity reflects in the more rapid rise of the f-d curve, Figure 4-6(b). However, the onset of the bifurcation point is not affected by the consideration of gas compressibility since it occurs at a lower deformation. Even if the gas compression is accounted for in the formulation, the response of the f-d curve remains unaffected by the gas compression, bold line in Figure 4-6(a), especially at low deformations. This is attributed to the low dimensionless gas pressure, $\hat{P}_A = 1.5\times10^{-3}$, which is a measure of the relative stiffness of gas compression to elasticity stiffness. Next, a case with relative high dimensionless pressure is examined, which has $\hat{P}_A = 1$ and $\hat{k}_b = 3\times10^{-5}$. It should be stressed that these parameters do not correspond to the properties of a shell covered with polymeric biomaterial, but they are employed only for the purposes of comparison. When $\hat{P}_A = 1$, the required force for buckling increases significantly, but the bifurcation point remains the same, Figure 4-7(a). In addition, as the shell is deformed, the internal (or gas) pressure increases in both cases, but its relative importance in comparison with the area dilatation modulus is greater when $\hat{P}_A = 1$.

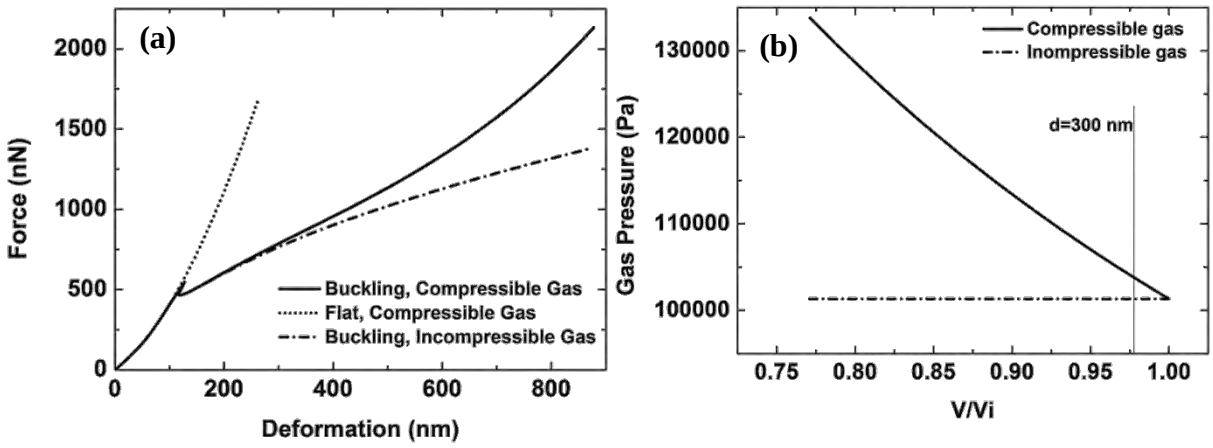

Figure 4-6: (a) Comparison of f-d curves for compressible and incompressible gas and **(b)** Gas pressure as function of volume.

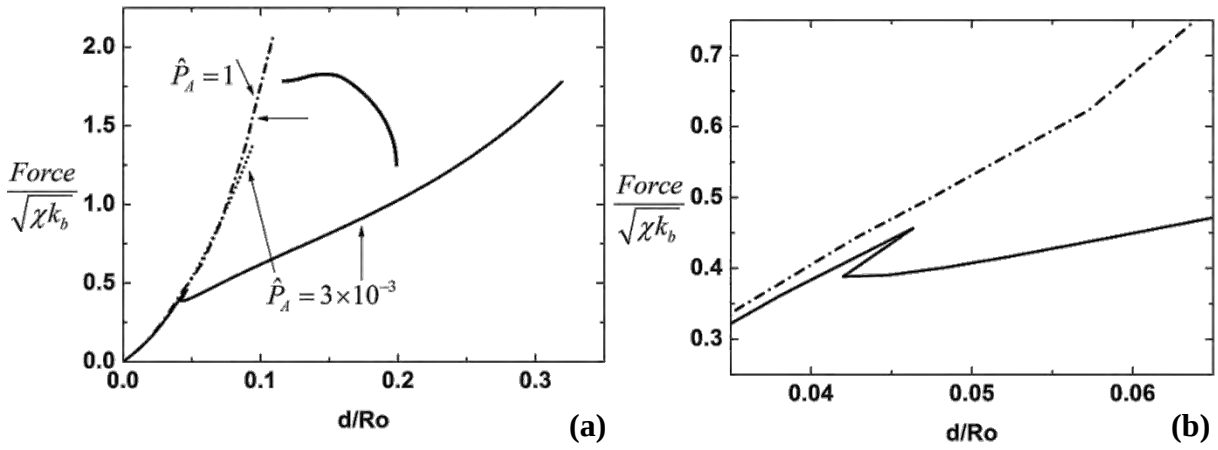

Figure 4-7: Comparison of **(a)** f-d curves of two microbubbles with the same dimensionless bending modulus $\hat{k}_b = 3\times10^{-5}$ and different dimensionless pressure; the solid curves correspond to negligible internal (or gas) pressure $\left(\hat{P}_A = 3\times10^{-3}\right)$ and the solid-dot line to a larger internal pressure $\left(\hat{P}_A = 1\right)$, **(b)** Zoom in the bifurcation regime.

Effect of pre-stress

In the present part of the parametric analysis the effect of pre-stress is investigated, assuming initially that the microbubble has lost some of the encapsulated gas. Thus, the shell volume decreases, compressive initial stresses are developed on the shell and consequently the starting point is not a stress-free state. In order to study the above scenario, a microbubble is considered with the same parameters as in the reference case, but an amount of pre-stress is assumed in the form of an initial radial displacement of $u=-10^{-3}$ μm. In Figure 4-8(a) the f-d curves for both pre- and post-buckling solutions of the pre-stressed shell are compared against the reference case, where zero residual stresses are assumed, u=0. As it can be gleaned the required force decreases significantly especially in buckling branch and the bifurcation point is shifted to lower values of force and deformation (d=98 nm, F=360 nN and θ_c=10°). In addition, eq. (2-72) predicts the initial gas pressure when the shell is pre-stressed. Thus, in the present case the internal pressure is less than the ambient since the surface tension is zero, Figure 4-9(a). Hence, the combined rigidity of the shell is smaller and this reflects in the lower slope of the equilibrium f-d curve. The results are exactly the opposite when the shell is assumed pre-stressed, but with tensile stresses. The bifurcation point is shifted to higher values of force and deformation (d=120 nm, F=560 nN and θ_c=12°). Based on the same concept as before the initial internal pressure is higher than the ambient and the combined rigidity of the shell is larger than the reference state, hence the larger slope

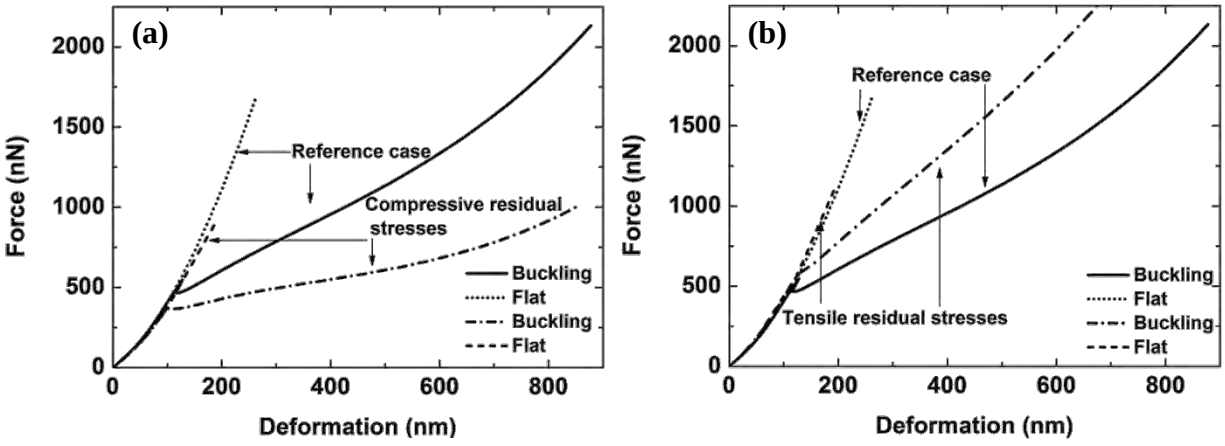

Figure 4-8: Comparison of f-d curves with pre-stress: **(a)** Compressive residual stresses, $u= -10^{-3}$ μm and **(b)** Tensile residual stresses, $u= +10^{-3}$ μm.

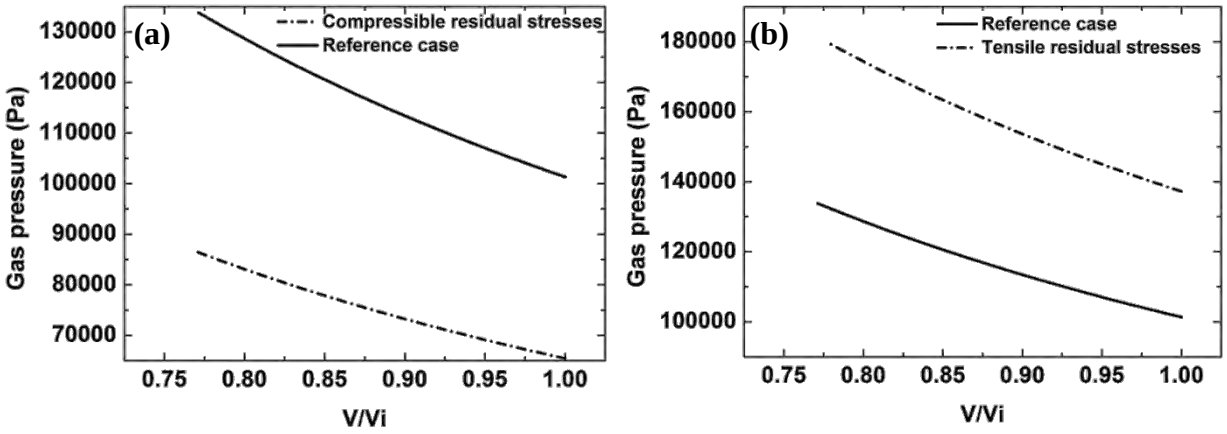

Figure 4-9: Comparison of gas pressure-volume curves with pre-stress: **(a)** Compressive residual stresses, u= -10^{-3} μm and **(b)** Tensile residual stresses, u= $+10^{-3}$ μm for buckling branches.

Effect of surface tension

Next the effect of the surface tension on the f-d curve is investigated for the classic contact problem when $\gamma_{BW}=4\times10^{-3}$ and 4×10^{-2} N/m. Figure 4-10(a) and (b) compare the response in f-d curves for both cases. Surface tension is seen to increase the resistance to shell compression by increasing the force required to achieve a certain deformation, especially at large deformation levels. The bifurcation point remains the same as in the reference case when $\gamma_{BW}=4\times10^{-3}$ N/m, but is moved to slightly higher values of force and deformation when $\gamma_{BW}=4\times10^{-2}$ N/m (d=120 nm, F=545 nm and θ_c=12°). As in the study of the pre-stress, the initial gas pressure is estimated by eq. (2-72). Thus when the surface tension is considered the initial gas pressure is higher than the ambient by a term of magnitude $2\gamma_{BW}$. Hence, as the volume decreases the gas pressure increases as well, but for each of the above cases it acquires a different starting value, see also Figure 4-11. In particular, when $\gamma_{BW}=4\times10^{-2}$ N/m gas compressibility is a significant resistance, and this explains the increased external load required in order to achieve a certain deformation.

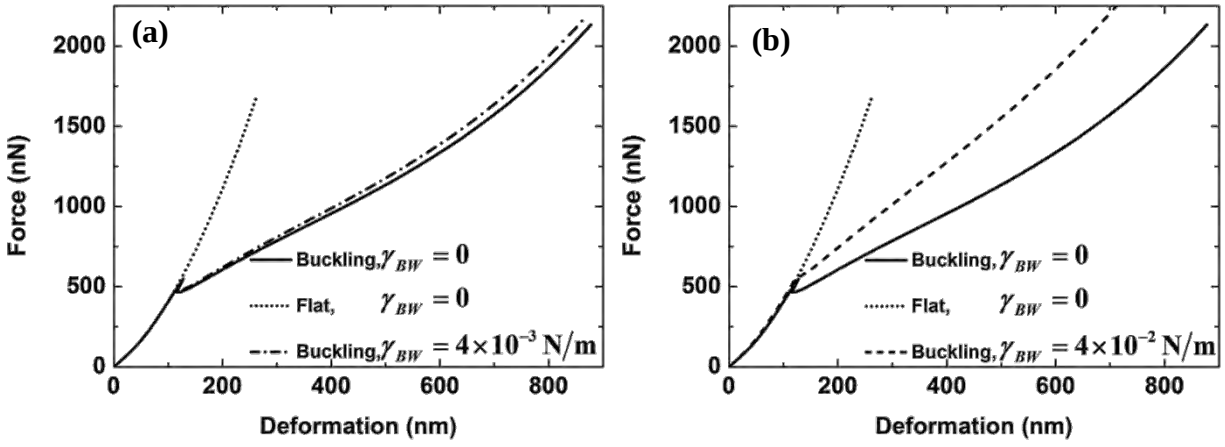

Figure 4-10: Comparison of f-d curves for different values of surface tension **(a)** $\gamma_{BW}=4\times10^{-3}$ N/m and **(b)** $\gamma_{BW}=4\times10^{-2}$ N/m against the reference case with γ_{BW}=0 N/m.

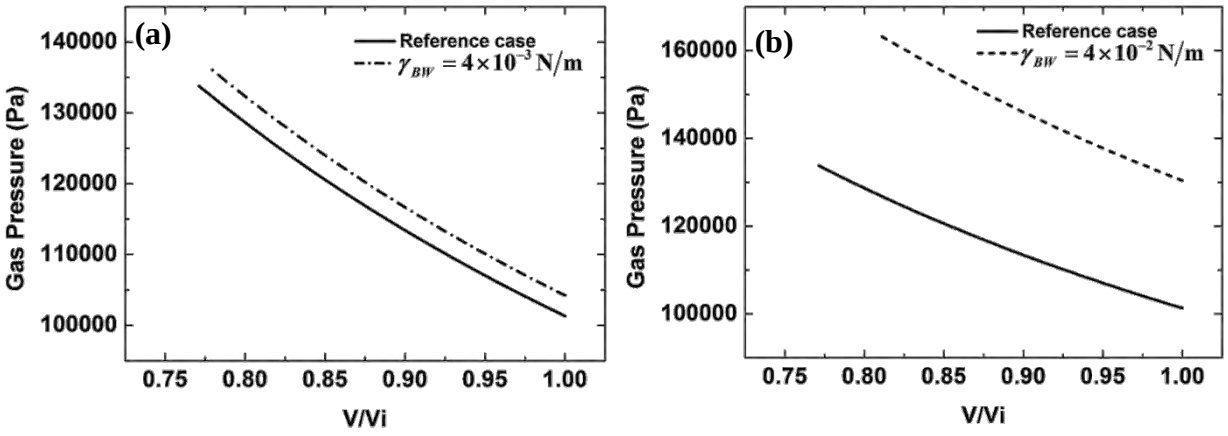

Figure 4-11: Comparison of gas pressure-volume curves for different values of surface tension (a) $\gamma_{BW}=4\times10^{-3}$ N/m and (b) $\gamma_{BW}=4\times10^{-2}$ N/m against the reference case with γ_{BW}=0 N/m for the buckling branch.

4.2 The intermolecular forces model

4.2.1 Study of a single microbubble

In the second part of the fourth chapter numerical results are demonstrated obtained with the model that accounts for the intermolecular forces between the cantilever and the elastic shell (see paragraph 2.3.2), which is mainly proposed for microbubbles covered with lipid monolayer. In contrast with lipid bilayers that have relatively high area dilatation modulus,χ~0.1 N/m, in comparison with their bending stiffness, k_b~10^{-19} Nm $k_b/\chi R_o^2 \sim 10^{-6}$, and thus they are modeled as vessels with constant area [63], a microbubble covered with a phospholipid monolayer has bending stiffness that more comparable with the area dilatation modulus. Thus, a microbubble with the parameters of Table 4-2 is considered. The above parameter values are taken from previous relevant studies [16, 29, 83], giving rise to the following dimensionless numbers:

$$\hat{k}_b = \frac{k_b}{\chi R_o^2} = 2.7\times10^{-3};\ \hat{P}_A = \frac{P_A R_o}{\chi} = 3;\ \hat{\gamma}_{BW} = \frac{\gamma_{BW}}{\chi} = 0;\ \hat{W}_o = \frac{W_o}{\chi} = 2\times10^{-3};\ \hat{\chi} = 1$$

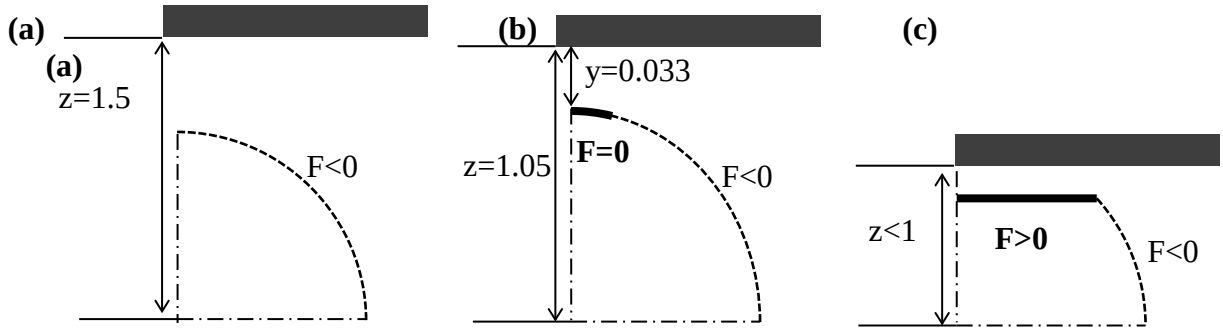

Figure 4-12: Schematic representation of the relative position of microbubble and cantilever: **(a)** The bodies are at relatively long distance-attraction (F<0), **(b)** Position of the maximum attraction, a small area around the pole is at distance $y=\delta_A=0.033$ (F=0), the rest of the shell is in attraction (F<0 or $y>>\delta_A$) and **(c)** Cantilever and microbubble are close, where the contact area is in repulsion (F>0 or $y<\delta_A$) and the rest of the shell remains in attraction ($y>>\delta_A$).

Bending modulus:	$k_b = 3\cdot10^{-16}$ Nm	Area dilatation modulus:	$\chi = 0.05$ N/m	
Initial radius:	$R_o = 1.5$ μm	Poisson ratio:	$\nu = 0.5$	
Constitutive law:	Mooney-Rivlin, (b=1)	Pre-stress:	$u = 0$ μm	
Surface tension:	$\gamma_{BW} = 0$ N/m	Polytropic index:	$\gamma = 1.07$	
Potential depth	$W_o = 1\times10^{-4}$ N/m	Potential length	$\delta_A = 50$ nm	400 elements

Table 4-2: Simulation parameters for the force-deformation curve of a microbubble covered with lipid monolayer.

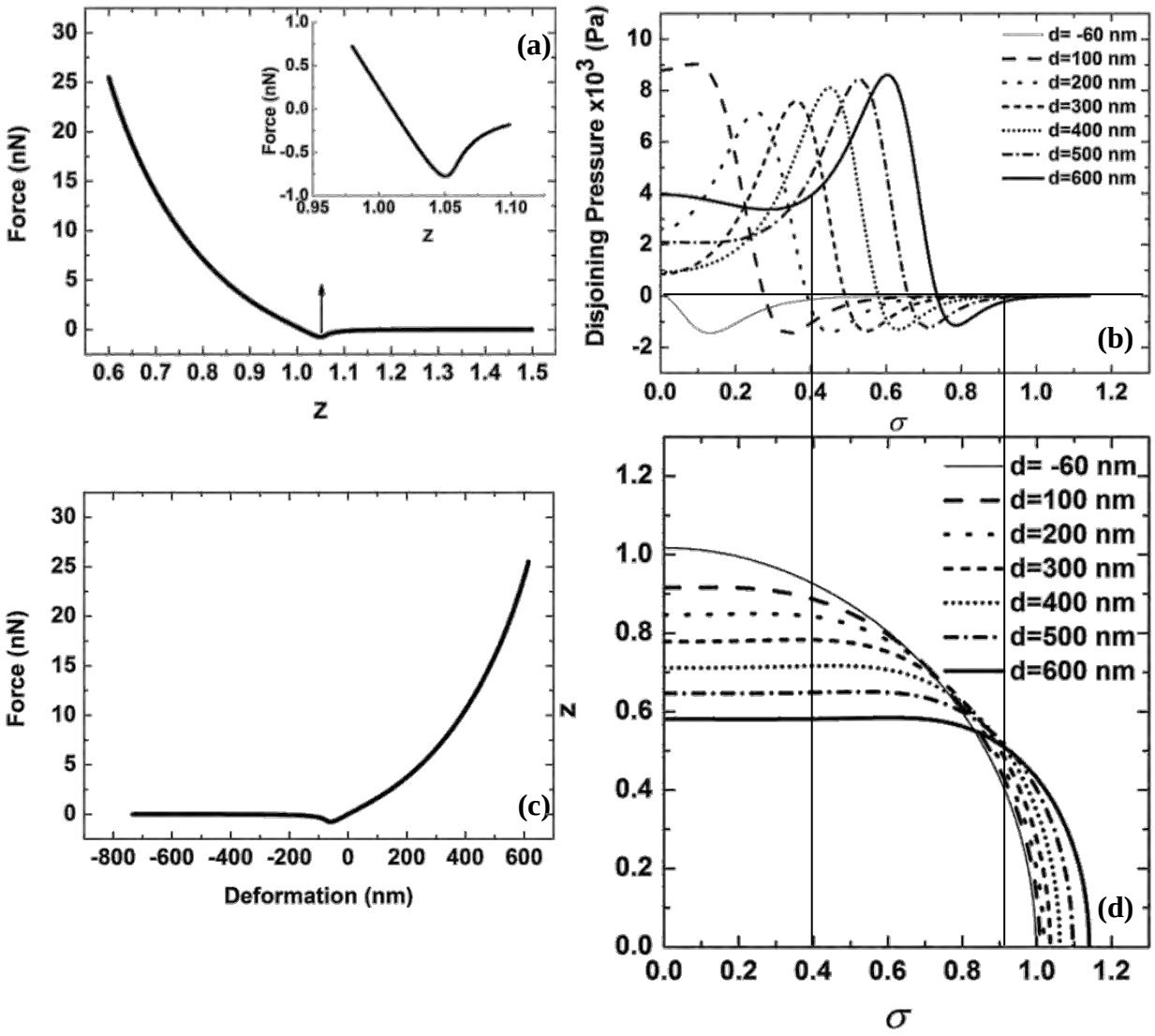

Figure 4-13: (a) Force-distance, **(b)** Distribution of the disjoining pressure along the distance from the axis of symmetry, **(c)** Force-deformation curve and **(d)** Microbubble in deformed configuration for selected values of deformation, (the axes z and σ are dimensionalized with the initial radius R_o).

Initially, the cantilever is placed in the reference spherical state at a vertical distance of z=1.5 from the shell equator, measured in terms of the initial radius R_0. Performing simple continuation by decreasing the vertical distance z the cantilever is seen to approach the shell. The resultant force is very small and negative for $z >> 1+\delta_A / R_0 \approx 1.05$, Figure 4-12(a), while the shape remains almost spherical because the whole shell and the cantilever are at a relatively long distance. However, as the cantilever approaches the shell (z ↓) the force remains negative, Figure 4-13(a), but its amplitude increases significantly in order to counteract the attractive force between the shell and cantilever. At around $z = 1.05$, the force reaches a maximum negative value. This is the point where the dimensionless water film thickness δ/R_0 is about 0.033, in dimensional form δ=50 nm$\approx\delta_A$, which is the characteristic length δ_A where the disjoining pressure and the force are zero, first curve in Figure 4-12(b), but the rest of the shell (the part not near pole) is still at relatively long distance from the cantilever. In this part of the shell the disjoining pressure is negative and therefore the

resultant force over the entire shell is still negative, i.e. attractive. The magnitude of this force represents the required pull-off force in order to overcome the resistance against increasing the water film thickness. For $z<1.033$, the water film decreases further, and the disjoining pressure around the pole becomes positive signifying the repulsive force between the shell and cantilever at very small distances, Figure 4-12(c). Therefore the total force turns to smaller negative values and eventually acquires positive values corresponding to overall repulsion; see also the distribution of the disjoining pressure along the distance from the axis of symmetry in Figure 4-13(b). As can be gleaned from the latter figure, there is a distance z, where the repulsive (positive) force is equal with the attractive (negative) force where the resulting total force on the shell is zero. The last value of z is used as reference for the estimation of the shell deformation, $d_i=\left[z\left(F=0\right)-z_i\right]R_o$, and the construction of the f-d curve that can be compared against experimental results. The progressively larger positive force required for larger deformations to be exhibited corresponds to the larger and larger repulsive force that needs to be overcome as the liquid film is thinning.

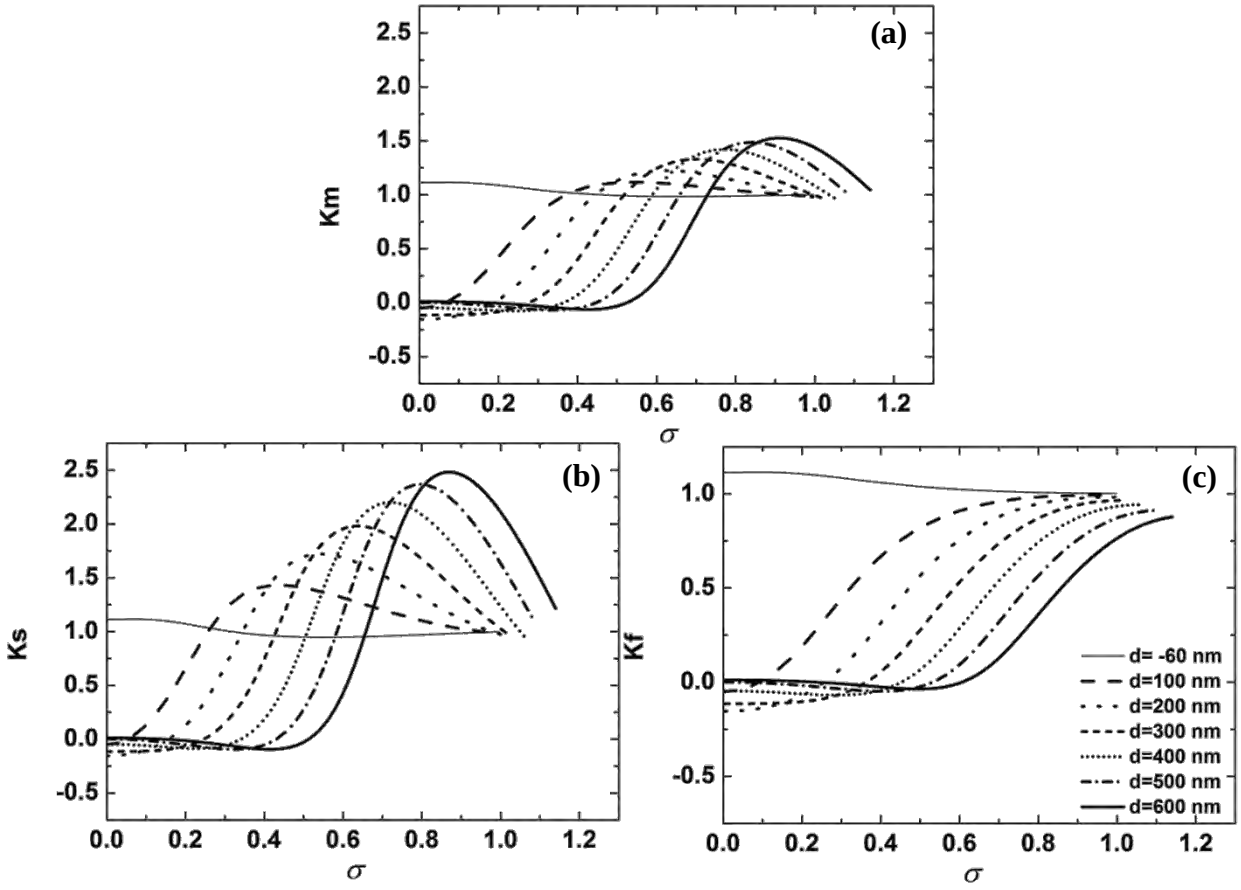

Figure 4-14: Distribution of the principal curvatures along the distance from the axis of symmetry (σ) **(a)** Mean curvature (k_m), **(b)** curvature on s direction (k_s) and **(c)** curvature on φ direction (k_φ).

In the present case $z(F=0)=1.01$. The f-d curve, Figure 4-13(c), is almost linear in the initial part and tends to curve upwards in higher values of deformation, indicating that buckling is not taking place, as it is expected from the analysis in paragraph 4.1. This becomes evident by plotting the shape of the microbubble in deformed configuration for selected values of deformation, Figure 4-13(d), where it can be seen that the shape around the contact area remains flattened. Moreover, the first deformed shape has negative deformation, because it corresponds to the point of the maximum adhesive force, i.e. it is the point where the shell undergoes the maximum attraction by the cantilever. The disjoining pressure around the contact area is not a constant function which means that the water film does not have a constant height (y). This is a result of the elastic nature of the shell coating that allows for small indentations of the shell near the pole. It is also of interest that the point where the disjoining pressure becomes zero is moved to the right as the deformation increases. Upon careful cross-examination of the deformed shape, the point where the disjoining pressure starts to increase can define the end of the contact regime, see vertical lines in Figure 4-13 (b) and (d). In between the previous point and the outer region it exhibits a maximum negative pick and after taking negative values it crosses to positive values in the outer region. This area can define a transition regime between the contact and outer regions of the shell, with the latter region characterized by zero disjoining pressure. Following this concept, the length of the transition regime is $\ell \sim 0.45$. Furthermore, plotting the principal and the mean curvatures along the deformed shell, Figure 4-14, it can be seen that there are small deviations from zero in the part of the shell that is in contact with the cantilever, and consequently the contact area is almost flattened. Moreover, at the end of the contact area, the curvature starts to increase and reaches values around one, which means that the shell exhibit a deformation in the area away from the contact as well. The interaction of the shell with the cantilever can also be seen in terms of the relative energies, namely stretching, bending, gas compression, adhesive potential and surface tension. The last energy is zero for the case investigated in this paragraph. In Figure 4-15(a) the total energy (the sum of all of the above energies) is plotted as a function of the deformation, while the relative importance of each of the energy components is depicted in Figure 4-15(b). For large negative deformations, the cantilever is away from the shell, thus all of the energy components vanish. As the cantilever approaches, the first energy that starts to increase is the energy due to adhesive potential, reflecting reduction of the film thickness that exists between the shell and the cantilever. When the attraction becomes strong enough, the energy due to stretching and bending start to increase as well. The energy due to bending is higher than stretching for deformation less than 200 nm and vice versa for higher deformations. On the other hand the energy due to gas compression is almost zero for deformation less than 300 nm, however for higher deformations the gas compression energy starts to increase introducing an additional stiffness on the equilibrium. Finally the energy of the adhesive potential is always negative, because the film even though is compressed, its height never becomes so small so that the potential becomes positive, see also Figure 2-5. The last result indicates that the presence of the adhesive potential reduces the total energy, thus leading to more stable configurations. Moreover, the above energies can be illustrated for selected values of deformation along the distance from the axis of symmetry, Figure 4-16. In the contact area the energy due to

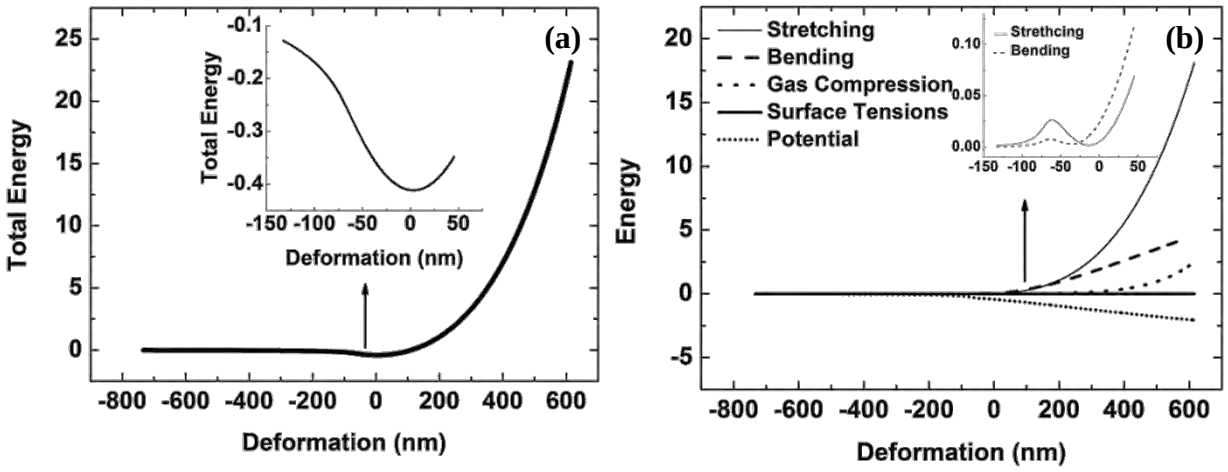

Figure 4-15: (a) Total energy as function of the deformation, **(b)** Components of the total energy as function of deformation. The dimensionalization of axes is based on paragraph 2.3.2.

bending is higher in comparison with the energy due to stretching for all of the selected deformations, but in the rest of the shell the opposite happens. The energy due to adhesive potential has a slight variation along the contact area, which is due to non-constant height of the film, as it is was explained above, and has a local maximum indicating a compression of the film ($y < \delta_A$) and a local minimum at the end of the contact area ($y = \delta_A$), where the disjoining pressure becomes zero. In the rest of the shell the potential tends to zero as the relative distance between the shell and the cantilever is quite large.

Finally, Figure 4-17 illustrates the distribution of the stresses and bending moments along the shell as a function of the distance from the axis of symmetry. When the shell is at the maximum attraction, tensions and moments are positive, because as it can be seen from Figure 4-17(d), the shell is elongated. When the force becomes positive (repulsive), the shape is compressed and the in plane stresses become progressively negative, with τ_{ss} being compressive in the entire shell and $\tau_{\varphi\varphi}$ only in the contact area, Figure 4-17(a) and (b). In the transition and the outer regimes $\tau_{\varphi\varphi}$ is positive, thus in φ direction of these two regimes the shell is elongated and the point where $\tau_{\varphi\varphi}$ changes sign coincides with the end of the contact region. In contrary with the previous model, paragraph 4.1, where the applied load is concentrated at a point and therefore the shear tension is a non-zero function only at the contact point, in this case the shear tension q, Figure 4-17(c), has a smooth distribution along the shell, reflecting the distribution of the applied disjoining pressure. As it can be seen, most of the shear tension is concentrated at the end of the contact region and its largest negative value is shifted on the right as the deformation increases and so does the contact length. The shear tension in the outer regime is very small and positive, indicating that, as it was described earlier, the shell has some deformation in this regime. In a similar way, the bending moments m_{ss} and $m_{\varphi\varphi}$ are constant and equal in the biggest part of the contact regime and before the end of this regime they start to increase and become zero at the end of contact, Figure 4-17 (d) and (e). In the transition regime, the bending moments are positive and increase, while in the outer regime they are also positive, but decrease.

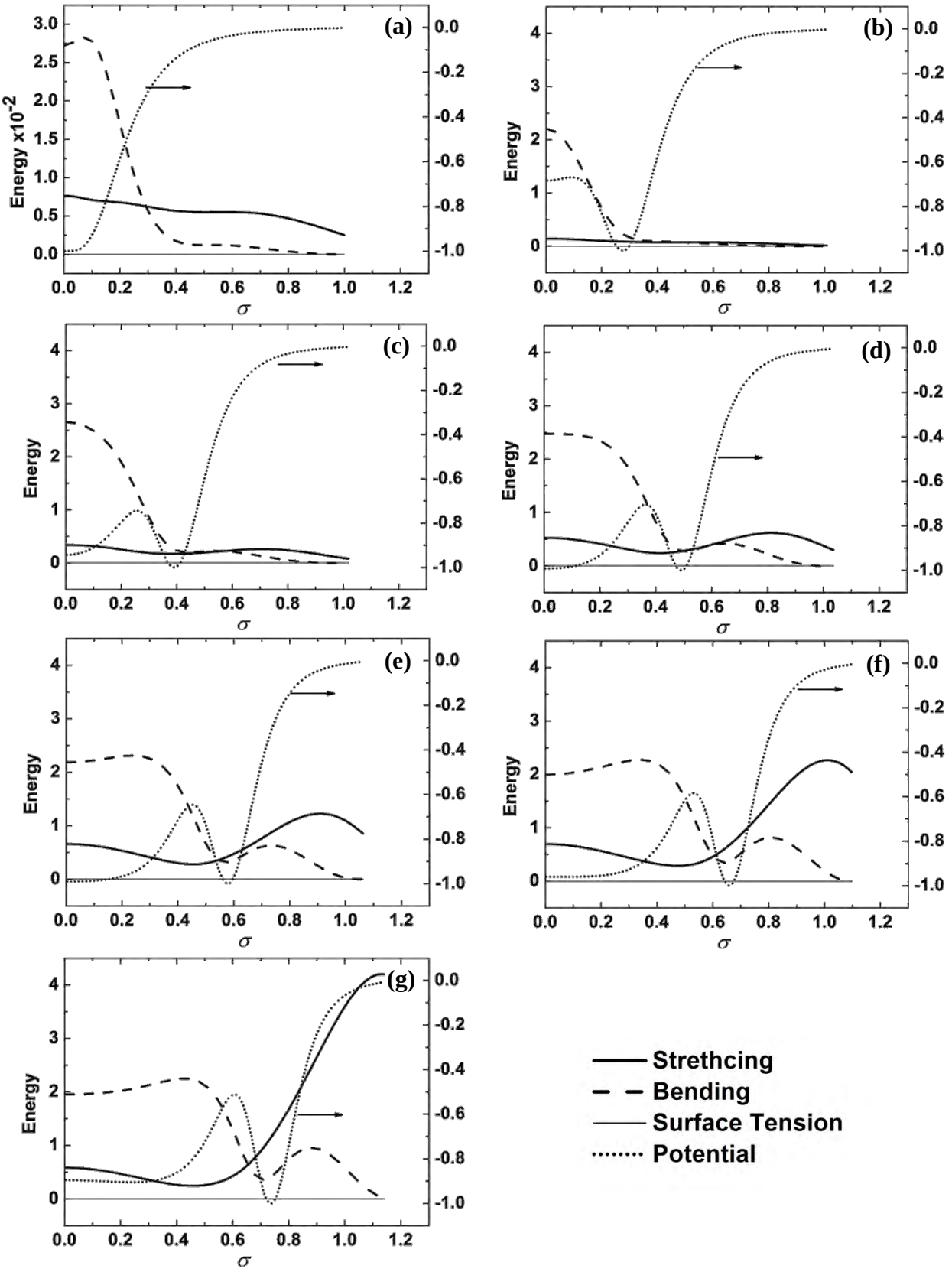

Figure 4-16: Distribution of the energy per unit area due to stretching, banding, surface tension and adhesive potential (right vertical axis) along the distance from the axis of symmetry (σ) for selected values of deformation **(a)** d=-60 nm, **(b)** d=100 nm, **(c)** d=200 nm, **(d)** d=300 nm, **(e)** d=400 nm, **(f)** d=500 nm and **(g)** d=600 nm. The dimensionalization of axes is based on paragraph 2.3.2.

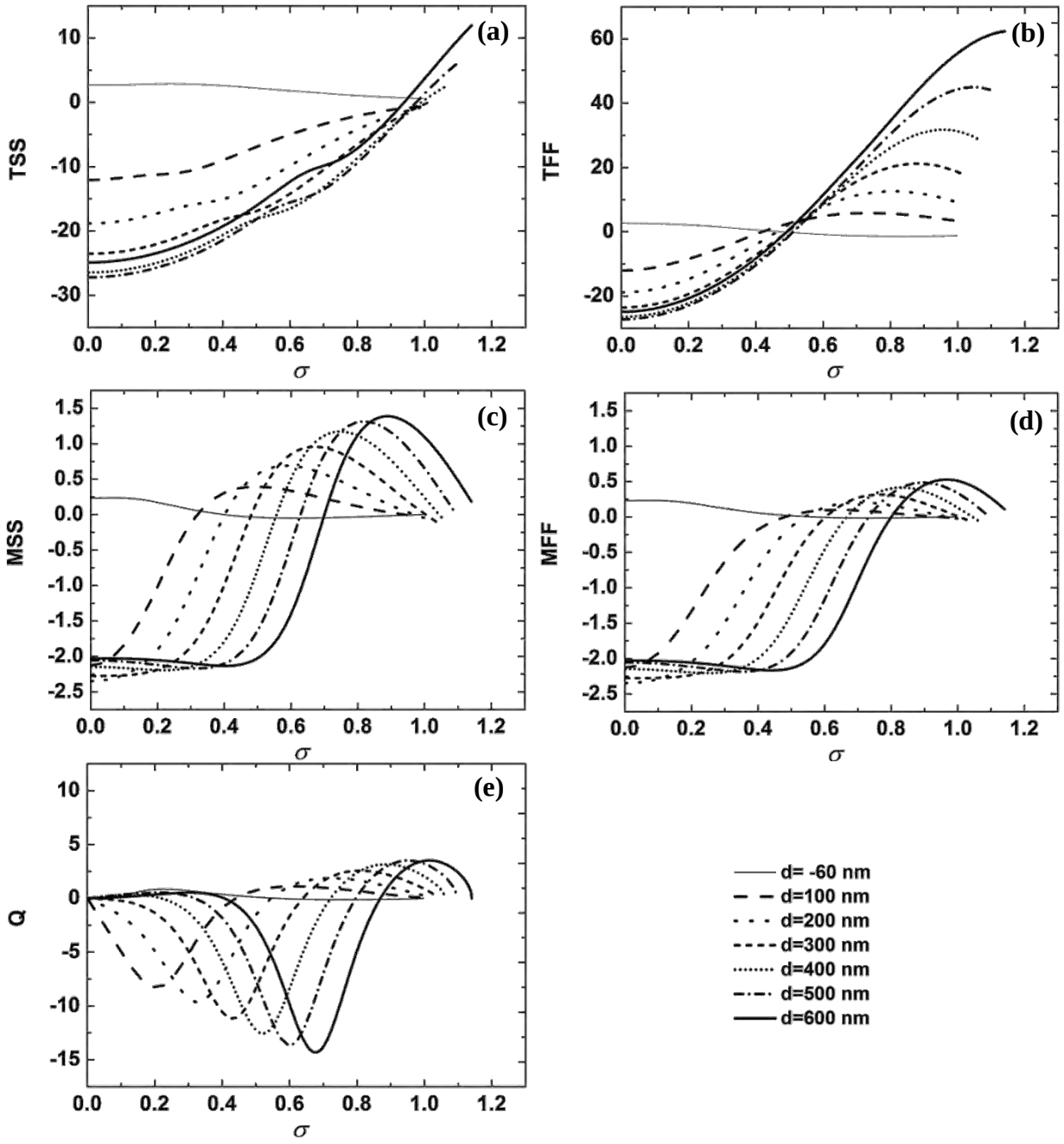

Figure 4-17: Distribution of the **(a)** in plane stress τ_{ss}, **(b)** in plane stress $\tau_{\varphi\varphi}$, **(c)** bending moment m_{ss}, **(d)** bending moment $m_{\varphi\varphi}$ and **(e)** shear stress q along the distance from the axis of symmetry (σ) for selected values of deformation. The dimensionalization of the axes is based on paragraph 2.3.2.

4.2.2 Parametric Study

In this subparagraph parametric study is performed in order to investigate the effect of different parameters of the shell coating in f-d curves, the deformed shapes and the contact, transition and outer regimes. The microbubble that was investigated in paragraph 4.2.1, pure elastic shell, is the reference and by changing one parameter a new case is studied in comparison with the first one. In the next, the effect of elasticity moduli, constitutive law, pre-stress, adhesive energy per unit area, surface tension and gas compression are investigated, in order to draw a complete picture of their influence, since in the literature the available experimental or numerical investigations for the estimation of the relevant properties of lipid monolayers are very limited.

Effect of the elasticity moduli (stretching-χ & bending k_b)

In paragraph 4.2.1 it was assumed that the area dilatation modulus is $\chi = 0.05\ \mathrm{N/m}$ and the bending modulus is $k_b = 3\times10^{-16}\ \mathrm{Nm}$. Thus the dimensionless bending modulus is $\hat{k}_b = 2.7\times10^{-3}$ and the relative importance of gas compression to area dilatation modulus is $\hat{P}_A = 3$. As it was shown in parametric analysis of the classic contact problem, when $\hat{P}_A \geq 1$ the gas compression is an important rigidity and thus affects the f-d curve even in small values of deformation. Therefore, in order to vanish its influence and consequently study the effect of elasticity moduli only, parametric analysis is carried out in the space of the dimensionless number $\hat{k}_b$ with $\hat{P}_A \ll 1$. Thus, the following cases are initially considered with: $k_b = 3.4\times10^{-13},\ 3.4\times10^{-14},\ 3.4\times10^{-15}\ \mathrm{Nm}$, $\chi = 51\ \mathrm{N/m}$, while the rest of the parameters are the same as in Table 4-2. Hence, the corresponding dimensionless bending modulus is $\hat{k}_b = 3\times10^{-3}, 3\times10^{-4}$ and 3×10^{-5} and the dimensionless pressure $\hat{P}_A = 3\times10^{-3}$. In addition, it should be stressed out that the above parameters, especially χ, do not necessarily correspond to microbubbles covered with phospholipid monolayer, but they are chosen for the purposes of the present parametric study. In Figure 4-18(a) the corresponding f-d curves are compared in dimensionless form, where the cases with the lower dimensionless bending stiffness exhibit a non-linear response associated with buckling of the shell around the contact area, Figure 4-18(b) and (c). On the other hand, the response of the $\hat{k}_b = 3\times10^{-3}$ case is strongly linear; indicating that buckling is not taking place, see also Figure 4-18(d), while the shape remains mostly spherical away from the contact region. In addition, the case with $\hat{k}_b = 3\times10^{-5}$ corresponds to a buckled shell which, around the dimple that is in contact with the cantilever, has a gradually higher curvature in comparison with the one from the case with $\hat{k}_b = 3\times10^{-4}$, which is a result of the increase of the dimensionless bending modulus, see also Figure 4-19. In the latter two cases the shape of the shell in the crater region resembles that of an inverted sphere with the same radius as the original shell. Moreover, the disjoining pressure of the

buckled cases is demonstrated in Figure 4-20, where it can be seen that when the shell is in the buckling stage the disjoining

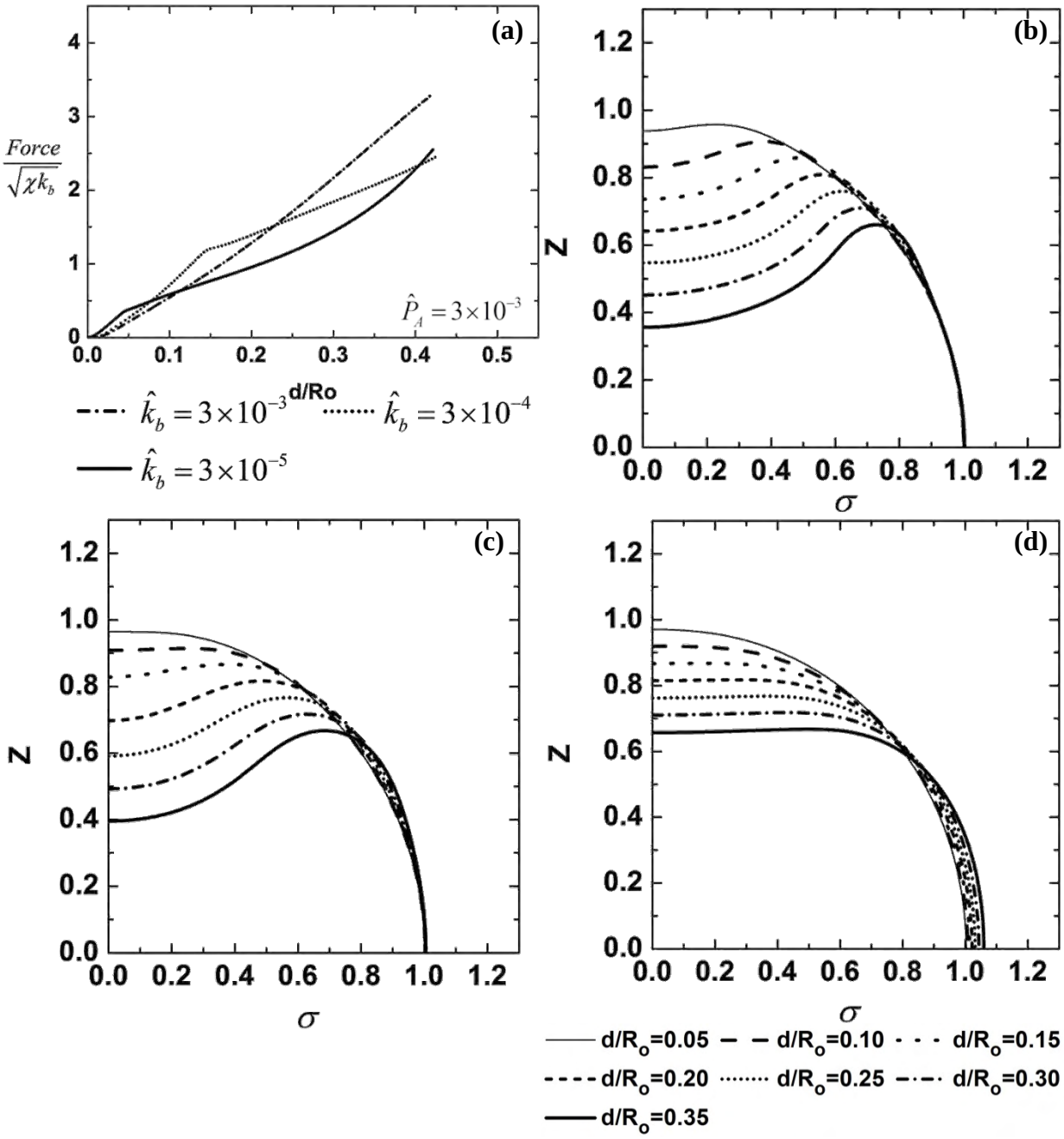

Figure 4-18: (a) Comparison of f-d curves for different values of the dimensionless bending modulus and negligible internal pressure, Shape of the microbubble in deformed configuration with **(b)** $\hat{k}_b = 3\times10^{-5}$, **(c)** $\hat{k}_b = 3\times10^{-4}$ and **(d)** $\hat{k}_b = 3\times10^{-3}$.

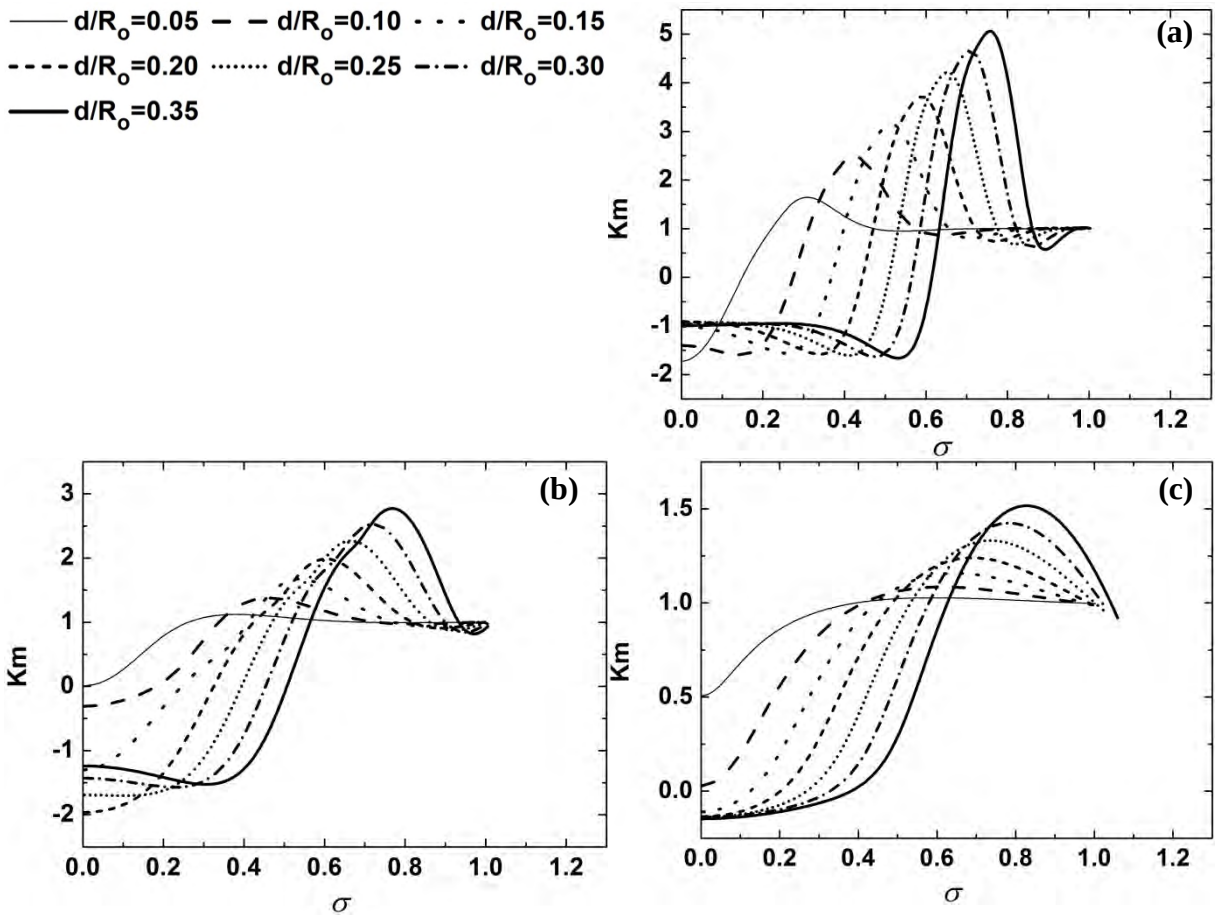

Figure 4-19: Mean curvature distribution along the distance from the axis of symmetry, σ. **(a)** $\hat{k}_b = 3\times10^{-5}$, **(b)** $\hat{k}_b = 3\times10^{-4}$ and **(c)** $\hat{k}_b = 3\times10^{-3}$. The axes are dimensionlized with the initial radius R_o.

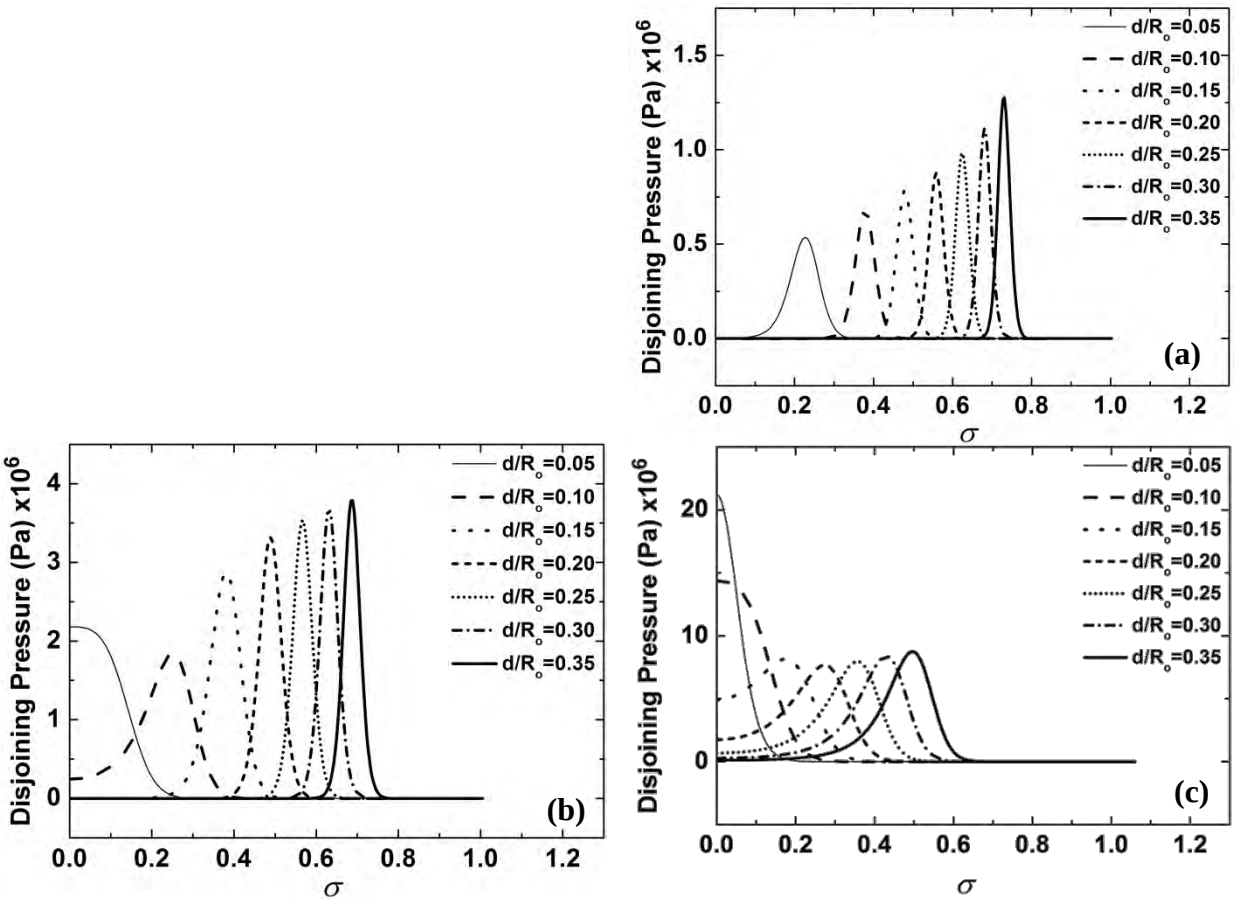

Figure 4-20: Disjoining pressure distribution along the distance from the axis of symmetry, σ. **(a)** $\hat{k}_b = 3\times10^{-5}$, **(b)** $\hat{k}_b = 3\times10^{-4}$ and **(c)** $\hat{k}_b = 3\times10^{-3}$. The horizontal axis is made dimensionless with the initial radius $R_{o.}$

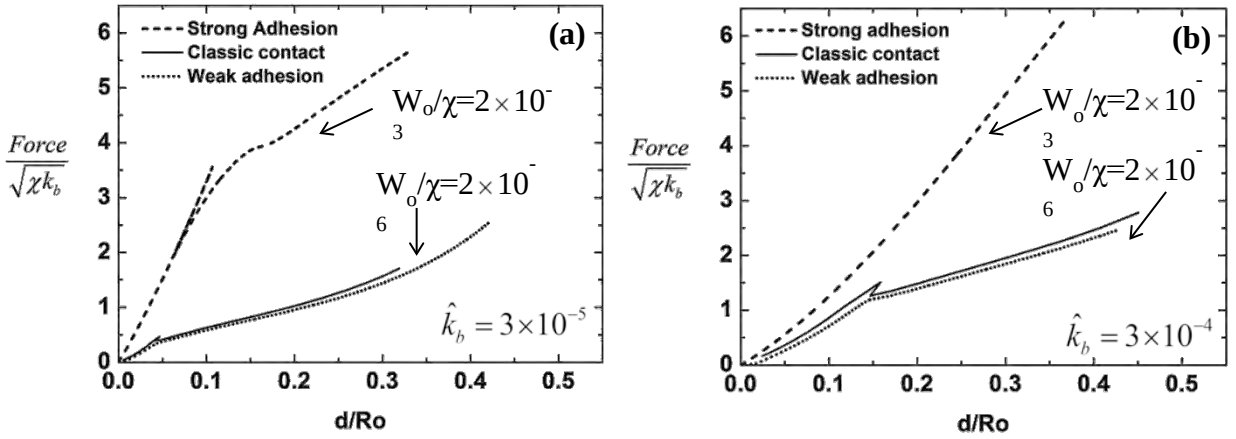

Figure 4-21: Comparison of f-d curves corresponding to classic contact model and the intermolecular forces model with weak ($W_o=1\times10^{-4}$ N/m) and strong ($W_o=10^{-1}$ N/m) adhesion, for **(a)** $\hat{k}_b = 3\times10^{-5}$ and **(b)** $\hat{k}_b = 3\times10^{-4}$; $\hat{P}_A = 3\times10^{-3}$.

pressure vanishes in the crater region, because the height of the liquid film is relatively large, and takes a non-zero value at the end of the dimple, which is practically in contact with the cantilever. In the last area the film is compressed and then the disjoining pressure takes a finite value. In case with $\hat{k}_b = 3\times10^{-4}$ the disjoining pressure is almost three times larger than the values of the case $\hat{k}_b = 3\times10^{-5}$, which indicates that the liquid film is more compressed in the latter case. It should also be stressed that the load distribution in the above cases conforms with that of a line distribution at the end of the dimple, panels a,b, and contact region, panel c. This justifies the approximation adopted by Updike and Kalnins [47-49], where they extended Reissner's solution for a uniform load distribution on a shallow thin shell, to solve the case with a line load at a prescribed angle with respect to the axis of symmetry as a means to simulate the case of a rigid flat plate compressing a spherical shell. The methodology introduced in the present study for the simulation of such contact problems provides a more realistic load distribution, for both hard and soft shells, that validates this approach. It will be seen in the following sections, where a comparison is provided between the simulations performed in the present study and the available AFM measurements of polymeric and lipid shells, that this is a very useful approach for obtaining asymptotic approximations on the f-d curves for both types of shells.

Furthermore, the cases with the lowest bending modulus have similar dimensionless parameters with the case investigated in paragraph 4.1.1, $\hat{k}_b = 3\times10^{-5}$ $\hat{P}_A = 3\times10^{-3}$, thus it is interesting to compare the response of the two contact model in the same graph, see Figure 4-21. The weak adhesion case, $W_o=10^{-4}$ N/m, has almost the same response with the classic contact model, but when the adhesion is strong, $W_o=10^{-2}$ N/m, the required force is higher and buckling is postponed, $\hat{k}_b = 3\times10^{-5}$, or even bypassed, $\hat{k}_b = 3\times10^{-4}$. The latter is clearly a result of the stabilization effected on the shell response by the adhesive action of the cantilever. The simulation via intermolecular forces captures the stable response pattern whether that involves buckling or just a prolonged Reissner type response and this constitutes a powerful tool for simulating contact problems for a wide range of configurations.

Next, in order to cover the second case of this part of parametric analysis simulations are also performed in the space of the dimensionless bending modulus, but for a microbubble where the internal pressure is important. Thus the following parameters are considered: $k_b = 3\times10^{-15}$, 3×10^{-16}, 3×10^{-17}, 3×10^{-18} Nm and $\chi = 0.05$ N/m and therefore, the dimensionless numbers are: $\hat{k}_b = 2.7\times10^{-2}, 2.7\times10^{-3}, 2.7\times10^{-4}$ and 2.7×10^{-5} and $\hat{P}_A = 3$. Thus, the case with $\hat{k}_b = 2.7\times10^{-3}$ corresponds to the pure elastic case investigated in paragraph 4.2.1. In Figure 4-22(a) the resulting f-d curves of the above four cases are compared, where the response of all curves is initially linear while exhibiting a non-linear curved up-wards behavior at large deformations, indicating that even a shell with small bending stiffness will remain almost flat when it is symmetrically compressed from above and below, see also Figure 4-22(b)-(d). Hence, in contrast with similar shells which have the same dimensionless bending modulus, here the compressibility of the gas acts as an extra rigidity that postpones buckling. Moreover, as the shell is compressed, the area around the equator is

expanded, as opposed to buckled shapes for which the shape remains almost spherical. In addition, the shell with the highest elastic rigidity, $\hat{k}_b = 2.7\times10^{-2}$, has the highest slope in the f-d curve being strongly linear for small deformations turning non-linear beyond relative deformation $d/R_o = 0.3$. On the other hand, the magnitude of the required force for the same deformation does not scale with the dimensionless bending stiffness. In fact non- linearity starts at a lower

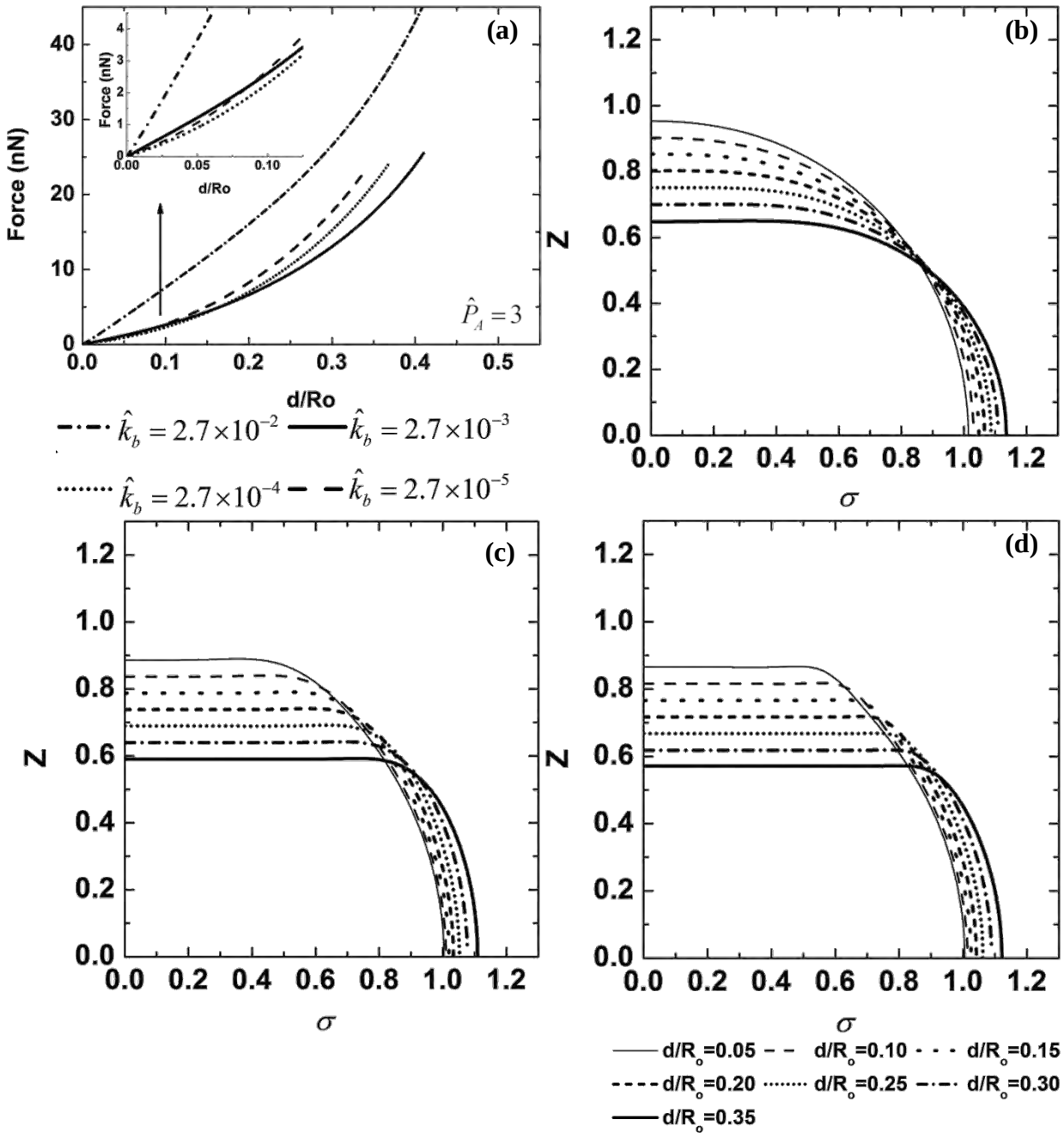

Figure 4-22: Comparison of f-d curves for different values of the dimensionless bending modulus and important internal gas pressure, Shape of the microbubble in deformed configuration with **(b)** $\hat{k}_b = 2.7\times10^{-2}$, **(c)** $\hat{k}_b = 2.7\times10^{-4}$ and **(d)** $\hat{k}_b = 2.7\times10^{-5}$.

deformation $d/R_o \approx 0.1$, which means that there is another rigidity that becomes important and hence the response is changed. The calculation of the total energy components for each of the above cases, Figure 4-23, reveals that the value of deformation for which the energy due to gas compression starts to become important is the same as the one for which the non-linear response sets in the f-d curve. Additional calculations of the disjoining pressure distribution along the distance of the shell surface show that in the stiffer shell the disjoining pressure exhibits a strong peak at the edge of the contact region, Figure 4-24(a), in contrast with softer shells with the same dimensionless pressure parameter $\hat{P}_A$. In fact, as $\hat{k}_b$ decreases, the distribution of the disjoining pressure has a plateau along the contact area, indicating that the film in this area has a progressively decreasing and almost uniform height. Finally, in the transition regime for the lower value of $\hat{k}_b$ is $\ell \sim 0.25$ and for the highest $\ell \sim 0.55$, thus $\hat{k}_b$ increases, the transition also increases.

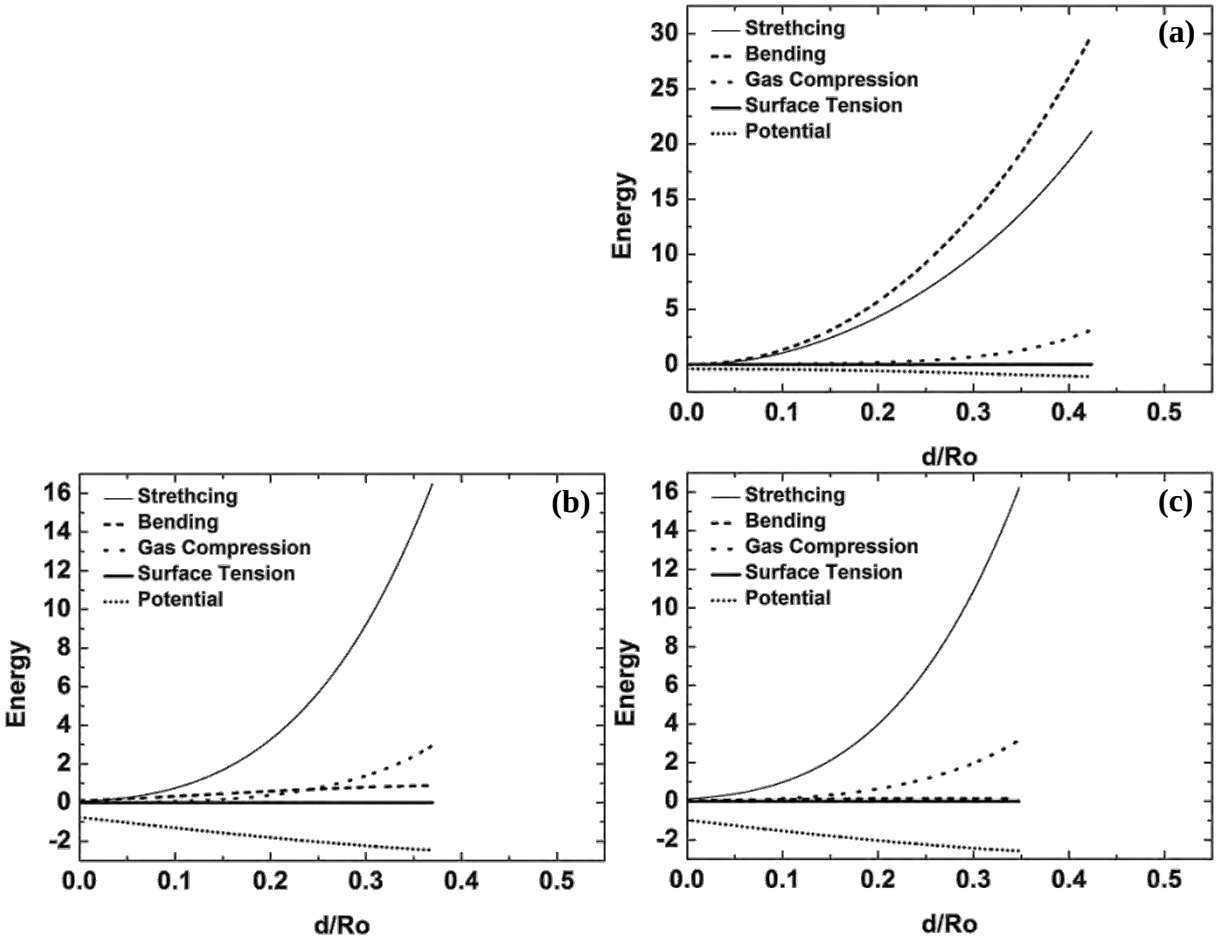

Figure 4-23: Components of total energy for the cases with **(a)** $\hat{k}_b = 2.7\times10^{-2}$, **(b)** $\hat{k}_b = 2.7\times10^{-4}$ and **(c)** $\hat{k}_b = 2.7\times10^{-5}$. The moduli of the vertical axes are dimensionlized as it is described in 2.3.2.

while the transition and outer regimes, σ_{tr} and σ_{out}, decrease. However, for the case of the lowest bending modulus, $\hat{k}_b = 2.7\times10^{-5}$, the transition length is almost the same as that for the case with $\hat{k}_b = 2.7\times10^{-4}$, revealing that the dependence of k_b and σ_{tr} is non-linear.

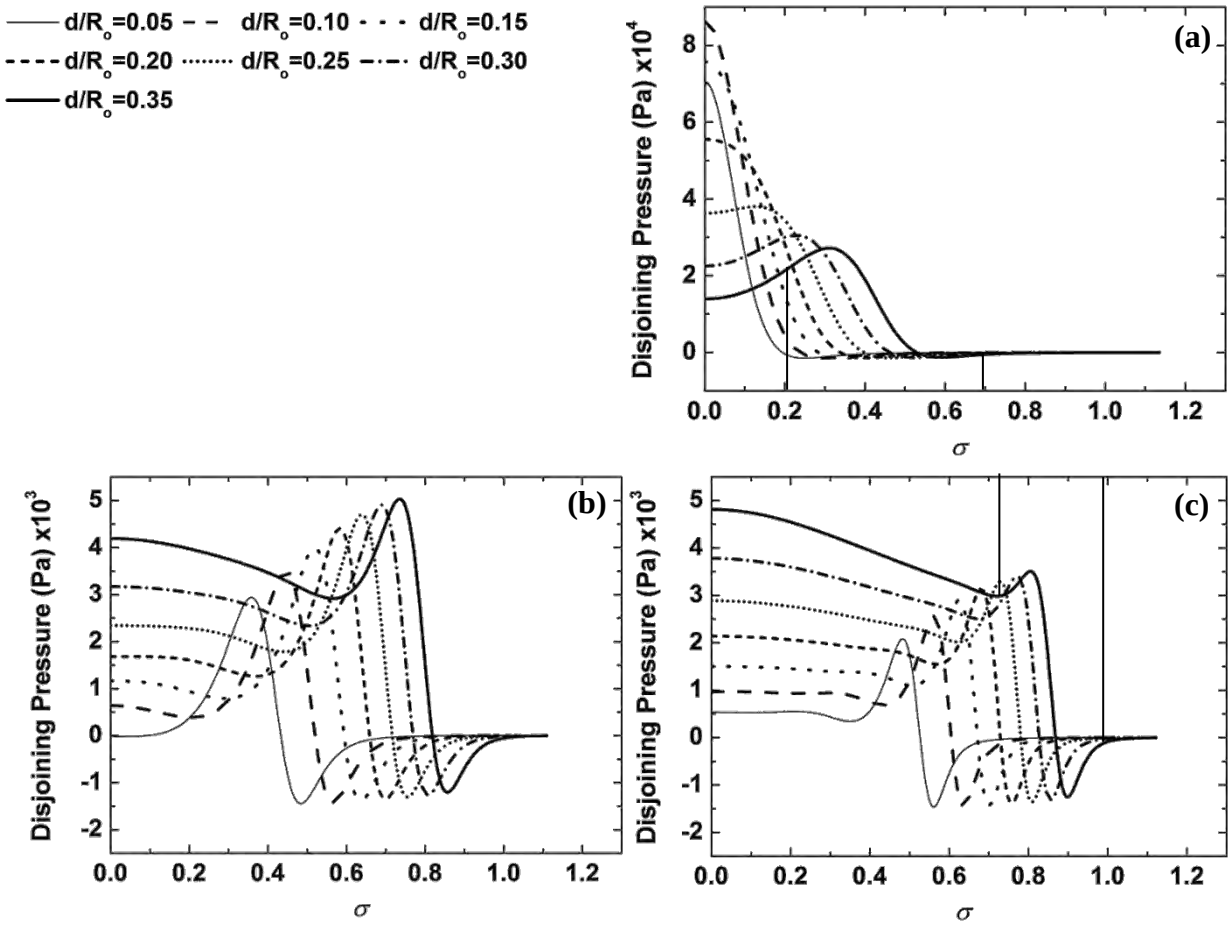

Figure 4-24: Disjoining pressure distribution for the cases with **(a)** $\hat{k}_b = 2.7\times10^{-2}$, **(b)** $\hat{k}_b = 2.7\times10^{-4}$ and **(c)** $\hat{k}_b = 2.7\times10^{-5}$.

Effect of the constitutive law (Hook and Mooney-Rivlin)

One of the main purposes of the present thesis is to characterize the constitutive behavior of the elastic coating. Thus, two constitutive laws are compared here, in order to understand their influence, when the intermolecular forces are also accounted for. In this direction, the purely elastic case is investigated once again (Mooney-Rivlin, b=1), but by assuming initially the linear constitutive law, Hook's law, and then the strain softening Mooney-Rivlin law with b=0 and 0.5. At this point, it is reminded that the parameter b defines the non-linearity of Mooney-Rivlin law, which takes values in the interval [0, 1]. The case *b*=0 corresponds to a neo-Hookean membrane whereas as *b* tends to zero the membrane becomes softer. The case of a strain-hardening material, i.e. Skalak's constitutive law, is not examined here, because in the relevant literature [13, 16, 67, 68] phospholipid monolayers are usually considered as strain-softening materials. In this context, in Figure 4-25 the f-d curves of the above cases are compared and it is seen that the influence of the constitutive law is negligible, even though the relative deformation is quite high $\left(\varepsilon = 500\,\text{nm}/1.5\,\mu\text{m} = 0.33 \text{ or } 33\%\right)$ in which case it was expected by Barthes et al. [68] that the change of constitutive law will affect the f-d curve. It should however be stressed that Barthes et al. [68] investigate, among other aspects, the effect of constitutive law on uniaxial loading. In the present study strain softening shells are mainly investigated whose effective elasticity modulus decreases when the area they occupy is expanded. Consequently the resulting f-d curve has different slope in comparison with linear materials. Furthermore, the shell shape is not uniformly deformed, in other words the area around the contact regime is compressed while the area in the transition and outer regimes is expanded. This becomes evident by calculating the stretching ratios λ_s and λ_φ for selected values of deformation along with the second invariant of the strain tensor I_2, which is a measure of the local area change as function of the distance from the axis of symmetry for the pure elastic case. As it can be gleaned from Figure 4-26, the second invariant I_2 is negative in the contact regime and it is positive in the rest of the shell. Thus, assuming a strain softening material, the effective elasticity modulus increases in the contact area and decreases in the rest of the shell leaving the average behavior almost the same like in the neo-Hookean case. Nevertheless, the overall force required to achieve a certain deformation tends to decrease as the degree of softness of the shell increases, i.e. as shell parameter b approaches zero, since a larger part of the shell, namely the outer region of the shell, becomes increasingly softer.

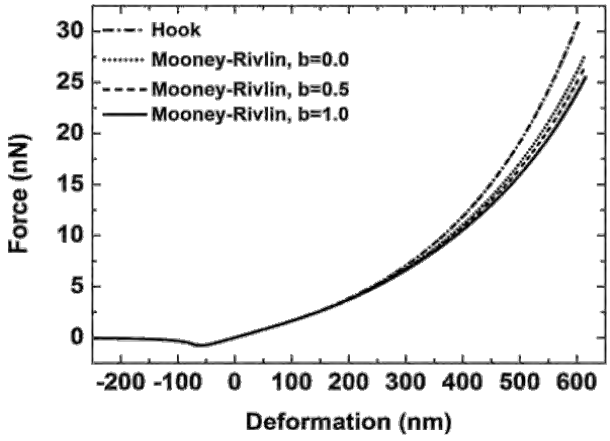

Figure 4-25: Comparison of force-deformation curves for different constitutive laws.

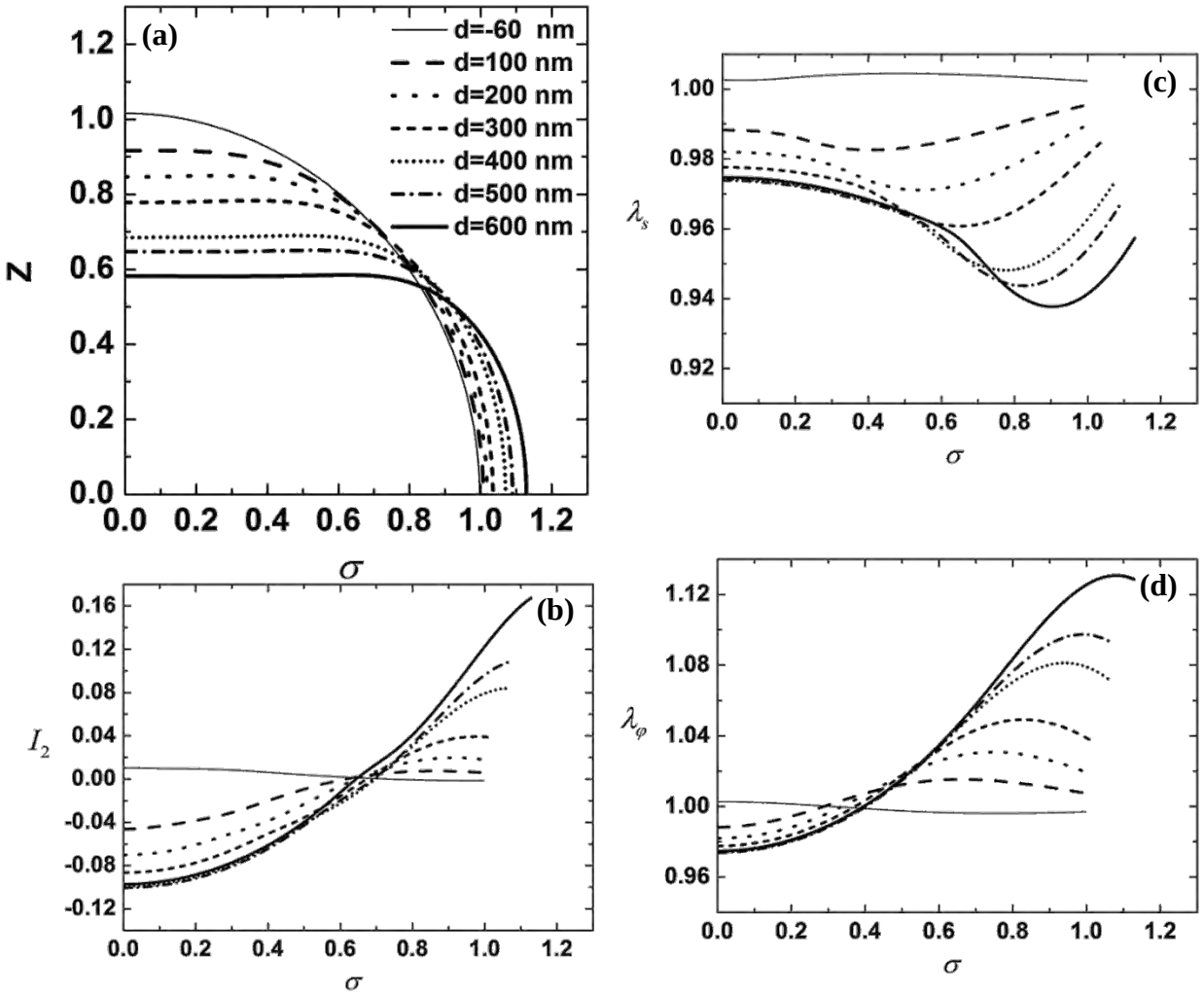

Figure 4-26: (a) Microbubble in deformed configuration, **(b)** Second invariant I_2 of the strain tensor, **(c)** Stretching ratio λ_s and **(d)** Stretching ratio λ_φ for selected values of deformation as function of the distance σ from the axis of symmetry, assuming the neo-Hookean constitutive law.

Effect of pre-stress (u)

As was mentioned above the microbubbles may lose some of their inner gas due to diffusion through the elastic membrane towards the liquid phase. Gas leakage causes an initial reduction of the shell volume and consequently residual compressive tensions develop on the shell before any interaction with the cantilever takes place. In this subsection, the effect of pre-stress is investigated by employing the formulation of paragraph 2.5, for gas leakage ($u<0$) or gas absorption ($u>0$), which is unlikely to happen when AFM measurements are considered. In the latter case, the residual stresses on the shell are tensile, because the volume of the pre-stressed shell increases. It should be stressed that parameter u defines the change of the initial radius in comparison with the stress-free state radius, see also paragraph 2.5. Hence, in Figure 4-27(a) the cases of gas leakage ($u<0$) and gas absorption ($u>0$) are compared in terms of f-d curves with the pure elastic shell, where the residual stresses are assumed to be zero (or $u=0$). As can be surmised by this figure, when the shell is assumed to have lost some gas the resulting force is smaller. On the contrary when the shell gains some gas it is higher. Moreover, the shape of the f-d curve of each case is the same, i.e. it is like a family of curves where the effect of a lower and higher internal pressure is depicted. In other words, when the shell is pre-stressed its initial internal pressure is estimated by eq. (2-72) for $\gamma_{BW}=0$. Thus, when the $u<0$, the initial internal pressure is less than the ambient and therefore the effect of gas compression is less important on the normal force balance. The opposite happens when $u>0$. Figure 4-27(b) shows how the internal gas pressure changes as the shell is compressed ($V\downarrow$), where V and V_i signify the current and the initial shell volume, respectively. The gas pressure increases as the shell is compressed, $V/V_i<1$, for all three cases, but the starting pressure is different. Hence, the required force is also different; see also the discussion in the subsection below dedicated to the effect of gas compressibility. In particular, a compressive prestress tends to reduce the force required for a certain deformation to take place since the overall shell rigidity, including volume compressibility, is lower when gas leakage has taken place; this is also clearly illustrated in the f-d curves shown in Figure 4-27(a). The disjoining pressure distribution of the two pre-stressed shells has minor differences in comparison with the pure elastic shell, thus the lengths of contact, transition and outer regimes remain the same. In addition, the corresponding shape is more or less flat. However, for large enough compressive residual stresses buckling does take place. In fact the existence of prestress tends to accelerate buckling on an otherwise similar shell; see also the discussion below when surface tension is accounted for.

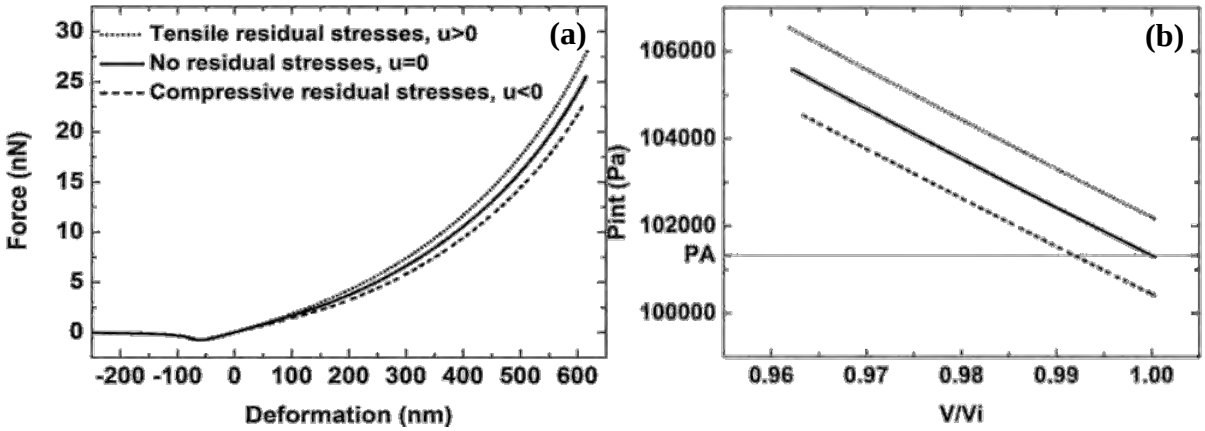

Figure 4-27: (a) Comparison of force-deformation curves for pre-stressed shells and **(b)** Pressure-volume curves for pre-stressed shells.

Effect of the adhesive energy per unit area (W_o-δ_A)

Upon introducing the disjoining pressure in the formulation of the static response of a coated microbubble two more parameters must be considered, namely the wetting parameter W_o and the characteristic length δ_A. In Figure 2-5 the functions that describe the adhesive energy and the disjoining pressure are plotted against the distance from the cantilever for $W_o = 1\times10^{-4}$ N/m and $\delta_A = 50$ nm, and it is seen that the minimum value of the adhesive energy is 10^{-4} when distance y= δ_A. Moreover, this is also the point where the disjoining pressure becomes zero. Consequently, it is important to explain how these two parameters affect the f-d curve, especially when AFM measurements are considered. Thus, simulations are performed for the purely elastic shell, i.e. no surface tension, while incorporating the interaction potential between the shell and cantilever as a means to obtain the load distribution. The cases with $W_o = 1\times10^{-2}, 1\times10^{-3}, 1\times10^{-4}$ and 1×10^{-5} N/m are examined setting δ_A to 50 nm.

Figure 4-28 demonstrates how the f-d curve changes for various values of the adhesive per unit area energy W_o. The lower values of W_o are considered as cases of weak adhesion, while the higher values correspond to strong adhesion between the shell and cantilever. This becomes mostly evident in the respective f-d curves. In the case of weak adhesion, Figure 4-28(a), the f-d curve of a pure elastic microbubble ($W_o=1\times10^{-4}$ N/m) is compared against the f-d curves of microbubbles with $W_o=10^{-5}$ and 10^{-3} N/m. The lowest value of $W_o=1\times10^{-5}$ does not significantly differ from the pure elastic curve, and the resulting adhesive force at maximal attractionis almost zero, see also embedded diagram in Figure 4-32(a). On the other hand, when $W_o=1\times10^{-4}$ or 1×10^{-3} N/m not only is the repulsive force higher for the same deformation as in the pure elastic case, but also the magnitude of maximum attraction, ~ -1 nN and ~ -5 nN, respectively. In Figure 4-28(b) the f-d curve pertaining to the case of strong adhesion, $W_0=1\times10^{-2}$ N/m, is compared against the f-d curve obtained for weak adhesion when $W_0=1\times10^{-4}$ N/m. The trend is again the same, i.e. the increase of W_o leads to a higher adhesive force while a stronger repulsive force is required to achieve the same deformation. In particular the maximum attractive force is on the order of -40 nN when $W_o=1\times10^{-2}$ N/m. Both effects are due to the stronger interaction between the shell and cantilever that generates significantly larger forces for the same distance between the cantilever and shell center of mass. It must also be noted that the initial position of the cantilever for weak adhesion is set to z=1.5, as in paragraph 4.2.1. However, a dimensionless distance of z=1.5 is a position of interaction between the shell and the cantilever in the case of strong adhesion, $W_o=1\times10^{-2}$ N/m, and consequently an initial position of z=3 for is used in the latter case. In addition, the increase of W_o leads to f-d curves, where the relative position of cantilever and shell is not a monotonically decreasing function. Thus, the arc-length continuation is the most appropriate way to proceed with the numerical solution. In the case of strong adhesion, continuation to small cantilever-shell separations occurs through the onset of two limit points that generate a hysteresis loop. It corresponds to the pull-off force required to equilibrate the strong adhesive force exerted on the shell by the cantilever.

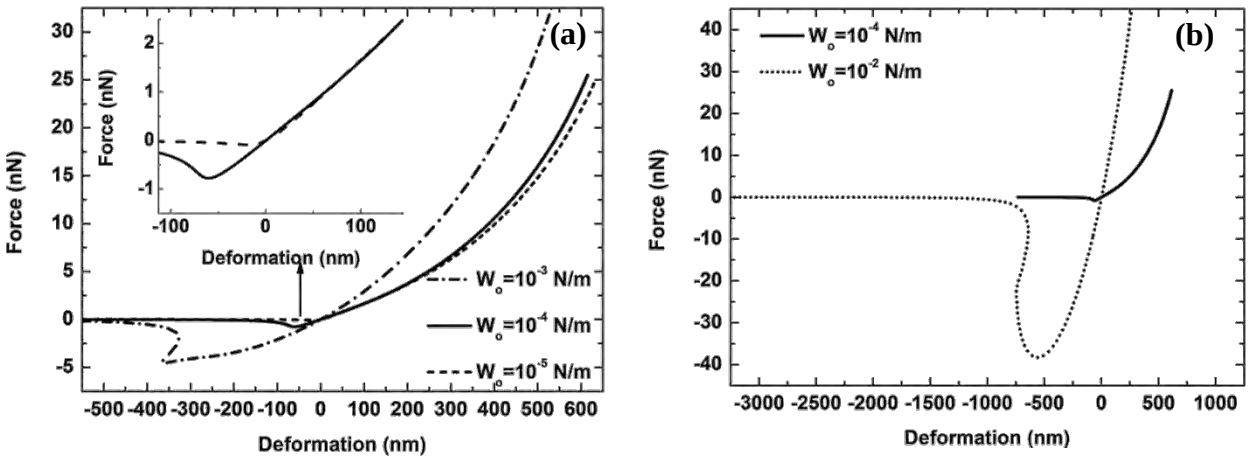

Figure 4-28: Comparison of force-deformation curves for different values of the adhesive energy per unit area (W_o), **(a)** Weak adhesion and **(b)** Strong adhesion.

The shape of the microbubble when $W_o=1\times10^{-3}$ N/m, Figure 4-29(b), is almost the same as in the case of a purely elastic shell, Figure 4-29(a), but the solution that corresponds to the maximum attractive force has a more spherical shape. As W_o increases the attraction is stronger, hence the shape that corresponds to the onset of repulsion is gradually more deformed in the pole area, i.e the thin line in Figure 4-29(b). During attraction and repulsion the shape of microbubbles for W_o in the interval between 10^{-5} and 10^{-3} N/m is characterized by obtuse wetting angles. However, in the case of the strongest adhesion the wetting angle is close to 90° as deformation increases, Figure 4-29(c). In addition, the values of deformation that are listed in the above graphs, corresponding to each one of the deformed shapes shown, refer to the equivalent f-d curve. As W_o increases the calculated deformations, see paragraph 4.2.1, differ significantly in the sense that they are based on the location of the pole in the reference configuration that registers a zero force. When the adhesion is strong a zero force does not correspond to a spherical shape. On the contrary, the position of the pole is significantly deformed; hence the resulting deformation differs from the actual pole displacement. During the AFM experiments that are discussed in the next chapter the adhesion is negligible. As a result, the measured deformation is very close to the pole displacement from its position corresponding to the spherical configuration. Consequently the above concept is a potential way that incorporates the interaction potential constitutes a promising alternative for obtaining the load distribution and simulating the static response of shells during contact experiments. In particular, identifying the maximal attraction during an AFM experiment provides a reliable means to estimate the interaction potential between the shell and cantilever. This can be combined with an optical measurement of the evolution of the contact length and the slope of the force-deformation curve in order to provide estimates of the area dilatation and bending stiffness. More details on this analysis are provided in the last chapter of this Thesis.

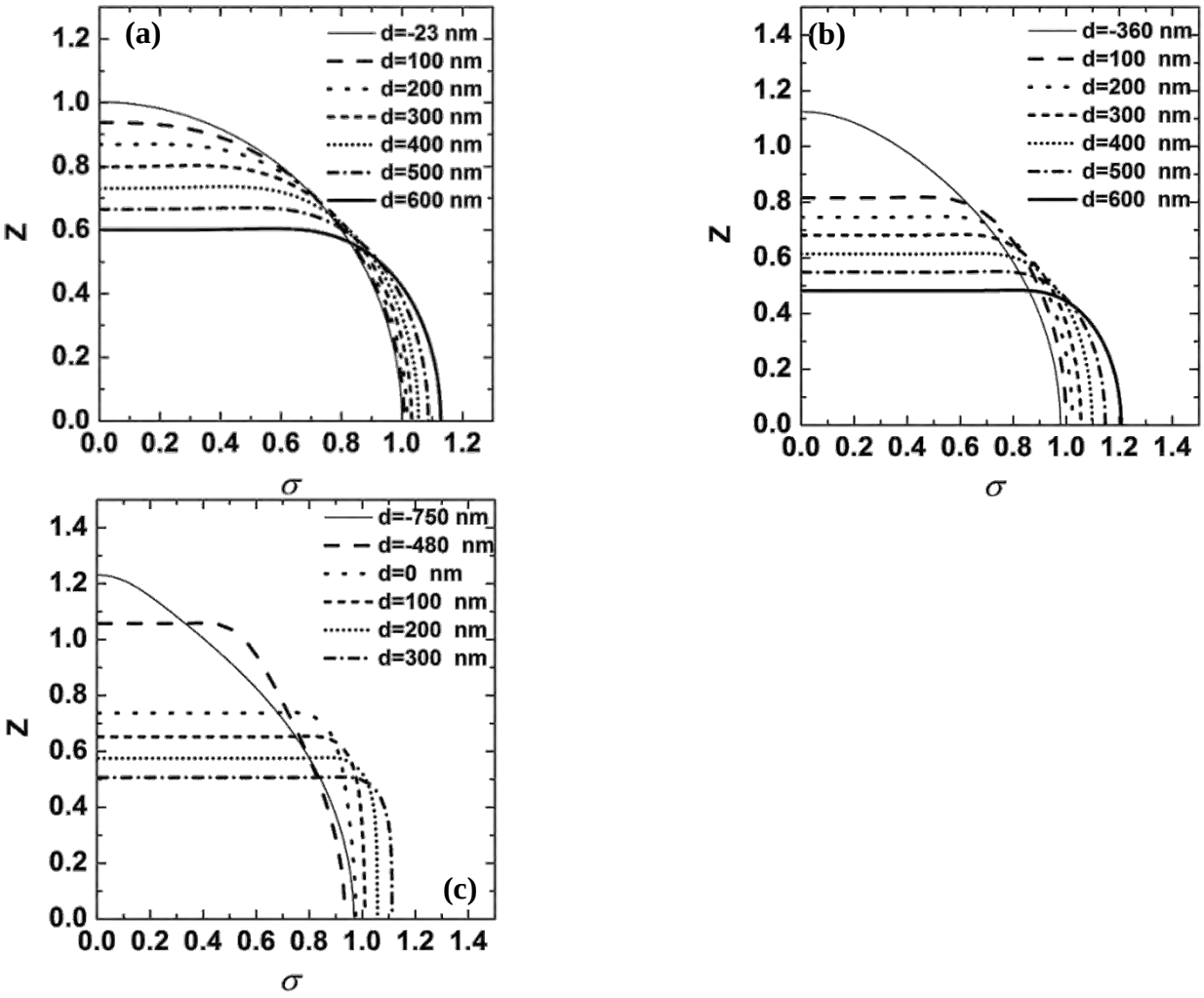

Figure 4-29: Microbubble in deformed configuration for selected values of deformation, (the axes z and σ are dimensionalized with the initial radius R_o). **(a)** $W_o=1\times10^{-5}$ N/m, **(b)** $W_o=1\times10^{-3}$ N/m and **(c)** $W_o=10^{-2}$ N/m.

The corresponding diagrams of the disjoining pressure distribution are shown in Figure 4-30. The disjoining pressure for the case with $W_o=1\times10^{-5}$ N/m is the same as for the purely elastic shell, but weaker in the transition regime. An indicative load distribution for the purely elastic case is provided in the context of the approximation adopted in [48] that is very similar with the one obtained in the above figure, see also Figure 3-7 from the previous section. As W_o increases the disjoining pressure reaches higher values, the contact length increases and the size of the transition regime is gradually compressed. Especially in the strongest adhesion case, the contact regime has zero disjoining pressure, which means that the height of the film is δ_A, and the disjoining pressure is non zero only in the very thin transition regime. The last case recovers the formulation of the classic contact problem, where the applied load is a non-zero point function at the end of contact. Thus, it can be assumed that the formulation of paragraph 4.1 is a limit case of the present analysis. More details on this approach are provided in the last section where a comparison with experiments is presented and the derivation of asymptotic approximations is carried out.

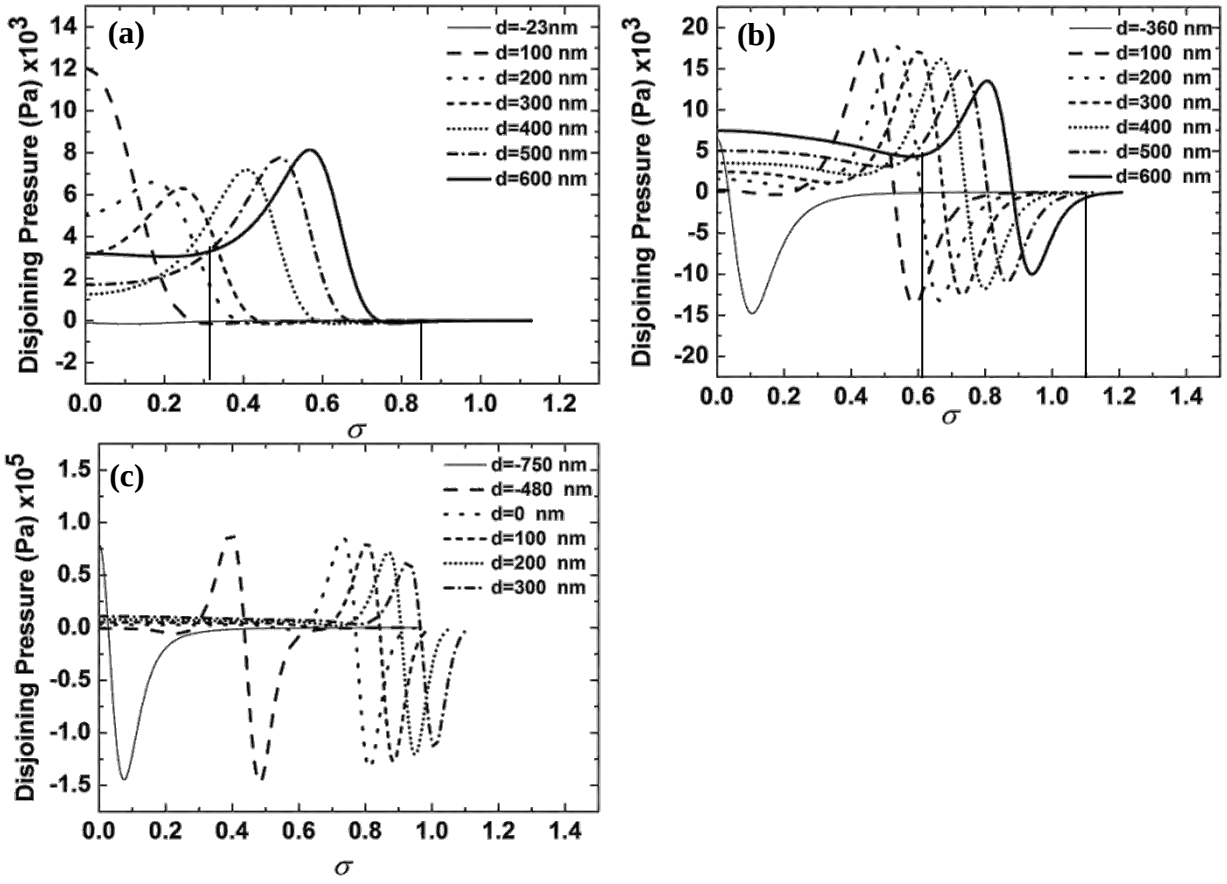

Figure 4-30: Distribution of the disjoining pressure along the distance from the axis of symmetry. **(a)** $W_o=1\times10^{-5}$N/m, **(b)** $W_o=1\times10^{-3}$ N/m and **(c)** $W_o=1\times10^{-2}$ N/m.

The energy due to intermolecular forces depends also on the characteristic length δ_A, where the energy is minimized or the disjoining pressure is zero. In the next, the effect of δ_A in f-d curve is investigated by performing simulations for the pure elastic shell $\left(\delta_A = 50 \text{ nm and } W_o = 10^{-4} \text{ N/m}\right)$, but for different values of δ_A, i.e. $\delta_A = 12.5, 25, 50, 75,$ 100 and 150 nm all of them with $W_o = 1\times10^{-4}$ N/m. As can be seen from Figure 4-31(a) the resulting force does not significantly change in comparison with the pure elastic case. However, the only important effect pertains to region around the maximum adhesion force, Figure 4-31(b). As δ_A increases, 75, 100 and 150 nm, the response becomes smoother, while for smaller values of δ_A, 12.5 and 25, the pick of adhesion force is sharper. The amplitude of the distribution of the disjoining pressure is not affected by changing the δ_A length. However, the contact and transition lengths are compressed, but the outer regime is expanded as the length δ_A decreases and vice versa when δ_A increases. a theoretical interpretation of the above trends is offered in chapter 6 where a comparison against experiments and an asymptotic analysis are presented.

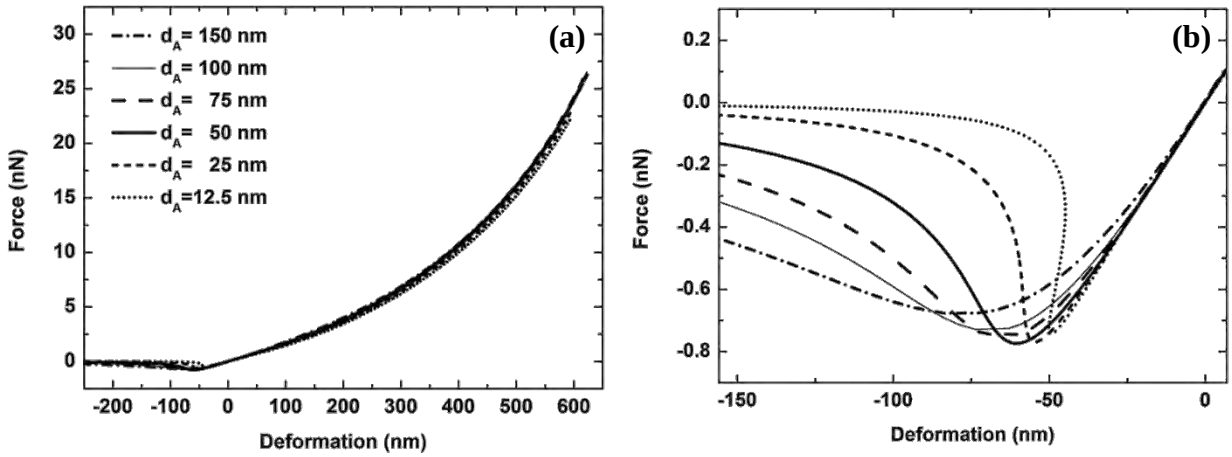

Figure 4-31: (a) Comparison of f-d curves for different values of δ_A. **(b)** Focus on the maximum adhesion area in f-d curve.

Effect of the surface tension (γ_{BW})

AFM experiments and clinical applications of microbubbles are performed in aqueous environment, thus surface tension between the shell coating and water is a parameter that requires investigation. The static response of coated microbubbles is mainly investigated in the context of classic shell mechanics [24, 25], where the surface tension is not accounted for. On the other hand, experiments that measure the surface tension of such coatings are very limited. A recent study by Segers et al. [83] demonstrates the synthesis and development of phospholipid monolayers, where they report that the surface tension of such coatings is very small or even near zero, $\gamma_{BW} \sim 1\times10^{-3}\ \mathrm{N/m}$. For the purposes of the present thesis, two cases are investigated with the same parameters as in 4.2.1, but for non-zero surface tension, i.e. $\gamma_{BW} = 4\times10^{-3}\ \mathrm{N/m}$ and $\gamma_{BW} = 4\times10^{-2}\ \mathrm{N/m}$:

In Figure 4-32(a) the f-d curves that correspond to the cases with surface tension are demostrated against the pure elastic shell $\gamma_{BW} = 0\ \mathrm{N/m}$. Surface tension significantly increases s the required force for the same deformation or, alternatively, surface tension adds an extra resistance on the shell. Moreover, the surface tension is an isotropic property that acts on the shell along with the in plane stresses τ_{ss} and $\tau_{\varphi\varphi}$, which depend on the direction. Thus, surface tension could be interpreted as the isotropic part of the stress tensor. This argument implies that surface energy consists of an isotropic part, namely surface tension, and the purely elastic part that depends on the extent of local deformation. Equation (2-72) implies that when the shell/liquid interface has surface tension, the initial gas pressure is higer than the ambient by a term of $2\gamma_{BW}$, which makes the gas compression a more significant term on the equilibrium; see also Figure 4-32(b) where the internal gas pressure (P_{int}=P_G) is plotted against the ratio of the current volume V with the initial volume V_i.

As in the purely elastic case shown in Figure 4-13 buckling is not observed in these two cases either, Figure 4-33(a) and (b), due to the stabilizing effect of surface tension. The disjoining pressure reaches higher values as the surface tension increases, but its distribution remains the same, i.e. repulsive in the contact regime, attractive in the transition regime and zero in the outer part of the shell, Figure 4-33(c) and (d). The increase in the disjoining pressure values indicates that the liquid film has been further compressed in the contact area. Identifying the contact regime as the part of the shell with the constant repulsive disjoining pressure, the transition regime with the repulsive and attractive disjoining pressure and the outer regime with the zero disjoining pressure, the length of the transition can be estimated based on the load distribution shown in Figure 4-33 (c) and (d). As can be gleaned, surface tension tends to decrease the contact length, increase the transition and the outer lengths. In addition, as surface tension increases the force required to sustain a certain deformation increases and as a result an almost flat and repulsive disjoining pressure distribution develops in the contact region. This is in contrast to the almost point load distribution obtained in the purely elastic case leading to a linear force deformation curve, at least in the initial part of the f-d curve before the resistance to volume compression dominates shell rigidity. It is due to the dominant resistance to volume compression that is exhibited by the shell when surface tension increases, as is the case in Figure 4-33 b and d, that the force deformation curve assumes an almost quadratic form that in its entirety. This is a pattern that distinguishes shells with significant

surface tension from purely elastic shells and will play a central role in the parameter estimation of lipid shells.

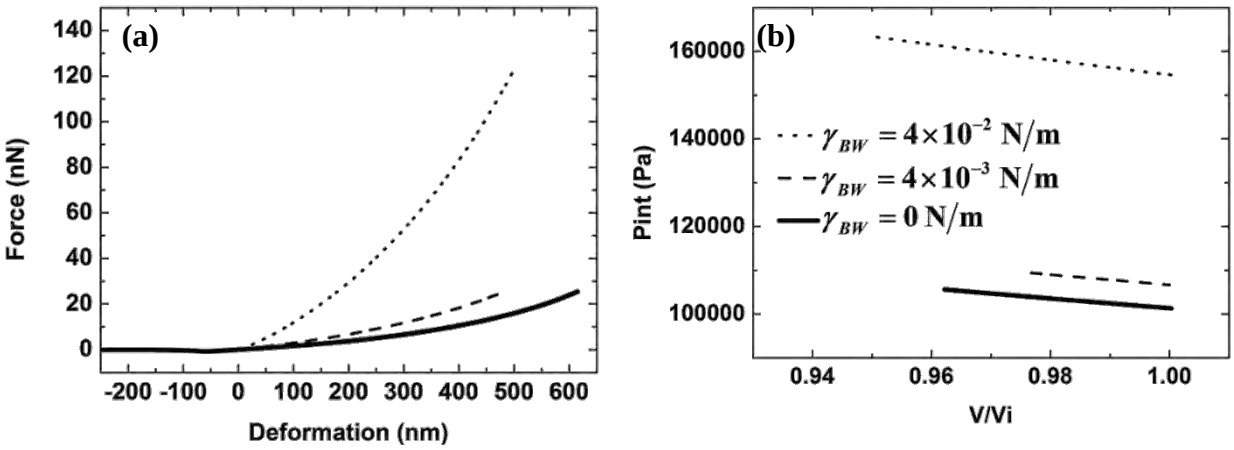

Figure 4-32: (a) Force-deformation curve and **(b)** Internal gas pressure as function of the volume ratio.

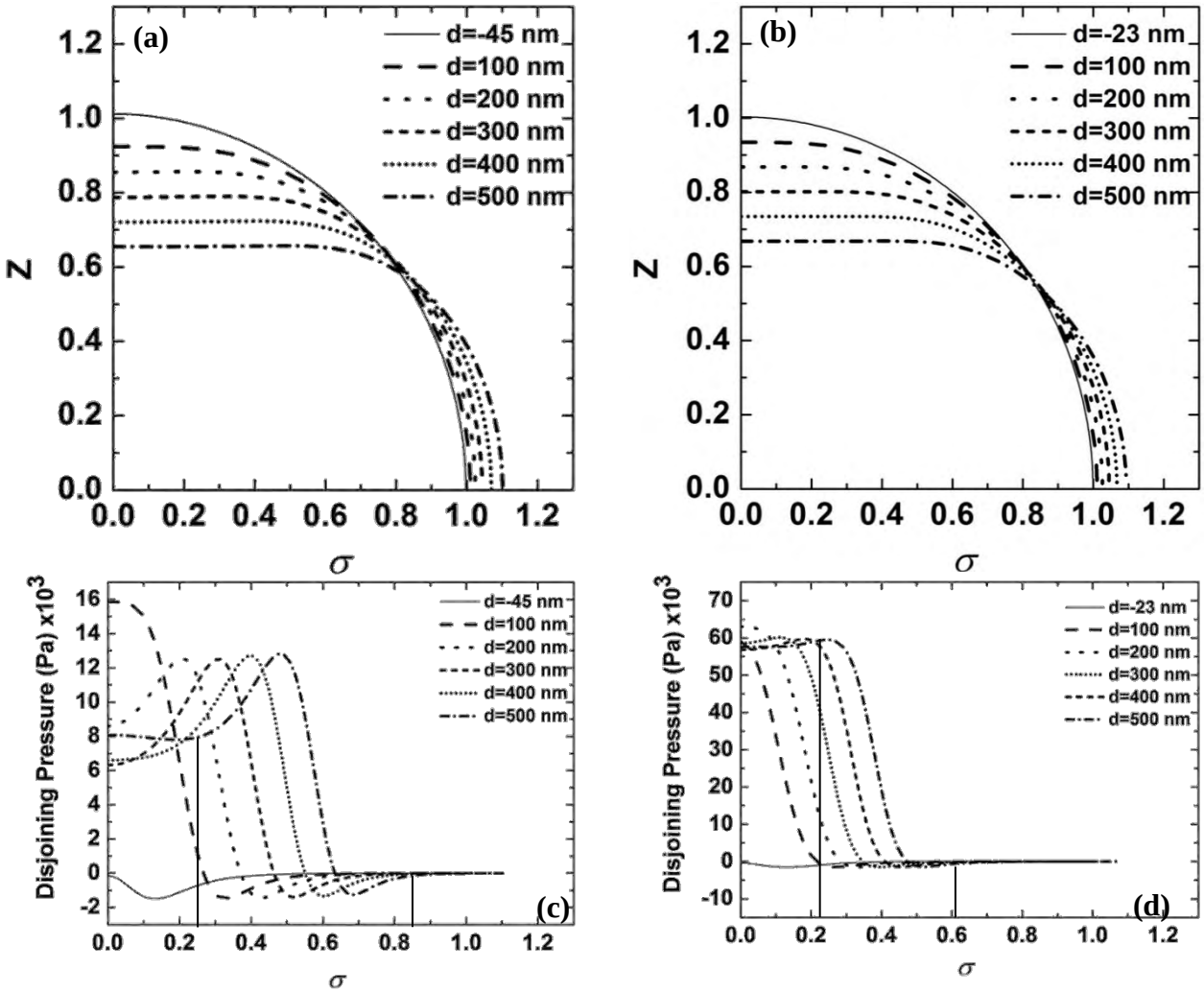

Figure 4-33: (a) and **(b)** Microbubble in deformed configuration for selected values of deformation, **(c)** and **(d)** Distribution of the disjoining pressure along the distance from the axis of symmetry. **(a)** and **(c)** $\gamma_{BW}=4\times10^{-3}$ N/m and **(b)** and **(d)** $\gamma_{BW}=4\times10^{-2}$ N/m, respectively.

Effect of gas compressibility (P_G-γ)

In paragraph 4.2.1 the encapsulated gas is assumed to undergo isothermal pressure variations, therefore the internal-gas pressure increases as the shell volume decreases. Even though it is not realistic to assume that the gas is incompressible, here the purely elastic case is investigated again, but for zero polytropic index, γ=0, i.e. the internal pressure remains constant as the volume changes. In Figure 4-34(a) an f-d curve obtained for an incompressible gas is compared with the case of a compressible one. The two curves respond the same way up to deformation of 200 nm and then the response curve of the incompressible gas continues almost linearly with the deformation, Figure 4-34(a), indicating that when the gas compressibility is comparable to its elasticity $P_A R_o/\chi = 3$, the former acts as an extra stiffness and the required force is higher. A similar result was found in [84], where microbubbles were investigated subject to a static point load. In Figure 4-34(b) the internal gas pressure (P_{int}=P_G) is plotted against the ratio between the current volume V and the initial volume V_i. As can be seen the gas pressure for the compressible case starts to increase as the shell is compressed, $V/V_i < 1$, while for the incompressible case the internal pressure remains constant,

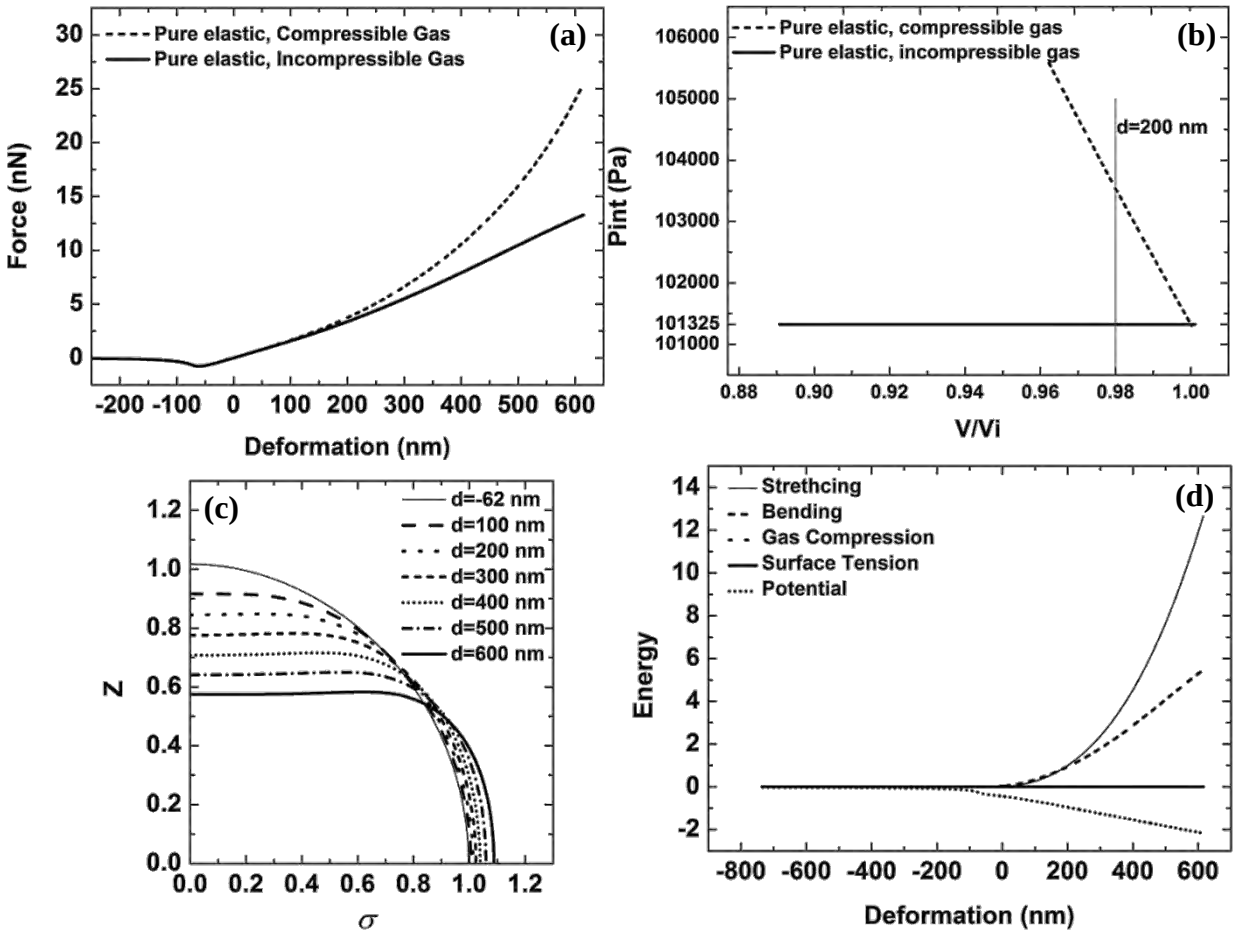

Figure 4-34: (a) Force-deformation curve of a pure elastic shell with compressible and incompressible gas, **(b)** Internal gas pressure as function of the volume ratio, **(c)** Pure elastic microbubble with incompressible gas in deformed configuration for selected values of deformation and **(d)** Components of the total energy as function of deformation. The dimensionalization of axes is based on paragraph 2.3.2

$P_{\text{int}} = P_A = 101325$ Pa . Moreover, in the latter case the reduction of the volume is much larger in comparison with the case where gas compressibility is accounted for, for the same deformation, while the corresponding shapes are again flat and don't exhibit buckling, Figure 4-34(c). The energy due to gas compression vanishes when γ is set to zero, whereas the energies due to bending and the adhesive potential are almost the same with the compressible case. On the contrary the energy due to stretching is less, ~12, Figure 4-34(d), while for the compressible case is ~17.5, Figure 4-15(b). This is a result of the non-linearity of the Mooney-Rivlin law, where the extension of the area leads to the reduction of the stretching energy. Finally, the distribution of tensions and moments is presented in Figure 4-35. The in plane stresses τ_{ss} and $\tau_{\varphi\varphi}$ have been increased significantly in comparison with the compressible case, as the diagram in Figure 4-35(a) shows. This can be explained by the normal force balance, where the contribution of the gas pressure is eliminated, hence it is the stretching terms that balance the same external load (disjoining pressure). The bending moments and the shear tension reach approximately the same values as in the purely elastic shell. In addition, when the gas is treated as incompressible the disjoining pressure in the contact regime for large deformations is zero or even positive, indicating that the intermediate liquid film is not compressed as in case of the compressible gas. Most of the disjoining pressure is located with a maximum value at the end of the contact regime, which is the same concept as in the classic contact problem, where the applied load is a point at the end of contact and the response is strongly linear before buckling Figure 4-35(f).

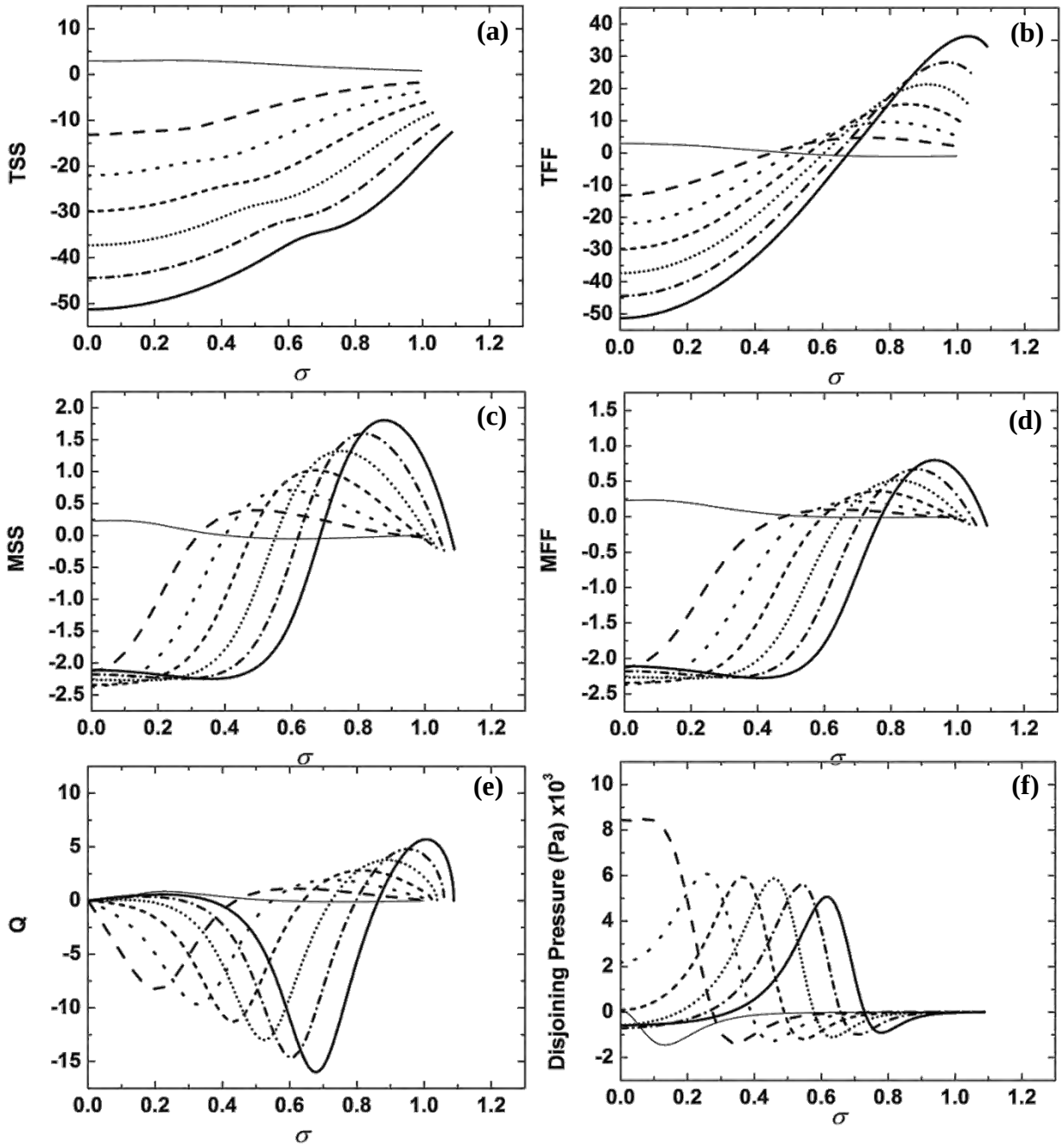

Figure 4-35: Distribution of the **(a)** in plane stress τ_{ss}, **(b)** in plane stress $\tau_{\varphi\varphi}$, **(c)** bending moment m_{ss}, **(d)** bending moment $m_{\varphi\varphi}$, **(e)** shear stress q and **(f)** disjoining pressure along the distance from the axis of symmetry (σ) for selected values of deformation. The dimensionalization of the axes is based on paragraph 2.3.2.

4.2.3 Study of a free microbubble

In this paragraph numerical results obtained with the formulation of the last part of the session 2.3.2 are presented. More specifically, it is assumed that the shell has no elastic rigidity and its static behavior is controlled only by surface tension and gas compressibility as it interacts with the cantilever. The present case will be referred to in the following as the «free» microbubble. Following the same concept as in paragraph 4.2.1, the cantilever is placed at a dimensionless distance z=1.5 from the equator of the shell. Upon performing simulations with the parameters of Table 4-3, a force-distance curve is obtained using simple continuation in the distance z, Figure 4-36(a). The following dimensionless numbers characterize the shell: $\hat{P}_A = \frac{P_A R_o}{\gamma_{BW}} = 38$; $\hat{\gamma}_{BW} = \frac{\gamma_{BW}}{\gamma_{BW}} = 1$ and $\hat{W}_o = \frac{W_o}{\gamma_{BW}} = 2.5 \cdot 10^{-2}$.

The response of a free microbubble in terms of a f-d curve is similar with that of a coated microbubble, Figure 4-36(b). Both curves exhibit the same maximum attractive force, because the same adhesive energy per unit area was assumed ($W_o = 1 \times 10^{-4}$ N/m). On the other hand, the response is more linear and with higher slope in the case of a coated microbubble. In addition, the deformation when the shell is under the maximum attraction is -107 nm in case of the free microbubble, while in the purely elastic case is -60 nm. This difference originates from the different value of z for which the total force becomes zero, $z\left(F = 0\right) = 0.99$ for the free microbubble. Moreover, the disjoining pressure, Figure 4-36(c), is positive (repulsion) around the contact area, negative in the transition regime and zero in the outer area, as in the purely elastic case. It must be noted, that in the present case the distribution of the disjoining pressure is almost uniform in the contact region, which indicates that the film height is almost constant as well around the contact area. Moreover, the shape that corresponds to this solution is again flat in the contact area, with no wrinkles, and buckling was not observed as it was expected, Figure 4-36(d). This is also confirmed by the distribution of the mean and principal curvatures, Figure 4-37, where it can be seen that along the contact regime the curvatures are constant and zero. As the deformation increases the principal curvatures, k_s and k_φ, reach values higher and less than one in the outer regime ($\sigma > 0.6$), respectively, which indicates that the shell in s direction is compressed and in φ is elongated thus confirming that the shell is not spherical in the outer regime. The total energy increases in comparison with the total energy of a pure elastic shell Figure 4-38(a), because the contribution of surface energy is relatively large. Decomposing the total energy in its components it is clear that most of the energy is due to surface tension. Moreover, the maximum value of the energy due to gas compression in the present case is $\hat{w}_c \approx 0.2$, while in the pure elastic shell it is $\hat{w}_c \approx 2.5$,

Initial radius:	$R_o = 1.5\,\mu\text{m}$			
Surface tension:	$\gamma_{BW} = 4 \cdot 10^{-3}$ N/m	Polytropic index:	$\gamma = 1.07$	
Potential depth	$W_o = 1 \times 10^{-4}$ N/m	Potential length	$\delta_A = 50$ nm	400 elements

Table 4-3: Simulation parameters for the f-d curve of a free microbubble.

because in the former case the corresponding final volume is $V_f = 0.98V_i$ of the initial and in the latter it is $V_f = 0.96V_i$. On the other hand, the dimensionless energy of the adhesive potential is $\hat{w}_{IF} \approx 2.5$ for both cases, which means that the liquid film between the shell and the cantilever is compressed by the same amount. In addition, the energies due to stretching and bending are zero, because it is assumed that the shell has no elasticity rigidity, thus it cannot store elastic energy. Finally, the energy due to surface tension is the integral of the surface tension over the deformed area and tends to increase with the deformation, bold solid line in Figure 4-38(b). Given the assumption of a constant surface tension across the shell, it is convenient to conclude that the surface tension energy increases owing to the area

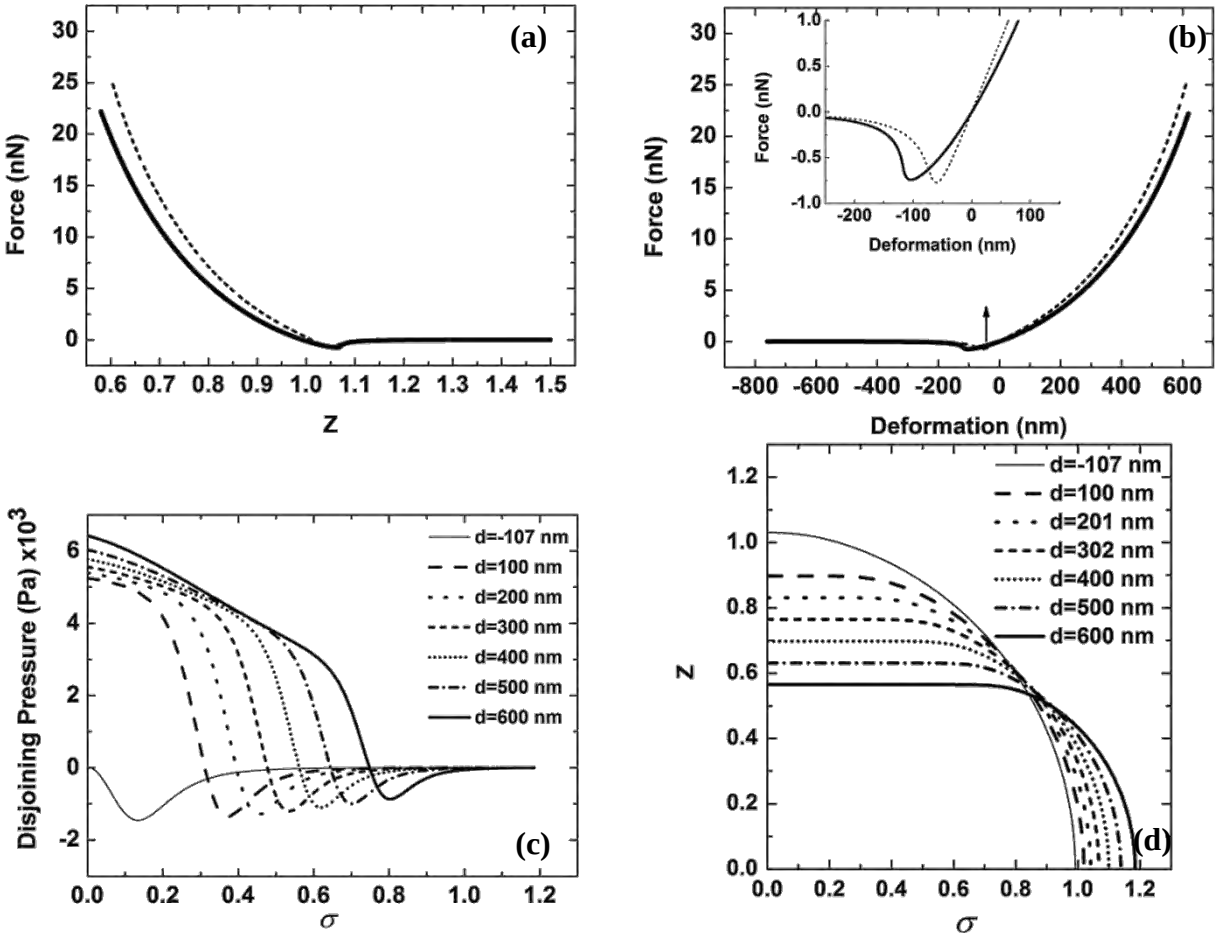

Figure 4-36: (a) Force-distance curve of a free microbubble (solid line) and a microbubble covered with an elastic shell (dashed line, see also paragraph 4.2.1), **(b)** Force-deformation curve, **(c)** Distribution of the disjoining pressure along the distance from the axis of symmetry for the free microbubble and **(d)** Free microbubble in deformed configuration for selected values of deformation, (the axes z and σ are dimensionalized with the initial radius R_o)

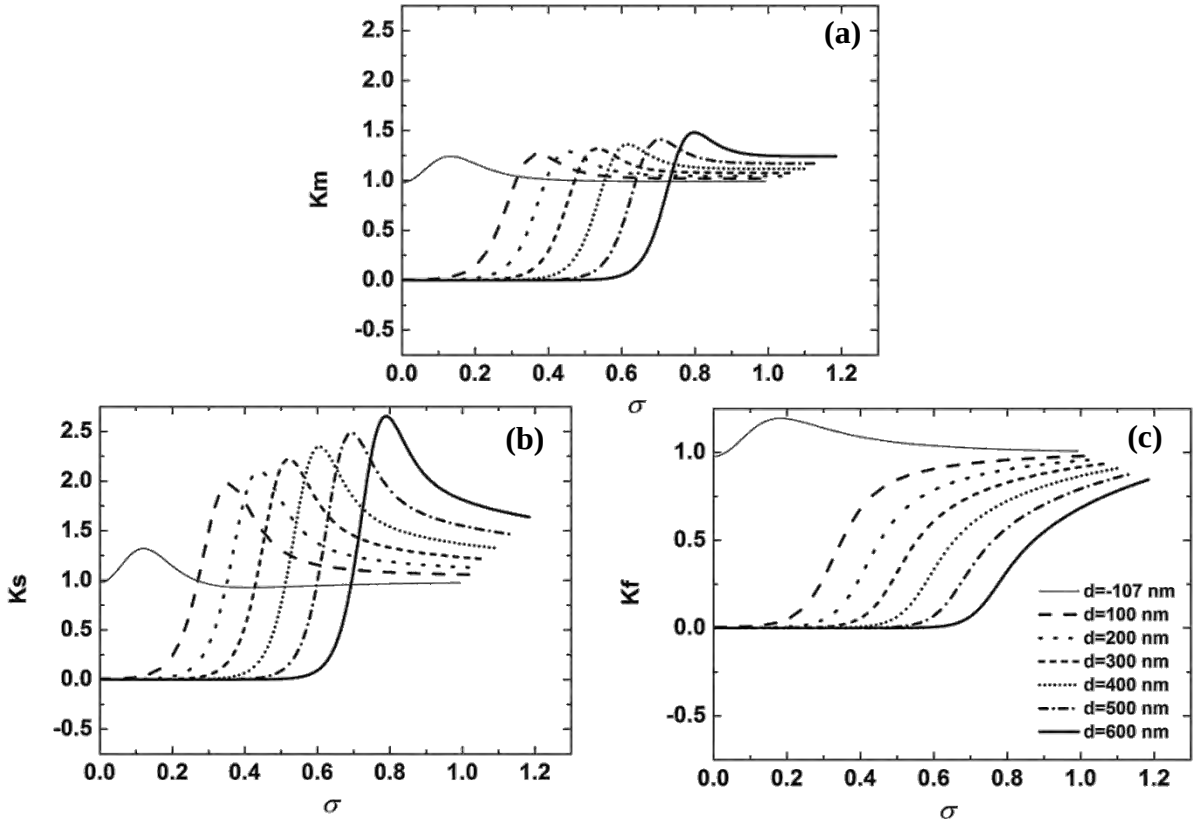

Figure 4-37: Distribution of the principal curvatures along the distance from the axis of symmetry (σ) for the free microbubble **(a)** Mean curvature (k_m), **(b)** curvature on s direction (k_s) and **(c)** curvature on φ direction (k_φ).

expansion. In contrast to the case of a drop where the increase in the inner pressure causes a reduction on the surface, in the present case an increase in the inner pressure can be followed by an increase of the surface, because the shell is not spherical, when it is deformed. Moreover, the importance of surface tension is also revealed on the fact that when the cantilever is at a long distance from the shell, i.e. the shell is not deformed, yet the energy due to surface tension is not zero, but it has a value of 250 confirming in this way a stabilizing role. In addition, the distribution of the total energy is depicted in Figure 4-38(c) for selected values of deformation, where the adhesive potential is seen to be almost constant-repulsive along the contact regime at the edge of which it with the transition region it reaches a minimum value of -1 (or $-W_o$ in dimensional form) before it drops to zero in the outer region. The minimum value is shifted to the right as deformation increases, which is in accordance with the evolution of the deformed shape and the length of the contact regime.

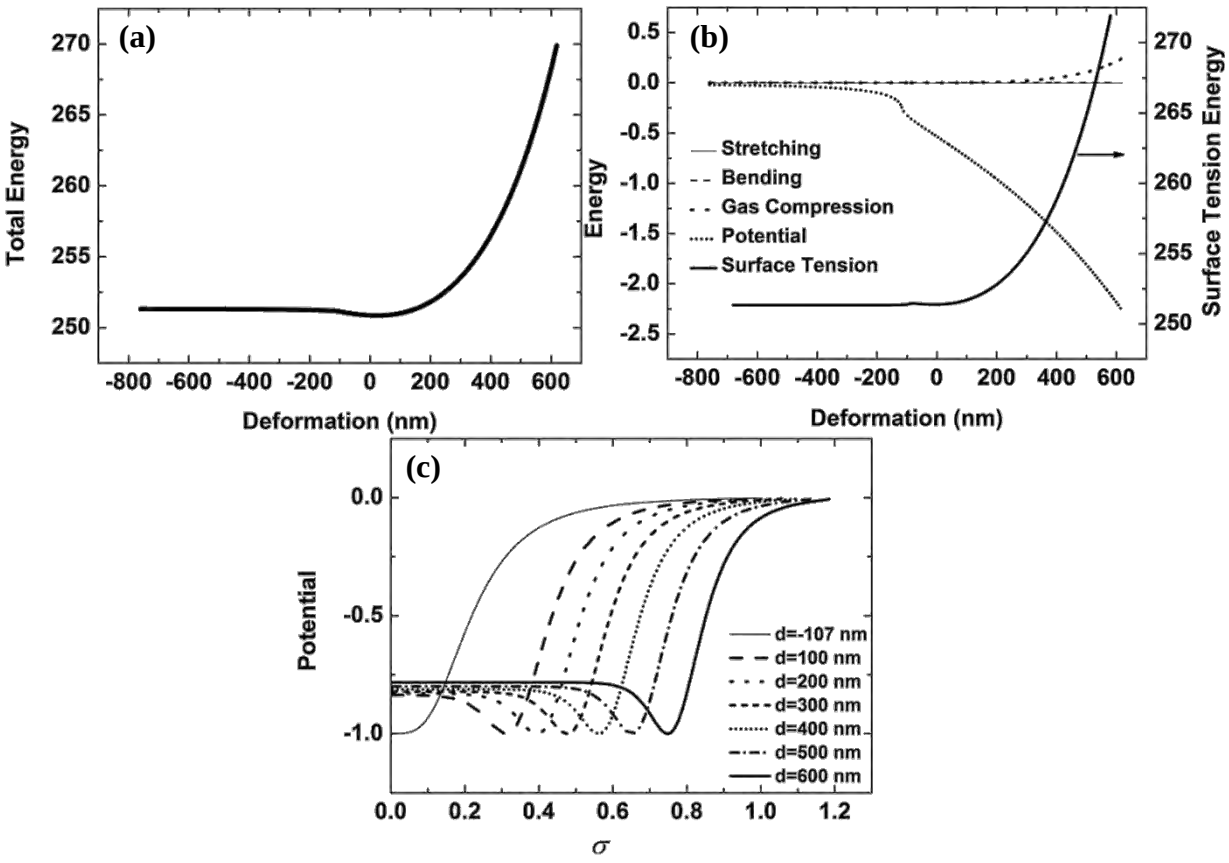

Figure 4-38: Energy diagrams of a free microbubble, **(a)** Total energy as function of the deformation, **(b)** Components of the total energy as function of deformation (surface tension right y axis). **(c)** Distribution of potential function along the distance from the axis of symmetry for selected values of deformation. The dimensionalization of axes is based on paragraph 2.3.2.

Effect of surface tension (γ_{BW})

One more case that is examined here, namely that of a free microbubble, but for higher surface tension, i.e. $\gamma_{BW} = 4\times10^{-2}\ N/m$. In Figure 4-39 the f-d curves for two free microbubbles are compared corresponding to different surface tension, where the case with higher surface tension has a significantly higher slope demonstrating the stabilizing role of surface tension. The shape of the deformed microbubble when $\gamma_{BW} = 4\times10^{-2}\ N/m$ is depicted in Figure 4-40(a) and the distribution of the disjoining pressure in Figure 4-40(b), where in comparison with the $\gamma_{BW} = 4\times10^{-3}\ N/m$ case the disjoining pressure is repulsive and one order of magnitude higher, which means that the film of liquid is considerably compressed since the same parameters of the adhesive potential (W_o, δ_A) are assumed. This argument is also supported by calculating the distribution of the adhesive potential along the shell, Figure 4-40(c). The values of the potential are constant and positive in contact regime, which means that the height of the liquid film is constant and less than δ_A. In addition, the components of total energy, namely gas compression, adhesive potential and surface tension, are depicted in Figure 4-40(d). As before, the dominant contribution is by the surface tension (right y-axis), but the energy due to gas compression also reaches higher values revealing that the internal pressure is significantly larger following the initially larger internal pressure. Overall, when the microbubble is treated as a surface tension interface the contact region offers the dominant contribution to the force that is exerted to the shell by the cantilever, in contrast to the purely elastic case for which the force arises from an almost linear load distribution at the junction between the contact and transition regions. This also explains the difference in the response pattern of the f-d curves being linear and quadratic for the elastic and surface tension dominated cases, respectively.

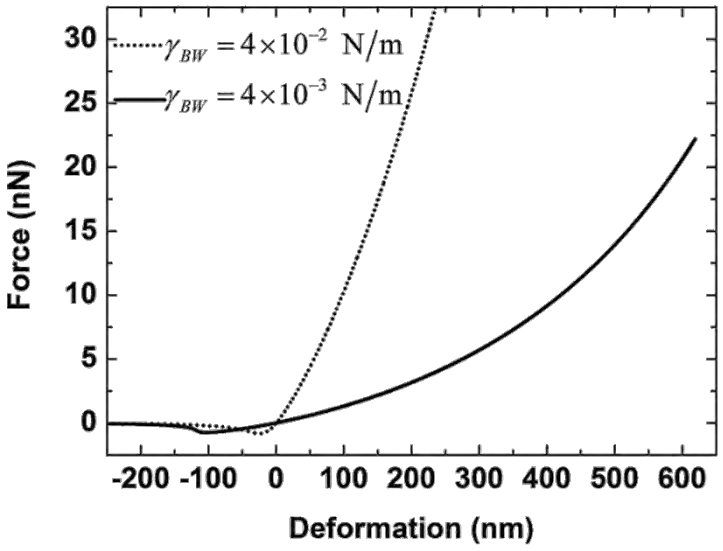

Figure 4-39: Comparison of f-d curves for different values of the surface tension γ_{BW}.

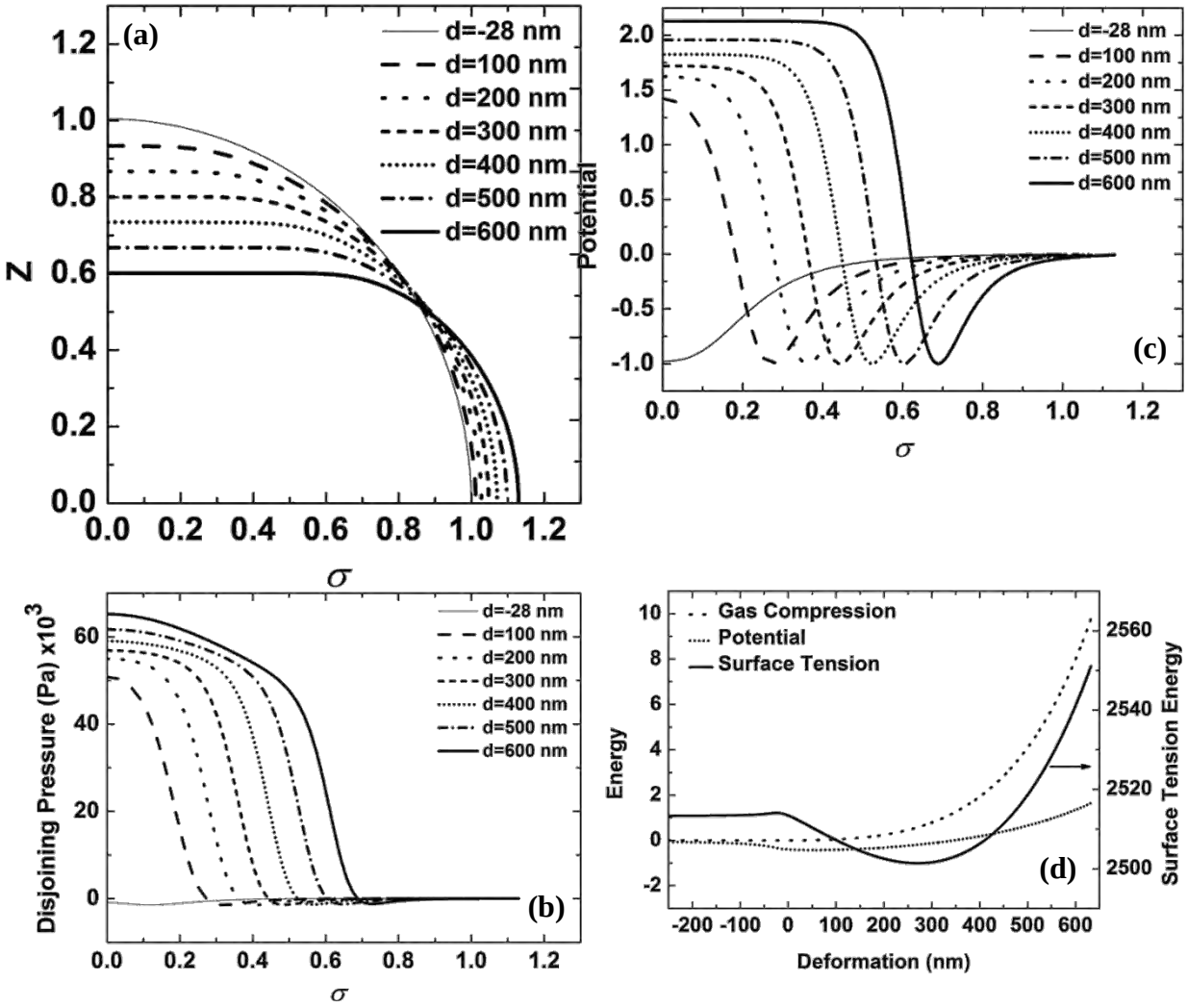

Figure 4-40: (a) Microbubble in deformed configuration for selected values of deformation, (the axes z and σ are dimensionalized with the initial radius R_o), **(b)** Distribution of the disjoining pressure along the distance from the axis of symmetry, **(c)** Distribution of the adhesive potential along the distance from the axis of symmetry, **(d)** Components of the total energy as function of deformation. The dimensionalization of axes is based on paragraph 2.3.2

Effect of the adhesive energy per unit area (W_o-δ_A)

In the following, the effect of adhesive energy is investigated, when the microbubble is assumed to be free of elasticity. Thus, simulations are performed for higher values of characteristic energy W_o, i.e. $W_o = 1\times10^{-3}$ and $3\times10^{-3}\ \mathrm{N/m}$ all of them with $\delta_A = 50\ \mathrm{nm}$. In Figure 4-41 the resulting force-distance curves are illustrated for different values of W_o, where the bold line corresponds to the reference case studied above. Increasing the adhesive energy, the maximum adhesion force increases as in the elastic shell. The deformed shapes and the distribution of the disjoining pressure are depicted in Figure 4-42 for each case. In contrast with the case of $W_o = 1\times10^{-4}\ \mathrm{N/m}$, for relatively large distances for which attractive forces prevail the shapes in Figure 4-42 (a) and (c) are significantly deformed around the pole and, as W_o increases, the shape has a shaper transition from the contact to outer regime. The disjoining pressure shown in Figure 4-42 (b) and (d) is positive in the contact regime for both cases indicating repulsion. It should also be noted that even though the graphs correspond to different values of W_o, the disjoining pressure reaches almost the same positive value (~5000 Pa) in the contact region which means that the liquid film height (y) in the case of $W_o = 1\times10^{-3}\ \mathrm{N/m}$ is lower than the case with the $W_o = 3\times10^{-3}\ \mathrm{N/m}$. This argument can be verified by the leading term of the disjoining pressure when the film is small, which is $\frac{4W_o\delta_A^4}{y^5}$. Thus, if W_o increases, the film height should also increase (not linearly) in order to obtain the same disjoining pressure. Moreover, the disjoining pressure in the transition regime for the $W_o = 3\times10^{-3}\ \mathrm{N/m}$ case reaches a negative pick which is about three times the pick in $W_o = 1\times10^{-3}\ \mathrm{N/m}$ case, indicating that the liquid film in this regime hasn't change, but it is only the W_o parameter that changes the amplitude of pressure. It should be noted however, that the form of the f-d curve changes significantly as the interaction potential increases. In particular two limit points appear as the region of repulsive forces is approached via simple continuation. Consequently, implementation of arc length continuation is required in order to properly follow the f-d curve from the regime of attraction to that of repulsion.

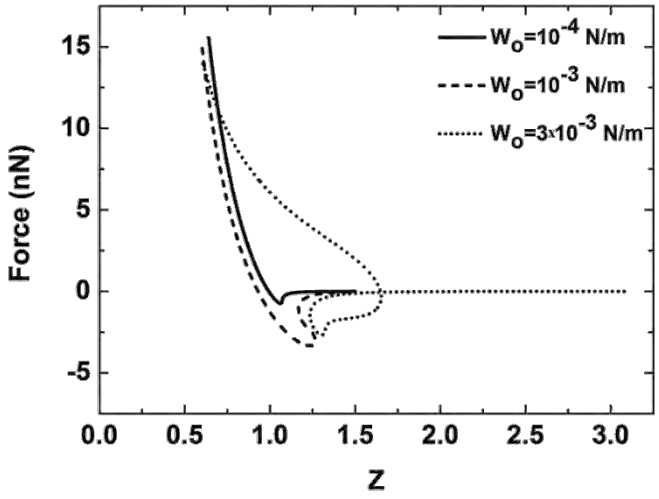

Figure 4-41: Comparison of force-distance curves for different values of W_o.

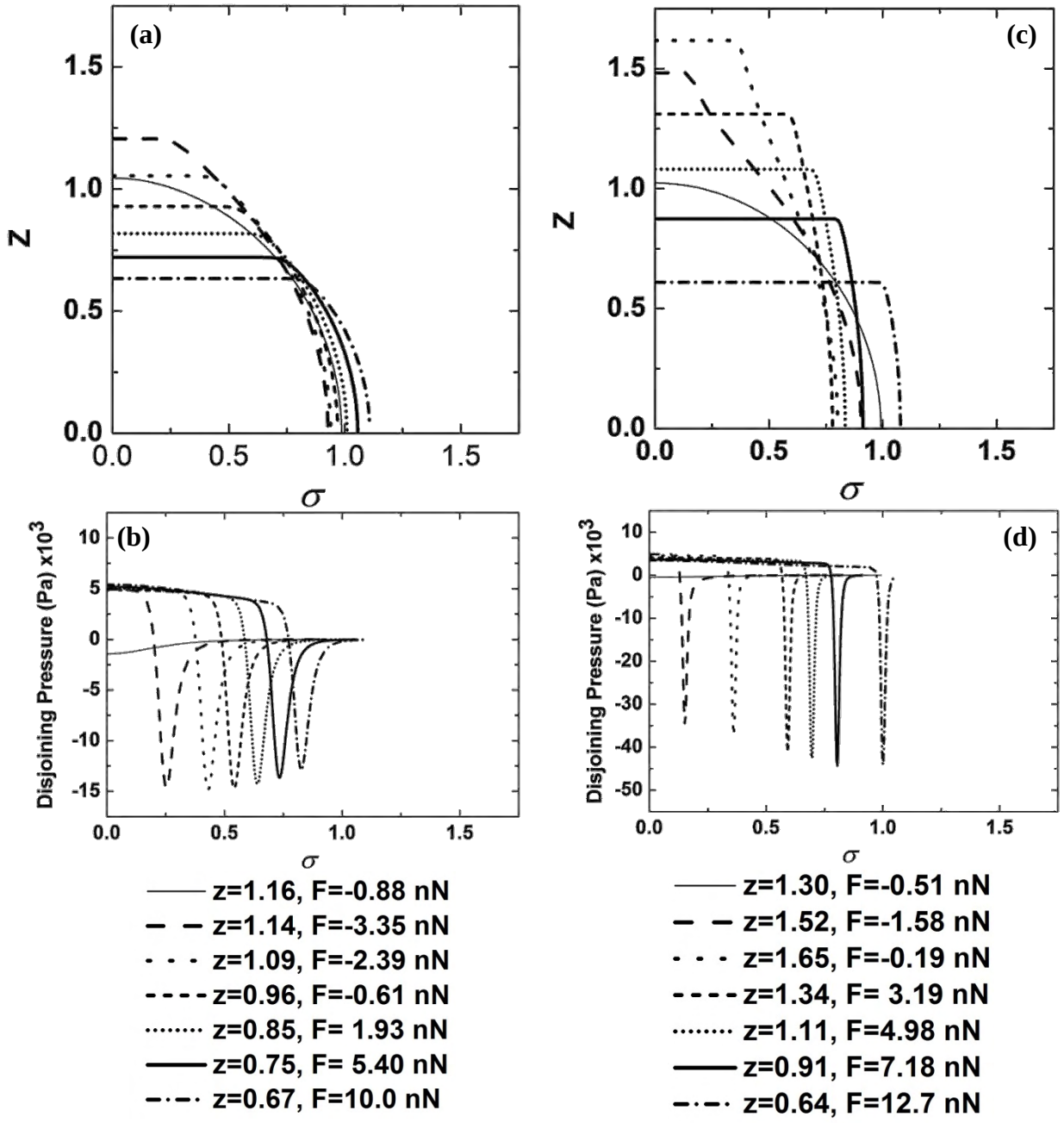

Figure 4-42: (a) Shape and **(b)** Distribution of the disjoining pressure for the case of $W_o=1\times10^{-3}$ N/m, **(c)** Shape and **(d)** Distribution of the disjoining pressure for the case of $W_o=3\times10^{-3}$ N/m.

In addition, the chosen values of W_o are less than the surface tension, which is $\gamma_{BW}=4\times10^{-3}$ N/m in all cases studied above. However, calculations with equal or even higher values than surface tension, i.e $W_o \geq 4\times10^{-3}$ N/m fail to converge as it was expected, since for such shells the following equation $\frac{W_o}{\gamma_{BW}}+1=\cos\theta_W$ holds [62, 63], where θ_W is the wetting angle and then for $W_o \geq 4\times10^{-3}$ N/m an unrealistic $\cos\theta_W$ is calculated.

As mentioned above, the adhesive energy per unit area depends also on the characteristic length δ_A. In the next, the effect of δ_A is investigated for the case of the free microbubble.

Thus, numerical calculations for $\delta_A = 10, 50 \text{ and } 100$ nm with $W_o = 1 \times 10^{-4}$ N/m are performed. Figure 4-43(a) illustrates the corresponding f-d curves for the above cases and Figure 4-43(b) focuses on the regime of the highest adhesive force. As in the pure elastic case, changing the parameter δ_A the f-d curves do not change significantly, but the response on the adhesive force regime becomes sharper as δ_A decreases. In addition, in Figure 4-44 the deformed shape and the distribution of the disjoining pressure are depicted for the two new cases investigated here. The disjoining pressure reaches higher values as δ_A decreases in the transition regime, see also Figure 4-44(c).

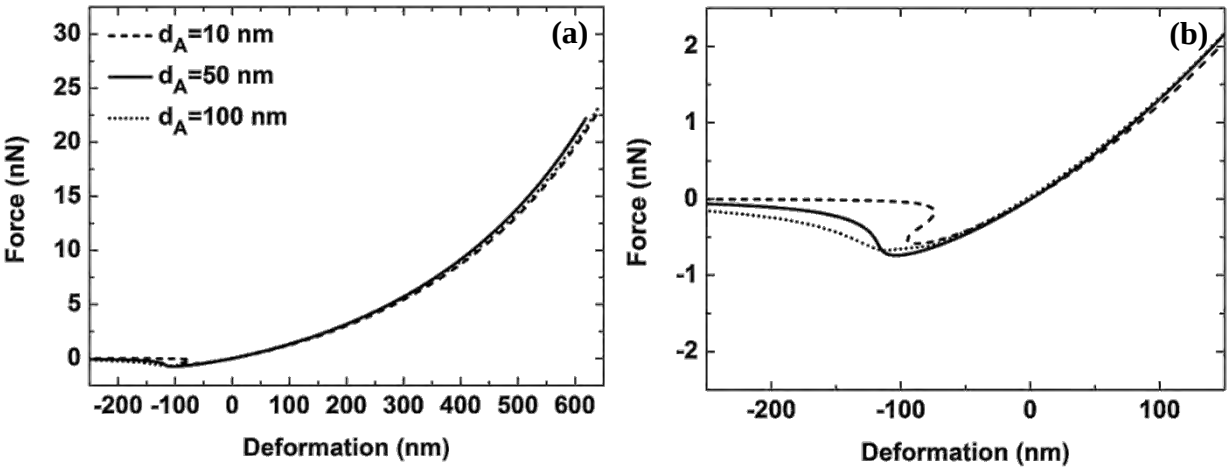

Figure 4-43: (a) Comparison of f-d curves for different values of δ_A. **(b)** Focus on the maximum adhesion area in f-d curve.

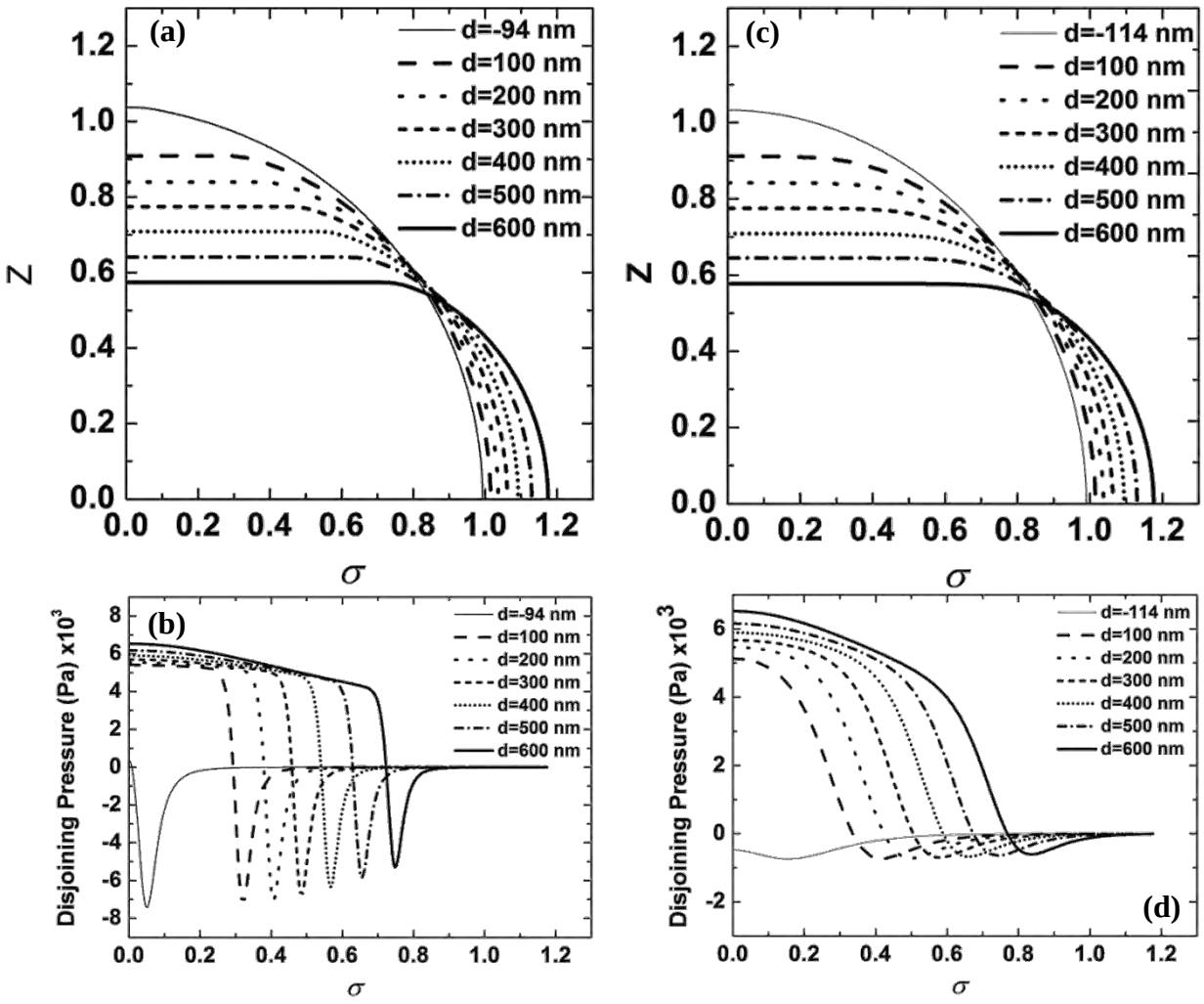

Figure 4-44: Shape and distribution of disjoining pressure with **(a)**, **(b)** δ_A=10 nm and **(c)**, **(d)** δ_A=100 nm.

Chapter 5. Numerical results: Bifurcation diagrams

In this chapter simulations are performed employing the formulation of paragraph 2.4 in order to investigate the static response of coated microbubbles subject to a uniform-normal load. As the overpressure, ε, increases the relative volume $\tilde{V} = V / V_0$ *decreases and the shape remains spherical, which is a stable solution, until the overpressure reaches the buckling threshold. At that point a bifurcation occurs that gives rise to the buckling solution, which is characterized by symmetric or asymmetric shapes with respect to the equator. Upon further increase of the external overpressure additional bifurcations occur. The sequence is a strong function of the parameters that determine the nature of the shell. An extensive parametric analysis is carried out in order to investigate the effect of different parameters on the bifurcation diagrams with emphasis placed on the dimensionless bending modulus* $\hat{k}_b = k_b / (\chi R_0^2) = \left[1/12/(1-\nu^2)\right]\left(h/R_0\right)^2$ *that monitors the relative rigidity between the bending and stretching resistances of the shell, and dimensionless pressure* $\hat{P}_A = P_A R_0 / \chi$ *that controls the relative importance of gas compressibility on the rigidity of the shell. The response of microbubbles covered with polymeric shells is studied in the first part, while the case of the softer coatings, lipids, is tackled in the second part of the chapter. Microbubbles coated with shells of the former type are characterized by smaller values of the above dimensionless parameters, primarily so for the dimensionless pressure due to the increased stiffness of the shell. In both cases the bifurcation diagram exhibits a local stability pattern in the vicinity of the primary bifurcations and a global pattern pertaining to the minimum energy among the possible stable configurations. The latter is expected to determine the static configuration during a dynamic simulation when sufficiently strong disturbances exist.*

As the area dilatation modulus increases the nature of the primary bifurcation varies depending on the degree of strain that can be tolerated by the shell. For large $\hat{k}_b$ *values the primary bifurcation evolves transcritically exhibiting oblate and prolate shapes with the latter inheriting the stability of the original spherosymmetric configuration. As the area dilatation increases the primary bifurcation is asymmetric and is linearly unstable. The shell exhibits a dimple in the region around the two poles where compressive strain is relaxed in favor of bending. As* $\hat{k}_b$ *further decreases symmetric shapes emerge as the primary bifurcation that again evolves transcritically. The supercritical part is linearly stable for a short range of external loads and is characterized by nearly prolate shapes. The subcritical part is also symmetric with shapes that exhibit one dimple at each pole in order to alleviate the extra energy generated due to the compressive stresses. This pattern holds for both types of shells. Furthermore, as the subcritical branches, symmetric or asymmetric, evolve towards smaller*

external overpressures they form a limit point and turn towards larger overpressures and larger volume compressions. The latter shapes tend to generate contact in the region around the two poles. In fact, those stemming from the primary bifurcation become linearly stable with minimum energy among possible solutions for the same parameters and determine static configuration in a dynamic response pattern. The post buckling shapes of polymers are characterized by big Legendre modes (P_{10}-P_{11}), while those of lipids by small ones (P_2-P_3). Furthermore, in the case of polymeric shells the bifurcation diagram before the formation of the limit point is nearly flat reflecting the negligible resistance to volume compression. As the latter increases the slope of the branch becomes larger and negative. This behavior may explain the tendency of polymeric shells to exhibit shapes with contact when perturbed above or below the primary bifurcation point; as such shapes constitute the absolute energy minimum. On the contrary lipid shells tend to achieve a static configuration with a certain amount of volume compression before full contact takes place and this reflects in their response during acoustic disturbances where compression only behavior is detected.

Considering the polymeric shells as Skalak elastic membranes causes an exchange in the order of appearance of post-buckling solution families, with the primary bifurcation characterized by symmetric shapes. On the other hand, when lipid coatings are treated with Hook's law the symmetric solution family that emerges at the primary bifurcation point evolves only subcritically exhibiting prolate shapes. Gas compression does not affect the response of polymer coatings for which, in contrast to the case with phospholipid shells, when the inner gas is treated as incompressible the limit point in the subcritical solution family disappears. Significantly compressed shapes appear in this case for marginally larger external overpressures. Finally, the parametric analysis for both types of coating shows that surface tension tends to increase the critical buckling load, while the order of appearance of the symmetric and asymmetric solution families remains unaffected.

5.1 Bifurcation diagrams of polymeric microbubbles

5.1.1 Study of a single microbubble

Based on the methodology developed in paragraph 2.4, an extensive numerical investigation was carried out of the static response of polymeric and phospholipid shells subject to external uniform load. These two types of shells are distinguished by the fact that the former are much stiffer in terms of both stretching and bending elasticities [13, 29, 30]. Furthermore, they are mostly characterized by Hooke's law [13, 16], whereas phospholipid shells are strain softening for relatively large deformations [85, 86]. In the present study, the response of both types of shells subject to a uniform external overpressure is studied while using elastic properties that are available from the literature. In the former case, Bisphere is used as the contrast agent coated by a polymeric shell with dimensionless parameters that govern the microbubble's mechanical response that are $\hat{k}_b \approx 10^{-4} - 10^{-5}$ and $\hat{P}_A \approx 10^{-3}$. On the other hand, microbubbles covered with phospholipid have smaller values for stretching and bending stiffness, as it already described in the previous chapter, with dimensionless numbers $\hat{k}_b \approx 10^{-3}$ and $\hat{P}_A \approx 10^{0}$. Thus, their static response subject to a uniform pressure is investigated separately in the rest of the present chapter. Initially, the response of a microbubble covered with polymer is investigated with indicative elastic constants presented in Table 5-1 and correspond to a shell that was also investigated by Tsiglifis & Pelekasis [86] and Marmottant et al. [16]. As described in the previous chapter, the fundamental properties for polymeric coatings are the Young modulus and the shell thickness, where the bending resistance is an elastic parameter which depends on the shell rigidity and thickness, see eq. (2-22). Hence, $k_b = 3.61\times10^{-16}$ Nm and $\chi = 6.1\,\mathrm{N/m}$, or more appropriately G_s=88 MPa and h=23.1 nm, correspond to dimensionless parameters: $\hat{k}_b = \dfrac{k_b}{\chi R_o^2} = \dfrac{1}{12\left(1-\nu^2\right)}\left(\dfrac{h}{R_0}\right)^2 = 5.9\times10^{-5}$ and $\hat{P}_A = \dfrac{P_A R_o}{\chi} = 1.66\times10^{-2}$. In view of the negligible resistance to compression of polymeric shells, in comparison with the area dilatation modulus, parameter $\hat{P}_A$ remains small throughout this section and the effect of bending to stretching resistance ratio, $\hat{k}_b$, is monitored by varying the shell thickness h for fixed shell radius R_0 and Poisson ratio ν; see also Table 5-1 below.

Then a spherical and stress-free microbubble is considered with a uniform and known overpressure ΔP applied along the shell surface, $\Delta\vec{P} = -\Delta P\vec{n}$, where $\vec{n}$ is the normal vector, pointing outwards from the shell surface. Employing the formulation of paragraph 2.4 a solution is sought regarding the deformed shape and the internal pressure. Starting from a small value of ΔP the resulting shape is compressed, but remains spherical throughout its surface. A sequel of solutions can be obtained by performing simple continuation by treating ΔP as the operating parameter. Then, the solution can be represented in a relevant pressure-volume diagram, Figure 5-1(a). As the overpressure increases, the volume is reduced and the

Shell thickness	$h = 23.1\,\text{nm}$	Shear modulus	$G_s = 88\,\text{MPa}$	
Initial radius:	$R_o = 1.0\,\mu\text{m}$	Poisson ratio:	$\nu = 0.5$	
Constitutive law:	Hook	Pre-stress:	$u = 0\,\mu\text{m}$	
Surface tension:	$\gamma_{BW} = 0\ \text{N/m}$	Polytropic index:	$\gamma = 1.07$	400 elements

Table 5-1: Simulation parameters for the bifurcation diagram of a microbubble covered with polymer.

shape is progressively compressed with a smaller radius, Figure 5-2 (a). Calculating the eigenvalues of the jacobian matrix by employing the dgeev Lapack routine, for the spherical solutions it is found that they are characterized by one negative eigenvalue, which is associated with the imposition of the bubble center of mass at the origin of the axes. It should be stressed that this unstable eigenvalue of the spherosymmetric configuration reflects the translational invariance of the system, it is always present in the eigenvalue spectrum of all the solution families, and does not determine the stability of the calculated static configurations.

The critical external overpressure is almost identical with the prediction of linear theory, $\Delta P_{cr} \approx 0.1878 MPa$ or $\varepsilon_{cr}^{Th} = 1.853$, while the critical load calculated by FEM is $\varepsilon_{cr}^{N} = 1.878$. The dominant eigenmode is the 11$^{\text{th}}$ Legendre mode, P_{11}, as can be verified by performing Fourier analysis [17, 38] of the numerically calculated dominant eigenvector at the bifurcation point, Figure 5-1(b). The emerging solution branch evolves subcritically, it is identified by two negative eigenvalues, and is characterized by shapes that exhibit a progressively more pronounced dimple, Figure 5-2(b). Further increase of the external overpressure reveals another bifurcating branch evolving from the main spherosymmetric solution family, that is characterized by a third unstable eigenvalue and whose eigenvector is characterized by an even Legendre mode, P_{10}; corresponding shapes are depicted in Figure 5-2 (b). This indicates the onset of a symmetric solution branch that emerges transcritically with three and two unstable eigenvalues below and beyond the bifurcation point, respectively, Figure 5-1(b). Both asymmetric and subcritical symmetric branches exhibit a limit point, where each of them loses a negative eigenvalue. The limit points are found in $\left(\varepsilon = 0.309, \tilde{V} = 0.968\right)$ for the asymmetric solution and in $\left(\varepsilon = 0.350, \tilde{V} = 0.941\right)$ for the subcritical symmetric. Subsequently, after the limit point they have one and two negative eigenvalues, respectively, Figure 5-1(c). The supercritical symmetric branch keeps the two negative eigenvalues for $\varepsilon \le 1.904$ and then a limit point appears that leads to a multibranch solution, see Figure 5-1(c), and its shape is characterized by multiple lobes, Figure 5-2(d). In addition, as the asymmetric solution is evolved the north pole of the shell approaches the origin of the z-axis and when the pole crosses the origin, the boundary condition $\theta = 0$ is not anymore true. Rather, condition $\theta = \pi$ should be used in both poles. Thus, the choice of a spherical coordinate system complicates the spline representation and the convergence is harder. Therefore for $\varepsilon > 1.14$ the Lagrangian markers are represented in a relevant cylindrical coordinate system (σ,z) with boundary conditions σ=0 in both poles, which can be handled more easily by the FEM and hence it is possible to reach an asymmetric configuration, where the two poles tend to coalesce, F shape in Figure 5-2(b). In the symmetric solution, such a difficulty is not faced and thus the solution is always represented in the original spherical coordinated system. Moreover, in both solutions

the position of the mass center is always at the origin of the axes in order to avoid the rigid body motion.

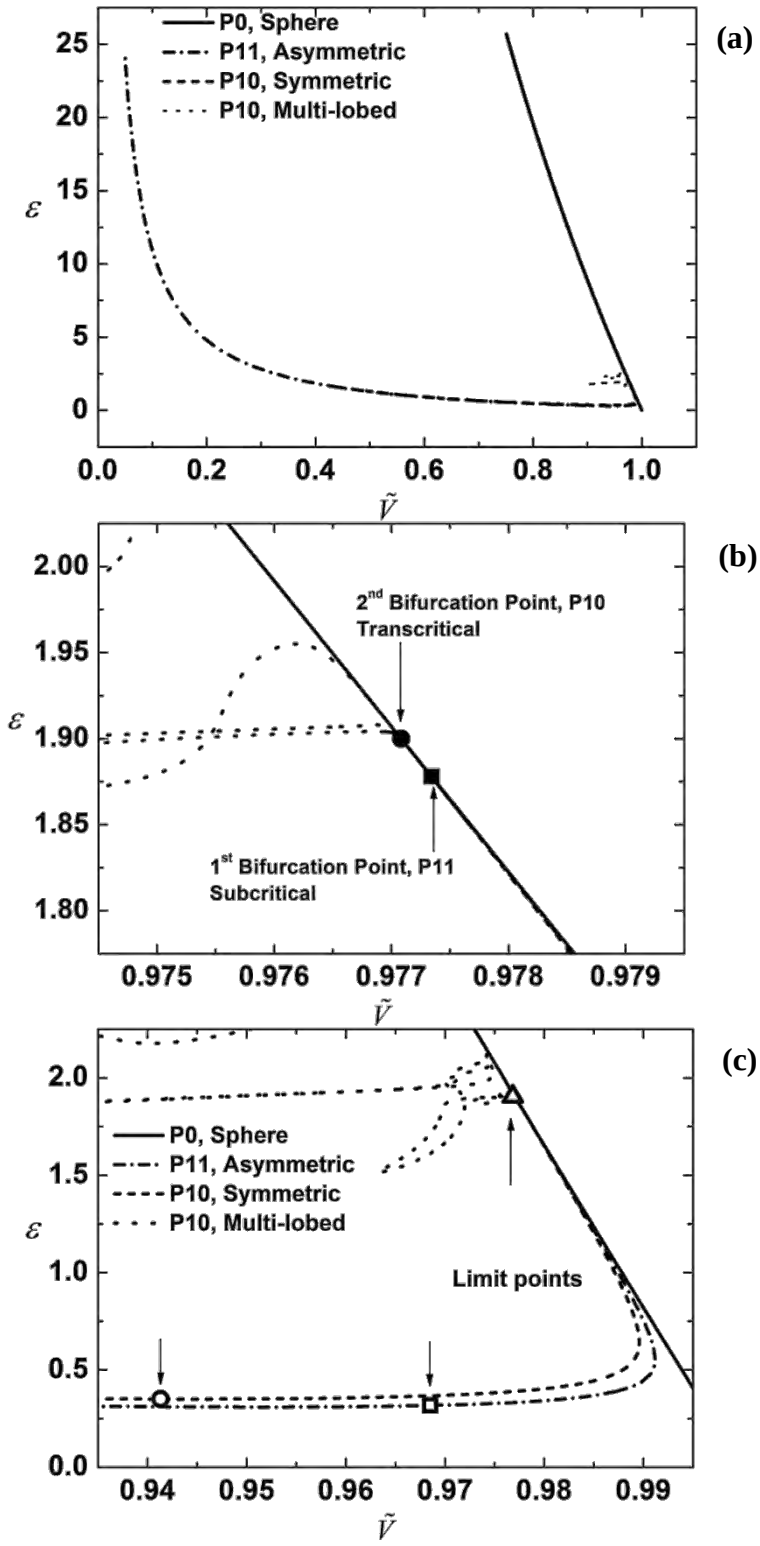

Figure 5-1: Bifurcation diagram for a microbubble with h=23.1 nm and G_s=88 MPa, **(a)** External overpressure as function of the volume, **(b)** Zoom in the bifurcation points and **(c)** Zoom in the area of limit points (circle, square and triangle). (χ=6.1 N/m, $k_b = 3.61\times10^{-16}$ Nm and $\hat{k}_b = 5.9\times10^{-5}$, $\hat{P}_A = 1.66\times10^{-2}$).

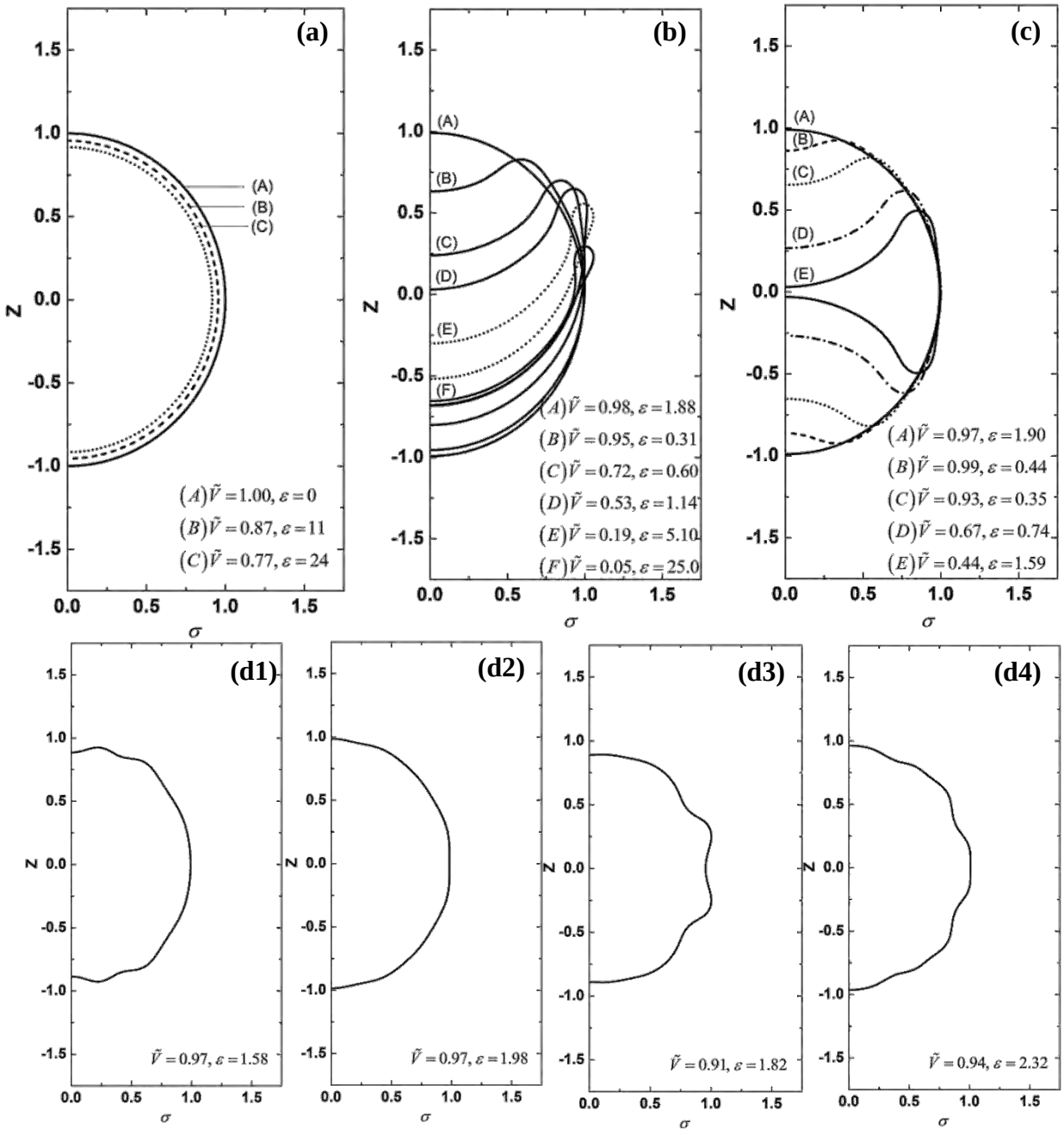

Figure 5-2: Microbubble in deformed configuration: **(a)** Spherical, **(b)** Asymmetric, **(c)** Symmetric and **(d1-4)** Multi-lobed solutions. The axes are dimensionalized with the initial radius R_o. (h=23.1 nm, G_s=88 MPa, χ=6.1 N/m, $k_b = 3.61\times10^{-16}$ Nm and $\hat{k}_b = 5.9\times10^{-5}$, $\hat{P}_A = 1.66\times10^{-2}$).

Figure 5-3(a) illustrates the evolution of the total energy pertaining to each one of the solution branches verifying the above assertion. In particular, both asymmetric and symmetric solutions have higher energy than the spherical shape as they evolve subcritically from the bifurcation point. However, after forming a limit point the number of unstable eigenvalues is reduced by one. In particular, the asymmetric branch becomes linearly stable and has lower energy than the spherical solution after $\left(\varepsilon = 0.341, \tilde{V} = 0.8977\right)$, Figure 5-3(b) and similarly the symmetric after $\left(\varepsilon = 0.389, \tilde{V} = 0.879\right)$, Figure 5-3(c). The corresponding shapes in this

part of the asymmetric solution branch exhibit progressively larger portions around the two poles where contact starts developing. The symmetric solution family that evolves supercritically eventually develops multiple lobes and its energy does not have a monotonic behavior as the pressure changes. It exhibits regions in the parameter space with either higher or lower total energy in comparison with the spherical solution, Figure 5-3 (d). In the regime with the multi-lobed shapes it is unstable with higher energy content. In the immediate supercritical regime it is linearly stable with shapes that are nearly prolate. Its energy content is lower than that of the spherosymmetric family but is higher than the one pertaining to the asymmetric solution family with contact, which constitutes an absolute minimum among the different solutions in this parameter range both above and below the critical bifurcation point. This pattern is corroborated by dynamic simulations of coated microbubbles [19] with the finite element methodology that leads to a static configuration that is characterized by such shapes both above and below the primary bifurcation point.

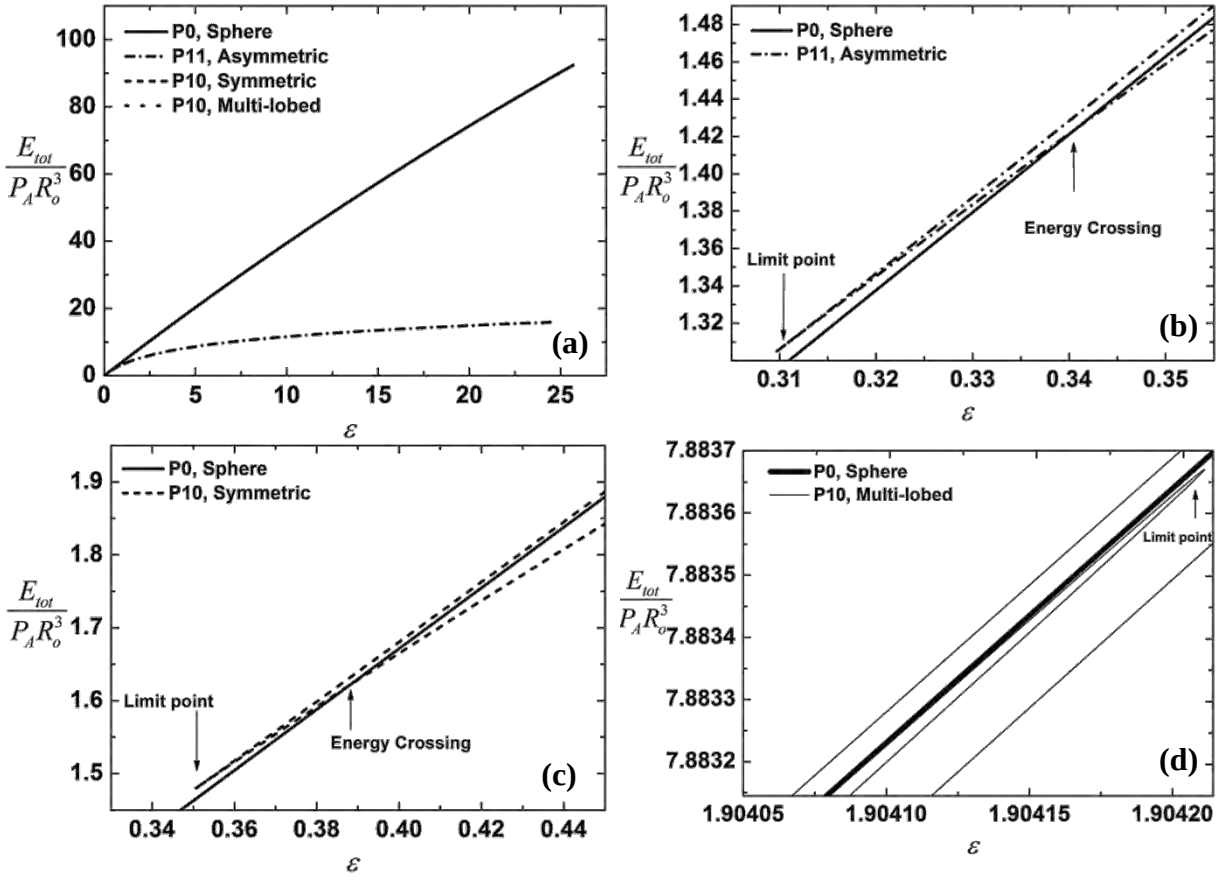

Figure 5-3: **(a)** Bifurcation diagram in terms of total energy for a microbubble with h=23.1 nm and G_s=88 MPa, **(b)**, **(c)** and **(d)** Zoom-in the bifurcation area of symmetric/asymmetric and the multi-lobed branches, respectively. The multilobed branch exhibits significant variation in the immediate vicinity of the main spherical branch. In (b) and (c) the curves with energy higher than sphere evolve from their bifurcation point and curves with lower energy evolve towards pole coalescence. (χ=6.1 N/m, $k_b = 3.61\times10^{-16}\,Nm$ and $\hat{k}_b = 5.9\times10^{-5}$, $\hat{P}_A = 1.66\times10^{-2}$).

Figure 5-4 depicts the distribution of the in plane and shear tension, along with bending moments as function of the Lagragian variable ξ for the spherical solution branch, where it is reminded that ξ=0 and 1 correspond to the north and south poles of the shell, respectively. In the spherical shells, which have a progressively smaller radius than the initial stress-free shell, only in plane compressive stresses are developed, as the spherical shell has no curvature variations along its surface. On the other hand, the in plane τ_{ss} tensions are tensile in the dimple of the asymmetric shapes, with a maximum compressive value at the end of the dimple, Figure 5-5(a). In the rest of the shell the τ_{ss} are compressive. The value of the maximum compressive tension follows the position of the dimple, as can be seen by comparing with the deformed shape, Figure 5-2(b). In addition, the tensile tensions are almost of the same magnitude with the compressive. The in plane $\tau_{\varphi\varphi}$ tensions are concentrated around the dimple area, while in the rest of the shell vanish, Figure 5-5(b). Similar is the behavior of the shear stress q, as it was expected, which follows the variations of the curvature, Figure 5-5(c). The bending moments are negative and constant in the inner part of the dimple, indicating mirror buckling (reversed sphere), positive around the dimple, where the curvature is higher than the one, as in Figure 4-14, and in the rest of the shell vanish, Figure 5-5(d) and (e). The tensions and moments for the symmetric solutions (P_{10}) are the same as in the asymmetric ones, while their distribution is symmetric with respect to the equatorial plane, ξ=0.5, Figure 5-6. Similarly, the calculation of tensions and moments is symmetric with respect to ξ=0.5 for the solutions with multiple lobes, but with more picks due to the larger number of areas with high curvature and length variations, Figure 5-7.

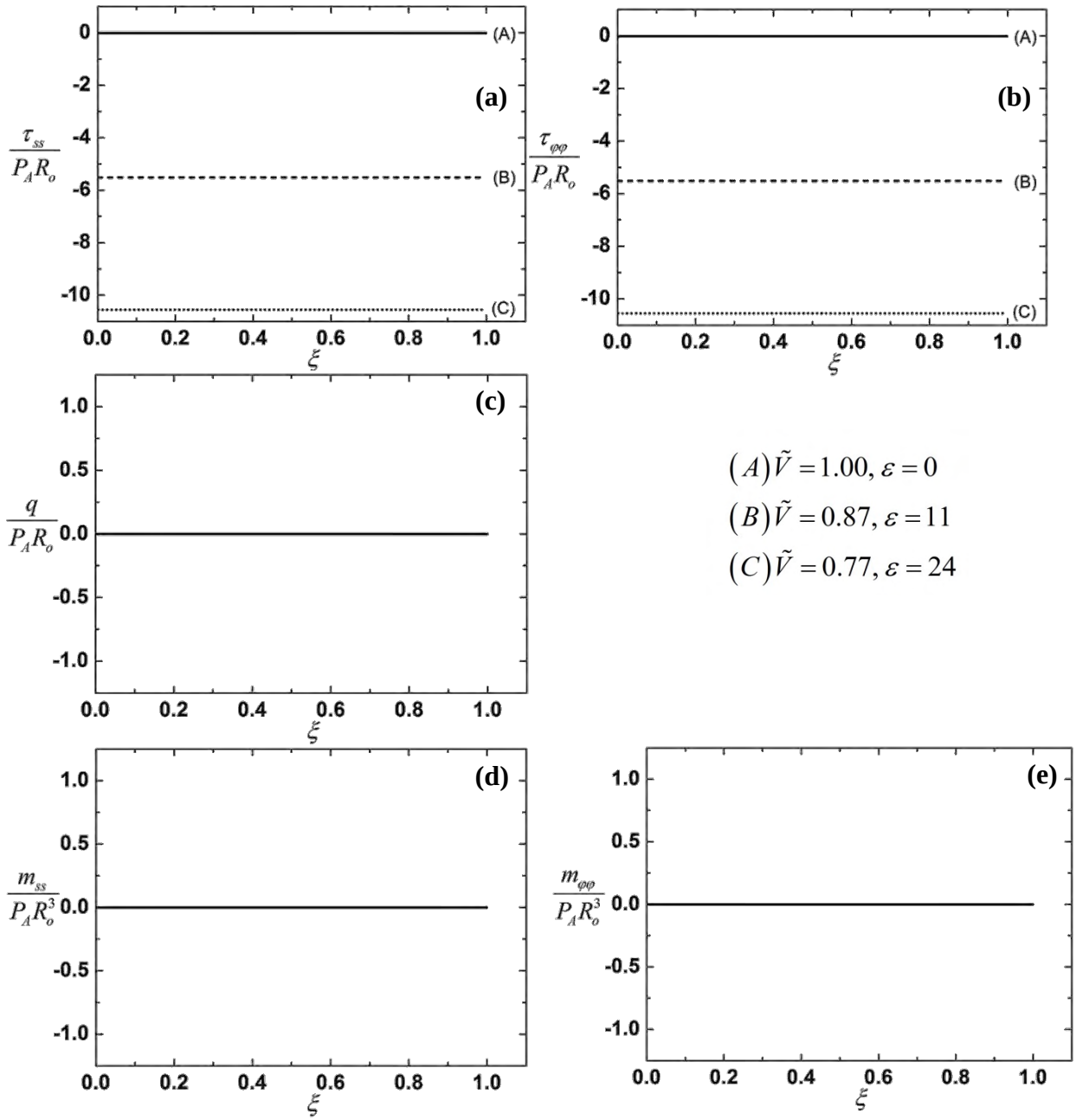

Figure 5-4: Distribution of the in plane tensions **(a)** τ_{ss} and **(b)** $\tau_{\varphi\varphi}$, **(c)** shear tension q and bending moments **(d)** m_{ss} and **(e)** $m_{\varphi\varphi}$ as function of the Lagrangian variable ξ for the *spherical* branch.

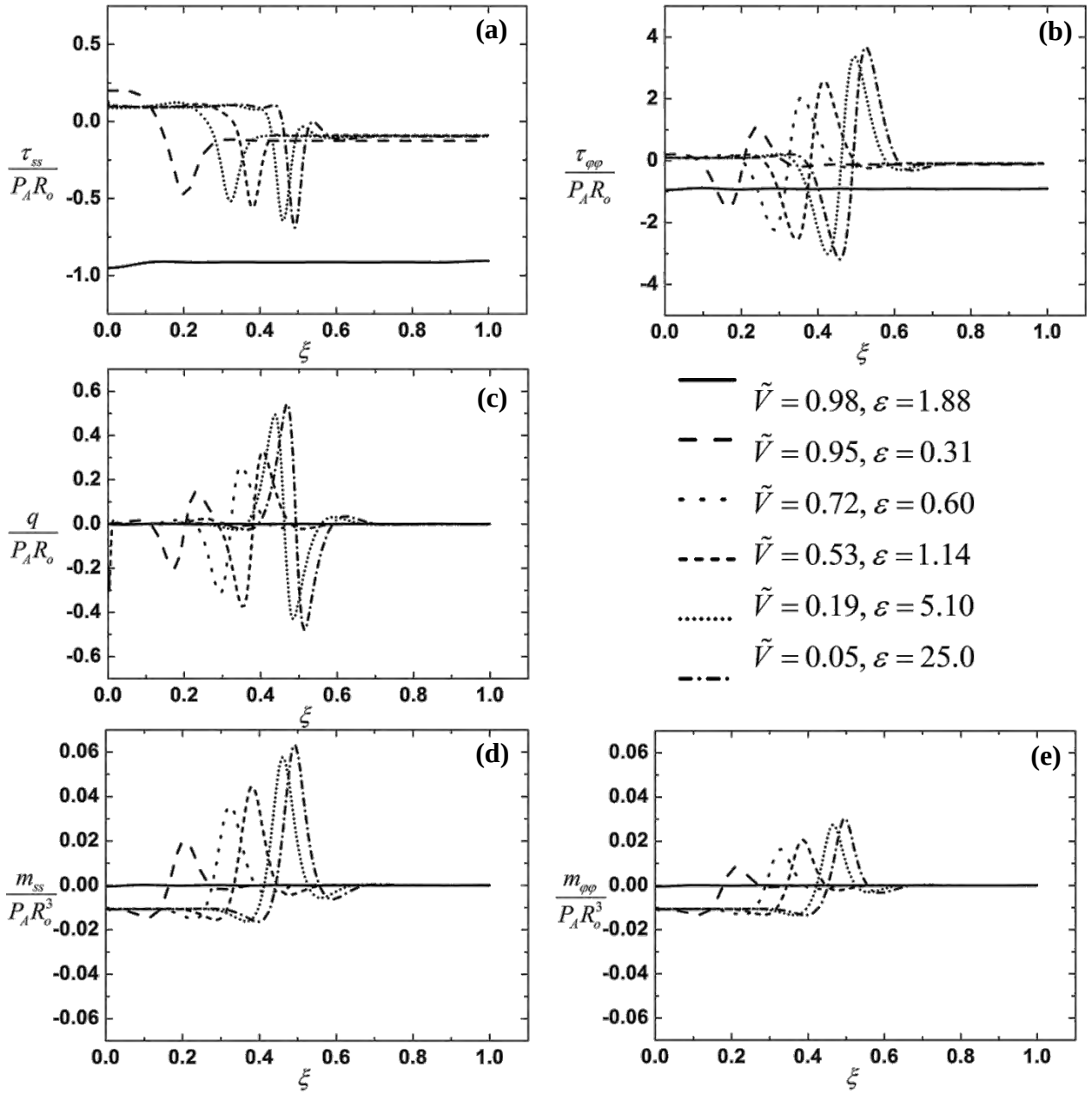

Figure 5-5: Distribution of the in plane tensions **(a)** τ_{ss} and **(b)** $\tau_{\varphi\varphi}$, **(c)** shear tension q and bending moments **(d)** m_{ss} and **(e)** $m_{\varphi\varphi}$ as function of the Lagrangian variable ξ for the *asymmetric* branch.

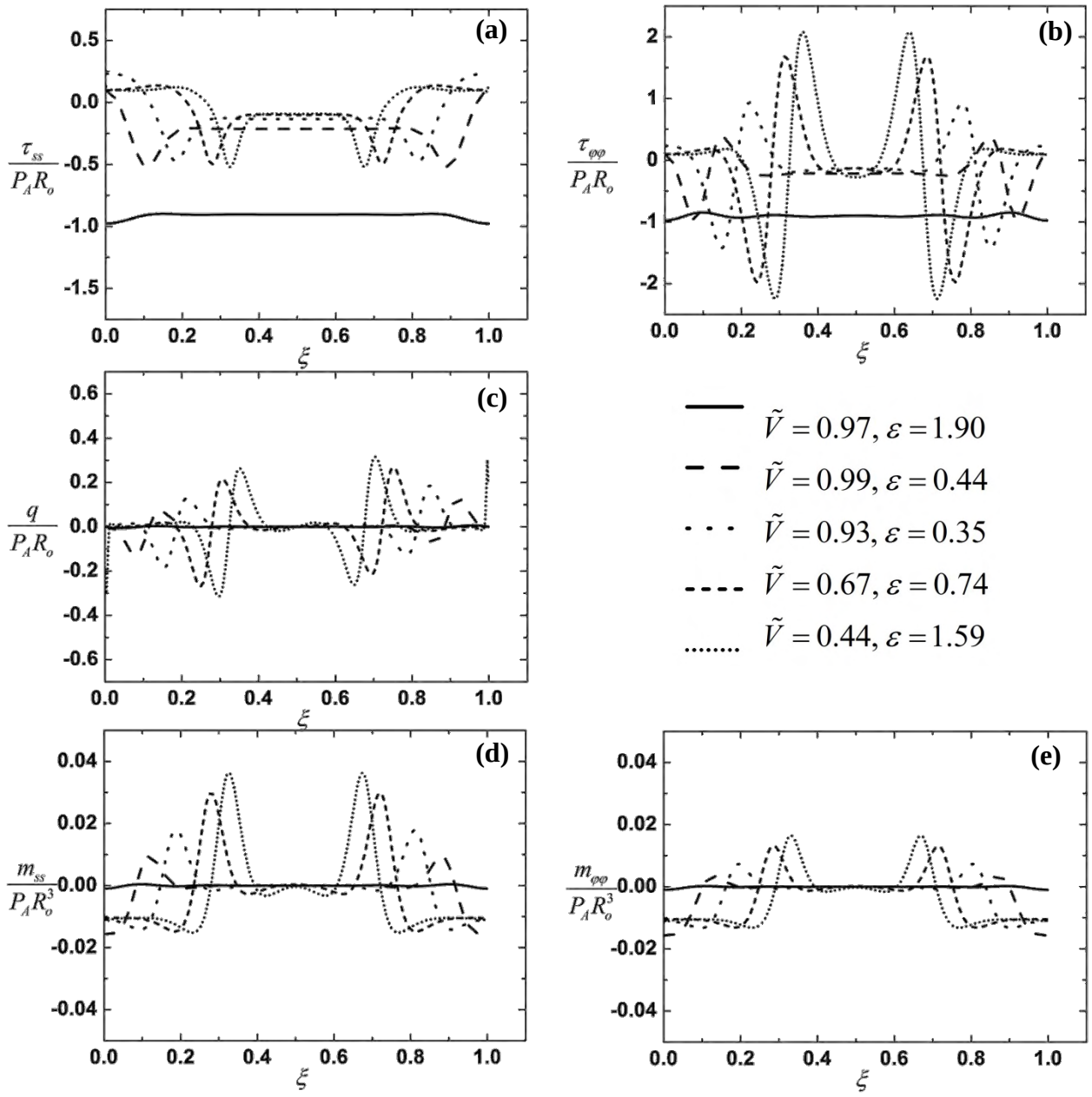

Figure 5-6: Distribution of the in plane tensions **(a)** τ_{ss} and **(b)** $\tau_{\varphi\varphi}$, **(c)** shear tension q and bending moments **(d)** m_{ss} and **(e)** $m_{\varphi\varphi}$ as function of the Lagrangian variable ξ for the *symmetric* branch.

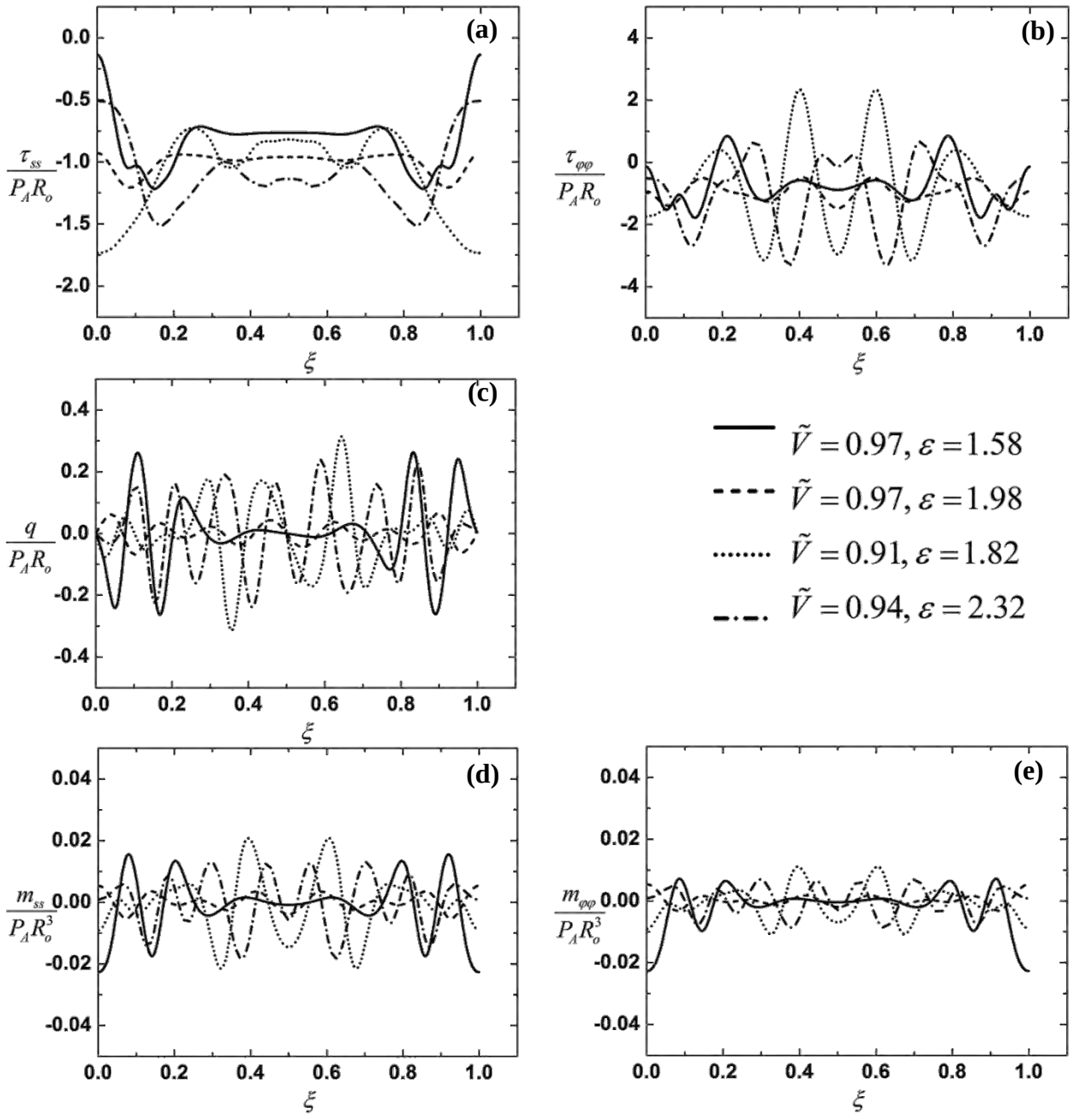

Figure 5-7: Distribution of the in plane tensions **(a)** τ_{ss} and **(b)** $\tau_{\varphi\varphi}$, **(c)** shear tension q and bending moments **(d)** m_{ss} and **(e)** $m_{\varphi\varphi}$ as function of the Lagrangian variable ξ for the *multiple lobes* branch.

5.1.2 Parametric study

In the following session a parametric study is carried out in order to investigate the effect of different parameters that are involved in the shell equilibrium, namely stretching and bending rigidity, constitutive law, surface tension and gas compressibility. In addition, the case investigated in subsection 5.1.1 will be used as the reference case.

Effect of elasticity moduli (stretching-χ & bending k_b)

Next, parametric analysis is performed in order to investigate the effect of the dimensionless bending modulus on the bifurcation diagram. Here the shell thickness is higher in comparison with the case investigated above, which probably is not a realistic value for polymeric coatings, which usually have thickness in the range of 10-50 nm [27, 29], however for the purpose of the present study, the simulation parameters are the same as in Table 5-1, but for h=115.5 nm. The corresponding dimensionless numbers are $\hat{k}_b = 1.48\times10^{-3}$ and $\hat{P}_A = 3\times10^{-3}$. It should be noted that changing the shell thickness both dimensionless parameters change, however, as mentioned above, the response is mainly controlled by the elasticity terms as long as $\hat{P}_A \ll 1$. Therefore, the stiffness due to gas compression does not affect the response and could be treated as the same with the case investigated in paragraph 5.1.1. As can be gleaned from Figure 5-8(a) in this case the bifurcation diagram is modified in comparison with Figure 5-1(a) in the sense that the symmetric solution branch (P_4) emerges transcritically as the primary instability of the basic spherical configuration, $\left(\varepsilon = 47, \tilde{V} = 0.8936\right)$ with two negative eigenvalues for the branch that evolves towards overpressures that lie below the critical buckling threshold (dashed line) and one negative eigenvalue for the branch that evolves towards larger overpressures (dot line), Figure 5-8(b). The former branch soon exhibits a new bifurcation point $\left(\varepsilon = 46, \tilde{V} = 0.8956\right)$ leading to an asymmetric shape, Figure 5-8(c). As the same symmetric branch further evolves, in contrast with the case investigated in 5.1.1, it maintains three negative eigenvalues and does not exhibit any limit points. This effect is attributed to the lower value of the gas compression rigidity of the present case that facilitates volume reduction without significant additional external overpressure. A similar behavior was previously presented by Lytra & Pelekasis [87] on the bifurcation diagrams with simulation parameters for a bisphere microbubble $\left(\hat{k}_b = 2.5\times10^{-5} \,\&\, \hat{P}_A = 2\times10^{-3}\right)$, where the primary instability is dominated by the P_{14} Legendre eigenmode. The primary bifurcation generates a symmetric solution family that evolves towards smaller overpressures and gives rise to a new bifurcation characterized by the P_{13} mode. The symmetric branch that evolves towards higher external overpressures exhibits only one negative eigenvalue, the one corresponding to pure translation, thus inheriting the stability of the spherosymmetric branch. It exhibits shapes that are slightly prolate, before the onset of a bifurcation point that destabilizes it eventually leading to a limit point that generates a branch with three negative eigenvalues and shapes characterized by a protrusion around the equator. The branch generated by the secondary bifurcation mentioned above was not pursued further.

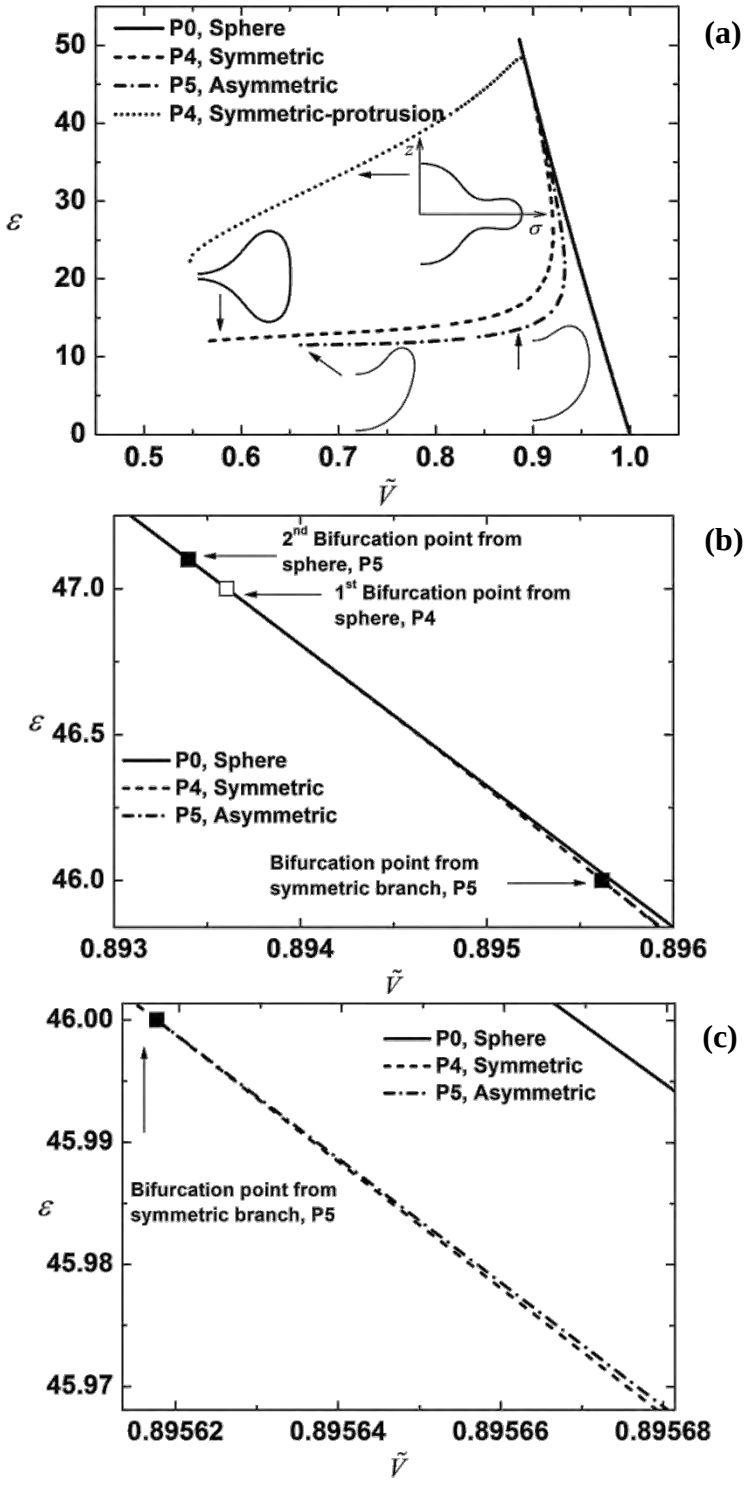

Figure 5-8: Bifurcation diagram for a microbubble with h=115.5 nm and G_s=88 MPa, **(a)** External overpressure as function of the volume,**(b)** and **(c)** Zoom in the bifurcation points area. (χ=31 N/m, $k_b = 4.52\times10^{-14}$ Nm and $\hat{k}_b = 1.48\times10^{-3}$, $\hat{P}_A = 3\times10^{-3}$). The edges of the shapes shown in panel (a) lie on the axis of symmetry z as depicted for one of them.

Upon further increasing the overpressure $\left(\varepsilon = 47.1, \tilde{V} = 0.8933\right)$ a second bifurcation point is detected on the spherosymmetric branch which is dominated by the P_5 mode, Figure 5-8(b). It was not possible to follow this second bifurcation away from the main solution

family to either higher or lower values with respect to the second critical load. However, disturbing the symmetric solution with the corresponding eigenvector at the bifurcation point detected at $\left(\varepsilon = 46, \tilde{V} = 0.8956\right)$, a branch is evolved subcritically that is characterized by two negative eigenvalues and an asymmetric shape that is dominated by the P_5 Legendre eignemode (dashed-dot line). It should be noted that parametric continuation along the latter asymmetric branch breaks before the two poles sufficiently approach each other, perhaps due to the center of mass moving away from the actual shape. Simulations are underway in order to remedy this situation that is expected to furnish the remaining asymmetric branch until pole coalescence takes place.

Finally, Figure 5-9(a) illustrates the total energy of the above solutions, where the sphere is the one with the lower energy than the subcritical symmetric and asymmetric solutions Figure 5-9(b), while the symmetric branch with the prolate-like shapes has lower energy than the sphere in the regime of one negative eigenvalue $\varepsilon \geq 43.5$, while beyond this point the spherosymmetric configuration becomes energetically favored again, Figure 5-9(c).

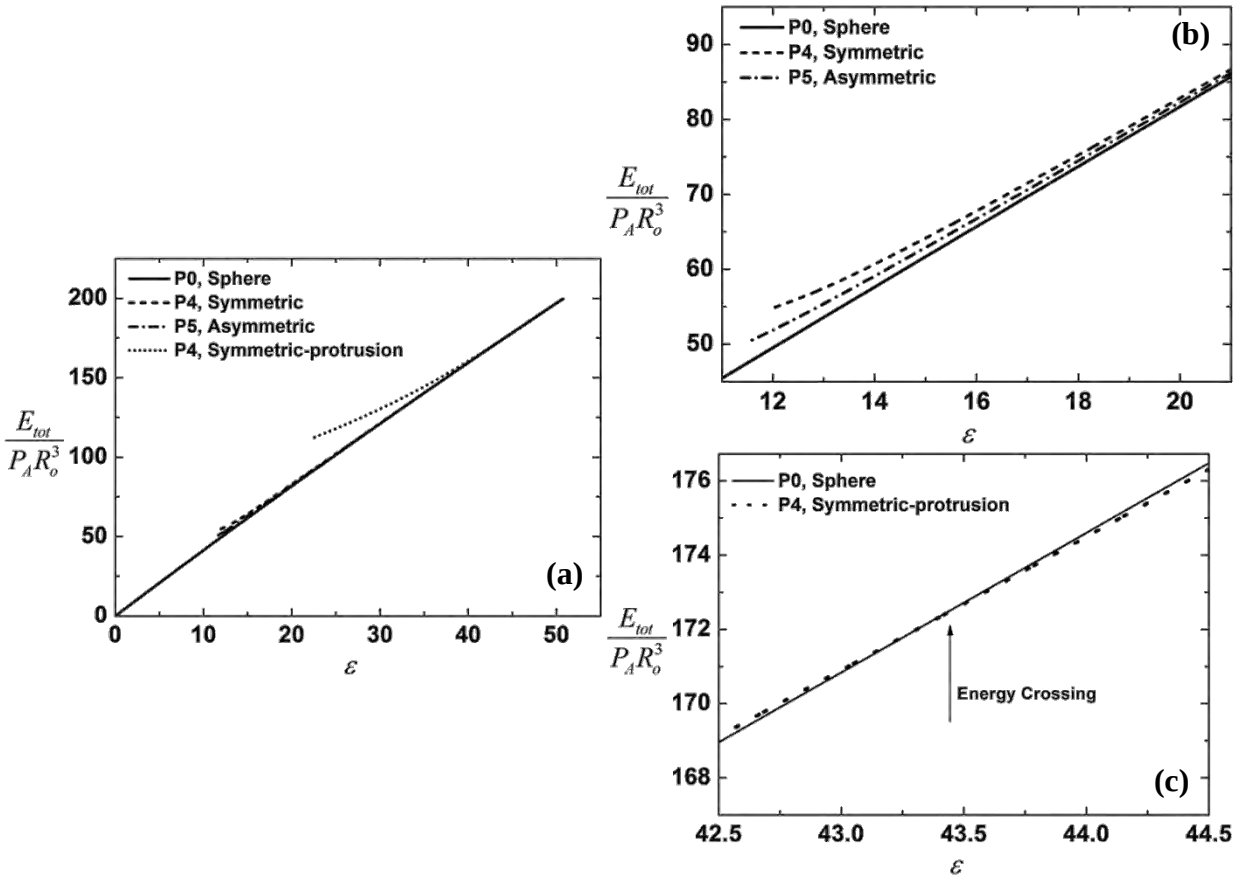

Figure 5-9: (a) Bifurcation diagram in terms of total energy for a microbubble with *h*=115.5 nm and G_s=88 MPa, **(b)** and **(c)** Zoom-in the bifurcation area of symmetric/asymmetric and the symmetric with protrusion branches, respectively. (χ=31 N/m, $k_b = 4.52 \times 10^{-14}$ Nm and $\hat{k}_b = 1.48 \times 10^{-3}$, $\hat{P}_A = 3 \times 10^{-3}$).

Next, a case with lower thickness than the previous is investigated with h=46.2 nm and the rest of the simulation parameters are the same as in Table 5-1. Therefore the area dilatation and bending modulus are χ=12.2 N/m, $k_b = 2.89\times10^{-15}$ Nm, respectively, while the dimensionless numbers $\hat{k}_b = 2.4\times10^{-4}$ and $\hat{P}_A = 8\times10^{-3}$. The first bifurcation point is detected for $\left(\varepsilon = 7.48, \tilde{V} = 0.9554\right)$ with the corresponding eigenvector being dominated by the 7th Legendre eigenmode (dashed dot line) and the second bifurcation point for $\left(\varepsilon = 7.49, \tilde{V} = 0.9552\right)$ with P_8 as the dominant eigenmode (dashed line). As before, the symmetric branch evolves towards to higher and lower values of the second critical buckling load. The subcritical branch has three negative eigenvalues, while the supercritical branch is initially characterized by two eigenvalues, where after a limit point at $\left(\varepsilon = 7.56, \tilde{V} = 0.9544\right)$, a multibranch behavior (dotted line) is detected as above with three eigenvalues, see also the bifurcation diagrams in Figure 5-10(a)-(b). Both asymmetric and symmetric solutions that

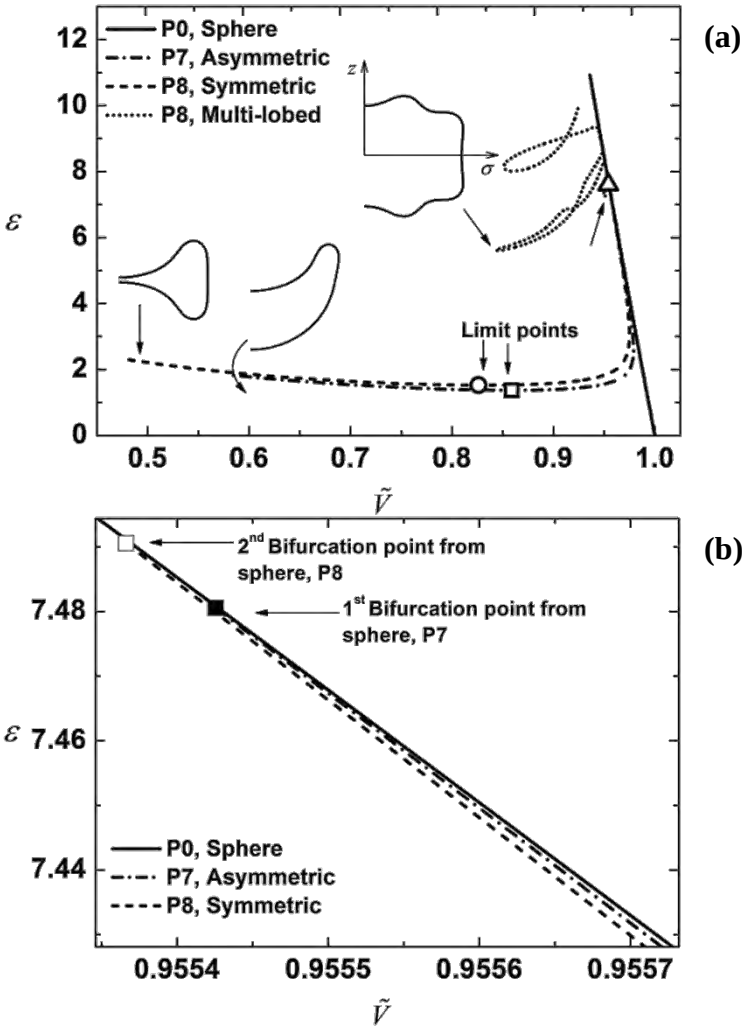

Figure 5-10: Bifurcation diagram for a microbubble with h=46.2 nm and G_s=88 MPa, **(a)** External overpressure as function of the volume and **(b)** Zoom in the bifurcation points area. (χ=12.2 N/m, $k_b = 2.89\times10^{-15}$ Nm and $\hat{k}_b = 2.4\times10^{-4}$, $\hat{P}_A = 8\times10^{-3}$). The edges of the shapes shown in panel (a) lie on the axis of symmetry z as depicted for one of them.

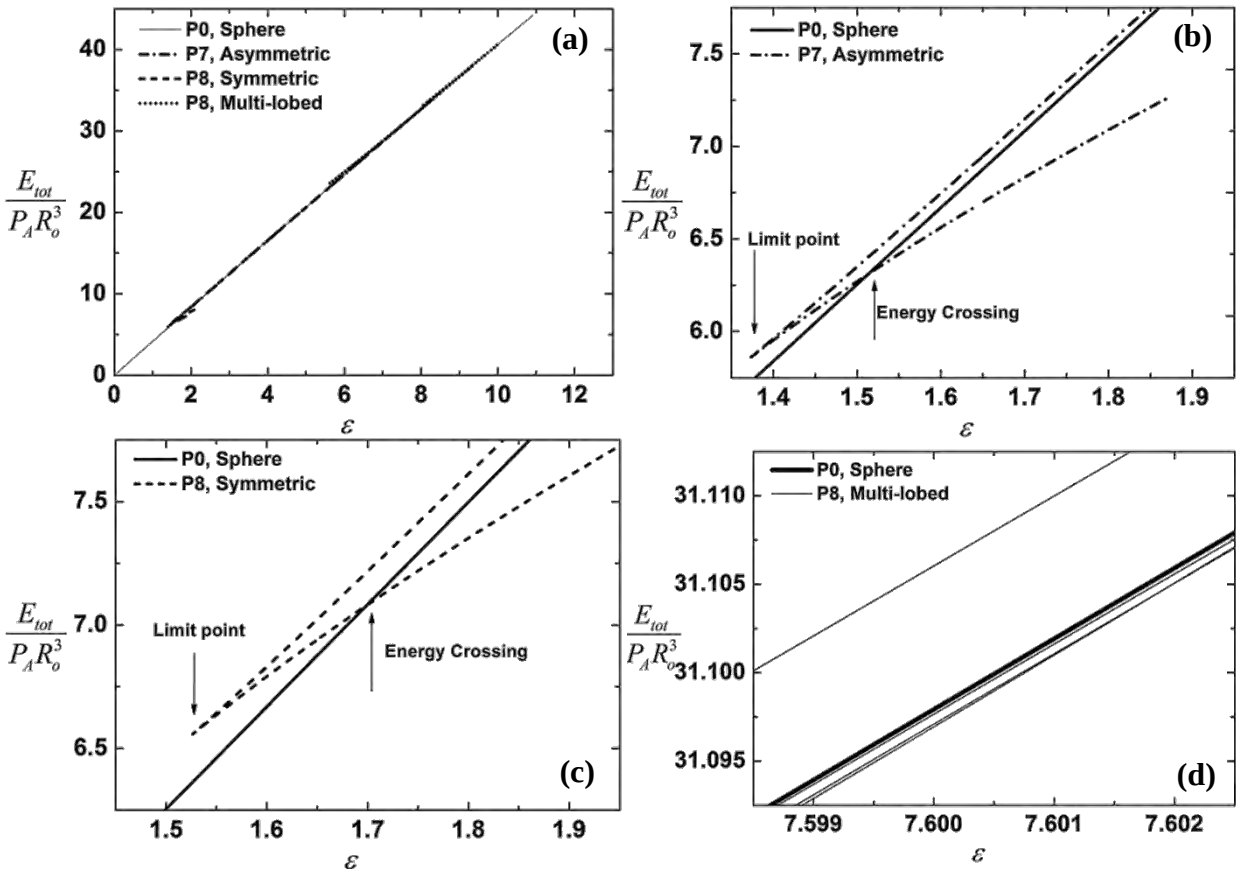

Figure 5-11: (a) Bifurcation diagram in terms of total energy for a microbubble with h=46.2 nm and G_s=88 MPa, **(b), (c)** and **(d)** Zoom-in the bifurcation area of asymmetric, symmetric and the multi-lobed branches, respectively. The multilobed branch exhibits significant variation in the immediate vicinity of the main spherical branch. In (b) and (c) the curves with energy higher than sphere evolve from their bifurcation point and curves with lower energy evolve towards pole coalescence. (χ=12.2 N/m, $k_b = 2.89\times10^{-15}$ Nm and $\hat{k}_b = 2.4\times10^{-4}$, $\hat{P}_A = 8\times10^{-3}$).

evolve subcritically become stable also in terms of their total energy, in comparison with the sphere, after $\left(\varepsilon = 1.512, \tilde{V} = 0.716\right)$ and $\left(\varepsilon = 1.711, \tilde{V} = 0.661\right)$, Figure 5-11(b), (c), respectively. On the other hand, the supercritical symmetric solution has initially lower energy, while after a limit point becomes unstable, Figure 5-11(d).

In Figure 5-12(a) the bifurcation diagram of a microbubble with lower shell thickness in comparison with Table 5-1 is presented, i.e. h=10 nm $\left(\hat{k}_b = 1.1\times10^{-5}\ \&\ \hat{P}_A = 3.9\times10^{-2}\right)$. In this case, the primary instability is dominated by the P_{17} Legendre eigenmode and it is followed by a second with P_{18} mode, Figure 5-12(b). The two solution branches evolve subcritically and after a limit point they evolve towards higher values of the overpressure, Figure 5-12(b). Decreasing further the shell thickness, h=5 nm $\left(\hat{k}_b = 2.7\times10^{-6}\ \&\ \hat{P}_A = 8\times10^{-2}\right)$, the first bifurcation is captured for an even lower pressure, ε=0.0924, as a result of the significantly reduced bending resistance. It is dominated by the even P_{24} mode whereas the second bifurcation point by the odd P_{23} eigenmode.

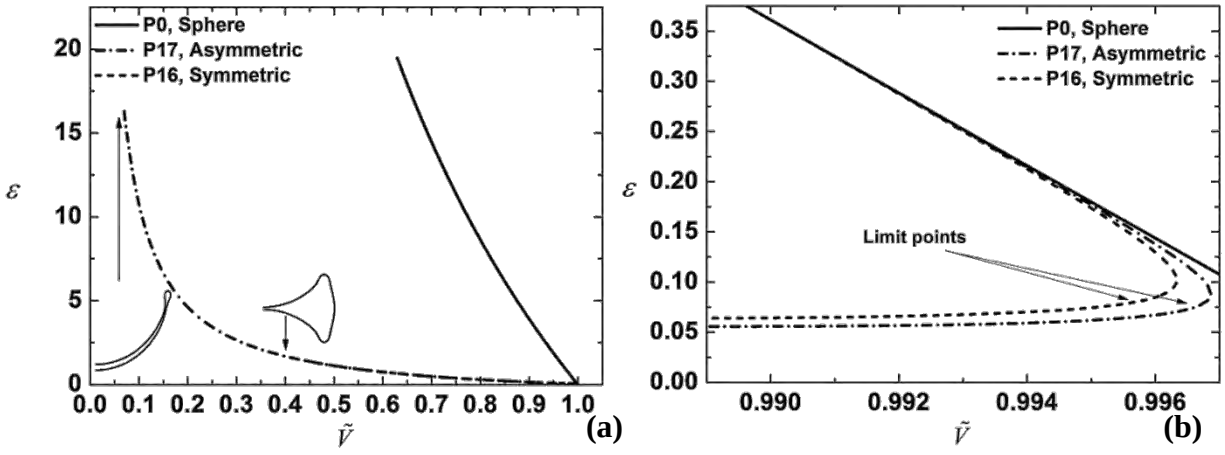

Figure 5-12: Bifurcation diagram for a microbubble with h=10 nm and G_s=88 MPa, **(a)** External overpressure as function of the volume and **(b)** Zoom in the bifurcation points area. (χ=2.64 N/m, $k_b = 2.93\times10^{-17}$ Nm and $\hat{k}_b = 1.1\times10^{-5}$, $\hat{P}_A = 3.9\times10^{-2}$).

As can be gleaned from the above parametric study, the bifurcation point is strongly depended on the dimensionless bending modulus. In particular, as the shell thickness increases for fixed radius, i.e. $\hat{k}_b$ increases indicating a thicker shell with relatively large bending resistance, buckling is translated towards higher values of the overpressure and it is in excellent agreement with the theoretical prediction, Figure 5-8 and Figure 5-10. The primary bifurcation is symmetric with the supercritical branch being almost prolate thus maintaining a certain amount of compression in the post buckling regime. As the shell thickness decreases, Figure 5-1, area dilatation consumes a significant amount of energy and thus rendering the asymmetric shape as the favored configuration in the post buckling regime, especially in its limiting state where contact is exhibited at the pole region. The indentation that forms at the pole region relaxes the shell from the compressive stresses in favor of the energetically favored bending stresses; see also Figure 5-4-Figure 5-7. Finally upon further reduction of the shell thickness, Figure 5-12, a single indentation is not enough to bring the energy down to an acceptable level for a static equilibrium to be achieved and a second indentation develops at the opposite pole thus bringing about the onset of symmetrically buckled shapes. It should be stressed however, that in most of the above cases the asymmetric shapes, whether they arise in the form of a primary or a secondary bifurcation, eventually gain stability through the process of pole coalescence and the emergence of shapes exhibiting contact.

$\hat{k}_b$	1.48×10^{-3}	2.40×10^{-4}	5.90×10^{-5}	1.11×10^{-5}	2.70×10^{-6}
1st Bifurcation point, ε_{cr}	47	7.48	1.878	0.3585	0.0924
Eigenmode	P4	P7	P11	P17	P24

Table 5-2: Evolution of the numerically evaluated bifurcation point pertaining to the asymmetric and symmetric branches stemming from the spherical solution family, as the dimensionless bending resistance decreases.

Effect of surface tension and gas compression

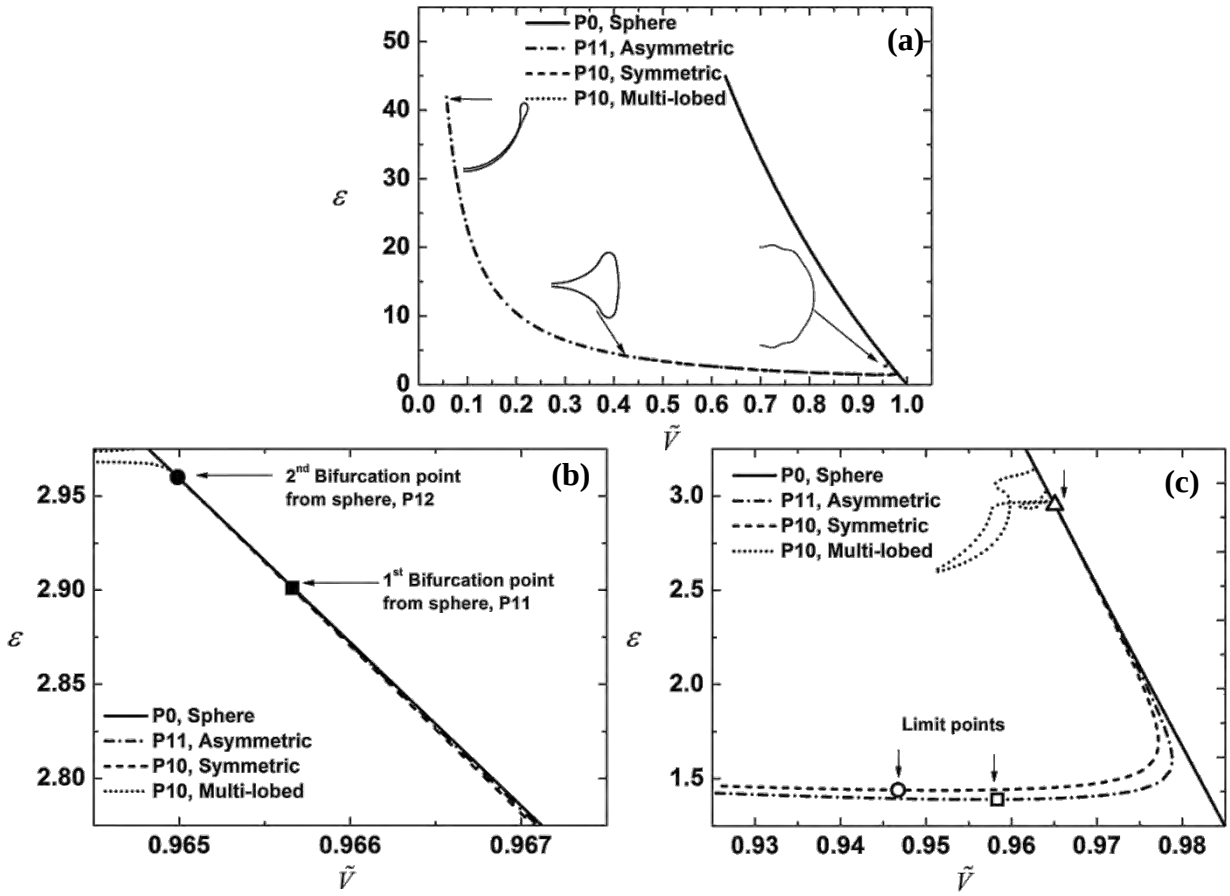

Figure 5-13: Bifurcation diagram for a microbubble with h=23.1 nm, G_s=88 MPa and γ_{BW}=0.051 N/m, **(a)** External overpressure as function of the volume, **(b)**, **(c)** Zoom in the bifurcation and limit points (χ=6.1 N/m, $k_b = 3.61\times10^{-16}$ Nm and $\hat{k}_b = 5.9\times10^{-5}$, $\hat{P}_A = 1.66\times10^{-2}$).

Adding surface tension, γ_{BW}=0.051 N/m, on the shell equilibrium and assuming the rest of parameters to be the same as in Table 5-1 a bifurcation diagram is constructed, Figure 5-13(a)-(c). The response is the same with the case studied in paragraph 5.1.1, $\gamma_{BW} = 0$, but the first instability is captured for a slightly higher value of the external overpressure $\left(\varepsilon = 2.9, \tilde{V} = 0.9656\right)$ dominated again by the P_{11} Legendre eigenmode, while the second instability is found in $\left(\varepsilon = 2.960, \tilde{V} = 0.9649\right)$ characterized by the P_{10} mode. Increasing further the surface tension, γ_{BW}=0.07 N/m, the first bifurcation is found at $\left(\varepsilon = 3.35, \tilde{V} = 0.9606\right)$ and the second in $\left(\varepsilon = 3.38, \tilde{V} = 0.9603\right)$ dominated again by the same modes as before. Clearly, in the above cases it is the internal pressure that increases as a result of interfacial tension, thus increasing parameter $\hat{P}_A = 2\gamma_{BW} R_0 / R_0 / \chi \sim 0.1$ and stabilizing the shell by increasing its resistance to volume compression, and shifts the bifurcation point to higher values in comparison with the theoretical critical buckling load. Finally, repeating both calculations while ignoring pressure changes in the microbubble does not result in any significant changes of the bifurcation diagram. In both cases the resistance to compression due to gas compressibility is negligible, $\hat{P}_A \ll 1$.

Effect of constitutive law

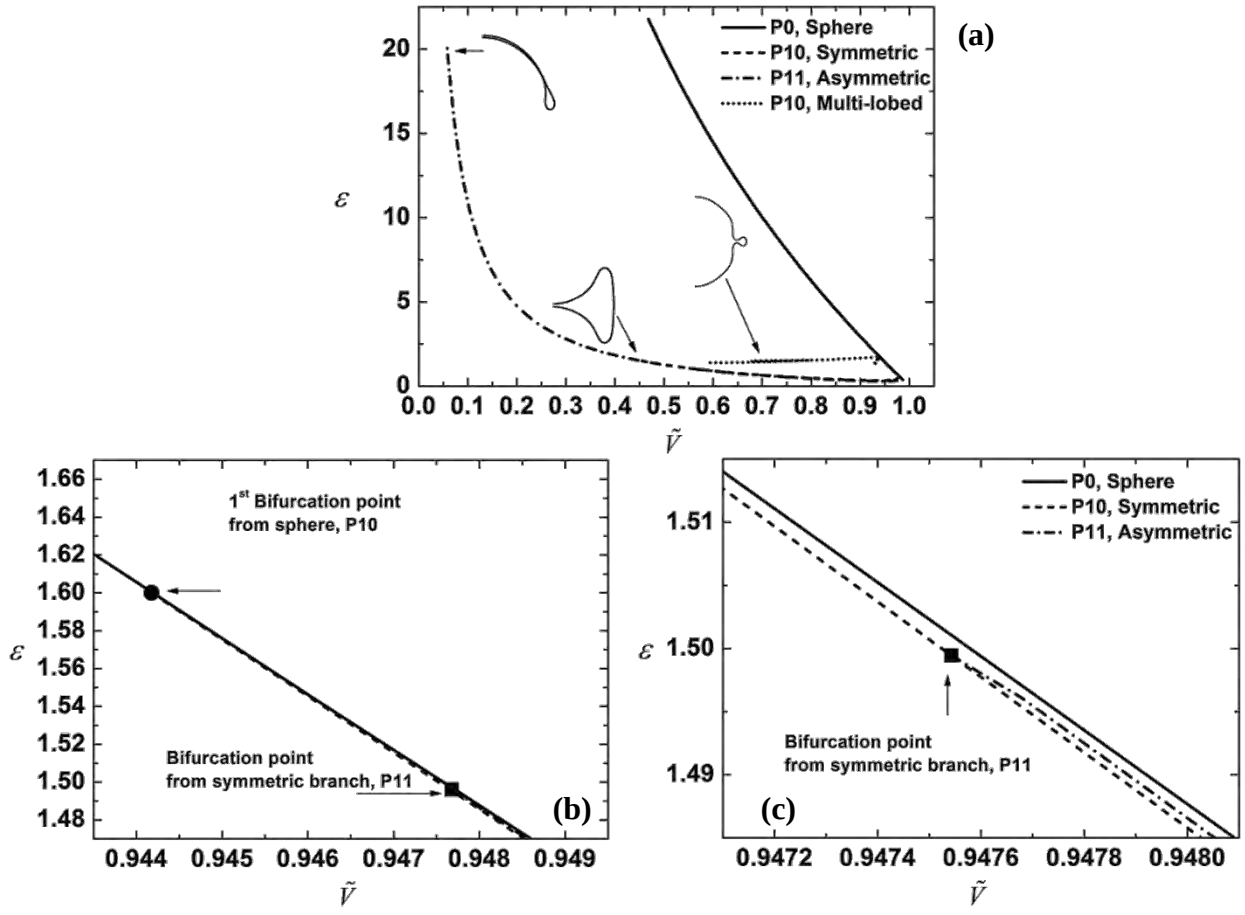

Figure 5-14: Bifurcation diagram for a microbubble with h=23.1 nm, G_s=88 MPa and Skalak's constitutive law, **(a)** External overpressure as function of the volume, **(b)** and **(c)** Zoom in the bifurcation points (χ=6.1 N/m, $k_b = 3.61\times10^{-16}$ Nm and $\hat{k}_b = 5.9\times10^{-5}$, $\hat{P}_A = 1.66\times10^{-2}$).

In Figure 5-14 the shell coating is assuming to follow the Skalak's law while the rest of the simulation parameters are the same as in Table 5-1. The bifurcation diagram is modified, with respect to the one presented in Figure 5-1, in the fashion shown in Figure 5-9, where the first instability is dominated by a symmetric mode. In the present case the first bifurcation $\left(\varepsilon = 1.6, \tilde{V} = 0.9441\right)$ is also dominated by an even Legendre mode, the P_{10} eigenmode, and evolves trancritically. In the subcritical branch a third eigenvalue appears from which the asymmetric branch (P_{11}) evolves with two unstable eigenvalues. The effective elasticity modulus of a Skalak shell is reduced when it is compressed, thus the effective dimensionless bending stiffness increases, which leads to a slightly higher buckling load and a transcritical symmetric primary bifurcation giving rise to prolate linearly stable in the immediate post-buckling regime

5.2 Bifurcation diagrams of lipid microbubbles

5.2.1 Study of a single microbubble

Next, the static response of microbubbles covered with a lipid monolayer are investigated assuming the parameters of Table 5-3: indicative dimensionless numbers are $\hat{k}_b = 1.9\times10^{-2}$ and $\hat{P}_A = 3$ corresponding to bending stiffness $k_b=3\times10^{-14}$ N·m and area dilatation modulus χ=0.12 N/m. The above parameters are characteristic of lipid monolayer shells in that they reflect the increased importance of resistance to bending and volume compression contrary to polymeric shells for which $\hat{k}_b, \hat{P}_A << 1$. As will be seen in the following, the importance of gas compressibility is a central effect of the softness of such shells since the bending to stretching resistance ratio is also small for polymeric shells. The bifurcation point is now detected at a lower normalized overpressure $\frac{\Delta P}{P_A} = \varepsilon = 1.65$ and relative volume $\frac{V}{V_i} = \tilde{V} = 0.556$, with the corresponding eigenvector dominated by the symmetric P_2 Legendre eigenmode. It marks the onset of a transcritical bifurcation with oblate and prolate solution families evolving to lower and higher overpressures, respectively, stemming from the critical overpressure. Disturbing the spherical shape with the eigenvector obtained at the critical buckling load the subcritical solution branch is followed which contains oblate shapes, Figure 5-15(a) and Figure 5-16(b). This branch is unstable but exhibits a limit point that, employing arc-length continuation, turns towards larger overpressures $\Delta\tilde{P}$ after $\tilde{V} = 0.57$, dashed line in Figure 5-15(a)-(b). The branch that evolves after the limit point is linearly stable with shapes that contain a progressively more intense dimple at each one of the two poles until eventually terminating with the two poles coalescing. More specifically, the shape described with the dotted line in Figure 5-16(b) corresponds to the last point of the oblate branch, where the simulation breaks, because as it is depicted in the shape, the relative position of the two poles is very close, indicating the point where the two opposite sides will form a contact line with further increase of the load, which the present formulation cannot predict.

In this case solutions can also be obtained from the buckling point that evolve towards higher values of the external load also dominated again the P_2 Legendre eigenmode, reflecting the transcritical nature of the bifurcation. There are two fundamental differences between the subcritical and supercritical branches. In the subcritical branch, the shape is compressed near

Bending modulus:	$k_b = 3\times10^{-14}$ Nm	Area dilatation:	$\chi = 0.12$ N/m	
Initial radius:	$R_o = 3.6$ μm	Poisson ratio:	$\nu = 0.5$	
Constitutive law:	Mooney-Rivlin (b=0)	Pre-stress:	$u = 0$ μm	
Surface tension:	$\gamma_{BW} = 0.051$ N/m	Polytropic index:	$\gamma = 1.07$	400 elements

Table 5-3: Simulation parameters for the bifurcation diagram of a microbubble covered with lipid.

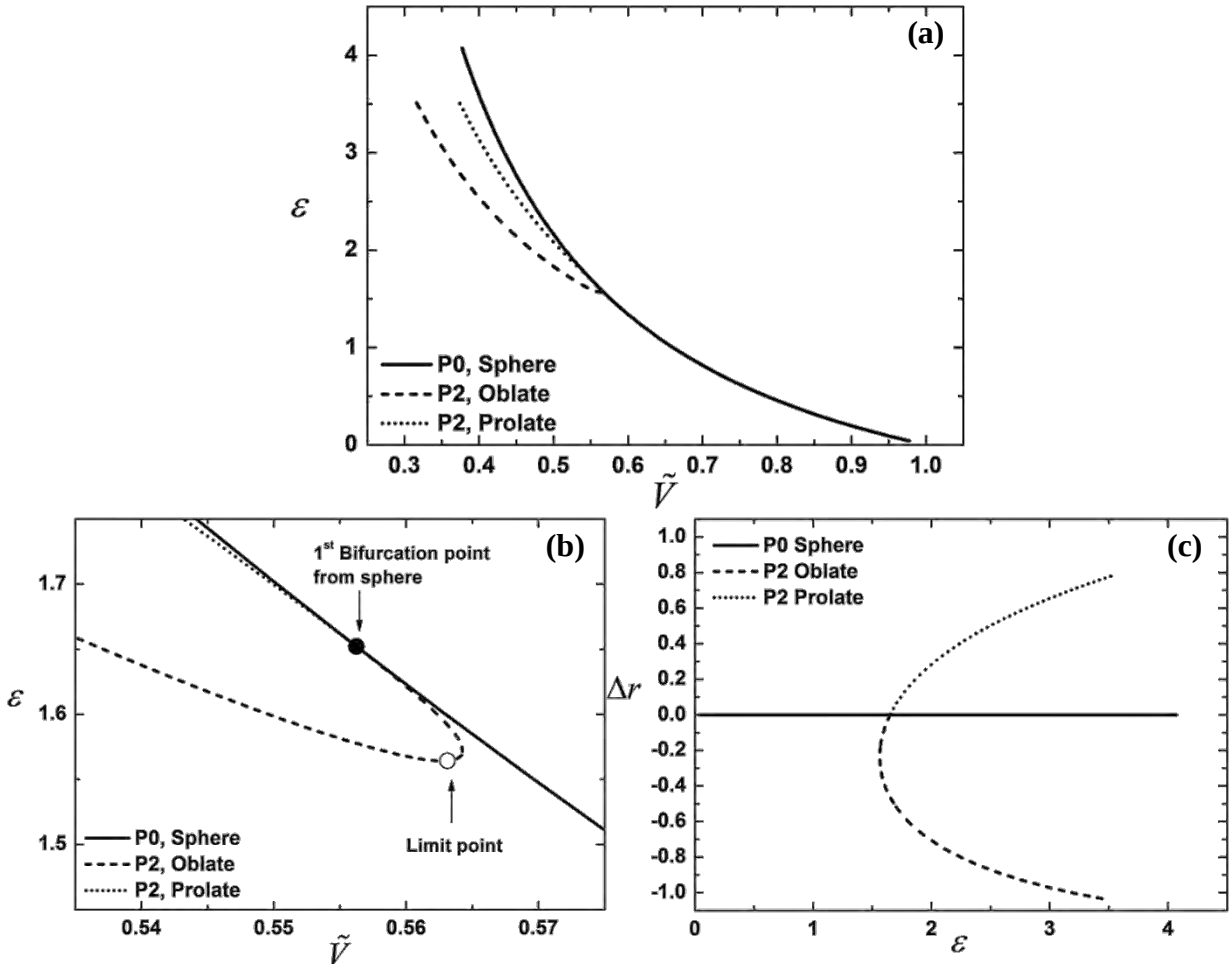

Figure 5-15: Bifurcation diagram for a microbubble with χ=0.12 N/m, $k_b = 3\times10^{-14}$ Nm and Mooney-Rivlin constitutive law. **(a)** External overpressure as function of the volume, **(b)** Zoom in the bifurcation and limit point and **(c)** Difference in radius between the north pole and equator as a function of the overpressure. ($\hat{k}_b = 1.9\times10^{-2}, \hat{P}_A = 3$).

the poles and expanded in the equator, oblate configuration, while the opposite happens with the shapes exhibited by the supercritical branch which are prolate. Thus, the bifurcation diagram could alternatively be described by the difference of the spherical radius in the pole and the equator (Δr), see Figure 5-15(c). Hence, in the spherical solution $\Delta r = 0$, in the oblate $\Delta r < 0$ and in the prolate $\Delta r > 0$. Indicative deformed shapes of each solution branch are depicted in Figure 5-16(b), (c). It should be noted that despite the fact that an asymmetric bifurcation arises on the main spherosymmetric branch for a larger overpressure than the above reported critical load, it was not possible to follow the corresponding solution family to either larger or smaller overpressures and its calculation was not pursued further as the stability was dominated by the symmetric solution families.

An important issue regarding the stability characteristics of the bifurcation diagram pertains to the local and global aspects of it. The subcritical branch (oblate) has two negative eigenvalues, while the spherical solution for the same overpressure, ε, has one. Nevertheless, after the limit point the oblate solution has also one negative eigenvalue thus becoming linearly stable as well. On the other hand, the supercritical solution has one negative

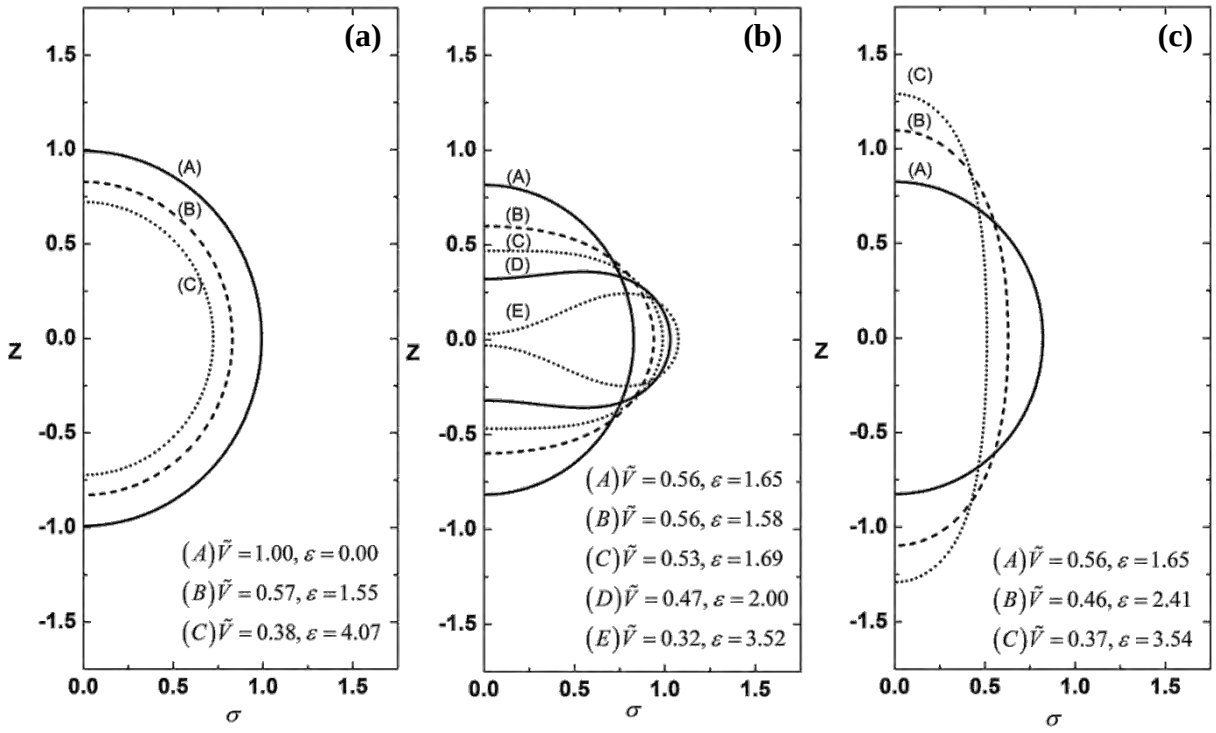

Figure 5-16: Microbubble in deformed configuration: **(a)** Spherical, **(b)** Oblate and **(c)** Prolate solutions. The axes are dimensionalized with the initial radius R_o. ($k_b = 3\times10^{-14}\,\text{Nm}$, $\chi = 0.12\,\text{N/m}$, and $\hat{k}_b = 1.9\times10^{-2}, \hat{P}_A = 3$).

eigenvalue whereas and for the same values of ε, the spherical solution has two or even more negative eigenvalues. In other words the prolate solution inherits the stability of the spherical branch before the bifurcation point and is thus linearly stable. As was above pointed out, that is the eigenvalue that reflects translational invariance of the system and does not affect the stability of the system in any way.

Figure 5-17(a) depicts the total energy of each branch, where it is clear that for every value of the external overpressure there is a global energy minimum despite the local linear stability characteristics of the system. Before the primary buckling instability the spherical configuration has the minimum energy among the different solution families, Figure 5-17(b). Beyond the critical load the prolate family is linearly stable and its energy is lower than that of the sphere, however, the oblate solution family that emerges after the limit point and turns to larger overpressures has an even lower energy content, Figure 5-17(c), and is expected to dynamically dominate static equilibrium.

More specifically, as we proceed along the subcritical oblate solution family after the bifurcation point $\left(\varepsilon = 1.65, \tilde{V} = 0.556\right)$, until the limit point $\left(\varepsilon = 1.56, \tilde{V} = 0.563\right)$ and slightly beyond it, the spherical configuration has lower energy in comparison with the oblate solution, which is in accordance with the number of negative eigenvalues. Beyond a certain overpressure the energy curves of the oblate and spherical solution family cross and the oblate family is energetically favorable, Figure 5-17(c). This happens very near the primary bifurcation point. In fact, beyond the primary bifurcation point the prolate family is linearly stable to small disturbances as well. However, for large enough initial geometric deviations

from the prolate shape the oblate static configuration will dominate since it is also linearly stable but, in addition, carries the minimum energy content among all the three solutions that were captured. In this context, Vlachomitrou & Pelekasis [19] performed dynamic simulations of the same microbubble in an unbounded flow and when static arrangement obtained above the primary bifurcation point, $\varepsilon = 2.0$ and $\tilde{V} = 0.47$, the shape is dominated by the oblate symmetric mode P_2 indicating the global characteristics of the system at this parameter range. Below the primary bifurcation point simulations always settle back to the spherical shape, irrespective of the intensity of the initial disturbance, reflecting the linearly stable nature of the spherical configuration in this parameter range.

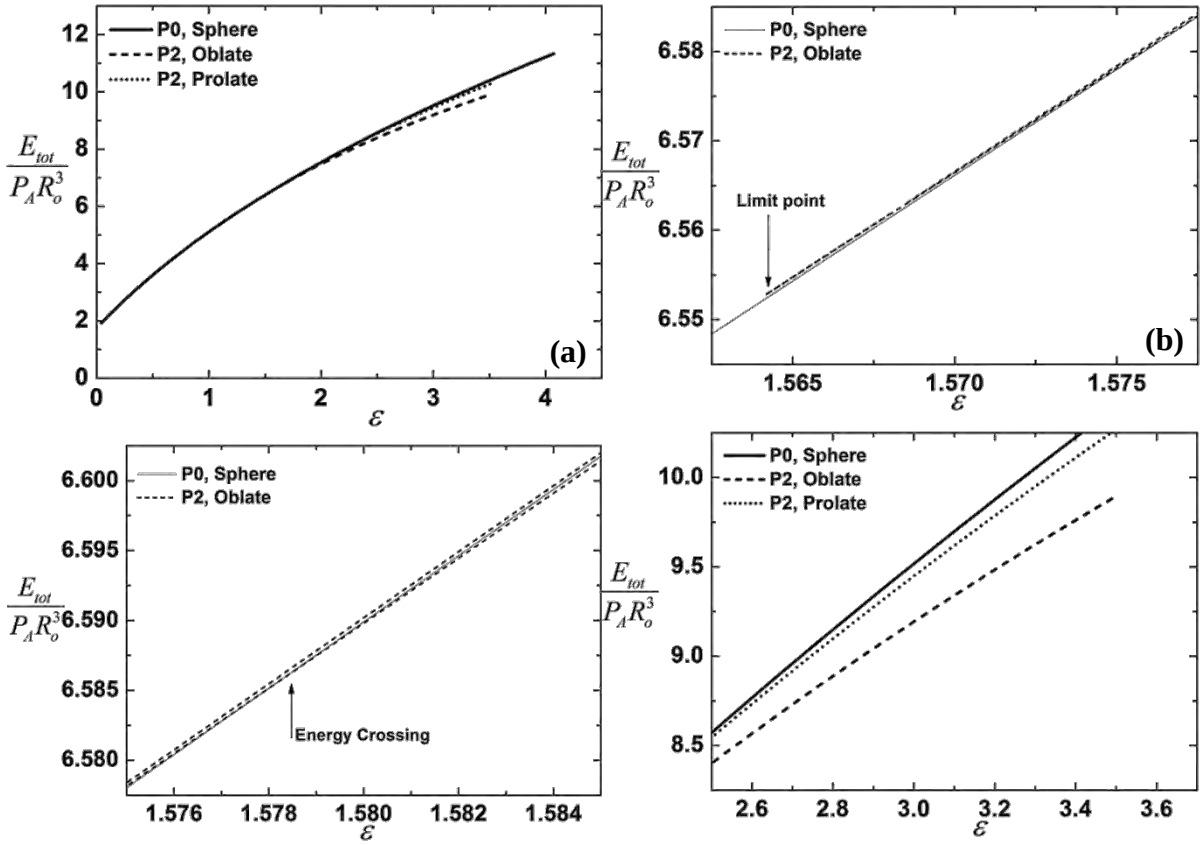

Figure 5-17: **(a)** Bifurcation diagram in terms of total energy for a microbubble with $k_b = 3\times10^{-14}$ Nm and $\chi = 0.12$ N/m, **(b)** and **(c)** Zoom-in the oblate branch. In (b) and (c) the curves with energy higher than sphere evolve from the bifurcation point and curves with lower energy evolve towards pole coalescence and **(d)** Zoom in higher values of overpressure ($\hat{k}_b = 1.9\times10^{-2}, \hat{P}_A = 3$).

5.2.2 Parametric Study

Effect of elasticity moduli (stretching-χ & bending k_b)

In this section a parametric study is conducted in order to capture the evolution of the bifurcation diagram pertaining to lipid monolayer shells, as the area dilatation modulus increases or, equivalently, as the dimensionless bending resistance $\hat{k}_b$ decreases. To this end, a microbubble with higher stretching modulus is investigated, subject to a uniform overpressure, with the same parameters as above, see Table 5-3, but with $\chi = 0.24\ \mathrm{N/m}$. Hence, the resulting dimensionless numbers are $\hat{k}_b = 0.96\times10^{-2}$ and $\hat{P}_A = 1.5$, i.e. both bending and gas compression are less important in comparison with stretching. The first bifurcation point is detected when $\varepsilon = 1.35$ and $\tilde{V} = 0.66$, it is dominated by the asymmetric P_3 Legendre eigenmode, followed by a second bifurcation point that arises for $\varepsilon = 1.43$ and $\tilde{V} = 0.65$ and

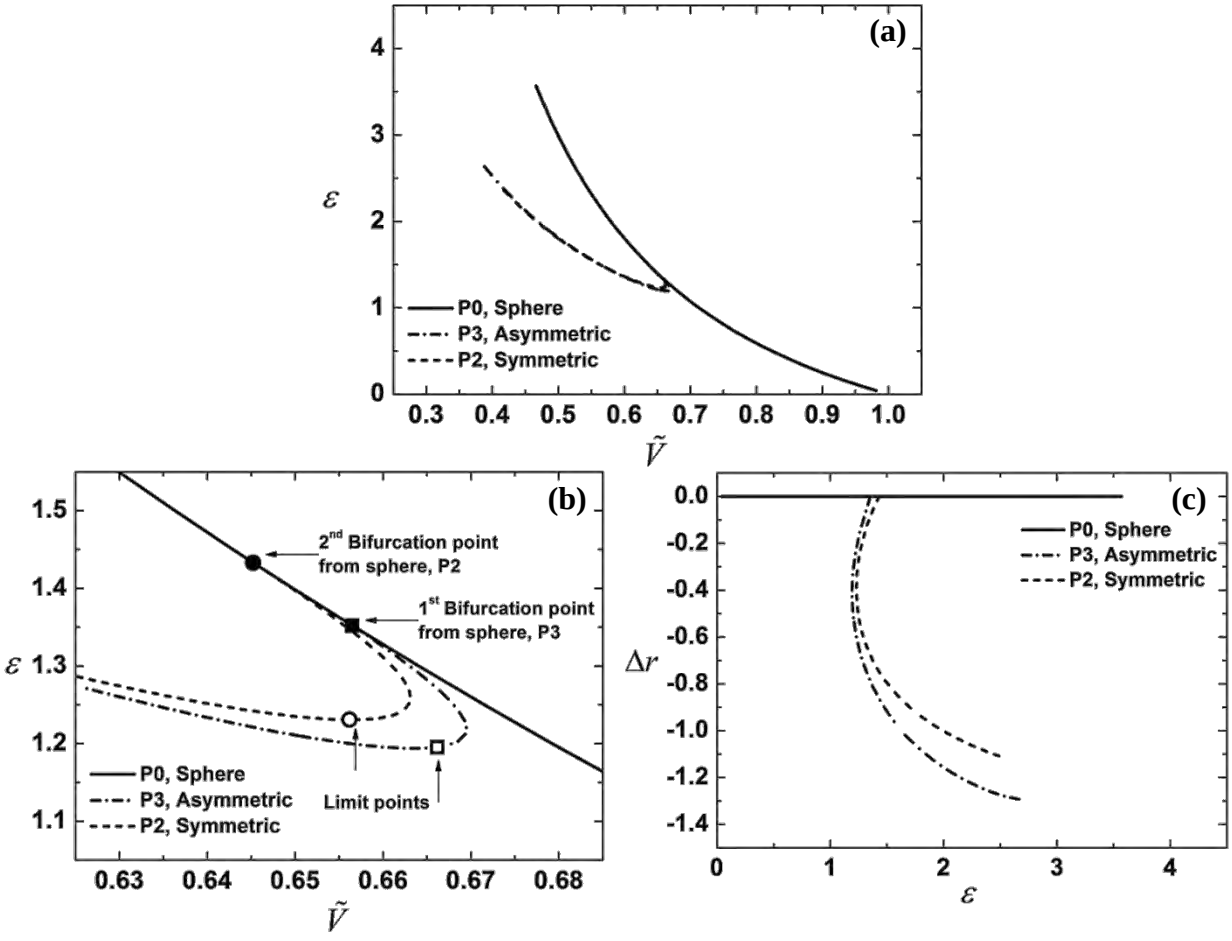

Figure 5-18: Bifurcation diagram for a microbubble with χ=0.24 N/m, $k_b = 3\times10^{-14}$ Nm and Mooney-Rivlin constitutive law. **(a)** External overpressure as function of the volume, **(b)** Zoom in the bifurcation and limit point and **(c)** Difference in radius between the north pole and equator as a function of the overpressure. ($\hat{k}_b = 0.96\times10^{-2}, \hat{P}_A = 1.5$).

that is dominated by the P_2 mode. In this case the symmetric solution arises in the form of a subcritical bifurcation and does not evolve towards higher values of the buckling pressure $(\varepsilon > 1.43)$ as in the previous case, see Figure 5-18 and Figure 5-19. In addition, the asymmetric and symmetric solutions have two and three negative eigenvalues, respectively, in contrast with the spherosymmetric solution that has only one and is linearly stable. As they evolve towards smaller external loads both branches develop limit points and turn towards larger overpressures while exhibiting significantly reduced volumes. The solution families that evolve past the limit points have one less negative eigenvalue than the branch which they stemmed from, i.e. the asymmetric has one and the symmetric two negative eigenvalues. Consequently, the asymmetric branch becomes linearly stable. As can be gleaned from Figure 5-20(a) portraying the evolution of the total energy associated with each solution family, both branches are energetically favorable over the spherosymmetric solution in this range of external loads, Figure 5-20(b) and (c). Moreover, the curves of the two secondary branches cross each other at $\varepsilon \approx 1.26$, but the asymmetric has always less energy than the symmetric in the range of parameters ε, see also Figure 5-20(d). In order to corroborate this pattern, it should be pointed out that dynamic response of the same microbubble was studied numerically by Vlachomitrou & Pelekasis [19] and it was seen that when static equilibrium is reached for the first time the shape is symmetric. However the latter shape is also destabilized and at the end of the simulation the asymmetric static configuration prevails, since it contains less energy than the symmetric one for the same overpressure ε. In addition, as in case examined in subsection 5.1.1, for the asymmetric solution a cylindrical coordinated system is considered

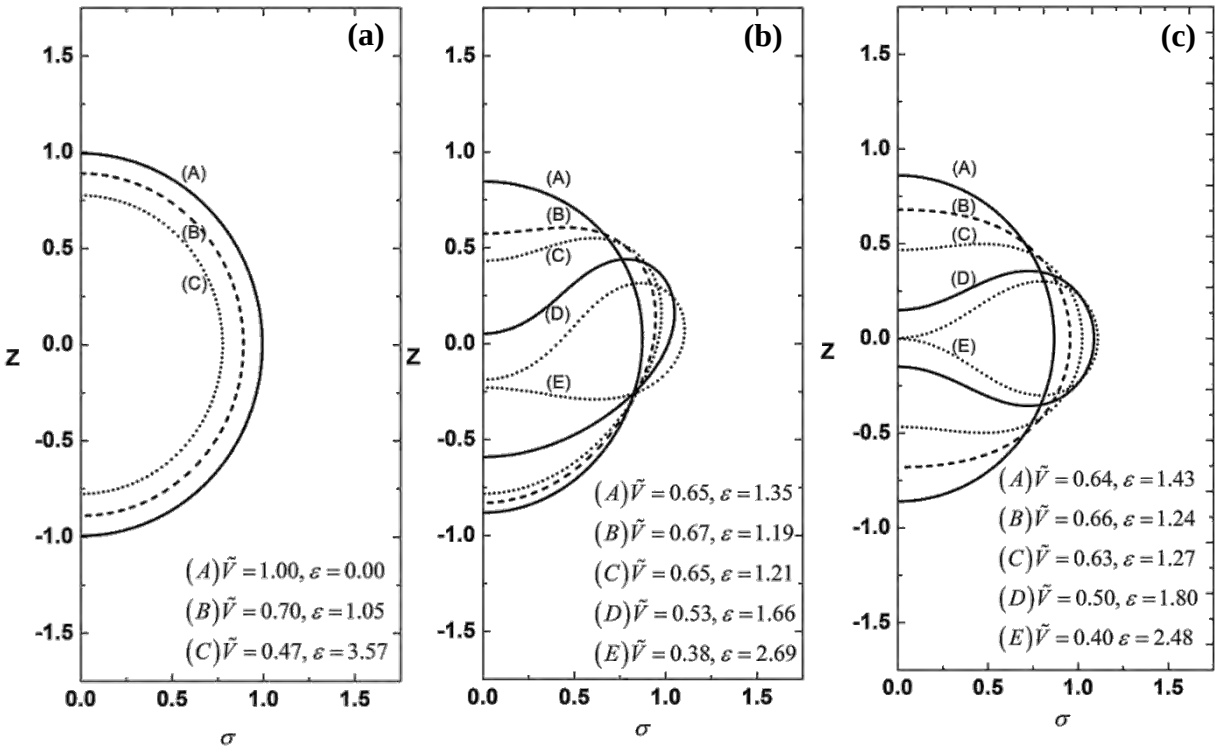

Figure 5-19: Microbubble in deformed configuration: **(a)** Spherical, **(b)** Asymmetric and **(c)** Oblate solutions. The axes are dimensionlized with the initial radius R_o. ($k_b = 3\times10^{-14}\,\mathrm{Nm}$, $\chi = 0.24\,\mathrm{N/m}$, and $\hat{k}_b = 0.96\times10^{-2}, \hat{P}_A = 1.5$).

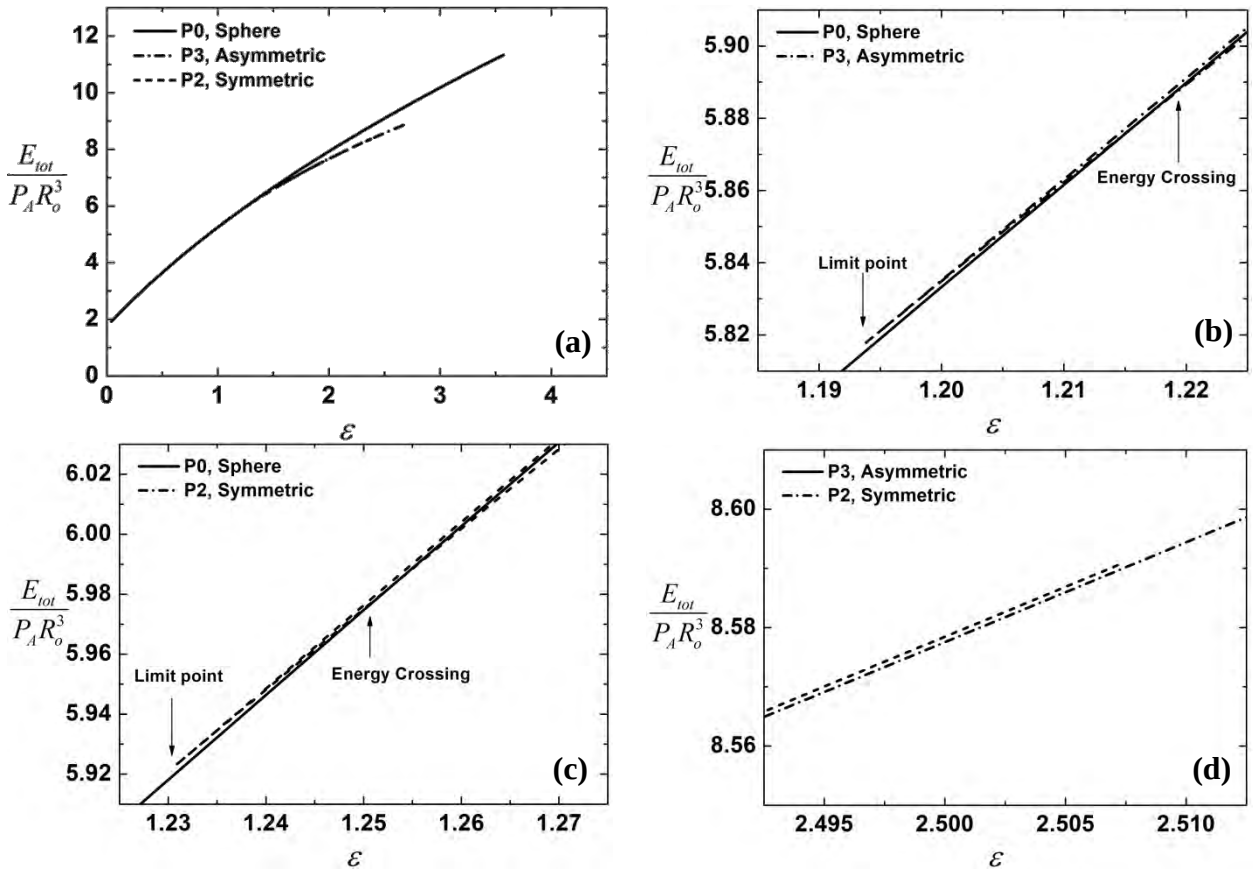

Figure 5-20: **(a)** Bifurcation diagram in terms of total energy for a microbubble with $k_b = 3\times10^{-14}\,\mathrm{Nm}$ and $\chi = 0.24\,\mathrm{N/m}$, **(b)** and **(c)** Zoom-in the asymmetric and symmetric branch. In (b) and (c) the curves with energy higher than sphere evolve from the bifurcation point and curves with lower energy evolve towards pole coalescence and **(d)** Zoom in higher values of overpressure ($\hat{k}_b = 0.96\times10^{-2}, \hat{P}_A = 1.5$).

after $\varepsilon > 1.66$ in order to accommodate shapes whose center of mass falls outside the volume of microbubble, and hence it was possible to follow the asymmetric solution family until the two poles almost coalesce, E shape in Figure 5-19(b). The symmetric solution family was also captured until pole coalescence takes place. Symmetric shapes are not energetically favored since they have a higher energy content than the asymmetric ones during pole coalescence as a result of the fact that the latter shapes exhibit contact over a larger portion of the interface, Figure 5-19(b) and (c).

As a final test the area dilatation modulus was further increased, i.e. $\chi = 0.96\,\mathrm{N/m}$, whice amounts to setting dimensionless parameters $\hat{k}_b = 0.24\times10^{-2}$ and $\hat{P}_A = 0.38$. The bifurcation diagram is obtained following the same concept as above and is depicted in Figure 5-21(a). The first bifurcation point is detected for a larger critical load, $\varepsilon = 1.18$ and $\tilde{V} = 0.82$, it is dominated by the P_4 eigenmode and evolves transcritically, Figure 5-21(b). The subcritical branch after a limit point has one unstable eigenvalue thus becoming linearly stable. It is characterized by the onset of an indentation around each pole region that grows deeper as the external overpressure further increases and the volume of the microbubble

decreases. It is a result of the large area dilatation modulus that generates large compressive stresses as the load increases. In the two dimpled regions the compressive stresses are relaxed in favor of bending that acts in such a way as to reduce the total energy of the shell.

The supercritical branch has also initially one negative eigenvalue, thus inheriting the stability of the original spherical solution family in the form of slightly prolate shapes, but it exhibits a limit point that leads to a solution that is characterized by multilobed shapes. The number of the unstable eigenvalues increases and the solution family is destabilized. The diagram of the total energy is shown in Figure 5-25(a) for each one of the solution families in the bifurcation diagram. It verifies the linear stability of the spherical shape that is superseded by the oblate and prolate shapes beyond the primary bifurcation point. In this range of external loads oblate shapes dominate static response since they correspond to a global minimum of the total shell energy among the possible solution branches, Figure 5-22(b) and (c).

Lipid shells also conform with the pattern exhibited by polymeric shells, namely that as the area dilatation modulus increases the primary instability evolves from a symmetric one characterized by oblate and prolate shapes to an asymmetric and back to a symmetric one with one or two dimpled regions around the poles as a means to alleviate the compressive stresses that develop with increasing external load, Table 5-4. Despite the local stability characteristics of the diagram around the primary bifurcation global stability is determined by the minimum energy content among the possible solution branches, with the spherical shape dominating the region below the bifurcation point and the symmetric or asymmetric shapes dominating above the bifurcation point. The latter shapes evolve from the primary bifurcation after the onset of a limit point that leads to shapes exhibiting one or two gradually more intense dimples at the two poles region until coalescence.

A major difference with polymeric shells lies in the fact that that the latter shapes, both above and below the primary bifurcation, possess a global minimum in the energy, for asymmetric shapes that almost exhibit contact between the two poles. Especially for loads that lie below the primary bifurcation this is a result of the very small resistance to volume

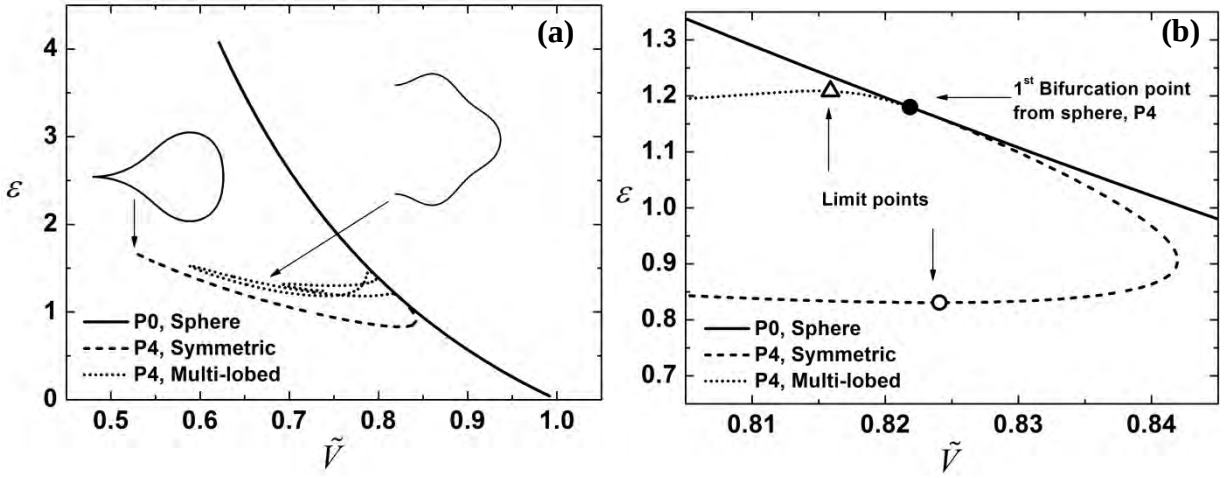

Figure 5-21: Bifurcation diagram for a microbubble with χ=0.96 N/m, $k_b = 3\times10^{-14}$ Nm and Mooney-Rivlin constitutive law. **(a)** External overpressure as function of the volume, **(b)** Zoom in the bifurcation and limit points ($\hat{k}_b = 0.24\times10^{-2}, \hat{P}_A = 0.38$).

compression, in comparison with stretching and bending resistance, that affords the onset of shapes with very small volumes for marginally larger external loads.

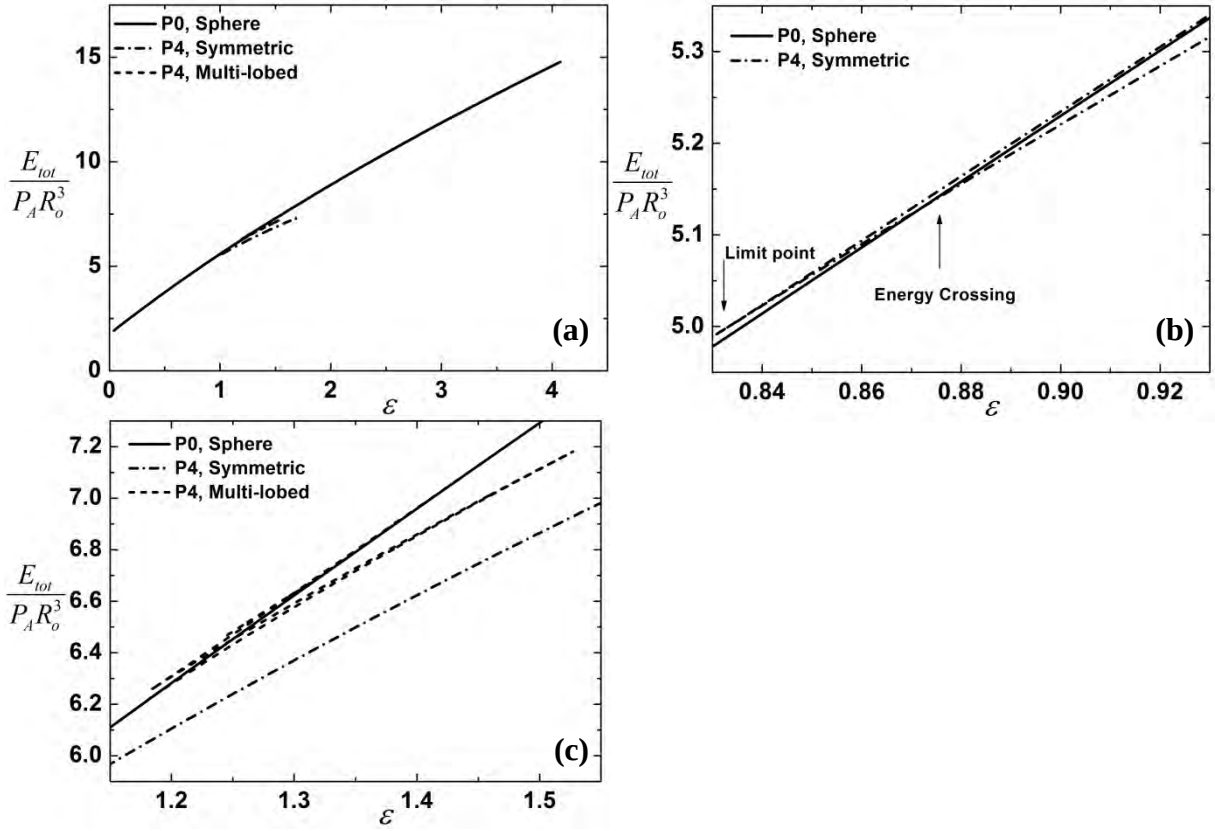

Figure 5-22: **(a)** Bifurcation diagram in terms of total energy for a microbubble with $k_b = 3\times10^{-14}\,\mathrm{Nm}$ and $\chi = 0.96\,\mathrm{N/m}$, **(b)** and **(c)** Zoom-in the asymmetric and symmetric branch. In (b) and (c) the curves with energy higher than sphere evolve from the bifurcation point and curves with lower energy evolve towards pole coalescence ($\hat{k}_b = 0.24\times10^{-2}, \hat{P}_A = 0.38$).

$\hat{k}_b$	1.9×10^{-2}	0.96×10^{-2}	0.24×10^{-2}
1st Bifurcation point, ε_{cr}	1.65	1.35	1.18
Eigenmode	P2	P3	P4

Table 5-4: Evolution of the numerically evaluated bifurcation point pertaining to the asymmetric and symmetric branches stemming from the spherical solution family, as the dimensionless bending resistance decreases.

Effect of surface tension

Next, the effect of the surface tension is investigated on the bifurcation diagram. Thus the case studied in paragraph 5.2.1, see Table 5-3, is recalled with $\gamma_{BW} = 0$ N/m and the corresponding bifurcation diagram is presented in Figure 5-23(a). As can be gleaned from the latter graph, the bifurcation point is detected at a lower overpressure, $\varepsilon = 0.65$ in comparison with the case where the surface tension is included $(\varepsilon = 1.66)$, which is attributed to the stabilizing role of the surface tension, that increases the effective resistance to volume compression thus preventing buckling. More specifically, in the case with a finite surface tension the initial internal gas pressure is higher, thus stabilizing the shell against buckling, since in the case of a lipid shell gas compressibility is comparable with the rigidity due to elasticity$\left(\hat{P}_A = 3\right)$; see also next paragraph for the effect of gas compressibility. The bifurcating branch evolves towards lower and higher values of the critical buckling load, dominated again by the symmetric Legendre eigenmode P_2 and characterized by oblate and prolate shapes, respectively. Moreover, the number of the unstable eigenvalues is the same for each branch as in the original case and the total energy is less, because the energy due to surface tension is zero, however, the relative order remains the same, see also Figure 5-23(b). Thus, it can be concluded that surface tension does not qualitatively affect the main attributes of the bifurcation diagram, but only affects the actual location of the bifurcation point.

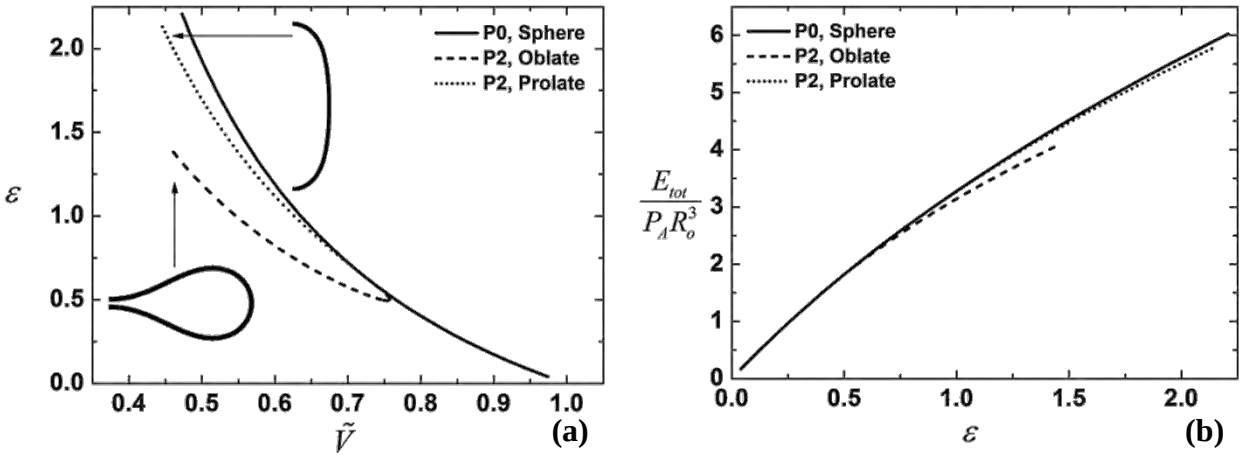

Figure 5-23: Bifurcation diagram for a microbubble with χ=0.12 N/m, $k_b = 3\times10^{-14}$ Nm, Mooney-Rivlin constitutive law and $\gamma_{BW} = 0$. **(a)** External overpressure as function of the volume, **(b)** Total energy diagram ($\hat{k}_b = 1.9\times10^{-2}, \hat{P}_A = 3$).

Effect of gas compressibility

As was already pointed out in the present thesis, microbubbles covered with lipids are characterized by a lower area dilatation modulus and thus the gas compressibility acts as an extra stiffness which in the f-d curve of the AFM problem defines a third regime curved upwards. Hence, it is of great importance to understand how gas compression affects the bifurcation diagram. Thus, the original case of this paragraph, see Table 5-3, is recalculated setting the polytropic index to zero, $\gamma = 0$, i.e. it is assumed that the internal gas pressure does not change as the volume decreases. The bifurcation diagram for this case is presented in Figure 5-24(a), where the bifurcation point is at $\varepsilon = 0.56$ and the secondary branch is dominated again the symmetric P_2 eigenmode, corresponding to a transcritical bifurcation that consists of an oblate and a prolate solution family. However, the solution curve that corresponds to the oblate configuration is characterized by an almost zero slope after the limit point, while in the original case, where gas compression is considered as an additional stiffness, the solution after the limit point has negative slope in the bifurcation diagram, see also Figure 5-15(a). In addition, in the oblate branch a limit point is not detected and therefore the whole branch has two unstable eigenvalues. Hence, for $\varepsilon \leq 0.56$ the sphere is the stable solution and for $\varepsilon > 0.56$ the prolate configuration, see also the diagram of total energy for each solution branch in Figure 5-24(b)-(d). The behavior observed here is also similar with the secondary branch of microbubbles covered with a polymeric shell, where due to the large value of the Young modulus (or equivalently the area dilatation modulus) the stiffness of gas compression is negligible, which is depicted in the secondary branch of the bifurcation diagram with an extended area of almost zero slope, see also Figure 5-8 and Figure 5-10. The same behavior is found for a BR14 microbubble with similar dimensionless numbers $\left(\hat{k}_b = 4\times10^{-3} \;\&\; \hat{P}_A = 2.27\right)$ by Lytra and Pelekasis [87], where the curves follow the same trend when the gas pressure is omitted. In such cases it is expected that once contact is established between the two poles the solution family will turn to higher overpressures required to achieve even a marginal volume reduction, see also [59]. The latter solution family will probably arise after a limit point is achieved that stabilizes the ensuing shapes with contact in the manner observed in the context of bifurcation diagrams illustrated in Figure 5-1, Figure 5-8, Figure 5-10. Such shapes will prevail when the spherical shape is sufficiently disturbed below the primary bifurcation point.

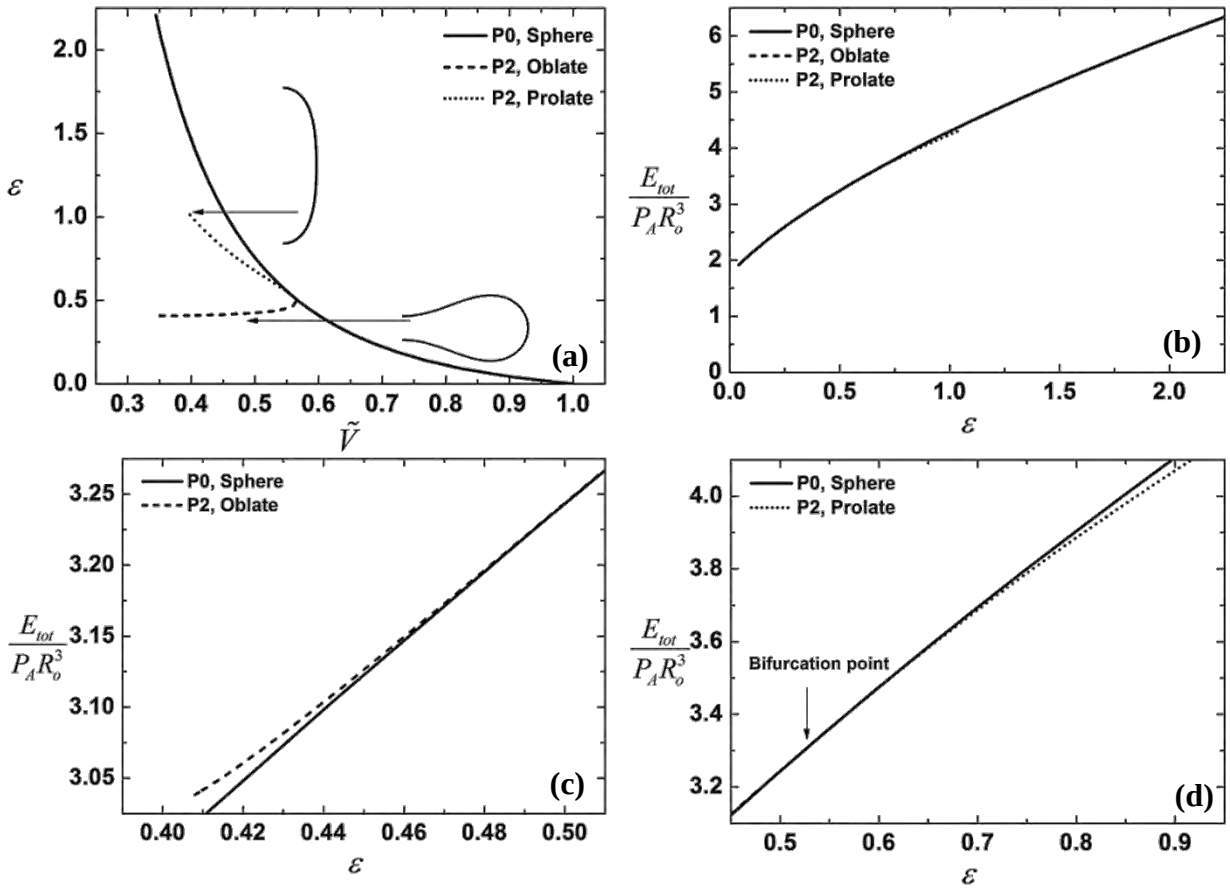

Figure 5-24: Bifurcation diagram for a microbubble with χ=0.12 N/m, $k_b = 3\times10^{-14}$ Nm, Mooney-Rivlin constitutive law and $\gamma = 0$ (incompressible gas). **(a)** External overpressure as function of the volume, **(b)** Total energy diagram, **(c)** and **(d)** Zoom in the energy of the oblate and prolate branches, respectively. ($\hat{k}_b = 1.9\times10^{-2}, \hat{P}_A = 3$).

Effect of constitutive law

Finally, the originally studied elastic shell is assumed to be governed by the linear constitutive law Hook and simulations are again performed in order to construct the resulting bifurcation diagram. The buckling point is detected when $\varepsilon = 2.1$ and $\tilde{V} = 0.45$ and the bifurcating branch is dominated by the symmetric P_2 Legendre eignemode that leads to prolate shapes that are linearly unstable. The oblate solution family is not captured in this case. The branch of prolate shapes evolves only subcritically until a limit point occurs, beyond which the solution family turns towards higher values of the external load, Figure 5-25(a)-(b), and significantly lower volumes. The energy of the prolate branch is higher than the energy of the spherical solution in the subcritical part where the former has two negative eigenvalues and similarly after the limit point until very near the primary bifurcation point, $\varepsilon \approx 2.075$. Beyond this point the prolate solution becomes energetically favorable, Figure 5-25(c)-(d), and is expected to dominate the static configuration in this parameter range. Clearly then the constitutive bears a significant effect for such shells and needs to be carefully accounted for when considering their dynamic response.

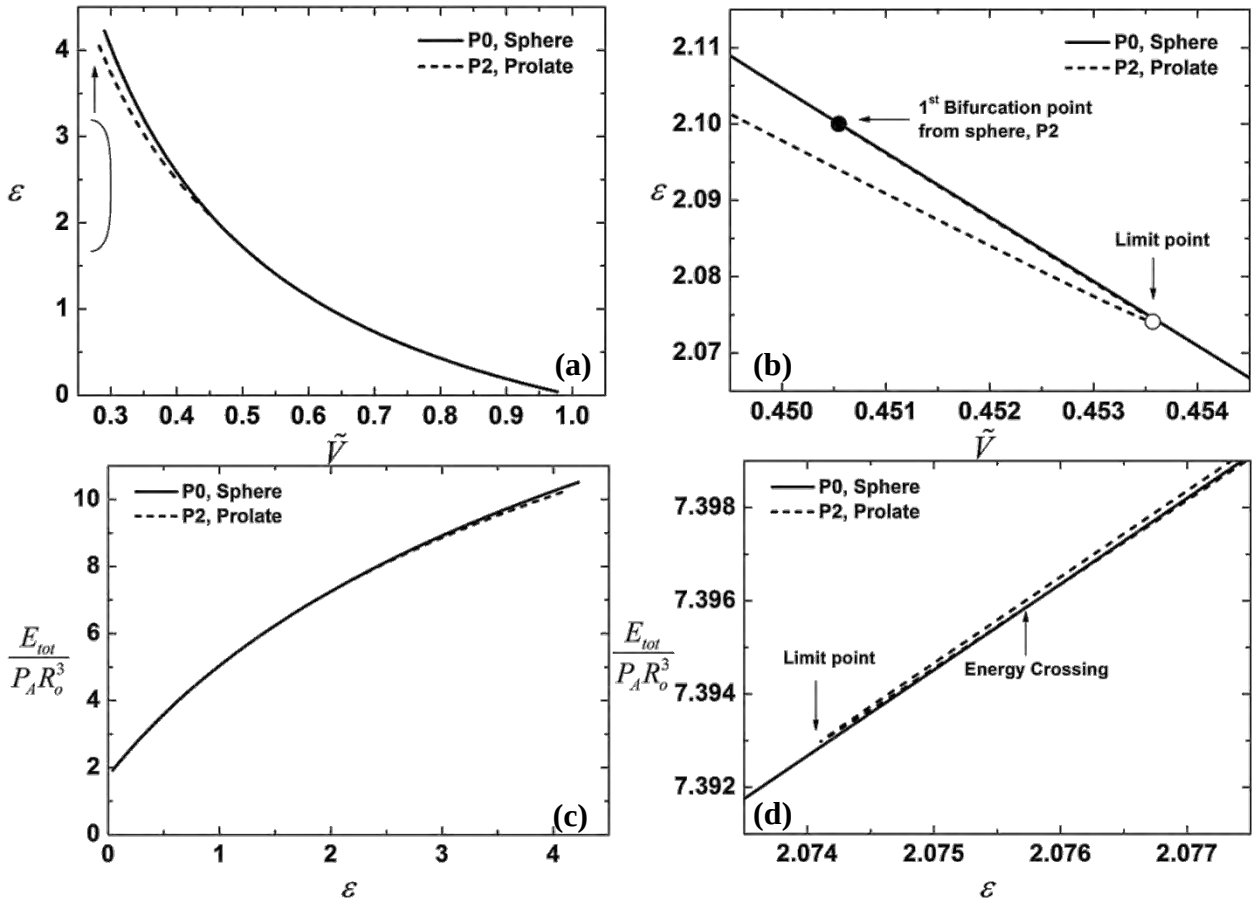

Figure 5-25: Bifurcation diagram for a microbubble with χ=0.12 N/m, $k_b = 3\times10^{-14}$ Nm, and Hook's constitutive law. **(a)** External overpressure as function of the volume, **(b)** Zoom in the bifurcation and limit point, **(c)** Total energy diagram and **(d)** Zoom in the energy near the limit point, the curve with energy higher than sphere evolves from the bifurcation point, while the curve with lower energy corresponds to progressively prolate shape. ($\hat{k}_b = 1.9\times10^{-2}, \hat{P}_A = 3$).

Chapter 6. Asymptotic Analysis - Comparison against experiments

In this chapter numerical simulations using the classic contact model and the methodology developed in the present Thesis are coupled with asymptotic analysis and available AFM measurements in order to characterize a wide range of coated microbubbles. The novel methodology proposed in the present study is based upon introducing intermolecular forces in the liquid medium that surrounds the microbubble as a means to mediate the force exerted by the cantilever. The hydrophilic nature of the shell and cantilever justify this approach as is verified by the analysis and the results of the simulations. The accuracy of the calculated response provided by the contact model that employs intermolecular forces suggests that introduction of the disjoining pressure constitutes a reliable novel approach of general validity that can describe the contact problem for a variety of materials.

In particular, the analytical expressions developed by Reissner [32, 33] *and Pogorelov* [34] *for the linear and non-linear regimes of a force-deformation curve are employed in available experimental-AFM data by Glynos et al.* [29] *for polymeric coatings. Combining the transition from the linear regime with flat shapes to the non-linear regime with buckled shapes both Young's modulus and shell thickness are estimated independently* [88-90]*. The calculated values are in excellent agreement with the experimental values of the Young's modulus and the shell thickness provided by the manufacturer* [31]*. Simulations are performed with the estimated values and the results are compared with the experimental curves employing both classic contact and intermolecular forces models. The simulations recover the transition to the buckling stage, while a third curved upwards regime in the experimental f-d is not recovered, possibly due to non-elastic phenomena. Furthermore, accounting for a variable level of prestress allows for recovering the reported multiplicity in experimentally obtained f-d curves for almost the same elastic and geometric parameters of the microbubble and the cantilever.*

The experimental f-d curves of phospholipid coatings (Definity) obtained with the AFM by Bucher Santos et al. [30] *respond almost linearly suggesting that buckling is not taking place. Thus, the Reissner to Pogorelov transition cannot be employed for parameter estimation. However, at relatively high deformations a regime curved upwards is detected which, as suggested by simulations, is governed by gas compression. A novel methodology for estimating the area dilatation modulus and bending stiffness is proposed, by coupling the slope of the experimental curve in the bending stiffness dominated Reissner regime with the cubic dependence on deformation in the gas compressibility dominated regime (Shanahan, Lulevich). The above two regimes correspond to the transition and contact region offering the major contribution, respectively, to the force exerted by the cantilever on the shell.*

6.1 Microbubble covered with polymer

6.1.1 Asymptotic Analysis - Parameter Estimation

As it is already mentioned the microbubbles covered with polymeric biomaterial are stiffer in comparison with the ones covered with a lipid monolayer in terms of elasticity modulus (E). Thus, the former are closer to conventional shells and therefore the related theory could be easily adapted. Initially, a point force, F, is assumed to be applied at the pole of the microbubble, in order to investigate its asymptotic behavior. Even though this assumption is not realistic when the AFM problem is considered, it is widely used for parameter estimation [24, 29, 88] due to its simplicity, especially for small values of deformation.

Thus, the pole of the microbubble is displaced by Δ when a point force is applied [40]. As far as the normalized deformation Δ/R_o is small, the area around the pole is compressed forming an almost flat and circular region with radius α. Beyond this area, which has a small deformation, the rest of the shell is assumed to remain spherical, Figure 6-1(a). Therefore, the normal elastic tension will be proportional to deformation, $\tau \sim Eh\Delta/R_o$, and the corresponding total stretching and bending energy will be $E_s \sim Eha^2\left(\Delta/R_o\right)^2$ and $E_b \sim Eh^3\left(\Delta/\alpha\right)^2$, respectively. Then, the ratio between stretching and bending is:

$$\frac{E_s}{E_b} \sim \frac{\alpha^4}{h^2 R_o^2} \tag{6-1}$$

and when bending and stretching are equally important $E_s \sim E_b$ or $\alpha \sim \sqrt{hR_o}$. In addition, the work done by the point force F is $W = F\Delta$. Therefore, varying the total energy with respect to Δ gives:

$$F \sim \frac{Eh^2\Delta}{R_o} \tag{6-2}$$

The above asymptotic approach is presented in [40] and was also obtained by Reissner is his pioneering work [32, 33] where he solves the above problem analytically employing the differential equations at equilibrium. Reissner proves that when a point force is acting on the pole, the force-deformation relation is linear and has the following form:

$$F = \frac{4}{\sqrt{3\left(1-\nu^2\right)}}\frac{Eh^2}{R_o}\Delta \quad \text{or} \quad F = \frac{8\sqrt{\chi k_b}}{R_o}\Delta \tag{6-3}$$

which is in accordance with eq (6-2).

Figure 6-1: Schematic representation of a microbubble subject to a point force at the pole. **(a)** Pre-buckling and **(b)** Post-buckling. Both configurations are exaggerated for visual reasons.

It is well known that increasing the point force *F*, the area around the pole will form a crater which, for the purposes of the present study, is assumed to be a mirror image of its original spherical shape, Figure 6-1(b). Most of the elastic energy is concentrated at the end of the crater, which has radius α and thickness *d*. The crater radius is assumed to be smaller in comparison with the shell radius R_o, therefore the angle $\theta_c \ll 1$, then $\alpha \sim R_o \sin\theta_c \approx R_o\theta_c$ and the crater depth is $\Delta \sim 2\left(R_o - R_o\cos\theta_c\right) \sim R_o\theta_c^2$. If ζ denotes the vertical displacement of the points on the inside of the crater, then the energies per unit area due to stretching and bending are $\tilde{E}_s \sim Eh\zeta^2/R_o^2$ and $\tilde{E}_b \sim Eh^3\zeta^2/d^4$, respectively. Moreover, $\zeta \sim \theta_c d \sim ad/R_o$ and then multiplying the energies with the dimple area $\left(\sim ad\right)$ gives, $E_s \sim Eh\alpha^3 d^3/R_o^4$ and $E_b \sim Eh^3\alpha^3/dR_o^2$. Again, when the two elastic energies are equally important, then $E_s \sim E_b$, which results in $d \sim \sqrt{hR_o}$. Substituting the value of dimple thickness (*d*) into energies and varying with respect to Δ provides the following relation originally derived by Pogorelov [34]:

$$F \approx \frac{Eh^{5/2}}{R_o}\Delta^{1/2} \tag{6-4}$$

The last result shows that when force becomes large enough for crater formation to take place, then the force-deformation relation is a non-linear equation. Pogorelov [34] extended Reissner's work by accounting for the possibility of the local mirror buckling and his analytical calculations gives a similar equation with (6-4):

$$F = \left[\frac{3.56E^2h^5}{\left(1-\nu^2\right)^2 R_o^2}\Delta\right]^{0.5} \tag{6-5}$$

Moreover, in order to investigate the above problem, but taking also into account the fact that the microbubble during the AFM is compressed by a flat cantilever, rather than a point force, the above asymptotic analysis is extended. Pauchard et al. [91] investigate a

spherical shell compressed by a flat and rigid plate. In their work, two stages are determined, stage I and II that describe the pre-and post-buckling configurations, respectively. Following this, the force-deformation relation for the stage I is assumed to have the form Giannakopoulos et al. [90]:

$$F = a\Delta + \beta\Delta^2 \tag{6-6}$$

and the coefficients α,β must be calculated. For very small values of deformation the above equation must satisfy the Reissner relation (6-3), or alternatively the dominant term is the linear and the coefficient α must be:

$$a = \frac{4}{\sqrt{3\left(1-\nu^2\right)}}\frac{Eh^2}{R_o} \tag{6-7}$$

as Reissner predicts. Then, in order for parameter β to be dimensionally correct it must have the following form:

$$\beta \sim \hat{\beta}(\nu)\frac{Eh}{R_o} \tag{6-8}$$

where $\hat{\beta}(\nu)$ is a function of the poisson ratio to be determined. Comparing the proposed function with numerical results obtained by Vaziri [52] and Shorter et al. [92], the following form of the force deformation equation is proposed for the pre-buckling stage [90] or stage I:

$$F = \frac{4}{\sqrt{3\left(1-\nu^2\right)}}\frac{Eh^2}{R_o}\Delta + 0.06543\frac{Eh}{R}\Delta^2 \tag{6-9}$$

and for the post buckling stage or stage II:

$$F = \frac{3.807Eh^{5/2}}{\left(1-\nu^2\right)^{3/4}R_o}\Delta^{1/2} \tag{6-10}$$

It is clear that the quadratic term in eq. (6-9) is negligible in comparison with the linear, thus the relation remains strongly linear.

Alternatively, and in the context of the classic contact analysis by Updike & Kalnins [47], see also the presentation in sections 2.3.1 and 3.3.1, the transition from the Reissner to the Pogorelov regime occurs in the form of a bifurcation point that marks the onset of dimpled shapes as energetically favored shapes over the original shapes that are flat at the pole region. Once the Poisson ratio is fixed the dimensionless force and deformation at the buckling point (Δ/h, $P_{Ext}/(\chi R_0)$) have a universal value that can be calculated numerically and can then be employed in order to provide estimates of the area dilatation modulus χ and the shell thickness h, based on experimental measurements of the above transition point. The latter, however, is a very sensitive measurement that is not always easy to obtain.

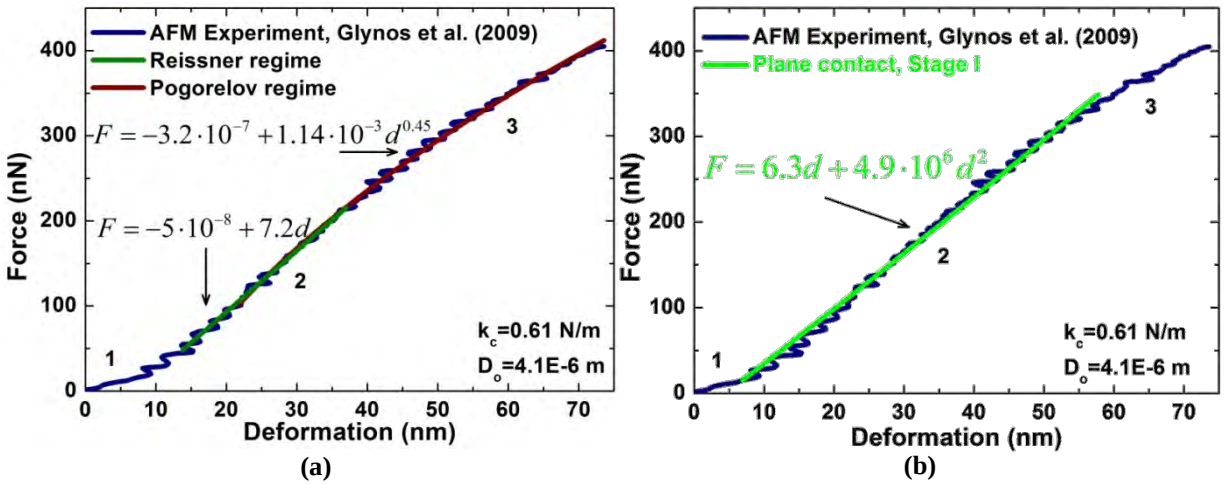

Figure 6-2: (a) Experimental force-deformation curve (blue line), along with fitting of Reissner (dark green) and Pogorelov (red) equations and **(b)** Experimental force-deformation curve (blue line), along with fitting of plane contact analysis (green).

The above analysis is of great importance as far as experimental results by the AFM are concerned, because the combination of Reissner-Pogorelov analysis with the point force and the proposed extension with the plane contact, or measurements of the force and deformation pertaining to the above transition, can provide the elasticity modulus and the shell thickness independently. Figure 6-2 illustrates a typical f-d curve [29] obtained via AFM, where three distinctly different regimes can be observed. An initial nonlinear regime, denoted with 1, occurs for very small values of the applied force - on the order of 10 nN and less - where the Albumin outer layer (thickness: ~10 nm) and intermolecular/surface adhesion forces between the shell and the cantilever are conjectured to participate in the dominant force balance with elastic forces. As the external load increases a linear regime appears, denoted with 2, followed by a nonlinear regime, denoted by 3, that is curved downwards. The linear regime is the Reissner [32, 33] regime where stretching and bending forces coming from the stiff polylactide shell balance each other over a flattened contact area that characterizes the microbubble shape. This is the part of the f-d curve that is typically used in the literature in order to infer the shell elasticity modulus once the shell thickness and radius are known [24, 29]. The third regime occurs as the external load further increases and it is known in the literature as Pogorelov [34] regime; it appears as the compressive load on the flattened part of the shell exceeds a certain value, in which case the shell bents forming a crater at the pole region while a dimple forms at some distance from the pole where most of the bending energy is stored. In the present thesis the possibility for using both Reissner and Pogorelov regimes is investigated in order to estimate the shell elastic modulus and thickness and the resulting parameters are compared against experimental values [88]. To this end, the asymptotic relations from Reissner's and Pogorelov's theory are fitted in the experimental curve; see Figure 6-2 (a), in order to obtain the slopes of the linear and nonlinear regimes, respectively:

$$\frac{F}{\Delta} = 7.2 \quad \text{and} \quad \frac{F}{\sqrt{\Delta}} = 1.14 \cdot 10^{-3} \tag{6-11}$$

with R^2=0.99 for both fitted functions. Then, solving for *E*, *h*:

$$E = 6.1\,\text{GPa} \quad \text{and} \quad h = 31\,\text{nm} \tag{6-12}$$

Similar calculations are performed with the proposed analysis developed in [89, 90], where the coefficients of stage I are calculated based on fitting in experimental data, Figure 6-2(b):

$$\text{linear coefficient} = 6.3 \text{ and quadratic coefficient} = 4.9 \cdot 10^{6} \tag{6-13}$$

with R^2=0.99. Substitution in eq. (6-9) gives E=4.6 GPa and h=33 nm.

The above calculations of the elastic modulus (E) and the thickness (h) of the shell have been repeated for all the available experimental measurements by Glynos et al. [29] and the results are in Table 6-1. The experimental estimates of the shell elastic modulus have been obtained using two different tipless cantilevers, with stiffness k_c=0.61 N/m and 1.14 N/m. Moreover, it should be stressed that they are based on Reissner's theory, eq (6-3). while adopting a linear empirical equation [31], h=1.5·10$^{-2}R_o$, for the shell thickness that is provided by the manufacturer.

As it becomes evident from Table 6-1, the calculated values for the elastic modulus and shell thickness obtained by combining the Reissner and Pogorelov asymptotic relations or the proposed extension, are in good agreement with the experimental estimates without requiring prior knowledge of the shell thickness. These findings corroborate the assertion of the present Thesis that the force-deformation curve is a sufficient measurement for the estimation of both of the elastic properties for microbubbles covered with polymeric material.

		Experimental Values [29]		Asymptotic Estimation-Point Load		Asymptotic Estimation-Plane contact-Stage I	
	D_o [μm]	E [GPa]	h [nm]	E [GPa]	h [nm]	E [GPa]	h [nm]
k_c=0.61 N/m							
	2.6	10-16	20	8.5	25	20	16
	4.1	2.5-6	31	6.1	31	4.6	33
k_c=1.14 N/m							
	3.1	6-10	23	3.4	35	10	19
	4.0	2.5-6	30	4.7	30	4.7	28
	4.9	1-3	37	4.5	31	4.9	28
	5.5	1-3	41	1.7	47	2	40

Table 6-1: Estimation of the Young's modulus (E) and shell thickness (h). Comparison between the experimental values and the asymptotic analysis.

6.1.2 Comparison between simulations and experimental-AFM data

Based on the numerical analysis developed for the classic contact model and the model that incorporates intermolecular forces, a series of simulations was carried out in order to capture the experimental curves obtained with an AFM by Glynos et al. [29] for microbubbles covered with polymeric biomaterial. Three different experimental curves are investigated here. The elasticity properties, which are used in the simulations, are the one that are estimated in paragraph 6.1.1 and the initial radius is measured with the AFM [29]. As already mentioned above, the response of various size microbubbles during the AFM experiment is different, even though they are encapsulated by the same material. Hence, in order to capture the multiplicity of f-d curves, the microbubbles are assumed to be pre-stressed and the surface tension is taken as the mean of the gas shell and bubble-water interface [17, 86], Table 6-2. The dimensionless numbers are: $\hat{k}_b = k_b / \chi R_o^2 = 2.3\times10^{-5}$, $\hat{P}_A = P_A R_o / \chi = 1.43\times10^{-3}$ and $\hat{\gamma}_{BW} = \gamma_{BW} / \chi = 3.6\times10^{-4}$. Thus, performing simulations with the classic contact model, a f-d curve is calculated and it is directly compared with the one from the AFM experiment [29], Figure 6-3 (a). It is found that the simulations recover the force - deformation curve with satisfactory agreement, compared to experimental results. The onset of buckling takes place at around the same value of deformation, which is d=60 nm, even though the bifurcation point in the experimental curve is not clearly defined, and corresponds to a contact angle of θ_c=10°. The numerical analysis presented here is an idealized description of the contact between the cantilever and the shell, and the bifurcation point causes a sharp change in f-d curve. On the contrary, the experimental approach leads to a smooth transition into buckling stage. Thus the bifurcation point cannot be easily defined from the f-d curve and additional optical measurements are required to identify more precisely the onset of buckling during the experiment. Furthermore, employing the intermolecular forces model, with the same simulation parameters as before and assuming $W_o=10^{-3}$ N/m and δ_A=50 nm both experimental and buckling curves of the classic contact model are recovered, indicating that the intermolecular forces model developed here is a reliable and novel theoretical and numerical tool, which can be used to simulate the contact problem of the AFM cantilever for both types of contrast agent microbubbles. It should be stressed that the initial nonlinear regime in the f-d curve cannot be fully captured due to lack of accurate data pertaining to the interaction potential between the cantilever and polymeric shell. Furthermore, the flat curve after the bifurcation point is not recovered, because for the elastic parameters considered here strongly favor buckling at large deformations. Finally, the experimental measurements presented in [29] register a multitude in the microbubble response for otherwise the same microbubble and cantilever geometry and materials. The simulations carried out in the context of the present Thesis attribute this behavior to the different level of shell pre-stress that is generated during sample preparation as a result of gas escaping the shell. Indeed a wide range of force deformation curves is accurately reproduced considering a certain amount of pre-stress in the form of a negative radial displacement, u, at the initial spherical configuration.

The shape of the microbubble in deformed configuration is illustrated in Figure 6-3 (b) and it can be seen that it corresponds to the linear part of the curve is flat around the contact

Shell thickness:	$h = 30$ nm	Young's modulus:	$E = 4.7$ GPa	
Initial radius:	$R_o = 2.00$ μm	Poisson ratio:	$\nu = 0.42$	
Constitutive law:	Hook	Pre-stress:	$u = -1.25 \cdot 10^{-3}$ μm	
Surface tension:	γ_{BW}=0.051 N/m	Polytropic index:	$\gamma = 1.07$	400 elements

Table 6-2: Simulation parameters for a microbubble covered with polymer (Bisphere).

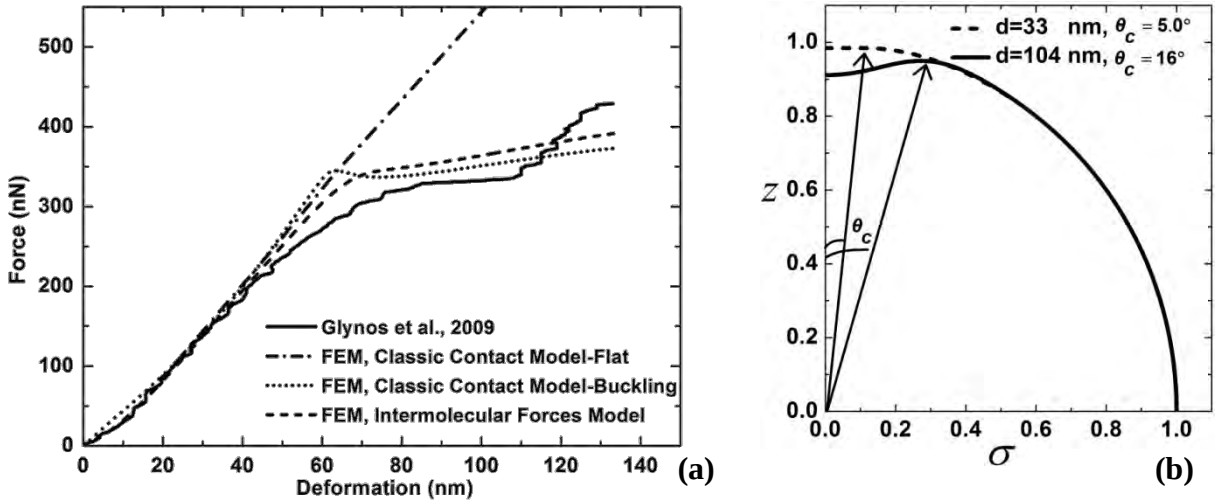

Figure 6-3: (a) Force-deformation curve, comparison of numerical (classic contact and intermolecular forces models) and experimental results, **(b)** Microbubble in deformed configuration.

area and buckling is taking place for larger values of deformation in the non-linear regime. Moreover, stability analysis on the static configuration produced by the fem curve as is presented in paragraphs 3.3.1 and 4.1 reveals exchange of stability between the pre- and post-buckling stages. However, as it is described in benchmark calculations the linear part of the pre-buckling stage could continue further on after the buckling point. In the same fashion, this part of the solution is seen to be unstable. The total energy graph for the pre- and post-buckling solutions recovers the fact that the total energy of the buckling branch is less in comparison with the linear solution after buckling, Figure 6-4 (a), thus it is preferable in the experiment. It must be noted that the total energy is the sum of the energies due to stretching, bending, gas compression and surface tension. The relative importance of the total energy components is depicted in Figure 6-4(b) for both pre- and post-buckling solutions. As can be gleaned from the last graph the energy components that vary the most as the external force increases are the energies due to elasticity, namely stretching and bending. They are equally important since bending and stretching have to balance each other for this type of shells, an equilibrium that also provides the slope of the f-d curve and the estimate of the elastic properties. It should also be noted that the stretching energy at zero deformation has a non-zero value, because the shell is treated as pre-stressed by imposing an initial negative radial displacement. The deformed area varies very little in both the pre and post buckling parts hence surface tension does not play a major role. Moreover, the energy due to the compression of the gas is negligible because the reduction of the shell volume is very small.

Next, simulations are performed for another two available experimental f-d curves [29] with the same type of coating while employing both contact models, Figure 6-5.R_o=1.75 μm, h=22 nm, E=4.22 GPa and initial radial displacement u=-0.0005 μm and and R_o=2.45 μm,

h=31 nm, *E*=1.58 GPa and *u*=-0.0016 μm; the rest of the simulation parameters are the same as in Table 6-2. The experimental curve presented in Figure 6-5 (a) was obtained with a softer cantilever, thus it was possible to capture the initial linear and the following non-linear regimes, while in Figure 6-5 (b) a stiffer cantilever can measure over a wider range of deformations. As illustrated by the above graph the response of the two numerical models is almost identical and recover the Reissner and Pogorelov regimes, but overestimate the critical buckling load. In addition, in the experiments with the stiffer cantilever a third regime is detected curved upwards, which the present modelling is not able to capture, even though the encapsulated gas is treated as compressible and it could define a regime dominated by the gas compression, see also Figure 4-6(a). However, the regime where the gas compression is relatively important is recovered by the simulations for higher values of deformation in comparison with the experimental range. Loading and unloading experimental curves show hysteresis indicating possible irreversible (plastic) deformation [29], which might explain the discrepancy between experiments and simulations in the high deformation range. However, the linear and non-linear regimes are governed by elastic behavior, they are in agreement with the present numerical (elastic) model and additionally, the estimation of the Young's modulus and the shell thickness is also in agreement with the experimental values and the shell thickness provided by the manufacturer.

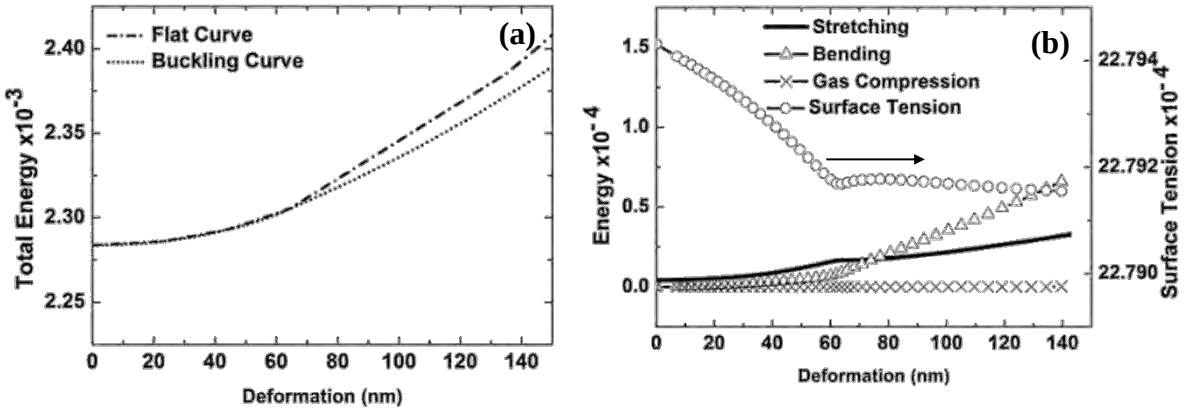

Figure 6-4: (a) Total energy as function of deformation for the two solutions after the buckling point, **(b)** Components of total energy for the pre- and post-buckling stages. The modulus of each energy is dimensionalized with the area dilatation, see session 2.3.1, and the values of surface tension energy are in the right y-axis.

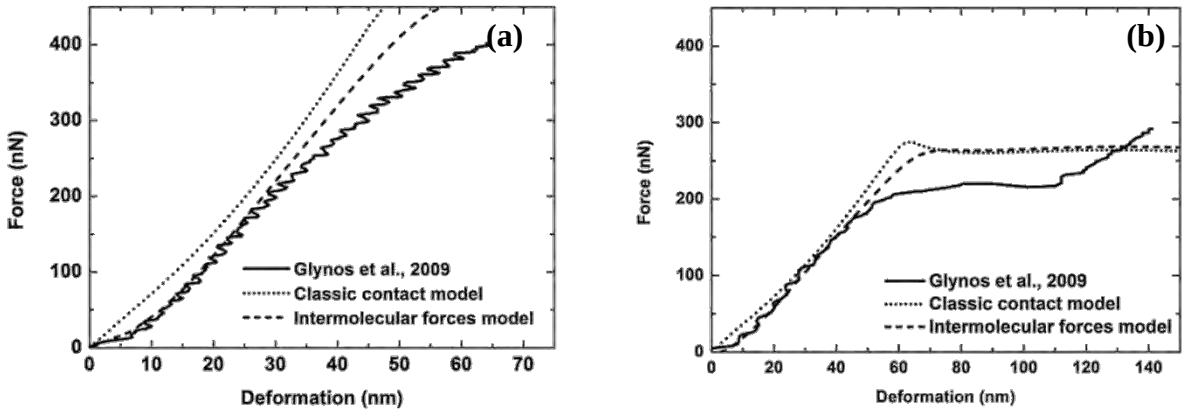

Figure 6-5: F-d curves, comparison between numerical and experimental results **(a)** R_o=1.75 μm and **(b)** R_o=2.45 μm.

6.2 Microbubble covered with phospholipid: Preliminary results

6.2.1 Asymptotic Analysis - Parameter Estimation

When lipid shells are interrogated with Atomic Force Microscopy [30] the force deformation curves that are obtained, besides a very narrow initial nonlinear regime where transition from attractive to repulsive intermolecular forces takes place between the shell and cantilever, they exhibit a quite distinct linear regime followed by a curved upwards nonlinear regime, Figure 6-6. This is in marked contrast with the response curves obtained from polymeric shells, Figure 6-2 and Figure 6-5, that exhibit a curved down response curve at large deformations that was attributed to the Pogorelov regime where shell buckling takes place leading to crater formation and the nonlinear behavior predicted by Eq. (6-5). Simulations of the static deformation of lipid shells that are compressed by a flat plate have been performed, using the methodology that invokes intermolecular forces between the shell and cantilever as a means to provide a smooth representation of the force exerted between the above two hydrophilic materials. The latter methodology was presented in section 2.3.2 and extensively used in section 4.2 in order to simulate the response of both polymeric and lipid shells. It was thus shown that this is indeed a methodology of general validity that provides reliable predictions of the static response of polymeric shells that provides a smooth transition from the flat linear to the nonlinear post-buckling regime, Figure 6-3 and Figure 6-5. An extensive parametric study was also presented in section 4.2 for a wide parameter range pertaining to both polymeric and lipid shells with accurate and reliable results.

As part of this parametric study simulations were performed fixing the product between bending and stretching resistance $k_b \cdot \chi$ in an effort to reproduce the slope of the linear part of the experimental curve based on the Reissner formula eq.(6-3), Figure 6-6(b). Next, upon fixing parameter $\hat{P}_A = P_A R_0 / \chi$ by setting the area dilatation modulus χ a series of simulations are conducted by varying k_b so that the product $8\sqrt{\chi k_b} / R_0$ conforms with the slope of the experimental F-Δ curve, see also Table 6-3. In this fashion a series of force deformation curves were obtained, Figure 6-11(a), varying both $\hat{k}_b$ and $\hat{P}_A$ while maintaining a fixed value of the product χk_b. Out of the f-d curves that were produced the one with $\hat{P}_A = 10$ reproduced the slope and range of the linear regime exhibited by the experimental curve, Figure 6-8, except for the initial nonlinear part of the curve. Due to lack of data regarding the interaction potential the value $W_0=10^{-4}$ N/m was chosen so that the f-d curve matches the maximum attractive force registered in the experiments, upon performing an initial parametric study on W_0 and the characteristic distance δ_A. The optimal value for the interaction potential was thus selected, 6-7(b), and was shown that the value of δ_A does not significantly affect the f-d curve, Figure 6-11(c). Figure 6-9(c)-(f) illustrate the evolution of the shape, the disjoining pressure, the in plane stresses and transverse shear q of the symmetrically compressed microbubble as the external force increases. Figure 6-9(a), (b) provides the actual shape as well as a blow-up of the region that joins the flat contact area with the almost spherical far field region where the interaction potential has no effect on the microbubble, illustrating the onset of a transition region that smoothly evolves the curvature of the shell from the flat contact region to the outer

region with mean curvature $k_m \sim O(1/R_0)$ and negligible disjoining pressure. Furthermore it is clear that as the force increases so does the transverse shear q which develops within the latter

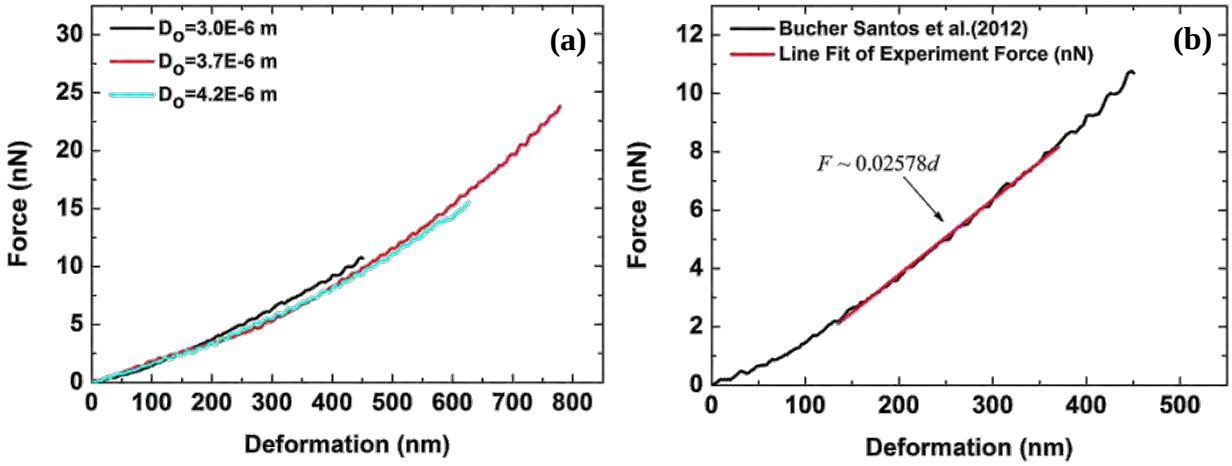

Figure 6-6: Experimental force-deformation curves for microbubbles covered with lipid monolayer, obtained via AFM by Bucher Santos et al. [30].

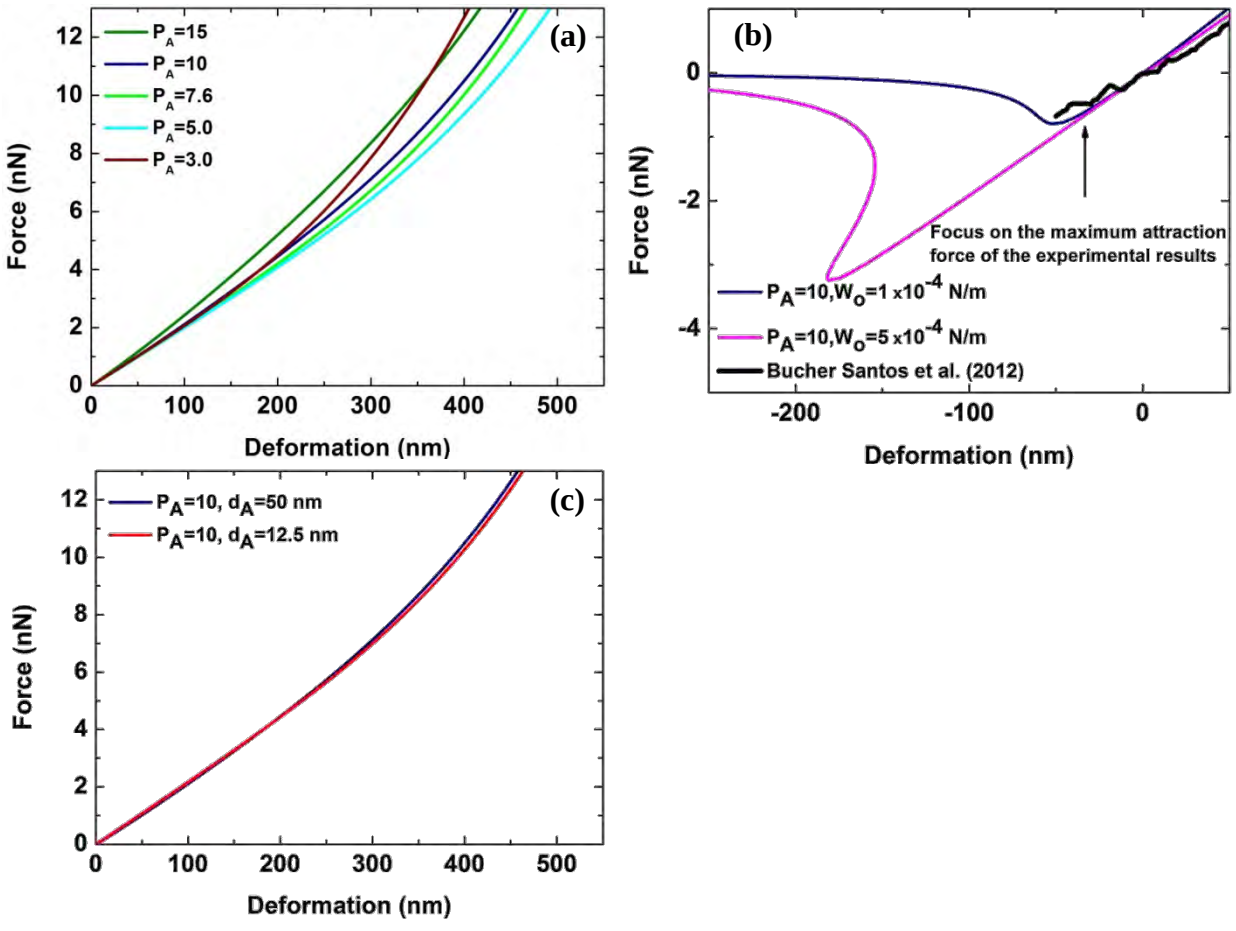

Figure 6-7: Numerical force-deformation curves for microbubbles covered with lipid monolayer obtained via FEM. During simulations $8\sqrt{\chi k_b}/R_0$ is constant, while **(a)** $\hat{k}_b$ and $\hat{P}_A$ vary as explained in Table 6-3, $W_o=1\times10^{-4}$ N/m, δ_A=50 nm, **(b)** $\hat{P}_A=10$, δ_A=50 nm and W_o varies and **(c)** $\hat{P}_A=10$, $W_o=1\times10^{-4}$ N/m and δ_A varies.

Area dilatation modulus χ [N/m]	Bending modulus k_b [Nm]	Dimensionless bending modulus $\hat{k}_b$	Dimensionless pressure $\hat{P}_A$
0.010	2.336×10^{-15}	1.0×10^{-1}	15
0.015	1.558×10^{-15}	4.6×10^{-2}	10
0.020	1.168×10^{-15}	2.6×10^{-2}	7.6
0.030	7.690×10^{-16}	1.1×10^{-2}	5.0
0.050	4.673×10^{-16}	4.2×10^{-3}	3.0

Table 6-3: Values for the area dilatation modulus and bending stiffness employed for simulation and comparison against experimental data.

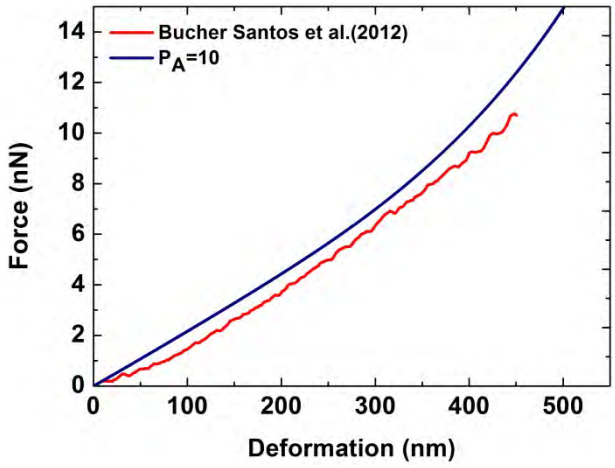

Figure 6-8: Comparison between numerical $\hat{P}_A = 10$, $W_o=1\times10^{-4}$ N/m, δ_A=12.5 nm and experimental curve [30].

transition layer [63] and is responsible for the compressive in plane stresses that develop in the contact and transition regions, mainly, of the shell. Blount et al. [63] studied free adhesion of 2-d vesicles on solid substrates via a long range attractive short range repulsive potential. Vesicles are liquid filled shells that are characterized by finite bending resistance, fixed volume and an infinite area dilatation modulus, i.e. fixed area. When the interaction potential is of equal importance as the bending resistance, $W_0R^2 / k_b = O(1),$ and the interaction length is much smaller than the bubble radius, $\delta_A / R_0 << 1,$ they recover a similar structure of the freely adhered vesicle as the one depicted in Figure 6-9and examine variations of the shape as the strength of the interaction increases. Proceeding along the same lines we can identify a similar structure of the static configuration of coated microbubbles subject to unidirectional compression, Figure 6-10(b). Our case differs from the one examined in [63] in the following ways: (a) the nature of the shell is different since in the present study it is characterized by a finite area dilatation modulus χ, (b) the geometry is axisymmetric rather than two dimensional and (c) it is not a case of free adhesion because an external force F is exerted on the cantilever and transferred to the shell via the intervening ultrathin liquid film. In the methodology developed here, see also section 4, the

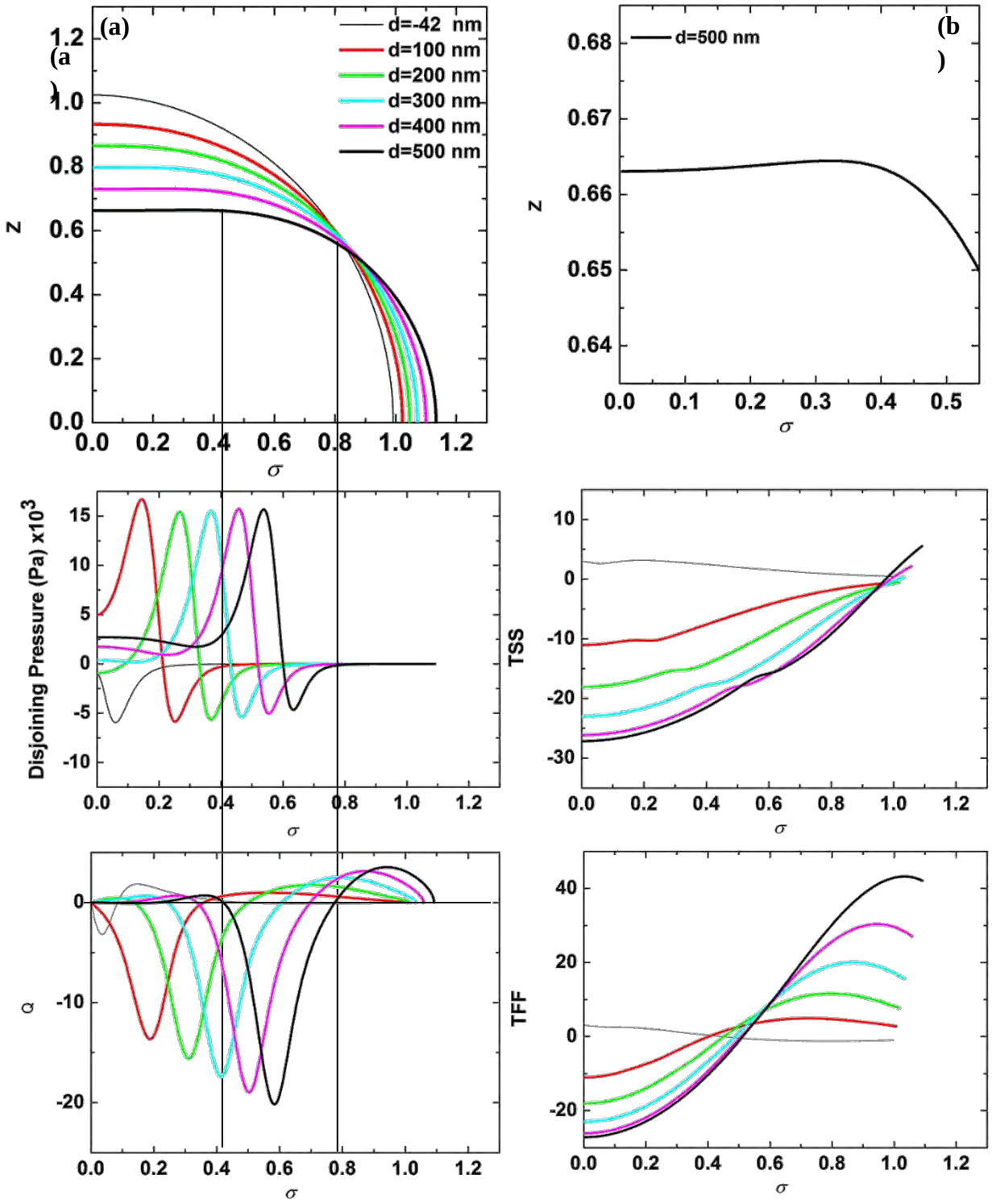

Figure 6-9: (a) Shape in deformed configuration, **(b)**. Blow up between the contact and outer regions, Distribution of **(b)** disjoining pressure, **(c)** in plane τ_{ss} tension, **(d)** shear tension q and **(e)** in plane tension $\tau_{\varphi\varphi}$ for selected values of deformation.

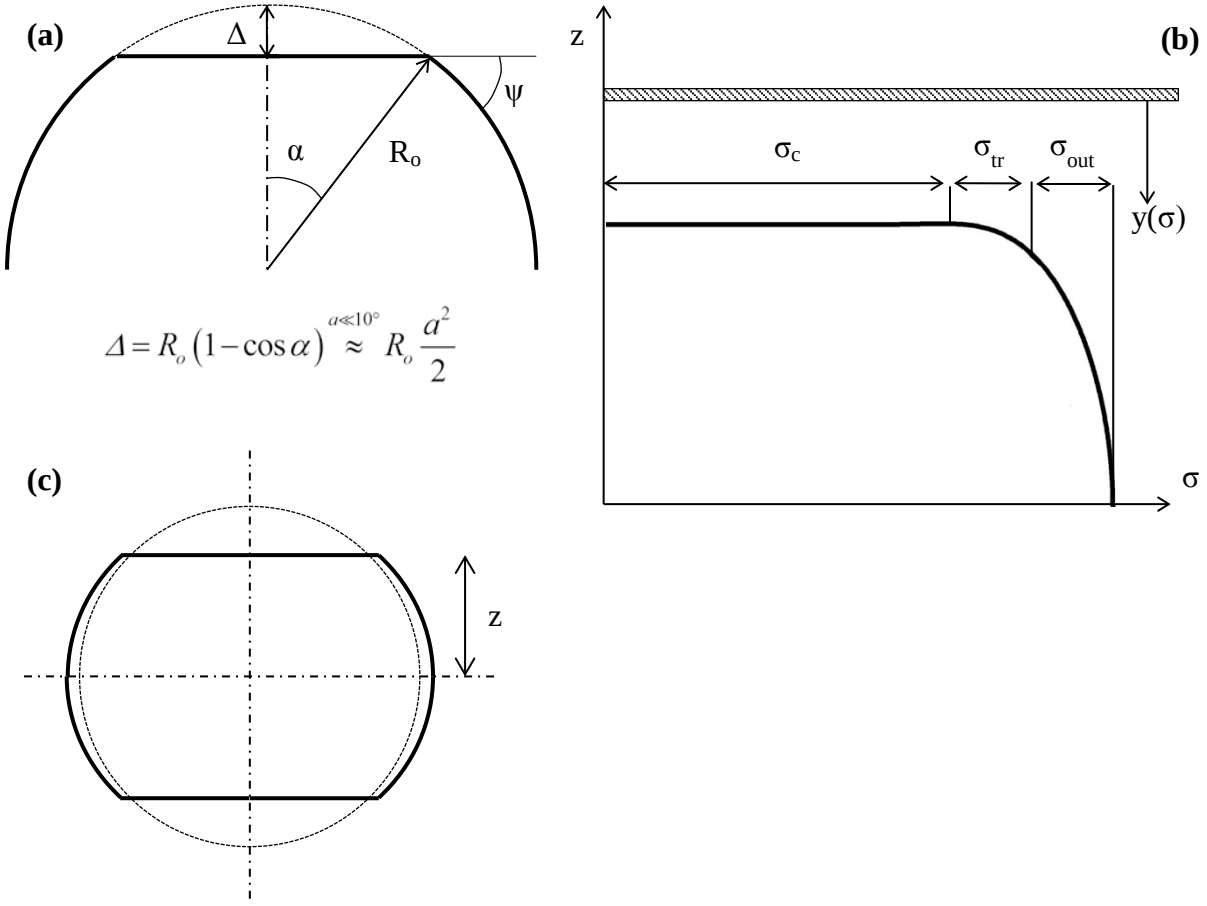

Figure 6-10: (a) Simple geometric explanation of deformation and contact angle, **(b)** Schematic representation of the contact, transition and outer regimes along the shell surface, **(c)** Microbubble compressed between two rigid plates.

force is implicitly fixed by setting the distance z_0 between the cantilever and the equatorial plane of the microbubble.

In particular we identify a flat contact region whose length-scales in the σ and z direction are L~R_0 and δ_A respectively; similarly the arc length s along the contact region scales like L as well. In this region the transverse shear q vanishes and the dominant force balance in the normal direction is formed by the disjoining pressure exerted by the film on the shell and the internal microbubble pressure that is adjusted in order to accommodate volume compression. In the tangential direction in plane stresses develop in response to area compression of the shell.

$$\begin{cases} \vec{n}: P_G - P_A \approx \dfrac{\partial W}{\partial n} \\ \vec{t}_s: \dfrac{\partial \tau_{ss}}{\partial s} \approx -\dfrac{1}{\sigma}\dfrac{\partial \sigma}{\partial s}\left(\tau_{ss} - \tau_{\varphi\varphi}\right) \end{cases} \qquad \text{(6-14a, b)}$$

The latter is mainly generated in the adjacent transition region where significant bending takes place and are enforced on the contact region via the matching condition at their interface. In the case of free adhesion the distance between the cantilever and the shell is δ_A in the contact region and the pressure in the microbubble is the same as that in the environment

P_A. During free adhesion the force on the shell is attractive and is established in the transition region. However, as the shell is compressed by the cantilever a repulsive disjoining pressure is exerted on the shell that is compensated by the internal gas pressure. Consequently, the shell thickness δ between the shell and cantilever decreases to reflect this change in ∂W/∂n. Therefore if $\hat{z} \equiv z/\delta_A$ then for not very large pressure changes, i.e. $\Delta P\left(=P_G-P_A\right)\delta_A/W_0 << 1,$ the dimensionless film thickness is but slightly decreased,

$$\hat{z}=\hat{z}_C \approx 1-\varepsilon \text{ and } \Delta P\delta_A/W_0 \approx 8\varepsilon \rightarrow \hat{z}_C \approx 1-\Delta P\delta_A/(8W_0), \tag{6-15}$$

In the adjacent transition layer the dominant balance is formed between the disjoining pressure and the bending stresses that develop as a result of the change is curvature that takes place in this region. The length-scale in the z direction remains ~δ_A whereas that in the radial direction σ adjusts its length scale, ℓ, in order to conform with the above balance, i.e.

$$k_b\frac{\delta_A}{\ell^4}\sim\frac{W_0}{\delta_A}\rightarrow \ell\sim\delta_A^{1/2}\left(k_b/W_0\right)^{1/4}\rightarrow \ell/R_0\sim\left(\delta_A/R_0\right)^{1/2}\left(\frac{k_b}{W_0R_0^2}\right)^{1/4}\rightarrow \ell << R_0 \tag{6-16}$$

Upon introducing $\hat{s}=\left(s-L\right)/\ell$, with L the length scale of the contact length for which it holds that L~R_0, we obtain as the dominant balance in the transition layer:

$$\begin{cases}\vec{n}: \ \dfrac{\partial\hat{q}}{\partial\hat{s}}\approx\dfrac{\partial W}{\partial n} \\ \vec{t}_s: \dfrac{\partial\tau_{\hat{s}\hat{s}}}{\partial\hat{s}}\approx -k_s\hat{q}\end{cases} \qquad q=\frac{q'}{k_b\left(1/R_0^2\right)}, \quad \hat{q}=\frac{q'}{k_b\left(\delta_A/\ell^3\right)} \tag{6-17}$$

$$q=\frac{\partial m_s}{\partial s}+\frac{m_s}{\sigma}\frac{\partial\sigma}{\partial s}-\frac{\partial\sigma}{\partial s}\frac{m_\phi}{\sigma}\xrightarrow{m_s\sim\hat{m}_s}\hat{q}\approx\frac{\partial\hat{m}_s}{\partial\hat{s}}$$

In other words the transverse shear q that is generated in the transition layer due to the development of the intermolecular forces results in the compressive in plane stresses that also compress the contact region. Finally, the total force exerted on the shell within the contact and transition zones is

$$F=F_C+F_{Tr}\approx\left(P_G-P_A\right)\pi L^2+q'2\pi L \tag{6-18}$$

where,

$$q=\int\frac{\partial W}{\partial n}d\hat{s}=\int\frac{\partial W}{\partial n}\frac{d\hat{s}}{d\psi}d\psi=\int\frac{\partial W}{\partial n}\frac{1}{k_s}d\psi\rightarrow q\sim\Delta\psi, \qquad k_m=k_s+k_\phi \tag{6-19}$$

In the above k_s, k_φ and km denote the curvature along the arc length of the generating curve of the shell, along the polar direction and the mean curvature of the shell, whereas Δψ signifies the turn of the normal at the edge of the contact region of the shell.

It is the relative importance between the above two contributions that determines the behavior of the force deformation curve. It depends on the relative rigidity due to bending and

volume compression. The shape of the shell in this region is provided by solving the above two equations along with appropriate matching conditions with the contact and outer regions. In particular, a shooting problem is solved with the following conditions:

$$\begin{aligned} &\hat{s}\to-\infty \quad \hat{z}\to\hat{z}_C, \quad \frac{d\hat{z}}{d\hat{s}}\to 0, \quad m_{\hat{s}}\to m_{\hat{s}c}, \quad \frac{d\hat{\sigma}}{d\hat{s}}\to 1, \quad \frac{d^2\hat{\sigma}}{d\hat{s}^2}\to 0 \\ &\hat{s}\to\infty \qquad \hat{q}\to 0 \end{aligned} \tag{6-20}$$

where $m_{\hat{s}}, m_{\hat{s}c},$ denote the bending moments at the where the contact and transition regions join. The last condition is a result of the difference in order of magnitude for the transverse shear between the transition and outer layers. In particular, based on eq. (6-17) $\hat{q}=q\left(\frac{\delta_A}{R_0}\right)^{1/2}\left(\frac{k_b}{W_0R_0^2}\right)^{3/4}$ in which case $\hat{q}\to 0$ as it approaches the outer region where q=O(1). The actual value of the transverse shear in the limit as the outer region is approached will be provided by the solution of the outer problem. On the other hand the bending moment m_s remains of the same order within the transition and outer layer, $\hat{m}_s=m_s\left(\frac{k_b}{W_0R_0^2}\right)^{1/2}$, provided $k_b\sim W_0R_0^2$ and consequently its value is calculated by solving the transition layer and used as a matching condition on the outer problem. This condition is used in the same fashion that the contact angle is used as a means to match the outer problem with the transition region for conventional drops and bubbles. Alternatively, and preferably, the curvature can be calculated within the transition region, $\hat{k}_s$, it is also of the same order as the curvature of the shell in the adjacent outer region, k_s, and used as a matching condition.

In the outer problem lengths scale with the microbubble radius, the disjoining pressure is negligible and a very similar version of the classic contact problem is recovered [46-48]:

$$\begin{cases} \vec{n}:\left(P_G-P_A\right)=k_s\tau_{ss}+k_\varphi\tau_{\varphi\varphi}-\dfrac{1}{\sigma}\dfrac{\partial\left(\sigma q\right)}{\partial s}+\gamma_{BW}\left(\vec{\nabla}_s\cdot\vec{n}\right) \\ \vec{t}_s:\dfrac{\partial\tau_{ss}}{\partial s}+\dfrac{1}{\sigma}\dfrac{\partial\sigma}{\partial s}\left(\tau_{ss}-\tau_{\varphi\varphi}\right)+k_s q=0 \end{cases} \tag{6-21a,b,c}$$

$$q=\frac{\partial m_s}{\partial s}+\frac{m_s}{\sigma}\frac{\partial\sigma}{\partial s}-\frac{\partial\sigma}{\partial s}\frac{m_\phi}{\sigma}, \qquad P_GV^\gamma=P_{G0}V_0^\gamma$$

coupled with symmetry conditions at the equatorial plane, $z=z_c$ with z_c denoting the distance between the cantilever and the microbubble's center of mass , and matching conditions at the contact point with the cantilever:

$$s=0: z=0, \quad dz/ds=0, \quad dr/ds=1, \quad k_s=\hat{k}_s \tag{6-22}$$

The transverse shear q at the contact point is obtained as part of the solution of the above outer problem. The distance z_c is a more appropriate geometrical property imposed on the

outer problem than the angle of contact φ_c since the latter is not as easy to measure in an experiment. In classic solutions of the contact problem [46-48] angle φ_c is used as a condition along with the bending moment m_φ calculated within the flat contact region. In view of the above it can be seen that such solutions constitute an outer problem of the contact configuration that are valid in cases for which the interaction potential is negligible. As a result the bending moments are not modified within the transition layer, the latter is absorbed in the outer region, and the flat region is in direct contact with the outer one.

Nevertheless, the solution of the outer problem as formulated here is also subject to the Reissner solution[32, 33], as is the case with the standard formulation presented in [46-48], provided a significant increase in the internal gas pressure does not take place. In such a situation, as can also be seen by the numerical solution provided by the simulations in Figure 6-9, the disjoining pressure is negligible in the contact region and exhibits a peak within the transition region and so does the transverse shear q. Then, provided the size of the transition region is small and the shell remains relatively shallow, i.e. deformation Δ remains much smaller than z_c (Figure 6-10(a)), the transverse shear q is exerted at the point of contact, the shell remains almost spherical and the Reissner solution is valid, thus corroborating the linear part of the f-d curve registered in AFM measurements, Figure 6-6, and recovered by the simulations, Figure 6-7.

However, the experiments as well as the simulations also capture a nonlinear curved upwards response pattern in the f-d curve which does not conform with the Reissner solution or the curved down post buckling regime. As indicated by the simulations and illustrated by the distribution of the disjoining pressure shown in Figure 6-9, this regime is associated with the onset of considerable rise in the gas pressure in the microbubble and a concomitant reduction in the film thickness in order to accommodate the balance in the contact region. When gas compressibility is of central importance in the response of coated bubbles to external forcing, it is the balance between pressure drop across the interface and in plane stresses that determine the f-d curve [25, 50]. Following the analysis presented by Shanahan [50], with the difference that an initial pre-stress is not considered herein, in the analysis presented below; we obtain for a symmetrically compressed microbubble. In view of the symmetry of the configuration, we concentrate on one of the two parts of the shell which we assume to be shallow, Figure 6-10 (c), and consequently to remain almost spherical. In the absence of compression the shell is assumed to be spherical with pressure P_0 equal with the external, P_A, and volume $V_0=4\pi R_0^3/3$.

Assuming that the contact length $L\approx R_0\sin\theta$, Figure 6-10(c), is larger than the size of the transition layer, $L >> \ell$, and that the shell is shallow, $\Delta<<z$, we obtain the following estimate for the shell volume when it is inflated at the equator, $R=R_0+\delta R$, due to the external force and at the same time it is flattened at the two poles. In the last two regions the shell volume is decreased by an amount equal to the volume of two spherical sectors of radius R and angle θ,

$$V=\frac{4\pi R^3}{3}\left[\frac{3}{2}\cos\theta-\frac{\cos^3\theta}{2}\right]\xrightarrow[\theta\ \text{small}]{R=R_0+\delta R}V\approx V_0\left(1-\frac{3\theta^4}{8}+3\frac{\delta R}{R_0}\right)\xrightarrow{\delta R/R_0=\lambda\theta^4}$$

$$V\approx V_0\left[1-3\theta^4\left(\frac{1}{8}-\lambda\right)\right]\xrightarrow[\gamma=1]{\text{Isothermal Compression}}P_G=\frac{P_A}{1-3\theta^4\left(\frac{1}{8}-\lambda\right)} \tag{6-23}$$

Next, treating the shell as neo-Hookean with negligible bending in the outer region and an almost spherical shape we obtain the following force balance:

$$P_G-P_A\approx\frac{2\chi}{R}\left(\frac{R^2}{R_0^2}-1\right)\approx\frac{2\chi}{R_0\left(1+\lambda\theta^4\right)}\left[\left(1+\lambda\theta^4\right)^2-1\right]\approx\lambda\frac{4\chi}{R_0}\theta^4 \tag{6-24}$$

Upon combining the last two equations we recover the following relation for λ and the pressure drop across the shell:

$$\lambda=\frac{1}{8}\frac{1}{\left(\frac{4\chi}{3R_0P_0}+1\right)},\quad P_G-P_A=3P_A\theta^4\left(\frac{1}{8}-\lambda\right) \tag{6-25}$$

In this fashion the force exerted on the shell at the contact region reads as:

$$F_C=\left(P_G-P_A\right)\pi L^2\approx\left(P_G-P_A\right)\pi R_0^2\sin^2\theta\xrightarrow{\theta\ small}F_C\approx3\theta^6\pi R_0^2P_0\left(\frac{1}{8}-\lambda\right)\xrightarrow{(6.25)}$$

$$F_C\approx\theta^6\pi R_0^2P_0\frac{3}{8}\left(1-\frac{1}{\frac{4\chi}{3R_0P_0}+1}\right)\xrightarrow{\chi/(R_0P_0)<<1}F_c\approx\pi R_0\chi\frac{\theta^6}{2}\xrightarrow{\Delta\sim\frac{\theta^2}{2}}F_c\approx\frac{4\pi\chi}{R_0^2}\Delta^3 \tag{6-26}$$

$$\chi=\frac{3R_oP_o}{4}\left(\frac{1}{1-\frac{s_3}{3\pi P_oR_o^2}}-1\right),\quad s_3=\frac{F}{\Delta^3} \tag{6-27}$$

which is the same as the formula developed in [25], when the Poisson ratio is set to 0.5, and employed in [30], for estimating the elastic properties of phospholipid shells. Based on the above analysis it is proposed that Reissner's linear formula, that holds when the force on the shell is balanced by bending stresses in the transition region, can be combined with the above formula (6-26), that holds when the force on the shell is balanced by pressure drop across the shell in the contact region, in order to provide reliable estimates of the shell area dilatation modulus and bending stiffness.

In this context, an effort was made to recover the shell area dilatation and bending moduli based on the above asymptotic results, .i.e. employing a combination of Eq's (6-3) and (6-26) in the way Eq. (6-3) was combined with Eq. (6-4) to obtain the respective properties of polymeric shells. In particular, for the case with $\hat{P}_A=10$ the slopes of the linear and non-linear regimes of the numerical curve are calculated, Figure 6-11(a). Both fitting curves conform

with the applied formulas with great reliability, R^2=0.99. Then employing eq. ((6-27) the area dilatation is estimated. The resulting value is $\chi = 1.49 \times 10^{-2}\ N/m$. Subsequently, the bending modulus is estimated by substituting in Reissner's eq. (6-3) the area dilatation modulus and the linear slope. The resulting value is $k_b = 1.269 \times 10^{-15} Nm$. Repeating the previous calculation for the $\hat{P}_A = 3$ numerical case, the resulting values of area dilatation and bending moduli are $\chi = 3 \times 10^{-2}\ N/m$ and $k_b = 5.99 \times 10^{-16} Nm$, respectively. As can be gleaned from Table 6-3 the above estimates are in satisfactory agreement with the values employed during simulation.

In addition, it should pointed out that Bucher Santos et al. [30] proposed the Lulevich et al. [25] model for the estimation of Young modulus of such coatings, which as described here is a cubic function of deformation. In the same study the Reissner model is not adopted, because it predicts unrealistically small values of the Young modulus, for a value of the shell thicknes, h=5 nm, provided by the industry. At this point, it is necessary to clarify that bending modulus of lipid monolayers is an independent parameter and is not related with the thickness or the elasticity modulus, as is also the case with red blood shells [71] which are coated with a phospholipid bilayer. The appropriate parameters in order to describe the mechanics of lipid monolayers are the bending modulus and the area dilatation modulus, which should be treated independently. Thus, it can be seen that the Reissner model is also valid for the experimental curves pertaining to phospholipid shells, but must be written in terms of the above elastic properties. Then, upon assuming a typical value of the bending modulus $k_b \sim 3 \times 10^{-16} Nm$ while applying Reissner's formula for the f-d slope that was obtained through AFM, the area dilatation modulus is $\chi \sim 0.08 N/m$ which is a reasonable value. In fact, in the study of Bucher Santos et al. the estimated value of the Young modulus turns out to be E~15 MPa or χ=0.075 N/m, Figure 4 in [30]. In addition, the simulations of the present thesis verify that the linear response of the experimental curves is a typical Reissner regime, Figure 6-8. Performing further calculations combined with experimental measurements obtained until higher deformations are achieved, within the curved upwards regime of the f-d curve, will validate the above methodology for estimating the elastic proeprties of lipid shells by combining the bending dominated, i.e.Reissner, with the gas compressibility dominated regime.

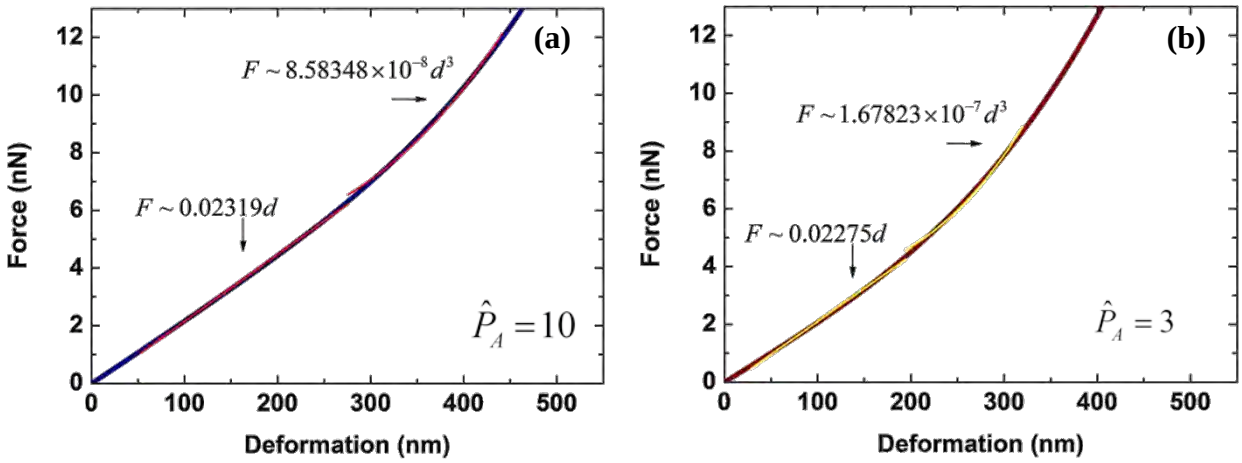

Figure 6-11: Fitting in linear and non-linear regimes of the numerical force-deformation curve for **(a)** $\hat{P}_A = 10$ and **(b)** $\hat{P}_A = 3$.

Chapter 7. Concluding remarks and future directions

7.1 Concluding remarks

The present thesis investigates the static response of microbubbles subject to static loads. Three major problems are studied:

- The contact problem
- The bifurcation diagrams
- The estimation of the elastic properties

In the first problem the microbubble is compressed by a rigid and flat surface in order to simulate the case of the atomic force microscope (AFM), while in the second problem the static buckling of a microbubble is studied, where the shell is subject to a uniform normal load. In both problems, the normal and tangential force balances are solved, coupled with the isothermal equation of the gas compression via FEM, assuming axisymmetry and employing the b-cubic splines as basis function. The numerical models are validated against similar analytical [46-48] and numerical [59] solutions with excellent agreement, while the results of the contact problem are also compared against available experimental AFM data [29, 30]. In addition, a methodology is proposed for the estimation of the shell properties by analyzing the different regimes in force-deformation (f-d) curves. Hence, the conclusions of the present thesis are demonstrated initially for the contact problem and the characterization of the shell and then for the bifurcations diagrams, while at the end of the chapter some ideas are discussed as means of future work.

7.1.1 The contact problem and characterization of the coating

In order to simulate a microbubble compressed by the cantilever of an AFM two numerical models are proposed. The first is a simple model, inspired by the analytical work of Updike & Kalnins [46], where the applied load is concentrated at the end of the contact between the cantilever and the shell, paragraphs 2.3.1 and 4.1. The last assumption was validated by the present thesis, where the calculation of the pressure distribution along the contact line shows that the loading is a point non-zero function at the end of contact. It is shown that as the shell is compressed the region near the cantilever (pole) is flat and the solution is characterized by one negative eigenvalue; it arises as a result of the translational invariance of the problem and is dominated by P1. After the buckling point, the shell buckles in the pole due to high compressive tensions, forming a dimple. The flat solution is still an option after the buckling point, but in comparison with the buckling solution it has higher energy and one more unstable eigenvalue. Thus, buckling is the energetically favorable state. It is not only the shape and the eigenvalues that distinguish the two solutions, but additionally their representation in f-d curves. The response of a flat f-d curve is linear, known as Reissner regime, while the buckling curve is non-linear curved downwards, known as Pogorelov regime. In other words, the f-d curve is a bifurcation diagram, with the force representing the integral quantity that changes for different values of deformation. In addition, non-dimensionalization of the governing equations gives rise in two dimensionless numbers,

$\hat{k}_b, \hat{P}_A$, which define the relative importance of bending and gas compression to the area dilatation modulus, respectively. The parametric analysis shows that an increase in the values of the dimensionless bending modulus $\hat{k}_b$ shifts the bifurcation point to higher values of force and deformation, because the definition of $\hat{k}_b$ is equivalent to the ratio of shell thickness to radius, especially for polymeric coatings. Thus, as $\hat{k}_b$ increases the shell becomes thicker, therefore buckling is postponed. The second dimensionless number is a nominal measure of the gas compressibility. As mentioned in the previous chapters the reduction of the shell volume raises the gas pressure and $\hat{P}_A$ defines how important the pressure increase is as an extra stiffness in the shell equilibrium. Shells with a relatively high area dilatation modulus are characterized by $\hat{P}_A \ll 1$. Therefore the effect of gas compression only manifests itself at high values of deformation in the buckling solution, where a third non-linear curved upwards regime is calculated. For these values of deformation the shell is significantly compressed and the pressure has increased sufficiently so that it contributes as an additional stiffness. Therefore the required force increases in comparison with a shell that has lower $\hat{P}_A$ or when the gas is treated as incompressible. When $\hat{P}_A > 1$ and buckling takes place, gas compressibility participates in the equilibrium for lower values of deformation, thus modifying the «curved downwards» post-buckling response earlier. Assuming an initially pre-stressed shell with residual compressive elastic tensions or accounting for the surface tension of the shell-liquid interface, the internal pressure decreases or increases, respectively, resulting in an equivalent change in the required force.

The second contact formulation, paragraph 2.3.2 and 4.2, is a model that takes into account the thin liquid film between the cantilever and the shell, due to the hydrophilic nature of lipid monolayers. In this model, as the cantilever approaches the microbubble the liquid phase is thinning and the pressure locally increases in comparison with the liquid bulk. The increase of pressure is known as disjoining pressure and represents the mechanism which transfers the forces from the cantilever to microbubble. The interaction of the two bodies is modelled with a sort-ranged potential, characterized by its minimum value (W_o) and the height of the film (δ_A) that minimizes the potential. Employing the formulation proposed here it is possible to calculate the force and the resulting deformation (Δ), when the distance between the cantilever and the center of mass of the microbubble is known, as will be the case in AFM measurement. The force is attractive / repulsive when the liquid film is higher or lower than the characteristic length δ_A, respectively. In any case, the response of the f-d curves is initially linear ($\sim\Delta$) with flat shapes while for relatively small dimensionless bending stiffness, $\hat{k}_b \sim 10^{-4} - 10^{-5}$, the response becomes non-linear ($\sim\Delta^{0.5}$) and buckling takes place in the area around the pole. In addition, when the gas compressibility is important, $\hat{P}_A \gg 1$, a third regime is detected in the post buckling regime that is curved upwards ($\sim\Delta^{2.5\text{-}3}$). However, for not large area dilatation moduli, $\hat{k}_b \sim 10^{-3} - 10^{-2}$, buckling is bypassed to a gas compression dominated regime. In addition, W_o represents the degree of adhesion between the cantilever and the microbubble. Thus, the regime with $W_0 / \chi \sim 1$ describes the strong adhesion state, while when

$W_0 / \chi \ll 1$ the adhesion is weak. Simulations show that when the adhesion is strong, buckling is postponed or bypassed, because strong tensile stresses are developed as the shell is strongly adhered on the cantilever.

Thus, both contact models can recover the transition from Reisssner to Pogorelov and then to pressure dominated regime or the transition from Reissner to pressure regime, when buckling is bypassed. However, the intermolecular forces model is more realistic, because it accounts for the existence of the liquid film and provides valuable information for the adhesion and the required pull-off force. In addition, calculation of the disjoining pressure profile along the shell surface confirms that most of the applied pressure is concentrated at the end of the contact regime, recovering the formulation proposed by the classic contact problem, where the applied load is a ring-line load at the end of the contact. Moreover, the shear tension in both problems follows the variations of the applied load. Thus, in the classic contact the shear tension has a discontinuity at the end of contact, while in the intermolecular forces model the shear tension is a smooth function over an area rather a point. The latter area is essentially a transition regime that connects the part of the shell that is in contact (contact regime) with the outer shell that in small deformations is almost spherical (outer regime). Updike and Kalnins [46-48] divide the shell into two areas, the contact and the outer, implying that the transition regime shrinks to a point. Estimation of the transition regime length based on the simulations performed in the context of the present thesis show that the transition regime increases as bending stiffness and the characteristic length increase or when the maximum value of the potential decreases.

It should also be pointed out, that in order to follow both flat and buckling curves of the classic contact problem a specific contact angle must be selected as the continuation parameter or alternatively the number of contact elements, which is a constraint, because for an angle that is not an integer multiple of the contact angle it is not possible to seek for a solution. On the other hand, when the contact problem is investigated with the adhesive potential, the continuation parameter is the relative distance between the cantilever and the shell, where a reasonable small step in distance can provide of the means for a parametric continuation of the solution as the force increases.

The experimental f-d curves obtained with an AFM for polymeric coatings by Glynos et al. [29] exhibit the above described transition from the linear-Reissner regime to non-linear Pogorelov regime. Thus, fitting the analytical expressions developed by Reissner [32, 33] and Pogorelov [34] is possible to calculate the slope of two regimes. Thus, both Young modulus and shell thickness can be calculated simultaneously [88, 89] from a single measurement and without prior knowledge of the thickness, which is usually provided by the manufacturer. In addition, the extension of the Reissner work by Giannakopoulos et al. [90] can also provide the above properties. In both ways, the calculated values are in excellent agreement with the experimental estimates.

On the other hand, Bucher Santos et al. [30] perform AFM measurements for phospholipid coatings. The f-d curves are linear indicating that buckling is not taking place, while exhibiting a distinct tendency to curve upwards for large deformations. Employing simulations with the intermolecular forces model for relatively big values of the dimensionless bending modulus the response of the above experiments is recovered. In addition, the fem

curve is initially linear and then is curved upwards. Thus, the Pogorelov regime is bypassed to a gas compression dominated regime. Combination of numerical results and asymptotic analysis provides analytical expressions to estimate the elastic properties by applying on the numerical curves Reissner's theory combined with an expression that was developed in the present study that extends Shanahan's [50] and Lulevich's et al. [25] theory to account for gas compressibility. In addition, the length of the transition regime is calculated via asymptotic analysis as a function of the elasticity and adhesive properties.

Finally, the main conclusions are outlined below:

- The intermolecular forces model is a novel tool that recovers the experimental f-d curve for microbubbles covered with either polymeric or phospholipid monolayer shells.
- The elastic properties of microbubbles covered with thin polymeric shells can be estimated from AFM [29] measurements by the transition from the flat (Reissner) to the buckled (Pogorelov) branch.
- Buckling for microbubbles covered with lipid monolayer [30] is not detected – The static response initially follows the linear Reissner solution where bending stiffness dominates and beyond a certain level of deformation resistance to compression dominates rigidity and a nearly cubic (Δ^3) response pattern is recovered.
- The elastic properties, namely area dilatation and bending modulus, of phospholipid shells can also be estimated from AFM measurements by the transition from the bending stiffness (Reissner) regime to a gas compressibility dominated regime.
- The parametric analysis shows that the dimensionless bending modulus controls the buckling point, but in case of strong adhesion buckling is postponed to higher values of force and deformation or it is totally bypassed.
- Based on the above analysis, it can be concluded that microbubbles covered with lipid monolayer behave like viscoelastic solids.

7.1.2 The uniform pressure problem and bifurcation diagrams

The second problem that is studied in the context of the present thesis is the buckling of coated microbubbles subject to a uniform and normal static load. Bifurcation diagrams are constructed for both types of materials and their response is investigated separately for indicative parameters available from the literature [16, 19, 86].

In both polymers and phospholipids, when the dimensionless bending modulus, $\hat{k}_b$, is relatively small the first instability on the spherical branch is dominated by a symmetric mode. Decreasing $\hat{k}_b$, which essentially is equivalent to an increase on the area dilatation modulus, χ, the first instability is dominated by an asymmetric mode. In this case the shell forms one dimple in order to relax the compressive tensions, which now are higher, because χ is higher. Further decrease of $\hat{k}_b$ causes a new exchange with symmetric shapes dominating again in the first instability, because in order to achieve static equilibrium two dimples are required to relax the compressive tensions. This trend is detected in both materials via parametric study for $\hat{k}_b$.

Furthermore, in both polymers and lipids, when the first bifurcation is dominated by an asymmetric mode, the secondary branch evolves subcritically and after a limit point evolves towards higher loads than the critical buckling load, where it tends to form a contact line in the region around the two poles. The second bifurcation is dominated by a symmetric mode which evolves transcritically. The subcritical branch evolves the same way as the asymmetric one and is characterized by oblate shapes. As the supercritical branch evolves it is characterized by prolate shapes. Both subcritical branches have more unstable eigenvalues in comparison with the sphere and higher energy, before exhibiting a limit point. However, after the limit point each of them loses one unstable eigenvalue in comparison with branch that emerges right after the bifurcation point. In fact the primary bifurcating branch, after the limit point, is linearly stable and additionally has lower energy as it evolves towards pole coalescence. The supercritical symmetric branch initially inherits the stability of the sphere and it is linear stable. In the case of polymeric shells, it exhibits a limit point very close to the bifurcation poin, which leads to a non-monotonic response, characterized by multi-lobed shapes. The same branch in lipids doesn't exhibit the limit point, it keeps the stability as explained above and it is characterized by progressively more prolate shapes.

In addition, for both materials, when the first instability on the spherical solution is symmetric, the second instability for a higher load is asymmetric and it was not possible to follow this branch to any direction. Only in the case of polymers, does the symmetric subcritical branch soon exhibit a new unstable eigenvalue. Disturbing the symmetric solution with the new eigenvector a new solution branch emerges with asymmetric shapes, which as the branch evolves tend to form a contact zone. This is conjectured to be the result of a mode coalescence event as the two bifurcation points coincide. In the parameter range beyond this coalescence the bifurcation diagram changes. The asymmetric branch evolves over a small interval of the external overpressure and is conjectured to terminate on the asymmetric branch in the form of an additional bifurcation point that appears on the symmetric branch and is also asymmetric in nature. In case of lipids the subcritical symmetric solution doesn't have any

additional unstable eigenvalue before the limit point, which could lead to an asymmetric solution as in polymers.

Furthermore, the above local satiability characteristics near the first bifurcation point are very important to understand the nature of the buckling, but there is a global stability behavior determined by minimum total energy. Below the bifurcation point and before the limit point, the energetically favorable configuration is a compressed sphere, but after the limit point the solutions with the lower energy are buckled which tend to coalesce. The above picture is corroborated when they are combined with numerical results from the dynamic buckling [19], where for loads higher than the buckling point buckled shapes characterize the solution, while below the bifurcation point spherical shapes are captured.

Moreover, as was repeatedly mentioned, microbubbles covered with lipids have lower area dilatation modulus and as they are compressed the increase of the internal pressure is comparable with the elasticity, which in the contact problem introduced a third regime in f-d curve. Here, the significant contribution of gas compression to the shell equilibrium is depicted with a rapid change in the slope of the bifurcation diagram after the limit point. In polymers, where the internal gas doesn't contribute in the equilibrium so much, the slope after the limit point changes very slowly. The last finding agrees well with parametric analysis for lipids, where as the area dilatation increases the importance of gas compression is less, hence the slope after the limit point is less. In addition, surface tension prevents buckling, whiletranslating the buckling point to higher values of load, but it doesn't change the order of appearance of the modes. On the other hand, changing the constitutive law of the elastic tensions can change the mode of the first instability. Considering a different constitutive law, strain softening or strain hardening, the effective area dilatation modulus increases or decreases in compression, respectively. Thus, the effective dimensionless bending modulus increases or decreases and the order of appearance of the first mode changes accordingly as described for the dimensionless bending modulus. To sum up:

- For relatively big values of bending modulus the first bifurcation is dominated by symmetric shapes, for intermediated values by asymmetric ones and for relatively small values of $\hat{k}_b$ symmetric shapes characterize again the first bifurcation.
- The asymmetric branches evolve only subcritically, while the symmetric ones transcritically.
- In polymers, when the first bifurcation is symmetric, an asymmetric branch emerges from the symmetric solution.
- As the subcritical branch of the primary bifurcation evolves towards lower external loads, it exhibits a limit point and becomes linearly stable with lower energy than the spherical branch and a contact area as the two poles merge
- The contact zone in polymers is obtained in very small values of the volume, while in lipids in higher.

7.2 Future directions

In the future the following aspects could be studied in order to improve the above results or starting from them to explore new problems:

Contact problem:

- Further calculations on the estimation of phospholipid elastic properties.
- Asymptotic analysis on the transition regime and extraction appropriate boundary conditions for trapped microbubbles.
- Experiments for phospholipid microbubbles to verify the curved upwards regime by focusing on higher deformations.
- Simulation of a trapped microbubble with the disjoining pressure.
- Considering the contact as a non-symmetric problem with respect to the equator, which will probably refine deviations between numerical and experimental results.
- Capturing of the third curved upwards regime in experimental f-d curves of polymeric coatings via FEM.
- Further calculations and simulations for a free microbubble, which could describe the behavior of nano-bubbles.
- Modelling of 3d deformations in order to investigate the limits of the axisymmetric hypothesis. However, it should be noted that in the AFM experiments the deformations are relatively small, especially for polymeric coatings, thus the axisymmetric analysis is sufficiently acceptable.

Bifurcation diagrams:

- Further calculations in order to better understand the nature of the supercritical symmetric branch as well as the secondary bifurcations it may entail.
- Verify the effect of mode coalescence in the bifurcation diagram for specific parameter values.
- Formulate and simulate the contact zone in relatively small volumes.

References

1. Gramiak, R. and P.M. Shah, *Echocardiography of the aortic root.* Invest Radiol, 1968. **3**(5): p. 356-66.
2. Ferrara, K., R. Pollard, and M. Borden, *Ultrasound Microbubble Contrast Agents: Fundamentals and Application to Gene and Drug Delivery.* Annual Review of Biomedical Engineering, 2007. **9**(1): p. 415-447.
3. Kaufmann, B.A., K. Wei, and J.R. Lindner, *Contrast Echocardiography.* Current Problems in Cardiology, 2007. **32**(2): p. 51-96.
4. Stanziola, A., M. Toulemonde, Y.O. Yildiz, R.J. Eckersley, and M.X. Tang, *Ultrasound Imaging with Microbubbles [Life Sciences]*. IEEE Signal Processing Magazine, 2016. **33**(2): p. 111-117.
5. Liu, Y., H. Miyoshi, and M. Nakamura, *Encapsulated ultrasound microbubbles: Therapeutic application in drug/gene delivery.* Journal of Controlled Release, 2006. **114**(1): p. 89-99.
6. Klibanov, A.L., *Ligand-Carrying Gas-Filled Microbubbles: Ultrasound Contrast Agents for Targeted Molecular Imaging.* Bioconjugate Chemistry, 2005. **16**(1): p. 9-17.
7. Ye, J., H. He, J. Gong, W. Dong, Y. Huang, J. Wang, G. Chen, and V.C. Yang, *Ultrasound-mediated targeted microbubbles: a new vehicle for cancer therapy.* Frontiers of Chemical Science and Engineering, 2013. **7**(1): p. 20-28.
8. Torzilli, G., F. Botea, F. Procopio, M. Donadon, L. Balzarini, F. Lutman, F. Calliada, and M. Montorsi, *Use of contrast-enhanced intraoperative ultrasonography during liver surgery for colorectal cancer liver metastases – Its impact on operative outcome. Analysis of a prospective cohort study.* European Journal of Cancer Supplements, 2008. **6**(11): p. 16-23.
9. Ramaswamy, K., V. Marx, D. Laser, T. Kenny, T. Chi, M. Bailey, M.D. Sorensen, R.H. Grubbs, and M.L. Stoller, *Targeted microbubbles: a novel application for the treatment of kidney stones.* BJU International, 2015. **116**(1): p. 9-16.
10. Unger, E.C., E. Hersh, M. Vannan, T.O. Matsunaga, and T. McCreery, *Local drug and gene delivery through microbubbles.* Progress in Cardiovascular Diseases, 2001. **44**(1): p. 45-54.
11. Sboros, V., *Response of contrast agents to ultrasound.* Advanced Drug Delivery Reviews, 2008. **60**(10): p. 1117-1136.
12. Thomas, D.H., P. Looney, R. Steel, N. Pelekasis, W.N. McDicken, T. Anderson, and V. Sboros, *Acoustic detection of microbubble resonance.* Applied Physics Letters, 2009. **94**(24): p. 243902.
13. Tsiglifis, K. and N.A. Pelekasis, *Nonlinear radial oscillations of encapsulated microbubbles subject to ultrasound: The effect of membrane constitutive law.* The Journal of the Acoustical Society of America, 2008. **123**(6): p. 4059-4070.
14. Blomley, M.J.K., J.C. Cooke, E.C. Unger, M.J. Monaghan, and D.O. Cosgrove, *Microbubble contrast agents: a new era in ultrasound.* BMJ, 2001. **322**(7296): p. 1222-1225.
15. Efthymiou, K., *Numerical study of the interaction of a microbubble with a wall, (PhD Thesis), Department of Mechanical Engineering*. 2015, University of Thessaly: Volos, (in Greek).
16. Marmottant, P., A. Bouakaz, N.d. Jong, and C. Quilliet, *Buckling resistance of solid shell bubbles under ultrasound.* The Journal of the Acoustical Society of America, 2011. **129**(3): p. 1231-1239.

17. Tsiglifis, K., *Numerical simulation of bubble dynamics in response to acoustic disturbances, PhD Thesis*, in *Department of Mechanical Engineering*. 2007, University of Thessaly: Volos.
18. van der Meer, S.M., B. Dollet, M.M. Voormolen, C.T. Chin, A. Bouakaz, N. de Jong, M. Versluis, and D. Lohse, *Microbubble spectroscopy of ultrasound contrast agents.* The Journal of the Acoustical Society of America, 2007. **121**(1): p. 648-656.
19. Vlachomitrou, M. and N. Pelekasis, *Dynamic simulation of a coated microbubble in an unbounded flow: Response to a step change in pressure.* Journal of Fluid Mechanics, Submitted 2016.
20. Binnig, G., C.F. Quate, and C. Gerber, *Atomic Force Microscope.* Physical Review Letters, 1986. **56**(9): p. 930-933.
21. Passeri, D., M. Rossi, E. Tamburri, and M.L. Terranova, *Mechanical characterization of polymeric thin films by atomic force microscopy based techniques.* Analytical and Bioanalytical Chemistry, 2013. **405**(5): p. 1463-1478.
22. Dokukin, Maxim E., Nataliia V. Guz, and I. Sokolov, *Quantitative Study of the Elastic Modulus of Loosely Attached Cells in AFM Indentation Experiments.* Biophysical Journal, 2013. **104**(10): p. 2123-2131.
23. Marchetti, M., G.J.L. Wuite, and W.H. Roos, *Atomic force microscopy observation and characterization of single virions and virus-like particles by nano-indentation.* Current Opinion in Virology, 2016. **18**: p. 82-88.
24. Fery, A. and R. Weinkamer, *Mechanical properties of micro- and nanocapsules: Single-capsule measurements.* Polymer, 2007. **48**(25): p. 7221-7235.
25. Lulevich, V.V., D. Andrienko, and O.I. Vinogradova, *Elasticity of polyelectrolyte multilayer microcapsules.* The Journal of Chemical Physics, 2004. **120**(8): p. 3822-3826.
26. Sboros, V., E. Glynos, S.D. Pye, C.M. Moran, M. Butler, J. Ross, R. Short, W.N. McDicken, and V. Koutsos, *Nanointerrogation of ultrasonic contrast agent microbubbles using atomic force microscopy.* Ultrasound in Medicine & Biology, 2006. **32**(4): p. 579-585.
27. Glynos, E., V. Sboros, and V. Koutsos, *Polymeric thin shells: Measurement of elastic properties at the nanometer scale using atomic force microscopy.* Materials Science and Engineering: B, 2009. **165**(3): p. 231-234.
28. Butt, H.-J., B. Cappella, and M. Kappl, *Force measurements with the atomic force microscope: Technique, interpretation and applications.* Surface Science Reports, 2005. **59**(1–6): p. 1-152.
29. Glynos, E., V. Koutsos, W.N. McDicken, C.M. Moran, S.D. Pye, J.A. Ross, and V. Sboros, *Nanomechanics of Biocompatible Hollow Thin-Shell Polymer Microspheres.* Langmuir, 2009. **25**(13): p. 7514-7522.
30. Buchner Santos, E., J.K. Morris, E. Glynos, V. Sboros, and V. Koutsos, *Nanomechanical Properties of Phospholipid Microbubbles.* Langmuir, 2012. **28**(13): p. 5753-5760.
31. Ottoboni, T., E. Tickner, R. Short, and R. Yamamoto, *Hollow microspheres with controlled fragility for medical use*. 2007, Google Patents.
32. Reissner, E., *Stresses and Small Displacements of Shallow Spherical Shells. II.* Journal of Mathematics and Physics, 1946. **25**(1-4): p. 279-300.
33. Reissner, E., *Stresses and Small Displacements of Shallow Spherical Shells. I.* Journal of Mathematics and Physics, 1946. **25**(1-4): p. 80-85.
34. Pogorelov, A.V., *Bendings of Surfaces and Stability of Shells*. 1988: American Mathematical Society.
35. Israelachvili, J.N., *Intermolecular and Surface Forces*. 2010: Elsevier Science.

36. Middleman, S., *Modeling axisymmetric flows : dynamics of films, jets, and drops*. 1995: San Diego : Academic Press, [1995].
37. Timoshenko, S. and S. Woinowsky-Krieger, *Theory of plates and shells*. 1959: McGraw-Hill.
38. Tsiglifis, K. and N.A. Pelekasis, *Parametric stability and dynamic buckling of an encapsulated microbubble subject to acoustic disturbances.* Physics of Fluids (1994-present), 2011. **23**(1): p. 012102-1-012102-28.
39. Zarda, P.R., S. Chien, and R. Skalak, *Elastic deformations of red blood cells.* Journal of Biomechanics, 1977. **10**(4): p. 211-221.
40. Landau, L.D., E.M. Lifshitz, A.M. Kosevich, and L.P. Pitaevskiĭ, *Theory of Elasticity*. 1986: Butterworth-Heinemann.
41. Elsner, N., F. Dubreuil, R. Weinkamer, M. Wasicek, F.D. Fischer, and A. Fery, *Mechanical Properties of Freestanding Polyelectrolyte Capsules: a Quantitative Approach Based on Shell Theory*, in *Characterization of Polymer Surfaces and Thin Films*, K. Grundke, M. Stamm, and H.-J. Adler, Editors. 2006, Springer Berlin Heidelberg: Berlin, Heidelberg. p. 117-123.
42. Gao, C., E. Donath, S. Moya, V. Dudnik, and H. Möhwald, *Elasticity of hollow polyelectrolyte capsules prepared by the layer-by-layer technique.* The European Physical Journal E, 2001. **5**(1): p. 21-27.
43. Grant, C.A., J.E. McKendry, and S.D. Evans, *Temperature dependent stiffness and visco-elastic behaviour of lipid coated microbubbles using atomic force microscopy.* Soft Matter, 2012. **8**(5): p. 1321-1326.
44. Mettu, S., M. Zhou, B.L. Tardy, M. Ashokkumar, and R.R. Dagastine, *Temperature dependent mechanical properties of air, oil and water filled microcapsules studied by atomic force microscopy.* Polymer.
45. Hertz, H., *Über die berührung fester elastischer Körper.* In: Miscellaneous Papers. Jones and Schott, Editors, J. reine und angewandte Mathematik 92, Macmillan, London (1896), English translation: Hertz, H., 1882: p. 156.
46. Updike, D.P. and A. Kalnins, *Axisymmetric Behavior of an Elastic Spherical Shell Compressed Between Rigid Plates.* Journal of Applied Mechanics, 1970. **37**(3): p. 635-640.
47. Updike, D.P. and A. Kalnins, *Axisymmetric Postbuckling and Nonsymmetric Buckling of a Spherical Shell Compressed Between Rigid Plates.* Journal of Applied Mechanics, 1972. **39**(1): p. 172-178.
48. Updike, D.P. and A. Kalnins, *Contact Pressure Between an Elastic Spherical Shell and a Rigid Plate.* Journal of Applied Mechanics, 1972. **39**(4): p. 1110-1114.
49. Johnson, K.L., K. Kendall, and A.D. Roberts, *Surface Energy and the Contact of Elastic Solids.* Proceedings of the Royal Society of London. A. Mathematical and Physical Sciences, 1971. **324**(1558): p. 301-313.
50. Shanahan, M.E.R., *A Novel Test for the Appraisal of Solid/Solid Interfacial Interactions.* The Journal of Adhesion, 1997. **63**(1-3): p. 15-29.
51. Vella, D., A. Ajdari, A. Vaziri, and A. Boudaoud, *Wrinkling of Pressurized Elastic Shells.* Physical Review Letters, 2011. **107**(17): p. 174301.
52. Vaziri, A., *Mechanics of highly deformed elastic shells.* Thin-Walled Structures, 2009. **47**(6–7): p. 692-700.
53. Lac, E., D. Barthès-Biesel, N.A. Pelekasis, and J. Tsamopoulos, *Spherical capsules in three-dimensional unbounded Stokes flows: effect of the membrane constitutive law and onset of buckling.* Journal of Fluid Mechanics, 2004. **516**: p. 303-334.
54. Timoshenko, S., *Theory of elastic stability*. 1961: McGraw-Hill.

55. Koga, T. and N.J. Hoff, *The axisymmetric buckling of initially imperfect complete spherical shells.* International Journal of Solids and Structures, 1969. **5**(7): p. 679-697.
56. Flaherty, J.E., J.B. Keller, and S.I. Rubinow, *Post Buckling Behavior of Elastic Tubes and Rings with Opposite Sides in Contact.* SIAM Journal on Applied Mathematics, 1972. **23**(4): p. 446-455.
57. Walter, J., A.-V. Salsac, and D. Barthes-Biesel, *Ellipsoidal capsules in simple shear flow: prolate versus oblate initial shapes.* Journal of Fluid Mechanics, 2011. **676**: p. 318-347.
58. Ramanujan, S. and C. Pozrikidis, *Deformation of liquid capsules enclosed by elastic membranes in simple shear flow: large deformations and the effect of fluid viscosities.* Journal of Fluid Mechanics, 1998. **361**: p. 117-143.
59. Knoche, S. and J. Kierfeld, *Buckling of spherical capsules.* Physical Review E, 2011. **84**(4): p. 046608.
60. Young, T., *An Essay on the Cohesion of Fluids.* Philosophical Transactions of the Royal Society of London, 1805. **95**: p. 65-87.
61. Kalliadasis, S. and H.C. Chang, *Apparent dynamic contact angle of an advancing gas–liquid meniscus.* Physics of Fluids, 1994. **6**(1): p. 12-23.
62. Chamakos, N.T., M.E. Kavousanakis, and A.G. Papathanasiou, *Enabling efficient energy barrier computations of wetting transitions on geometrically patterned surfaces.* Soft Matter, 2013. **9**(40): p. 9624-32.
63. Blount, M.J., M.J. Miksis, and S.H. Davis, *The equilibria of vesicles adhered to substrates by short-ranged potentials.* Proceedings of the Royal Society of London A: Mathematical, Physical and Engineering Sciences, 2013. **469**(2153).
64. Cantat, I., K. Kassner, and C. Misbah, *Vesicles in haptotaxis with hydrodynamical dissipation.* Eur Phys J E Soft Matter, 2003. **10**(2): p. 175-89.
65. Leite, F.L., C.C. Bueno, A.L. Da Róz, E.C. Ziemath, and O.N. Oliveira, *Theoretical Models for Surface Forces and Adhesion and Their Measurement Using Atomic Force Microscopy.* International Journal of Molecular Sciences, 2012. **13**(10): p. 12773.
66. Weatherburn, C.E., *Differential geometry of three dimensions*. 1961: The University Press.
67. Pozrikidis, C., *Modeling and Simulation of Capsules and Biological Cells*. 2003: Taylor & Francis.
68. Barthès-Biesel, D., A. Diaz, and E. Dhenin, *Effect of constitutive laws for two-dimensional membranes on flow-induced capsule deformation.* Journal of Fluid Mechanics, 2002. **460**: p. 211-222.
69. Mooney, M., *A Theory of Large Elastic Deformation.* Journal of Applied Physics, 1940. **11**(9): p. 582-592.
70. Rivlin, R.S., *Large Elastic Deformations of Isotropic Materials. IV. Further Developments of the General Theory.* Philosophical Transactions of the Royal Society of London A: Mathematical, Physical and Engineering Sciences, 1948. **241**(835): p. 379-397.
71. Skalak, R., A. Tozeren, R.P. Zarda, and S. Chien, *Strain Energy Function of Red Blood Cell Membranes.* Biophysical Journal, 1973. **13**(3): p. 245-264.
72. Holzapfel, G.A., *Nonlinear Solid Mechanics: A Continuum Approach for Engineering*. 2000: Wiley.
73. Libai, A. and J.G. Simmonds, *The Nonlinear Theory of Elastic Shells*. 2005: Cambridge University Press.
74. Lac, E. and D. Barthès-Biesel, *Deformation of a capsule in simple shear flow: Effect of membrane prestress.* Physics of Fluids, 2005. **17**(7): p. 072105.

75. Pelekasis, N.A., J.A. Tsamopoulos, and G.D. Manolis, *Equilibrium shapes and stability of charged and conducting drops.* Physics of Fluids A: Fluid Dynamics (1989-1993), 1990. **2**(8): p. 1328-1340.
76. Prenter, P.M., *Splines and Variational Methods*. 1975: Wiley.
77. Bathe, K.J., *Finite Element Procedures in Engineering Analysis*. 1982: Prentice-Hall.
78. Reddy, J.N., *An Introduction to Nonlinear Finite Element Analysis*. 2004: OUP Oxford.
79. Stroud, A.H. and D.U. Secrest, *Gaussian quadrature formulas*. 1966: Prentice-Hall.
80. Vrahatis, M., *Numerical Analysis*. 2002: Ελληνικά γράμματα, (in Greek).
81. Binous, H. and A.A. Shaikh, *Introduction of the arc-length continuation technique in the chemical engineering graduate program at KFUPM.* Computer Applications in Engineering Education, 2015. **23**(3): p. 344-351.
82. Pelekasis, N., *A study on drop and bubble dynamics via a hybrid boundary - element-finite element methodology, PhD Thesis, State University of New York at Buffalo* 1991.
83. Segers, T., L. de Rond, N. de Jong, M. Borden, and M. Versluis, *Stability of Monodisperse Phospholipid-Coated Microbubbles Formed by Flow-Focusing at High Production Rates.* Langmuir, 2016. **32**(16): p. 3937-3944.
84. Lytra, A., *Numerical study of the static response of coated microbubbles subject to distributed load incliding the gas compressibility, (Master Thesis), Department of Mechanical Engineering*. 2013, University of Thessaly: Volos, (in Greek).
85. Paul, S., A. Katiyar, K. Sarkar, D. Chatterjee, W.T. Shi, and F. Forsberg, *Material characterization of the encapsulation of an ultrasound contrast microbubble and its subharmonic response: Strain-softening interfacial elasticity model.* The Journal of the Acoustical Society of America, 2010. **127**(6): p. 3846-3857.
86. Tsigklifis, K. and N.A. Pelekasis, *Simulations of insonated contrast agents: Saturation and transient break-up.* Physics of Fluids (1994-present), 2013. **25**(3): p. -.
87. Lytra, A. and N. Pelekasis, *Static response and stability of coated microbubbles—multiplicity of solutions and parameter estimation.* Fluid Dynamics Research, 2014. **46**(4): p. 041422.
88. Lytra, A., N. Pelekasis, V. Sboros, E. Glynos, and V. Koutsos, *Static Response of Coated Microbubbles: Modeling Simulations and Parameter Estimation.* Procedia IUTAM, 2015. **16**: p. 123-133.
89. Lytra, A., N. Pelekasis, V. Zafiropoulou, T. Zisis, A. Giannakopoulos, V. Sboros, E. Glynos, and V. Koutsos, *Static response of coated microbubbles: Modelling simulations and parameter estimation*, in *8th GRACM*. 2015: Volos.
90. Aristeia, *Characterization of microbubbles with elastic coating (contrast agents) for medical imaging applications and drug delivery via ultrasound, using theoretical & computational analysis of their static & dynamic response*, in *3rd Biannual Project Report*, http://contrast-aristeia.mie.uth.gr, Editor. 2015, University of Thessaly.
91. Pauchard, L., Y. Pomeau, and S. Rica, *Déformation des coques élastiques* C. R. Acad. Sci. Paris, Mécanique des solides et des structures, 1997. **Série II, b**: p. 411-418.
92. Shorter, R., J.D. Smith, V.A. Coveney, and J.J.C. Busfield, *Axial compression of hollow elastic spheres.* Journal of Mechanics of Materials and Structures, 2010. **5**(5): p. 693-705.
93. Hildebrand, F.B., *Methods of Applied Mathematics*. 2012: Dover Publications.

Appendix A: Derivation of unit vectors and curvatures

Spherical representation (r, θ, φ) [66]

The covariant tangent vectors along the s and φ direction are defined as:

$$\vec{t}_s = \frac{\partial \vec{R}}{\partial s} = \frac{\partial \left(r\vec{e}_r \right)}{\partial s} = \frac{\partial r}{\partial s}\vec{e}_r + r\frac{\partial \vec{e}_r}{\partial s} = r_s\vec{e}_r + r\theta_s\vec{e}_\theta$$

$$\vec{t}_\varphi = \frac{\partial \vec{R}}{\partial \varphi} = \frac{\partial \left(r\vec{e}_r \right)}{\partial \varphi} = \frac{\partial r}{\partial \varphi}\vec{e}_r + r\frac{\partial \vec{e}_r}{\partial \varphi} = 0\vec{e}_r + r\sin\theta\vec{e}_\varphi = r\sin\theta\vec{e}_\varphi$$

Therefore, the normal unit vector is:

$$\vec{n} = \frac{\vec{t}_s \times \vec{t}_\varphi}{\left| \vec{t}_s \times \vec{t}_\varphi \right|} = \frac{r\theta_s\vec{e}_r - r_s\vec{e}_\theta}{\sqrt{r_s^2 + r^2\theta_s^2}} = r\theta_s\vec{e}_r - r_s\vec{e}_\theta, \qquad \left(\sqrt{r_s^2 + r^2\theta_s^2} = 1 \right)$$

The contravariant vectors are given by the next formula:

$$\vec{t}^{\,i} = \frac{(-1)^j \vec{t}_j \times \vec{n}}{\left| \vec{t}_1 \cdot \vec{t}_2 \times \vec{n} \right|}, \quad \text{where } i, j = 1,2 \left(\text{or } s \text{ and } \varphi \right) \text{ and } i \neq j$$

Which by substituting of the covariant vectors, become:

$$\vec{t}^{\,s} = \vec{t}_s \text{ and } \vec{t}^{\,\varphi} = \frac{1}{r\sin\theta}\vec{e}_\varphi$$

Then the surface gradient operator is:

$$\vec{\nabla}_s = \sum_{i=1}^{2} \vec{t}^{\,i} \frac{\partial}{\partial u_i} = \vec{t}^{\,s}\frac{\partial}{\partial s} + \vec{t}^{\,\varphi}\frac{\partial}{\partial \varphi}$$

The principal curvatures k_s and k_φ are:

$$k_s = \vec{t}^{\,s} \cdot \frac{\partial \vec{n}}{\partial s} =$$

$$= \vec{t}^{\,s} \cdot \frac{1}{\sqrt{r_s^2 + r^2\theta_s^2}} \left[\left(2r_s\theta_s + r\theta_{ss} + r\theta_s A \right)\vec{e}_r + \left(r\theta_s^2 - r_{ss} - r_s A \right)\vec{e}_\theta \right] =$$

$$= \frac{r_s^2\theta_s + r\left(r_s\theta_{ss} - r_{ss}\theta_s \right)}{\sqrt{r_s^2 + r^2\theta_s^2}} + \theta_s\sqrt{r_s^2 + r^2\theta_s^2}, \quad A = rr_s\theta_s^2 + r^2\theta_s\theta_{ss} + r_s r_{ss}$$

$$k_\varphi = \vec{t}^{\,\varphi} \cdot \frac{\partial \vec{n}}{\partial \varphi} = \vec{t}^{\,\varphi} \cdot \frac{r\theta_s\sin\theta - r_s\cos\theta}{\sqrt{r_s^2 + r^2\theta_s^2}}\vec{e}_\varphi = \frac{1}{\sqrt{r_s^2 + r^2\theta_s^2}} \left(\theta_s + \frac{r_s\cot\theta}{r} \right)$$

The infinitesimal arc length along the generative curve is: $ds = \sqrt{r_s^2 + r^2\theta_s^2}$ and it is related with the lagrangian variable ξ via the chain rule: $s_\xi = \frac{ds}{d\xi} = \sqrt{r_\xi^2 + r^2\theta_\xi^2}$.

Cylindrical representation (σ, z, φ) [66]

The covariant tangent vectors along the s and φ direction (spherical) are defined as:

$$\vec{t}_s = \frac{\partial \vec{R}}{\partial s} = \frac{\partial\left(\sigma\vec{e}_\sigma + z\vec{e}_z\right)}{\partial s} = \frac{\partial \sigma}{\partial s}\vec{e}_\sigma + \frac{\partial z}{\partial s}\vec{e}_z = \sigma_s\vec{e}_\sigma + z_s\vec{e}_z$$

$$\vec{t}_\varphi = \frac{\partial \vec{R}}{\partial \varphi} = \frac{\partial\left(\sigma\vec{e}_\sigma + z\vec{e}_z\right)}{\partial \varphi} = \sigma\vec{e}_\varphi$$

Therefore, the normal unit vector is:

$$\vec{n} = \frac{\vec{t}_s \times \vec{t}_\varphi}{\left|\vec{t}_s \times \vec{t}_\varphi\right|} = \frac{\sigma_s\vec{e}_z - z_s\vec{e}_\sigma}{\sqrt{\sigma_s^2 + z_s^2}} = \sigma_s\vec{e}_z - z_s\vec{e}_\sigma, \qquad \left(\sqrt{\sigma_s^2 + z_s^2} = 1\right)$$

The contravariant vectors are given by the next formula:

$$\vec{t}^{\,i} = \frac{(-1)^j \vec{t}_j \times \vec{n}}{\left|\vec{t}_1 \cdot \vec{t}_2 \times \vec{n}\right|}, \quad \text{where } i, j = 1,2 \left(\text{or } s \text{ and } \varphi\right) \text{ and } i \neq j$$

Which by substituting of the covariant vectors, become:

$$\vec{t}^{\,s} = \vec{t}_s \text{ and } \vec{t}^{\,\varphi} = \frac{1}{\sigma}\vec{e}_\varphi$$

Then the surface gradient operator is:

$$\vec{\nabla}_s = \sum_{i=1}^{2} \vec{t}^{\,i}\frac{\partial}{\partial u_i} = \vec{t}^{\,s}\frac{\partial}{\partial s} + \vec{t}^{\,\varphi}\frac{\partial}{\partial \varphi}$$

The principal curvatures k_s and k_φ are:

$$k_s = \vec{t}^{\,s} \cdot \frac{\partial \vec{n}}{\partial s} =$$

$$= \vec{t}^{\,s} \cdot \left(\frac{\sigma_{ss}\vec{e}_z - z_{ss}\vec{e}_\sigma}{\sqrt{\sigma_s^2 + z_s^2}} - \frac{\left(\sigma_s\vec{e}_z - z_s\vec{e}_\sigma\right)\left(\sigma_s\sigma_{ss} + z_s z_{ss}\right)}{\sqrt{\sigma_s^2 + z_s^2}^{\,3}} \right) = \frac{\sigma_{ss}z_s - \sigma_s z_{ss}}{\sqrt{\sigma_s^2 + z_s^2}^{\,3}}$$

$$k_\varphi = \vec{t}^{\,\varphi} \cdot \frac{\partial \vec{n}}{\partial \varphi} = \vec{t}^{\,\varphi} \cdot \frac{-z_s}{\sqrt{\sigma_s^2 + z_s^2}}\vec{e}_\varphi = \frac{-z_s}{\sigma\sqrt{\sigma_s^2 + z_s^2}}$$

The infinitesimal arc length along the generative curve is: $ds = \sqrt{\sigma_s^2 + z_s^2}$ and it is related with the lagrangian variable ξ via the chain rule: $s_\xi = \frac{ds}{d\xi} = \sqrt{\sigma_\xi^2 + z_\xi^2}$.

The above expressions for both spherical and cylindrical coordinates could also be obtained by the first and second fundamental forms of the surface.

Appendix B: Minimization of the energy due to intermolecular forces for axisymmetric body

The energy due to intermolecular forces is: $\hat{w}_{IF} = \iint_A W_{IF}\, dA$, therefore, its variation for an axisymmetric shell in cylindrical (σ, z, φ) coordinates is:

$$\delta\hat{w}_{IF} = \iint_A \vec{\nabla} W_{IF} \cdot \delta\vec{r}\, dA + \iint_A W_{IF}\, \frac{\delta(dA)}{\delta\vec{r}} \cdot \delta\vec{r} \;=$$
$$= \int_0^1 2\pi\, \vec{\nabla} W_{IF}\, \sigma\sqrt{\sigma_\xi^2 + z_\xi^2} \cdot \delta\vec{r}\, d\xi + \int_0^1 2\pi\, W_{IF}\, \frac{\delta\left(\sigma\sqrt{\sigma_\xi^2 + z_\xi^2}\right)}{\delta\vec{r}} \cdot \delta\vec{r}\, d\xi \tag{B-1}$$

The first term assumes the form:

$$\vec{\nabla} W_{IF} = \cancel{\frac{\partial W_{IF}}{\partial\sigma}}_{\,0}\, \vec{e}_\sigma + \frac{\partial W_{IF}}{\partial z}\vec{e}_z = \frac{\partial W_{IF}}{\partial z}\vec{e}_z = \frac{\partial W_{IF}}{\partial z}\left(z_s\vec{t}_s + \sigma_s\vec{n}\right) = \frac{\partial W_{IF}}{\partial s}\vec{t}_s + \frac{\partial W_{IF}}{\partial n}\vec{n}\,. \tag{B-2}$$

Employing the general rule of variation [93]

$\delta F(x, y, x', y') = \frac{\partial F}{\partial x}\delta x + \frac{\partial F}{\partial y}\delta y + \frac{\partial F}{\partial x'}\delta x' + \frac{\partial F}{\partial y'}\delta y'$, $(\;)' = \frac{d}{d\xi}$, where ξ is an independent parameter, that does not vary, the variation of the metric becomes:

$$\delta g = \int_0^1 2\pi W_{IF}\, \frac{\delta\left(\sigma\sqrt{\sigma_\xi^2 + z_\xi^2}\right)}{\delta\vec{r}}\, d\xi =$$
$$= \int_0^1 2\pi \left[W_{IF}\sqrt{\sigma_\xi^2 + z_\xi^2}\,\delta\sigma + W_{IF}\sigma\frac{1}{2}\frac{2\sigma_\xi}{\sqrt{\sigma_\xi^2 + z_\xi^2}}\delta\sigma_\xi + W_{IF}\sigma\frac{1}{2}\frac{2z_\xi}{\sqrt{\sigma_\xi^2 + z_\xi^2}}\delta z_\xi \right] d\xi \;=$$
$$= \int_0^1 2\pi \left[W_{IF}\sqrt{\sigma_\xi^2 + z_\xi^2}\,\delta\sigma - \frac{d}{d\xi}\left(\frac{\sigma\sigma_\xi W_{IF}}{\sqrt{\sigma_\xi^2 + z_\xi^2}}\right)\delta\sigma - \frac{d}{d\xi}\left(\frac{\sigma z_\xi W_{IF}}{\sqrt{\sigma_\xi^2 + z_\xi^2}}\right)\delta z \right] d\xi +$$
$$+ \underbrace{\left(\frac{2\pi\sigma\sigma_\xi W_{IF}}{\sqrt{\sigma_\xi^2 + z_\xi^2}}\delta\sigma + \frac{2\pi\sigma z_\xi W_{IF}}{\sqrt{\sigma_\xi^2 + z_\xi^2}}\delta z \right)_0^1}_{=0 \text{ for a closed body}} \Rightarrow$$

$$\delta g = \int_0^1 2\pi W_{IF} \sqrt{\sigma_\xi^2 + z_\xi^2}\, \delta\sigma\, d\xi +$$

$$+\int_0^1 2\pi \left[\left(-\frac{\sigma\sigma_\xi}{\sqrt{\sigma_\xi^2 + z_\xi^2}} \frac{dW_{IF}}{d\xi} - W_{IF} \frac{\left(\sigma_\xi^2 + \sigma\sigma_{\xi\xi}\right)\left(\sigma_\xi^2 + z_\xi^2\right) - \sigma\sigma_\xi\left(\sigma_\xi\sigma_{\xi\xi} + z_\xi z_{\xi\xi}\right)}{\left(\sigma_\xi^2 + z_\xi^2\right)^{3/2}} \right) \delta\sigma \right] d\xi \qquad \text{(B-3)}$$

$$+\int_0^1 2\pi \left[\left(-\frac{\sigma z_\xi}{\sqrt{\sigma_\xi^2 + z_\xi^2}} \frac{dW_{IF}}{d\xi} - W_{IF} \frac{\left(\sigma_\xi z_\xi + \sigma z_{\xi\xi}\right)\left(\sigma_\xi^2 + z_\xi^2\right) - \sigma z_\xi\left(\sigma_\xi\sigma_{\xi\xi} + z_\xi z_{\xi\xi}\right)}{\left(\sigma_\xi^2 + z_\xi^2\right)^{3/2}} \right) \delta z \right] d\xi$$

The integrals in (B-3) represent the components of a vector in σ and z direction, which has the following form $\int_0^1 \left(A_\sigma\, \delta\sigma + A_z\, \delta z\right) d\xi = \int_0^1 \left(A_\sigma\, \vec{e}_\sigma + A_z\, \vec{e}_z\right) \cdot \left(\delta\sigma \vec{e}_\sigma + \delta z \vec{e}_z\right) d\xi = \int_0^1 \vec{A} \cdot \delta\vec{r}\, d\xi$.

Alternatively, it is possible to express $\vec{A}$ in the normal (n) and tangential (s) directions $\vec{A} = A_n \vec{n} + A_s \vec{t}_s$ by taking the inner products $\vec{A} \cdot \vec{n}$, $\vec{A} \cdot \vec{t}_s$, and add the result to eq B-1 containing the variation of the interaction potential W_{IF}.

Consequently, the above integral formally reads as:

$$\delta g = \int_0^1 \left(A_n\, \vec{n} + A_s\, \vec{t}_s\right) \cdot \delta\vec{r}\, d\xi \qquad \text{(B-4)}$$

and in the following we proceed to obtain A_n and A_s:

$$A_s = 2\pi W_{IF}\sqrt{\sigma_\xi^2+z_\xi^2}\,\sigma_s +$$

$$+2\pi\left[\left(-\frac{\sigma\sigma_\xi}{\sqrt{\sigma_\xi^2+z_\xi^2}}\frac{dW_{IF}}{d\xi}-W_{IF}\frac{\left(\sigma_\xi^2+\sigma\sigma_{\xi\xi}\right)\left(\sigma_\xi^2+z_\xi^2\right)-\sigma\sigma_\xi\left(\sigma_\xi\sigma_{\xi\xi}+z_\xi z_{\xi\xi}\right)}{\left(\sigma_\xi^2+z_\xi^2\right)^{3/2}}\right)\sigma_s\right]$$

$$+2\pi\left[\left(-\frac{\sigma z_\xi}{\sqrt{\sigma_\xi^2+z_\xi^2}}\frac{dW_{IF}}{d\xi}-W_{IF}\frac{\left(\sigma_\xi z_\xi+\sigma z_{\xi\xi}\right)\left(\sigma_\xi^2+z_\xi^2\right)-\sigma z_\xi\left(\sigma_\xi\sigma_{\xi\xi}+z_\xi z_{\xi\xi}\right)}{\left(\sigma_\xi^2+z_\xi^2\right)^{3/2}}\right)z_s\right]=$$

$$=2\pi\left[-\frac{\sigma\left(\sigma_s\sigma_\xi+z_s z_\xi\right)}{\sqrt{\sigma_\xi^2+z_\xi^2}}\frac{dW_{IF}}{d\xi}\right]+$$

$$+2\pi\left[W_{IF}\sqrt{\sigma_\xi^2+z_\xi^2}\,\sigma_s-W_{IF}\sigma_s\frac{\left(\sigma_\xi^2+\sigma\sigma_{\xi\xi}\right)\left(\sigma_\xi^2+z_\xi^2\right)-\sigma\sigma_\xi\left(\sigma_\xi\sigma_{\xi\xi}+z_\xi z_{\xi\xi}\right)}{\left(\sigma_\xi^2+z_\xi^2\right)^{3/2}}\right]-$$

$$-2\pi W_{IF}z_s\frac{\left(\sigma_\xi z_\xi+\sigma z_{\xi\xi}\right)\left(\sigma_\xi^2+z_\xi^2\right)-\sigma z_\xi\left(\sigma_\xi\sigma_{\xi\xi}+z_\xi z_{\xi\xi}\right)}{\left(\sigma_\xi^2+z_\xi^2\right)^{3/2}}=$$

$$=-2\pi\sigma\frac{dW_{IF}}{ds}\sqrt{\sigma_\xi^2+z_\xi^2}+2\pi W_{IF}\left[\frac{\sigma_\xi\left(\sigma_\xi^2+z_\xi^2\right)^2-\sigma_\xi\left(\sigma_\xi^2+\sigma\sigma_{\xi\xi}\right)\left(\sigma_\xi^2+z_\xi^2\right)+\sigma\sigma_\xi^2\left(\sigma_\xi\sigma_{\xi\xi}+z_\xi z_{\xi\xi}\right)}{\left(\sigma_\xi^2+z_\xi^2\right)^2}\right]$$

$$+2\pi W_{IF}\left[\frac{-z_\xi\left(\sigma_\xi z_\xi+\sigma z_{\xi\xi}\right)\left(\sigma_\xi^2+z_\xi^2\right)+\sigma z_\xi^2\left(\sigma_\xi\sigma_{\xi\xi}+z_\xi z_{\xi\xi}\right)}{\left(\sigma_\xi^2+z_\xi^2\right)^2}\right]$$

$$=-2\pi\sigma\frac{dW_{IF}}{ds}\sqrt{\sigma_\xi^2+z_\xi^2}$$

$$+2\pi W_{IF}\frac{\overbrace{\left(\sigma_\xi^2+z_\xi^2\right)\left[\sigma_\xi\left(\sigma_\xi^2+z_\xi^2\right)-\sigma_\xi\left(\sigma_\xi^2+\sigma\sigma_{\xi\xi}\right)-z_\xi\left(\sigma_\xi z_\xi+\sigma z_{\xi\xi}\right)+\sigma\left(\sigma_\xi\sigma_{\xi\xi}+z_\xi z_{\xi\xi}\right)\right]}^{=0}}{\left(\sigma_\xi^2+z_\xi^2\right)^2}\Rightarrow$$

$$\boxed{A_s=-2\pi\frac{dW_{IF}}{ds}\sqrt{\sigma_\xi^2+z_\xi^2}\,\sigma} \qquad \text{(B-5)}$$

In the same way, the projection in normal direction is:

$$A_n =$$

$$2\pi\left[W_{IF}\sqrt{\sigma_\xi^2+z_\xi^2}\,(-z_s)-\frac{\sigma\sigma_\xi}{\sqrt{\sigma_\xi^2+z_\xi^2}}\frac{dW_{IF}}{d\xi}(-z_s)-W_{IF}\frac{\left(\sigma_\xi^2+\sigma\sigma_{\xi\xi}\right)\left(\sigma_\xi^2+z_\xi^2\right)-\sigma\sigma_\xi\left(\sigma_\xi\sigma_{\xi\xi}+z_\xi z_{\xi\xi}\right)}{\left(\sigma_\xi^2+z_\xi^2\right)^{3/2}}(-z_s)\right]$$

$$+2\pi\left[-\frac{\sigma z_\xi}{\sqrt{\sigma_\xi^2+z_\xi^2}}\frac{dW_{IF}}{d\xi}\sigma_s-W_{IF}\frac{\left(\sigma_\xi z_\xi+\sigma z_{\xi\xi}\right)\left(\sigma_\xi^2+z_\xi^2\right)-\sigma z_\xi\left(\sigma_\xi\sigma_{\xi\xi}+z_\xi z_{\xi\xi}\right)}{\left(\sigma_\xi^2+z_\xi^2\right)^{3/2}}\sigma_s\right]$$

$$=2\pi\frac{dW_{IF}}{d\xi}\frac{\sigma\left(\sigma_\xi z_s-z_\xi\sigma_s\right)}{\sqrt{\sigma_\xi^2+z_\xi^2}}$$

$$+2\pi\left[-W_{IF}z_s\sqrt{\sigma_\xi^2+z_\xi^2}+W_{IF}z_s\frac{\left(\sigma_\xi^2+\sigma\sigma_{\xi\xi}\right)\left(\sigma_\xi^2+z_\xi^2\right)-\sigma\sigma_\xi\left(\sigma_\xi\sigma_{\xi\xi}+z_\xi z_{\xi\xi}\right)}{\left(\sigma_\xi^2+z_\xi^2\right)^{3/2}}\right]$$

$$-2\pi W_{IF}\sigma_s\frac{\left(\sigma_\xi z_\xi+\sigma z_{\xi\xi}\right)\left(\sigma_\xi^2+z_\xi^2\right)-\sigma z_\xi\left(\sigma_\xi\sigma_{\xi\xi}+z_\xi z_{\xi\xi}\right)}{\left(\sigma_\xi^2+z_\xi^2\right)^{3/2}}$$

$$=2\pi\frac{dW_{IF}}{d\xi}\frac{\overbrace{\sigma\left(\sigma_\xi z_\xi-z_\xi\sigma_\xi\right)}^{=0}}{\sqrt{\sigma_\xi^2+z_\xi^2}}\frac{d\xi}{ds}$$

$$+2\pi\frac{d\xi}{ds}\left[-W_{IF}z_\xi\sqrt{\sigma_\xi^2+z_\xi^2}+W_{IF}z_\xi\frac{\left(\sigma_\xi^2+\sigma\sigma_{\xi\xi}\right)\left(\sigma_\xi^2+z_\xi^2\right)-\sigma\sigma_\xi\cancel{\left(\sigma_\xi\sigma_{\xi\xi}+z_\xi z_{\xi\xi}\right)}}{\left(\sigma_\xi^2+z_\xi^2\right)^{3/2}}\right]$$

$$-2\pi W_{IF}\frac{d\xi}{ds}\sigma_\xi\frac{\left(\sigma_\xi z_\xi+\sigma z_{\xi\xi}\right)\left(\sigma_\xi^2+z_\xi^2\right)-\sigma z_\xi\cancel{\left(\sigma_\xi\sigma_{\xi\xi}+z_\xi z_{\xi\xi}\right)}}{\left(\sigma_\xi^2+z_\xi^2\right)^{3/2}}=$$

$$=2\pi W_{IF}\frac{d\xi}{ds}\sigma\sqrt{\sigma_\xi^2+z_\xi^2}\left[-\frac{z_\xi}{\sigma}+\frac{\sqrt{\sigma_\xi^2+z_\xi^2}\left[z_\xi\left(\cancel{\sigma_\xi^2}+\sigma\sigma_{\xi\xi}\right)-\sigma_\xi\left(\cancel{\sigma_\xi z_\xi}+\sigma z_{\xi\xi}\right)\right]}{\sigma\left(\sigma_\xi^2+z_\xi^2\right)^{3/2}}\right]=$$

$$=2\pi W_{IF}\sigma\sqrt{\sigma_\xi^2+z_\xi^2}\left[-\frac{z_\xi}{\sigma\sqrt{\sigma_\xi^2+z_\xi^2}}+\frac{\sigma_{\xi\xi}z_\xi-\sigma_\xi z_{\xi\xi}}{\left(\sigma_\xi^2+z_\xi^2\right)^{3/2}}\right]=2\pi W_{IF}\left[\underbrace{-\frac{z_s}{\sigma\sqrt{\sigma_s^2+z_s^2}}}_{k_s}+\underbrace{\frac{\sigma_{ss}z_s-\sigma_s z_{ss}}{\left(\sigma_s^2+z_s^2\right)^{3/2}}}_{k_\varphi}\right]\sigma\Rightarrow$$

$$\boxed{A_n=2\pi W_{IF}\sigma\sqrt{\sigma_\xi^2+z_\xi^2}\,2k_m} \tag{B-6}$$

Thus, substituting (B-2), (B-5) and (B-6) into (B-1):

$$\delta\hat{w}_{IF}=\iint_A\left(\frac{\partial W_{IF}}{\partial s}\vec{t}_s+\frac{\partial W_{IF}}{\partial n}\vec{n}\right)\cdot\delta\vec{r}\;dA+\iint_A\left(-\frac{dW_{IF}}{ds}\vec{t}_s+W_{IF}\,2k_m\,\vec{n}\right)\cdot\delta\vec{r}\;dA\Rightarrow$$

$$\boxed{\delta\hat{w}_{IF}=\iint_A\left(\frac{\partial W_{IF}}{\partial n}+2k_mW_{IF}\right)\vec{n}\cdot\delta\vec{r}\;dA} \tag{B-7}$$